

Effect of the Sediment Layer on the Excitation of Acoustic Modes and Lateral Waves in Shallow Sea

E. L. Borodina and Yu. V. Petukhov

*Institute of Applied Physics, Russian Academy of Sciences, ul. Ul'yanova 46,
Nizhni Novgorod, 603600 Russia
e-mail: bel@hydro.appl.sci-nnov.ru*

Received June 17, 1999

Abstract—The simplest model of a shallow sea in the form of an isovelocity water layer and a fluid sediment layer overlying a homogeneous elastic halfspace is used to investigate the effect of the thickness of the sediment layer and the sound velocity in it on the behavior of the frequency dependences of the amplitudes of trapped and leaky modes and shear and longitudinal lateral waves that are excited by an acoustic point source in a shallow-water oceanic waveguide. © 2000 MAIK “Nauka/Interperiodica”.

It is well known that the acoustic field formed in an oceanic waveguide can be represented as a superposition of modes that belong to a discrete spatial spectrum and to a continuous one [1–3]. In the framework of the integral representation of the acoustic field in a plane-layered waveguide with the use of the approach to the deformation of the path of integration in the complex plane from [1–3], the modes of the discrete spectrum are represented by the residues at the poles of the integrand. These poles are the roots of the dispersion equation for the corresponding waveguide system and are usually called modes. Naturally, the dispersion equation may have both real and complex roots [2, 3], where the former correspond to the trapped modes and the latter correspond to the leaky ones (quasi-modes [3]) responsible for the reradiation of energy to the bottom of the oceanic waveguide. The modes belonging to the continuous spatial spectrum of the field are represented by the integrals over the edges of the corresponding cuts originating from the branch (ambiguity) points of the integrand, and these modes correspond to lateral waves [1–3].

Evidently, because of the additional exponential decay of the leaky modes and the faster decrease in the amplitudes of lateral waves with distance as compared to the trapped modes [2, 3], the acoustic field formed in an oceanic waveguide at large distances from the source will mainly be determined by the trapped modes [1–3]. However, from general considerations, one can expect that, even at relatively small distances, the effect of the leaky modes and lateral waves on the formation of the spatial interference structure of the acoustic field in an oceanic waveguide will be noticeable only in the case of the propagation of a small number of modes. Therefore, the determination of the contribution of leaky modes and lateral waves to the total field is possible only for relatively low radiation frequencies and, hence, on the background of a small number of trapped modes [4–6]. In real oceanic waveguides, the conditions corresponding to the propagation of a small num-

ber of modes at relatively low radiation frequencies are usually observed in shallow-water regions of the ocean [7], because the number of trapped modes decreases with decreasing water depth, as well as with decreasing radiation frequency.

Since the propagation of acoustic waves in shallow-water oceanic waveguides is strongly affected by the ocean bottom, it is important to study the dependence of the contributions of the leaky modes and lateral waves to the total field on the geoacoustic parameters of the bottom. For the simplest situations, namely, for the shallow sea bottom modeled by a homogeneous fluid halfspace, the effects of the leaky modes [5, 6] and lateral waves [5, 6, 8–10] on the formation of the spatial interference structure of the acoustic field had been investigated earlier. However, similar studies with the use of the bottom model in the form of a homogeneous elastic halfspace were performed only for longitudinal and shear waves [10–12] the effect of which (according to [12]) is noticeable only near the critical frequencies of the corresponding leaky and trapped modes. Evidently, the results of such investigations are absent even for the simplest single-layer model of the fluid sediment layer of the sea bottom with a fluid or elastic base (bedrock). It should be noted that the effect of geoacoustic parameters of the fluid sediment layer on the frequency dependence of the excitation of only trapped modes was adequately investigated in the framework of the fluid base model [1, 13–17] and was not considered in detail in the framework of the model with an elastic base [13, 18, 19]. Therefore, the aim of our work is to study the effect of the thickness of the sediment layer and the sound velocity in it on the behavior of the frequency dependences of the amplitudes of modes and lateral waves excited by a point source in a shallow-water oceanic waveguide that is modeled by an isovelocity water layer and a fluid sediment layer overlying a homogeneous elastic halfspace.

To solve this problem, we proceed from the following assumptions. Firstly, a point source emitting an acoustic signal of frequency f is positioned at a depth z_s in an isovelocity water layer with thickness H , sound velocity c , and water density ρ ; a receiver is positioned in the same water layer at a depth z_r . Secondly, a fluid sediment layer with thickness h , sound velocity c_s , and density ρ_s overlies a homogeneous elastic halfspace with velocities c_t and c_l of shear and longitudinal waves, respectively, and a density ρ_l . Then, by virtue of the cylindrical symmetry of the problem, in the corresponding coordinate system (r, z) , where r is the horizontal distance and z is the vertical axis originating at the water surface and directed upwards, the solution for the sound pressure in the water layer can be represented in the form [3, 11–13]

$$p' = p_m R_0 \varphi(k, r) e^{-i\omega t}, \quad (1)$$

where

$$\varphi(k, r) = \int_{-\infty}^{\infty} \psi(\xi) H_0^{(1)}(\xi r) \xi d\xi \quad (2)$$

is the displacement potential and p_m is the pressure amplitude generated by the point source in free space on a spherical surface of radius R_0 . Here, $H_0^{(1)}(\xi r)$ is the Hankel function of the first kind; ξ is the projection of the wave vector on the r axis; $\omega = 2\pi f$ is the cyclic frequency; $k = \omega/c$; t is time; and the expression for $\psi(\xi)$ is determined from the boundary conditions, which imply a zero sound pressure at the free (upper) surface of the water layer $z = 0$, the continuity of the vertical component of the particle velocity and pressure at its lower boundary $z = -H$, and the continuity of the vertical components of the particle velocity and stress tensor and the zero values of the tangential components of the stress tensor at the lower boundary of the sediment layer $z = -(H + h)$:

$$\psi(\xi) = \frac{2v \Phi(x_1) \sin(z_r x/H)}{k \Phi(x) \gamma_1}, \quad z_s \leq z_r \leq 0, \quad (3)$$

$$\begin{aligned} \Phi(x) = S \frac{\gamma_4}{\gamma_1} \sin(x) [Rb^4 v^4 \gamma_2 \cos(x_2) - S\gamma_4 g \sin(x_2)] \\ + \cos(x) [Rb^4 v^4 \gamma_2 \sin(x_2) + S\gamma_4 g \cos(x_2)]. \end{aligned} \quad (4)$$

In expressions (3) and (4), the following notation is used for convenience:

$$\begin{aligned} R = \rho/\rho_l, \quad S = \rho/\rho_s, \quad a = c/c_l, \quad b = c/c_t, \\ d = c/c_s, \quad v = k/\xi, \end{aligned}$$

$$\gamma_1 = \sqrt{v^2 - 1}, \quad \gamma_2 = \sqrt{1 - a^2 v^2},$$

$$\gamma_3 = \sqrt{1 - b^2 v^2}, \quad \gamma_4 = \sqrt{1 - v^2 d^2},$$

$$x = kH\gamma_1/v, \quad x_1 = (z_s + H)x/H,$$

$$x_2 = kh\gamma_4/v, \quad g = (1 + \gamma_3^2)^2 - 4\gamma_2\gamma_3.$$

For $-H \leq z_r \leq z_s$, the expression for $\psi(\xi)$ is obtained from expression (3) by interchanging z_s and z_r (see [12]).

As in our previous publications [11, 12], we analyze expression (2) by using the standard procedure for the transformation of this kind of integrals [1–3]. Then, the integration from $-\infty$ to ∞ will be reduced to the determination of the residues at the singular points of the integrand and to the calculation of the integrals over the edges of the cuts originating from the branch points $\xi = ak$, $\xi = bk$, and $\xi = dk$. Since the integrand (3) is symmetric with respect to the substitution of $-\gamma_4$ for γ_4 , the integral taken over the edges of the cut corresponding to the point $\xi = kd$ is zero. As a result, expression (2) for $\varphi(k, r)$ can be represented as a sum of three terms:

$$\varphi(k, r) = \varphi_{\text{mod}}(k, r) + \varphi_l(k, r) + \varphi_t(k, r), \quad (5)$$

where $\varphi_{\text{mod}}(k, r)$ corresponds to the modes, and $\varphi_l(k, r)$ and $\varphi_t(k, r)$ correspond to the longitudinal and shear lateral waves, respectively.

As was mentioned above, $\varphi_{\text{mod}}(k, r)$ is determined by the sum of residues at the poles of the integrand from expression (2). Therefore, from formulas (2) and (3) with the use of the Hankel function asymptotics for $\xi r \gg 1$, we obtain

$$\varphi_{\text{mod}}(k, r) = \frac{1}{\sqrt{r}} \sum_{m=0}^M A_m e^{ikr/v_m}, \quad (6)$$

where

$$A_m = 2 \sqrt{\frac{2\pi k D_1(v_m)}{i D_2(v_m)}} \sin(z_s x_m/H) \sin(z_r x_m/H); \quad (7)$$

$$\begin{aligned} D_1(v) = iS\gamma_4^2 [Rb^4 v^4 \gamma_2 \cos(x_2) \\ - S\gamma_4 g \sin(x_2)] / (v \cos(x)), \end{aligned}$$

$$D_2(v) = S \sin(x) \left[Rb^4 v^4 \cos(x_2) \right.$$

$$\left. \times \left(\gamma_1 \gamma_2 - \gamma_4 \left(\frac{\gamma_1}{\gamma_2} + \frac{\gamma_2}{\gamma_1} \right) \right) \right]$$

$$+ S\gamma_1 \gamma_4 \cos(x_2) \left(g \left(\frac{\gamma_4^2}{\gamma_1^2} - 2 \right) - 4\gamma_4^2 q \right) \Big]$$

$$+ \frac{S\gamma_4^2 k}{v \cos(x)} \left(H + Sh \left(\sin^2(x) + \frac{\gamma_1^2}{S^2 \gamma_4^2} \cos(x) \right) \right)$$

$$\times (Rb^4 v^4 \cos(x_2) - S\gamma_4 g \sin(x_2))$$

$$- \frac{\gamma_1^2}{\gamma_2} \cos(x) (Rb^4 v^4 \gamma_4 \sin(x_2) - S(g + 4\gamma_4^2 q) \gamma_2 \cos(x_2)),$$

$$q = 2\gamma_2 \gamma_3 + \frac{\gamma_2}{\gamma_3} + \frac{\gamma_3}{\gamma_2} - 2(1 + \gamma_3^2).$$

Here, M is the total number of modes whose contributions are taken into account, $x_m = x(v_m)$, and v_m are dimensionless (normalized to c) phase velocities of modes with the numbers $m = 0, 1, 2, \dots$; these velocities are the solutions to the dispersion equation

$$\Phi(x) = 0 \quad (8)$$

for the radiation frequencies exceeding the critical frequencies f_m of the modes. For the zeroth (fundamental) mode with $m = 0$, the critical frequency is $f_0 = 0$, and for other trapped modes with the numbers $m = 1, 2, \dots$, the critical frequencies $f_m = f_{t,m}$ are determined from the following equation obtained at $v_m = b$:

$$\tan(x_3) = -\Omega_1 \left(1 + \frac{(1 + \Omega_2^2) \tan(x_4)}{\Omega_2(1 - \Omega_2 \tan(x_4))} \right), \quad (9)$$

where

$$\Omega_1 = \frac{\sqrt{1-b^2}}{R\sqrt{b^2-a^2}}, \quad \Omega_2 = \frac{S\sqrt{d^2-b^2}}{R\sqrt{b^2-a^2}}, \quad (10)$$

$$x_3 = kH\sqrt{1-b^2}, \quad x_4 = kh\sqrt{d^2-b^2}.$$

If we take into account only a finite number of leaky modes whose contributions to the total field is substantial, namely, the modes whose reradiation into the elastic halfspace is caused by the presence of the shear wave in it, we can determine the approximate values of the phase velocities and critical frequencies of the modes with a sufficient degree of accuracy.

In this connection, we note that the reradiation of energy through leaky modes into shear waves occurs for the following interval of the angles of incidence of the Brillouin waves corresponding to these modes: $\arcsin(a) \leq \theta \leq \arcsin(b)$, i.e., the interval within which the total internal reflection of the aforementioned incident waves from the lower boundary of the sediment layer is absent. The same modes exist in the form of trapped modes in the absence of shear waves ($c_t = 0$), which is caused by the total internal reflection of the corresponding Brillouin waves from the lower boundary of the sediment layer in the range of the angles of incidence $\arcsin(a) \leq \theta \leq \pi/2$. The real part of the phase velocity $v_{R,m} = \text{Re}\{v_m\}$ of each of these leaky modes can be determined within the range of values

$$\begin{cases} 1/b \leq v_{R,m} < 1/a, & (b < 1) \\ 1 \leq v_{R,m} < 1/a, & (b > 1) \end{cases} \quad (11)$$

with fair accuracy from the dispersion equation corresponding to the three-layer fluid waveguide model [13]

$$\tan(kHv_1) \left[\frac{R}{S} v_3 + \mu v_2 T \right] = -\frac{v_1}{Sv_2} \left[v_2 + \frac{R}{S} v_3 T \right], \quad (12)$$

where

$$v_1 = \frac{\sqrt{v_{R,m}^2 - 1}}{v_{R,m}},$$

$$v_2 = \begin{cases} \sqrt{v_{R,m}^2 d^2 - 1}/v_{R,m}, & v_{R,m} > 1/d \\ \sqrt{1 - v_{R,m}^2 d^2}/v_{R,m}, & v_{R,m} < 1/d, \end{cases} \quad (13)$$

$$v_3 = \frac{\sqrt{1 - a^2 v_{R,m}^2}}{v_{R,m}},$$

$$\mu = \begin{cases} -1, & v_{R,m} > 1/d \\ 1, & v_{R,m} < 1/d, \end{cases} \quad T = \begin{cases} \tan(khv_2), & v_{R,m} > 1/d \\ \tan(khv_2), & v_{R,m} < 1/d. \end{cases}$$

Naturally, every value of $v_{R,m}$ determined from equation (12) will be a fair approximation for the determination of the exact value of the complex quantity $v_m = v_{R,m} - iv_{I,m}$ from the dispersion equation (8). The imaginary part $v_{I,m}$ of this quantity is responsible for the radiation of energy through the corresponding mode to the elastic halfspace. The critical frequencies of the corresponding leaky modes $f = f_{p,m}$ can be determined with sufficient accuracy from the equation

$$\tan(kH\sqrt{1-a^2}) \tan(kh\sqrt{d^2-a^2}) = \frac{1}{S} \sqrt{\frac{1-a^2}{d^2-a^2}}, \quad (14)$$

which is obtained from equation (12) at $v_{R,m} = 1/a$.

Here, it is appropriate to note that, as will be seen from the results of the numerical simulation described below, such an approach to the determination of the frequency dependences of $v_{R,m}$ and $v_{I,m}$ in the framework of the specific oceanic waveguide model has certain advantages over the approach based on the introduction of an effective complex depth [20–22].

Now, we consider the contributions of the longitudinal $\phi_l(k, r)$ and shear $\phi_s(k, r)$ lateral waves, which (according to the above description and [1–3, 11, 12]) are determined by the following integral expressions obtained from formulas (2)–(4):

$$\phi_l(k, r) = 2RS^2 b^4 k^4 \int_{ak+i0}^{ak+i\infty} \frac{\sin(z_s x/H) \sin(z_r x/H) \gamma_2 \gamma_4^2 (b^2 k^2 - 2\xi^2)^2 H_0^{(1)}(\xi r) d\xi}{S^2 \gamma_4^2 (b^2 k^2 - 2\xi^2)^4 X_1^2 - [Rb^4 k^4 X_2 - 4S\gamma_3 \gamma_4 \xi^4 X_1]^2 \gamma_2^2}, \quad (15)$$

$$\varphi_l(k, r) = 8RS^2b^4k^4 \int_{bk+i0}^{bk+i\infty} \frac{\sin(z_s x/H) \sin(z_r x/H) \gamma_2^2 \gamma_3^2 \gamma_4^2 \xi^4 H_0^{(1)}(\xi r) d\xi}{[Rb^4k^4\gamma_2X_2 + S(b^2k^2 - 2\xi^2)^2\gamma_4X_1]^2 - 16S^2\gamma_2^2\gamma_3^2\gamma_4^2\xi^8X_1^2}, \quad (16)$$

where

$$X_1 = -S\gamma_4 \sin(x) \sin(x_2) + \gamma_1 \cos(x) \cos(x_2),$$

$$X_2 = S\gamma_4 \sin(x) \cos(x_2) + \gamma_1 \cos(x) \sin(x_2).$$

To obtain the approximate expressions that are convenient for the integration and to determine the analytical dependences $\varphi_l(k, r)$ and $\varphi_t(k, r)$ resulting from them, we perform an approximate analysis of expressions (15) and (16). We begin with the study of the longitudinal lateral wave. Restricting our consideration to the first term of the known asymptotic expansion of the Hankel function for large values of its argument and applying the change of variables as in the method of steepest descent [1–3, 11, 12]

$$\xi = ak + i\eta^2/r, \quad (17)$$

we represent the expression for the longitudinal lateral wave (15) in the form of an integral with respect to the new real variable $\eta \in [0, \infty)$:

$$\varphi_l(k, r) = \frac{4\sqrt{2}i}{\sqrt{\pi r}} e^{iakr} RS^2b^4 \int_0^\infty \frac{P_l(\eta)}{Q_l(\eta)} \eta^2 e^{-\eta^2} d\eta, \quad (18)$$

where

$$P_l(\eta) = (d^2 - T_l^2)(b^2 - 2T_l^2)^2 \times \sqrt{T_l(a + T_l)} \sin(x_{l,z_s}/H) \sin(x_{l,z_r}/H),$$

$$Q_l(\eta) = krS^2(b^2 - 2T_l^2)^4 (d^2 - T_l^2) X_{1,l}^2 + i[iRb^4X_{2,l} - 4S\sqrt{b^2 - T_l^2}\sqrt{d^2 - T_l^2}T_l^2X_{1,l}]^2 (a + T_l)\eta^2,$$

$$X_{1,l} = -S\sqrt{d^2 - T_l^2} \sin(x_l) \sin(x_{2,l}) + \sqrt{1 - T_l^2} \cos(x_l) \cos(x_{2,l}),$$

$$X_{2,l} = S\sqrt{d^2 - T_l^2} \sin(x_l) \cos(x_{2,l}) + \sqrt{1 - T_l^2} \cos(x_l) \sin(x_{2,l}),$$

$$x_l = kH\sqrt{1 - T_l^2}, \quad x_{2,l} = kh\sqrt{d^2 - T_l^2},$$

$$T_l = a + i\eta^2/(kr).$$

From the analysis of the behavior of the integrand in (18), it follows that the presence of the exponential factor in this function limits the significant range of integration in expression (18) to relatively small values of the integration variable $\eta \leq \eta_{\max}$, where η_{\max} is about several units. Thus, the approximate expression (18) not only considerably simplifies the numerical calculations

for $\varphi_l(k, r)$, but also allows one to obtain the corresponding analytical dependences. At large distances from the source $kr \gg 1$, we can assume that the ratio $\zeta = \eta^2/(kr) \ll 1$ is small. Then, we can restrict our consideration to the zeroth and first terms of the expansions of the functions $P_l(\eta)$ and $Q_l(\eta)$ in powers of ζ , provided that the following conditions are met:

$$\left\{ \begin{array}{l} \frac{4a\eta_{\max}^2}{kr(b^2 - 2a^2)} \ll 1, \quad \frac{2a\eta_{\max}^2}{kr(1 - a^2)} \ll 1, \quad \frac{2a\eta_{\max}^2}{kr(d^2 - a^2)} \ll 1 \\ \frac{\eta_{\max}^2}{kr} \ll 1, \quad \frac{H}{r} \frac{a\eta_{\max}^2}{\sqrt{1 - a^2}} \ll 1, \quad \frac{h}{r} \frac{a\eta_{\max}^2}{\sqrt{d^2 - a^2}} \ll 1. \end{array} \right. \quad (19)$$

Performing the approximate transformations corresponding to conditions (19) for the integrand from (18), we obtain an expression for the longitudinal lateral wave in the form that is more convenient for analytical calculations:

$$\varphi_l(k, r) = \frac{8i Rab^4 \sin(x_{a,z_s}/H) \sin(x_{a,z_r}/H)}{\sqrt{\pi} (b^2 - 2a^2)^2 X_{1,a}^2} \times \frac{e^{iakr}}{kr^2} \int_0^\infty \frac{\eta^2 e^{-\eta^2} d\eta}{F_1(\eta)}, \quad (20)$$

where

$$X_{1,a} = -S\sqrt{d^2 - a^2} \sin(x_a) \sin(x_{2,a}) + \sqrt{1 - a^2} \cos(x_a) \cos(x_{2,a}),$$

$$X_{2,a} = S\sqrt{d^2 - a^2} \sin(x_a) \cos(x_{2,a}) + \sqrt{1 - a^2} \cos(x_a) \sin(x_{2,a}),$$

$$x_a = kH\sqrt{1 - a^2}, \quad x_{2,a} = kh\sqrt{d^2 - a^2},$$

$$F_1(\eta) = 1 + i\alpha\eta^2/(kr),$$

$$\alpha = \frac{2a}{(b^2 - 2a^2)^4} \left[\frac{iRb^4X_{2,a}}{S\sqrt{d^2 - a^2}X_{1,a}} - 4a^2\sqrt{b^2 - a^2} \right]^2.$$

In the derivation of the final analytical dependences for $\varphi_l(k, r)$, we consider two limiting situations (as in [1–3, 11, 12, 23]). First, if, in addition to conditions (19), the conditions

$$\left\{ \begin{array}{l} |\alpha|\eta_{\max}^2/(kr) \ll 1 \\ X_{1,a} \neq 0 \end{array} \right. \quad (21)$$

are met, we assume that $F_1(\eta) \approx 1$ and, performing the integration in expression (20), by analogy with [2] we obtain

$$\varphi_l(k, r) \approx \frac{2iRab^4 \sin(x_a z_s/H) \sin(x_a z_r/H) e^{iakr}}{(b^2 - 2a^2)^2 X_{1,a}^2 kr^2}. \quad (22)$$

Second, if the conditions opposite to (21) are met:

$$\begin{cases} |\alpha|\eta_{\max}^2/(kr) \gg 1 \\ X_{1,a} \rightarrow 0, \end{cases} \quad (23)$$

which is possible when the radiation frequency tends to the critical frequency of one of the leaky modes, $f \rightarrow f_{p,m}$ (where the critical frequency is determined from equation (14) identical with the equality $X_{1,a} = 0$), we obtain $F_1(\eta) \approx i\alpha\eta^2/(kr)$. Performing the integration in expression (20), by analogy with [2] we obtain

$$\begin{aligned} \varphi_l(k, r) &\approx -\frac{2S^2}{Rb^4} (d^2 - a^2)(b^2 - 2a^2)^2 \\ &\times \frac{\sin(x_a z_s/H) \sin(x_a z_r/H) e^{iakr}}{X_{2,a}^2 r}. \end{aligned} \quad (24)$$

To derive the corresponding approximate dependences for the shear wave field, we use the same approach as in the analysis of the expression for $\varphi_l(k, r)$ (15); namely, we use the asymptotics of the Hankel function for $\xi r \gg 1$ and a change of variables similar to (17) and typical of the method of steepest descent:

$$\xi = bk + i\eta^2/r. \quad (25)$$

As a result, expression (16) takes the form

$$\varphi_t(k, r) \approx -\frac{16\sqrt{2}i}{\sqrt{\pi}r} RS^2 b^4 e^{ibkr} \int_0^\infty \frac{P_t(\eta)}{Q_t(\eta)} \eta^2 e^{-\eta^2} d\eta, \quad (26)$$

where

$$\begin{aligned} P_t(\eta) &= (a^2 - T_t^2)(d^2 - T_t^2) T_t^{5/2} \sqrt{b + T_t} \\ &\times \sin(x_t z_s/H) \sin(x_t z_r/H), \\ Q_t(\eta) &= kr[iRb^4 \sqrt{a^2 - T_t^2} X_{2,t} \\ &- S(b^2 - 2T_t^2)^2 \sqrt{(d^2 - T_t^2)} X_{1,t}]^2 \\ &+ i16S^2(a^2 - T_t^2)(d^2 - T_t^2)(b + T_t) T_t^4 X_{1,t}^2 \eta^2, \\ X_{1,t} &= -S\sqrt{d^2 - T_t^2} \sin(x_t) \sin(x_{2,t}) \\ &+ \sqrt{1 - T_t^2} \cos(x_t) \cos(x_{2,t}), \end{aligned}$$

$$\begin{aligned} X_{2,t} &= S\sqrt{d^2 - T_t^2} \sin(x_t) \cos(x_{2,t}) \\ &+ \sqrt{1 - T_t^2} \cos(x_t) \sin(x_{2,t}), \\ x_t &= kH\sqrt{1 - T_t^2}, \quad x_{2,t} = kh\sqrt{d^2 - T_t^2}, \\ T_t &= a + i\eta^2/(kr). \end{aligned}$$

Here, it should be noted that, as expression (18), expression (26) is convenient for numerical integration owing to the fast decay of the integrand with growing η .

Assuming that, at large distances from the source $kr \gg 1$, the conditions

$$\begin{cases} \frac{2b\eta_{\max}^2}{kr(b^2 - 2a^2)} \ll 1, \quad \frac{2b\eta_{\max}^2}{kr(1 - b^2)} \ll 1, \quad \frac{2b\eta_{\max}^2}{kr(d^2 - b^2)} \ll 1 \\ \frac{\eta_{\max}^2}{kr} \ll 1, \quad \frac{H}{r} \frac{b\eta_{\max}^2}{\sqrt{1 - b^2}} \ll 1, \quad \frac{h}{r} \frac{b\eta_{\max}^2}{\sqrt{d^2 - b^2}} \ll 1 \end{cases} \quad (27)$$

are met and performing approximate transformations of the integrand in (26) in the same way as in going from expression (18) to expression (20), we obtain an approximate formula for the displacement potential of the shear lateral wave:

$$\begin{aligned} \varphi_t(k, r) &\approx \frac{iRb^2 \beta \sin(x_b z_s/H) \sin(x_b z_r/H)}{\sqrt{\pi} X_{1,b}^2} \\ &\times \frac{e^{ibkr}}{kr^2} \int_0^\infty \frac{\eta^2 e^{-\eta^2} d\eta}{F_2(\eta)}, \end{aligned} \quad (28)$$

where

$$\begin{aligned} X_{1,b} &= -S\sqrt{d^2 - b^2} \sin(x_b) \sin(x_{2,b}) \\ &+ \sqrt{1 - b^2} \cos(x_b) \cos(x_{2,b}), \\ X_{2,b} &= S\sqrt{d^2 - b^2} \sin(x_b) \cos(x_{2,b}) \\ &+ \sqrt{1 - b^2} \cos(x_b) \sin(x_{2,b}), \\ x_b &= kH\sqrt{1 - b^2}, \quad x_{2,b} = kh\sqrt{d^2 - b^2}, \\ F_2(\eta) &= 1 - i\beta\eta^2/(kr), \\ \beta &= \frac{32(b^2 - a^2)}{b^3 Q^2}, \quad Q = \frac{RX_{2,b}}{SX_{1,b}} \sqrt{\frac{b^2 - a^2}{d^2 - b^2}} + 1. \end{aligned}$$

Suppose that, in addition to conditions (27), the situation under study meets the conditions

$$\begin{cases} \beta\eta_{\max}^2/(kr) \ll 1 \\ Q(f) \neq 0, \end{cases} \quad (29)$$

which occur at frequencies widely different from the critical frequencies of trapped modes, $f \neq f_{t,m}$ (where the critical frequencies are determined from equation (9) identical with the equality $Q(f) = 0$). Then, we can assume that $F_2(\eta) \approx 1$, and, by analogy with [2], from expression (28) we obtain

$$\varphi_t(k, r) \approx \frac{i}{4} R b^2 \beta \frac{\sin(x_b z_s / H) \sin(x_b z_r / H) e^{i b k r}}{X_{1,b}^2 k r^2}. \quad (30)$$

If the conditions opposite to conditions (29) are met, i.e., if the frequency is a critical one $f = f_{t,m}$, we assume that $F_2(\eta) \approx -i \beta \eta^2 / (k r)$, and, by analogy with [2], from expression (28) we obtain

$$\varphi_t(k, r) \approx -\frac{R b^2 \sin(x_b z_s / H) \sin(x_b z_r / H) e^{i b k r}}{2 X_{1,b}^2 r}. \quad (31)$$

The approximate analytical dependences obtained for the displacement potentials of the longitudinal (22), (24) and shear (30), (31) lateral waves allow us to make some qualitative conclusions concerning the relative contributions of these waves to the total field.

Near the critical frequencies of the leaky $f = f_{p,m}$ and trapped $f = f_{t,m}$ modes, the amplitudes of the longitudinal and shear lateral waves, respectively, decrease with distance much slower, namely, as $\varphi_l(k, r) \sim 1/r$ (24) and $\varphi_s(k, r) \sim 1/r$ (31), than at other frequencies at which the dependences $\varphi_l(k, r) \sim 1/r^2$ (22) and $\varphi_s(k, r) \sim 1/r^2$ (30) take place. Hence, at large distances from the source, the frequency dependences of the amplitudes $|\varphi_l(k, r)|$ (15) and $|\varphi_s(k, r)|$ (16) of lateral waves should exhibit narrow, quasi-resonance peaks at the corresponding characteristic frequencies $f = f_{p,m}$ and $f = f_{t,m}$. The characteristic widths of the peaks, $\Delta f_{p,m}(r)$ and $\Delta f_{t,m}(r)$, decrease with distance and with increasing order number of the critical frequency, because, in both these cases, the dimensionless parameter, which governs the

corresponding asymptotic behavior of $|\varphi_l(k, r)|$ and $|\varphi_s(k, r)|$, increases: $k r \gg 1$.

Owing to the described features of the behavior of lateral waves (for a lateral wave in a waveguide with a homogeneous fluid bottom, these features were described earlier in [2]), a pulsed excitation of the waveguide will be accompanied by a narrow-band filtering in the longitudinal and shear wave pulses.

Expressions (6), (18), and (26) derived above allow us to study the effect of the sediment layer on the frequency dependences of the excitation amplitudes of trapped and leaky modes (6), as well as longitudinal (18) and shear (26) lateral waves.

To perform the corresponding numerical calculations, we use the acoustic parameters of the shallow-water oceanic waveguide and the transmission and reception depths that correspond to the conditions of the full-scale experiments [11, 12, 18]: $c = 1538$ m/s, $c_s = 1700$ m/s, $c_t = 2400$ m/s, $c_l = 4000$ m/s, $\rho = 1 \times 10^3$ kg/m³, $\rho_s = 1.6 \times 10^3$ kg/m³, $\rho_l = 3 \times 10^3$ kg/m³, $H = 45$ m, $h = 0-20$ m, $|z_s| = 12$ m, and $|z_r| = 39$ m. As in our previous publications [11, 12, 18], we restrict ourselves to studying the behavior of $\varphi_{\text{mod}}(k, r)$ (6), $\varphi_l(k, r)$ (18), and $\varphi_s(k, r)$ (26) in the low-frequency range $0 < f < 60$ Hz within which the corresponding types of waves noticeably affect the formation of the space-frequency interference structure of the acoustic field. To simplify the comparison of the calculated values, we consider the frequency dependences of the normalized amplitudes of trapped A_c and leaky A_b modes and shear A_t and longitudinal A_l lateral waves:

$$A_c = |A_m|/A, \quad A_b = |A_m| \exp\left(-\frac{k r}{|v_m|^2} v_{l,m}\right)/A, \quad (32)$$

$$A_t = \sqrt{r} |\varphi_t(k, r)|/A, \quad A_l = \sqrt{r} |\varphi_l(k, r)|/A.$$

In formulas (32), the amplitudes are normalized to the maximum value A of the sum of the amplitudes of trapped modes in the frequency range under study, $0 < f \leq 60$ Hz, in the absence of the sediment layer ($h = 0$):

$$A = \max \left\{ \sum_m |A_m| \right\}_{h=0}. \quad (33)$$

The results of our numerical simulations are presented in Figs. 1–5. From the analysis of these results, we draw the following conclusions.

First (Fig. 1), with increasing sediment layer thickness h , the amplitude of the zeroth (seismic) mode steeply decreases in the lower-frequency part $0 < f < 40$ Hz of the frequency range under study and slightly increases at higher frequencies $f > 40$ Hz. According to our previous publication [25], a decrease in the sound velocity in the sediment layer by 100 m/s leads to a considerable decrease in the amplitude of this mode only for $f > 20$ Hz. Thus, in the frequency range $0 < f < 20$ Hz, the amplitude of the zeroth mode will be mainly

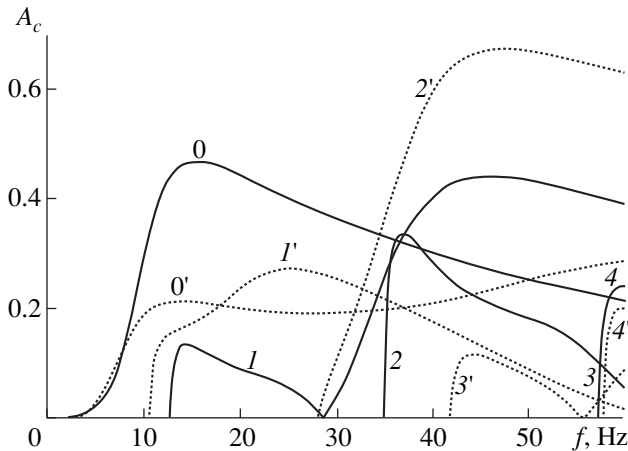


Fig. 1. Dependences of the normalized amplitudes of trapped modes A_c (32) on the frequency f for $h = 0$ (solid lines) and 20 m (dotted lines). The mode numbers are indicated near the corresponding curves.

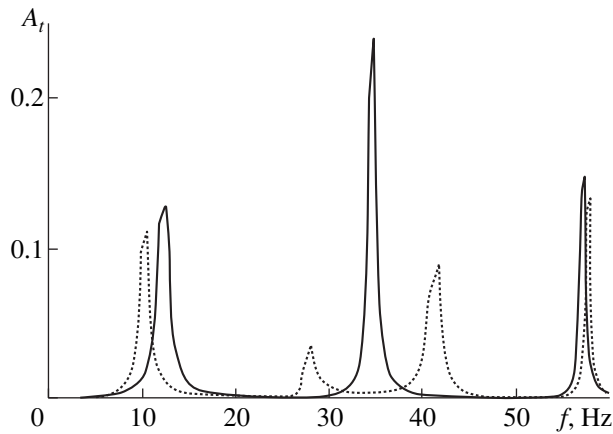


Fig. 2. Dependence of the normalized amplitude of the shear lateral wave A_t (32) on the frequency f at the distance $r = 20H$ for $h = 0$ (solid line) and 20 m (dotted line).

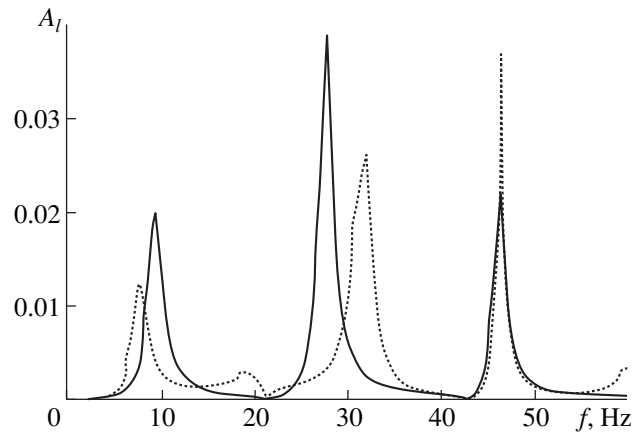


Fig. 3. Dependence of the normalized amplitude of the longitudinal lateral wave A_l (32) on the frequency f at the distance $r = 20H$ for $h = 0$ (solid line) and 20 m (dotted line).

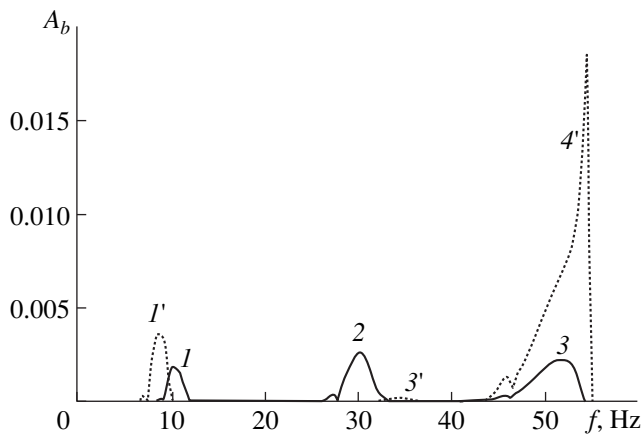


Fig. 4. Dependences of the normalized amplitudes of leaky modes A_b (32) on the frequency f at the distance $r = 20H$ for $h = 0$ (solid lines) and 20 m (dotted lines). The mode numbers are indicated near the corresponding curves.

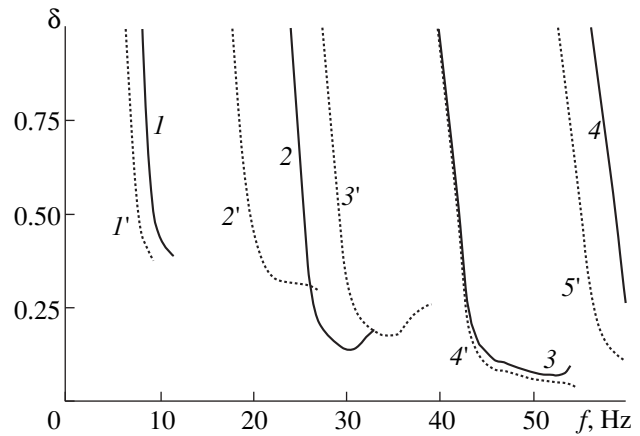


Fig. 5. Frequency dependences of the leaky mode reradiation (attenuation) coefficients $\delta = \frac{c_l}{|v_m|^2} v_{l,m}$ normalized to the longitudinal wave number $k_l = \omega/c_l$ for $h = 0$ (solid lines) and 20 m (dotted lines). The mode numbers are indicated near the corresponding curves.

determined by the sediment layer thickness with all other conditions being the same.

Second (Figs. 2, 3), the amplitude of the shear lateral wave is by almost an order of magnitude greater than the amplitude of the longitudinal lateral wave. With an increase in the sediment layer thickness, the narrow peaks in the frequency dependences of the amplitudes of the shear (at the critical frequencies of trapped modes $f = f_{t,m}$) and longitudinal (at characteristic frequencies of leaky modes $f = f_{p,m}$) lateral waves are shifted toward lower frequencies. Simultaneously, the height of the lowest-frequency peak of the shear lateral wave decreases by less than 30%, while the height of the corresponding peak of the longitudinal wave decreases. A decrease in the sound

velocity in the sediment layer leads to noticeable changes in the amplitudes of the shear and longitudinal lateral waves only in the higher-frequency range $f > 20$ Hz (see [25]). Naturally, the widths of all spectral peaks of lateral waves are considerably reduced with distance (see [25]).

Third (Figs. 4, 5), In the absence of the sediment layer, the leaky modes that occur in the frequency range under study within distances $r > 20H$ make a negligible contribution to the total field, and this contribution is by an order of magnitude less than even that of the longitudinal lateral waves. In addition, the frequency dependences of the leaky modes and the longitudinal lateral waves have different positions of the corresponding peaks. With increasing thickness of the sediment layer,

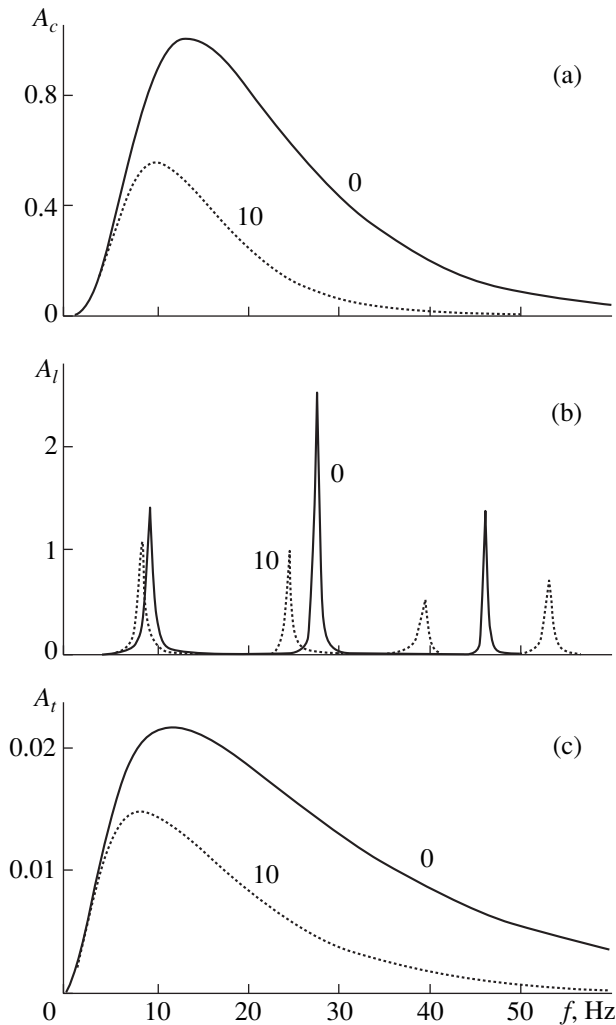


Fig. 6. Frequency dependences of the normalized amplitudes of (a) the zeroth mode A_c , (b) the longitudinal lateral wave A_l , and (c) the shear lateral wave A_t at the distance $r = 20H$ for $c_s = 1700$ m/s and $c_t = 1500$ m/s. The numbers near the curves indicate the corresponding values of the sediment layer thickness: $h = 0$ and 10 m.

the maximum values of the leaky mode amplitudes noticeably increase, this increase being the greater the higher the sound velocity in the sediment layer is (see [25]). However, because of the exponential decay of the leaky modes with distance, their contribution to the total field can be neglected for $r > 20H$.

Here, we should note an interesting fact: the frequency dependences of the attenuation (reradiation) coefficients of some leaky modes have single relative minima at certain frequencies (Fig. 5). With increasing sediment layer thickness, the number of leaky modes having such minima increases, and the corresponding minimum values of the attenuation coefficients first increase and then decrease. A slight decrease in the minimum values of the attenuation coefficients of leaky modes is also observed with a decrease in the sound velocity in the sediment layer.

On the basis of the above theoretical study of the behavior of the frequency dependences of the mode and lateral wave amplitudes in the specific propagation conditions [11, 12], one can conclude that the space-time interference structure of broadband sound that was observed in the experiments [11, 12] in the frequency range below the critical frequency of the first mode, $0 < f \leq f_{i,1}$, can be only caused by the interference of the seismic zeroth mode with the shear lateral wave. This conclusion is justified by the fact that, at such relatively low frequencies, the dominant contribution to the total field is made by the zeroth mode and the shear lateral wave whose amplitudes are comparable in magnitude for various allowed values of the sediment layer thickness.

Naturally, the above conclusions concerning the contributions of different types of waves to the total field are generally valid for shallow-water oceanic waveguides with acoustic parameters of the bottom of the same kind as those in the experiments [11, 12, 18], i.e., with $c_t > c$. However, the situation is entirely different when the sound velocity in water exceeds the shear wave velocity in the bottom. Already as $c_t \rightarrow c$, the critical frequencies of the trapped modes increase without bound: $f_{i,m} \rightarrow \infty$. Hence, for the velocities $c_t < c$, only one trapped mode will remain, namely, the zeroth mode corresponding to the Rayleigh surface wave modified by the presence of the water and sediment layers. This will result in the disappearance of the narrow peaks in the frequency dependence of the amplitude of the shear lateral wave. However, such peaks will remain for the longitudinal lateral wave, which now will predominate in amplitude (Fig. 6). With increasing thickness of the sediment layer, the only relatively wide peak in the frequency dependence of the amplitude of the shear lateral wave noticeably decreases in height and moves toward lower frequencies. Similar changes are observed in the corresponding dependence for the zeroth mode (Fig. 6).

Thus, in shallow-water oceanic waveguides with an elastic bottom, the fluid sediment layer substantially affects the frequency dependences of the amplitudes of the trapped and leaky modes, as well as shear and longitudinal lateral waves, not only at relatively high frequencies $f > c/H$, but also at relatively low frequencies $f < c/H$.

In closing, we note that, by now, there exist efficient methods that allow one to perform numerical calculations on the basis of the initial integral expressions for different parameters of acoustic fields in oceanic waveguides with a complex bottom structure (see, e.g., [24]). However, the known approximate methods used in this paper for determining the contributions of different types of waves to the total field (see [1–3]) remain of interest for the interpretation of the results of the corresponding numerical [24] and, in particular, of the full-scale [11, 12, 18] experiments.

ACKNOWLEDGMENTS

This work was supported by the Russian Foundation for Basic Research (project nos. 98-02-16402 and 98-05-64652) and the Competition Center for Basic Natural Sciences (no. 97-8.2-78).

REFERENCES

1. C. L. Pekeris, in *Propagation of Sound in the Ocean* (Waverly, Baltimore, 1948; Inostrannaya Literatura, Moscow, 1951).
2. Yu. L. Gazaryan, *Akust. Zh.* **4**, 233 (1958) [*Sov. Phys. Acoust.* **4**, 237 (1958)].
3. L. M. Brekhovskikh, *Waves in Layered Media* (Nauka, Moscow, 1973; Academic, New York, 1980).
4. D. C. Stickler, *J. Acoust. Soc. Am.* **57**, 856 (1975).
5. V. D. Krupin, *Vopr. Sudostr., Ser. Akust., No. 16*, 72 (1983).
6. V. D. Krupin, *Akust. Zh.* **40**, 626 (1994) [*Acoust. Phys.* **40**, 556 (1994)].
7. B. G. Katsnel'son and V. G. Petnikov, *Acoustics of Shallow Sea* (Nauka, Moscow, 1997).
8. E. Ammicht and D. C. Stickler, *J. Acoust. Soc. Am.* **67**, 2018 (1980).
9. A. V. Kondrashova, K. A. Pestov, and O. S. Tonakanov, *Vestn. Mosk. Univ., Ser. 3: Fiz., Astron.* **34** (6), 85 (1993).
10. O. M. Grudskaya, S. M. Grudskii, and E. A. Rivelis, *Akust. Zh.* **35**, 752 (1989) [*Sov. Phys. Acoust.* **35**, 437 (1989)].
11. E. L. Borodina and Yu. V. Petukhov, *Acoust. Lett.* **21**, 1 (1997).
12. E. L. Borodina and Yu. V. Petukhov, in *Proceedings of the Fourth European Conference on Underwater Acoustics* (CNR-IDAC, Rome, 1998), Vol. II, p. 781.
13. W. M. Ewing, W. S. Jardetsky, and F. Press, *Elastic Waves in Layered Media* (McGraw-Hill, New York, 1957).
14. N. S. Ageeva and V. D. Krupin, *Akust. Zh.* **27**, 669 (1981) [*Sov. Phys. Acoust.* **27**, 372 (1981)].
15. N. S. Ageeva and V. D. Krupin, *Akust. Zh.* **29**, 721 (1983) [*Sov. Phys. Acoust.* **29**, 427 (1983)].
16. N. S. Ageeva and V. D. Krupin, *Akust. Zh.* **34**, 391 (1988) [*Sov. Phys. Acoust.* **34**, 228 (1988)].
17. N. S. Ageeva and V. D. Krupin, *Akust. Zh.* **35**, 385 (1989) [*Sov. Phys. Acoust.* **35**, 229 (1989)].
18. E. L. Borodina and Yu. V. Petukhov, *Acoust. Lett.* **19**, 159 (1996).
19. N. R. Chapman, C. T. Tindle, and E. K. Westwood, *J. Acoust. Soc. Am.* **100**, 3631 (1996).
20. D. M. F. Chapman and P. D. Ward, *J. Acoust. Soc. Am.* **87**, 601 (1990).
21. C. T. Tindle and Z. Y. Zang, *J. Acoust. Soc. Am.* **93**, 205 (1993).
22. M. A. Ainslie, C. H. Harrison, and M. N. Packman, *J. Acoust. Soc. Am.* **103**, 1804 (1998).
23. L. S. Metlov, *Akust. Zh.* **30**, 507 (1984) [*Sov. Phys. Acoust.* **30**, 303 (1984)].
24. L. A. Bespalov, A. M. Derzhavin, A. V. Kudryavtsev, and A. G. Semenov, *Akust. Zh.* **45**, 25 (1999) [*Acoust. Phys.* **45**, 19 (1999)].
25. E. L. Borodina and Yu. V. Petukhov, Preprint No. 493, IPF RAN (Institute of Applied Physics, Russian Academy of Sciences, Nizhni Novgorod, 1999).

Translated by E. Golyamina

Improvement of the Focusing Quality by Parametric Phase Conjugation of Ultrasonic Beams in a Ferrite Cylinder with Grooved Working Surface

A. P. Brysev and L. M. Krutyanskiĭ

*Wave Research Center, General Physics Institute, Russian Academy of Sciences,
ul. Vavilova 38, Moscow, 117942 Russia*

e-mail: brysev@orc.ru, krut@orc.ru

Received June 11, 1999

Abstract—Results of direct measurements of the acoustic pressure distribution in a phase-conjugate ultrasonic beam in the focus of a converging lens are presented for two types of parametric phase-conjugating elements, namely, with flat and grooved working surfaces. It is demonstrated that grooving noticeably improves the quality of focusing of an ultrasonic beam generated in water by a solid phase-conjugating element.
© 2000 MAIK “Nauka/Interperiodica”.

Currently, researchers connect the progress in the utilization of the phenomenon of ultrasonic phase conjugation [1] mainly with such applications as acoustic microscopy [2, 3] and ultrasonic hyperthermia [4]. In these and many other cases of practical interest, focused acoustic beams propagating in a liquid or liquid-like media are used. We should note that, e.g., in hyperthermia, high-quality focusing must be provided for high-intensity and, therefore, nonlinear ultrasonic beams. Evidently, the possibility of the practical usage of phase-conjugating systems for such applications is determined in many respects by the quality of phase conjugation of focused ultrasonic beams, which is provided by these systems.

Parametric phase-conjugating systems operating beyond the threshold of the absolute parametric instability of acoustic oscillations are among the most promising devices. As it is known [1, 5], they are capable of real-time generation of phase-conjugate beams with an intensity several orders of magnitude higher than the intensity of an incident beam. The first quality studies of phase-conjugate ultrasound in parametric systems using polycrystalline ferrite materials were presented in our previous papers [6, 7]. It was demonstrated that considerable nonuniformity of the angular dependence of the efficiency of phase-conjugating conversion is inherent in cylindrical phase-conjugating elements with flat faces loaded by a liquid medium. This may lead to a deterioration in the quality of phase-conjugate beams with a broad spatial spectrum because of the unequal conversion of different spatial components of the incident beam spectrum. It was also found that the best results in smoothing off the angular dependence of the efficiency of phase-conjugating conversion are attained by using the effect of phase-conjugating compensation of the phase distortions, which are intro-

duced by inhomogeneities directly at the input to the phase-conjugating medium. In this case, it was possible to expand the angular range of the phase-conjugating conversion of plane waves incident from water upon the phase-conjugating element up to $\pm 16^\circ$ (at the level -3 dB) without introducing any additional loss.

However, the evaluation of the quality of phase conjugation by the form of the angular dependence of the efficiency of phase-conjugating conversion is not always convenient in practice. Therefore, a direct study of the phase-conjugating focusing for one or another specific conditions seems to be quite important.

This paper presents the results of direct measurements of the acoustic pressure distribution in a phase-conjugate ultrasonic beam in the focus of a converging lens for two types of the parametric phase-conjugating element: with flat and grooved working surfaces. It is demonstrated that grooving noticeably improves the quality of focusing of an ultrasonic beam generated in water by a solid phase-conjugating element.

The experimental scheme is given in Fig. 1. An ultrasonic pulse with the duration $20 \mu\text{s}$ and the carrier frequency $f = 6.23$ MHz is radiated into water by a focusing transducer (1) with the diameter 15 mm and the focal length 39 mm. The incident beam intensity is low, so that its propagation is purely linear. A cylindrical phase-conjugating element (2) made of nickel-cobalt ferrite with a diameter of 36 mm and a length of 150 mm is placed into an inductance coil and positioned at a distance of 132 mm from the transducer. This distance is selected in such way that, in the geometric approximation, the incident beam entirely falls into the aperture of the phase-conjugating element. Two ferrite samples were used in the experiments: one of them had plane-parallel faces, while the other had a special profile on

its liquid-loaded surface. The profile had the form of closely cut concentric grooves that were 2.5 mm wide and 0.6 mm deep (the curvature radius of the groove cross-section was 1.59 mm).

When an ultrasonic pulse gets inside the phase-conjugating element, a parametric pumping pulse with the frequency $2f = 12.46$ MHz and duration $100 \mu\text{s}$ is fed to the coil, which leads to the generation of a phase-conjugate and amplified ultrasonic pulse (a more detailed description of the operation of the used parametric phase-conjugating system is given in our earlier papers [1, 5, 7]). While propagating in water in the opposite direction, the conjugate beam is focused almost at the same point as the incident beam.

The measurements of the transverse distribution of the sound pressure amplitude were conducted in the focal plane using a PVDF membrane-type hydrophone (3) connected to a Tektronix TDS340A digital oscilloscope via a wide-band amplifier. A short interval ($\sim 1 \mu\text{s}$) close to the maximum of the envelope of the phase-conjugate pulse is selected for the analysis, and the difference between the maximum and minimum pressures is calculated within it. Averaging over 64 samples is used to increase the precision of the results. The hydrophone positioning is performed by a scanning system with the step 0.2 mm. Since the transmission loss is small (< 3 dB), the hydrophone is almost transparent to acoustic waves in the operating frequency range. In combination with the small size of the sensitive element of the hydrophone (~ 0.5 mm), this allowed almost unperturbed measurements of the parameters of both incident and reflected waves with a relatively high spatial resolution. The absence of disturbances introduced into the incident wave is fundamentally important for the experiments on the real-time studies of the phase-conjugation quality.¹ The angular uniformity of reception is determined by the sufficiently wide directivity pattern of the hydrophone (30° at the level -3 dB).

Figure 2 shows the results of the measurements. The peak-to-peak pressure amplitude in the focus of the phase-conjugate beam reached the value ~ 1.5 MPa for both samples. The wave had the form given at the top right of Fig. 2. The dots in the figure show the normalized transverse distribution of the pressure amplitude in the incident wave. The deviation of the incident field distribution from the theoretical dependence $J_1(\alpha r)/\alpha r$ is explained by both the imperfection of the focusing transducer and the finite dimensions of the receiving part of the hydrophone, which lead to the effect of field averaging. At the same time, the size of the main focal spot is close to the theoretical value for the given lens: $1.22F\lambda/d \approx 0.77$ mm, where λ is the acoustic wavelength and d and F are the aperture and the focus length, respectively. The dashed line corresponds to the conjugate wave generated by the sample with a flat operating

¹ Earlier, we used laser sounding of acoustic fields for this purpose.

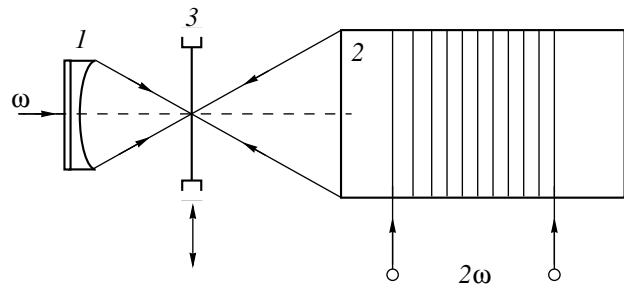


Fig. 1. Simplified experimental scheme. (1) A focusing ultrasonic transducer; (2) a phase-conjugating element made of magnetostrictive ferrite with a parametric pumping coil; and (3) a PVDF hydrophone scanned in the focal plane. Thin lines with arrows show the paths of the direct and phase-conjugate ultrasonic beams.

surface. The misfit of curves clearly manifests itself for large displacements from the acoustic axis ($r \approx 1-3$ mm) and demonstrates the distortions taking place in this phase-conjugating conversion.

The normalized distribution of a phase-conjugate wave produced by the sample with the grooved surface is shown in Fig. 2 by the solid line. As one can see, there is a noticeable improvement in the quality of the reproduction of the initial field. As against the previous case, a considerable suppression of the side peaks occurs in the phase-conjugate wave, with simultaneous insignificant broadening of the central spot.

The observed improvement of quality can be explained in the following way. The plane interface between the liquid and the solid plays the role of a complex set of narrow-band filters because of the total reflection of some components of the incident beam spectrum and a highly nonuniform (in amplitude) refraction of other components. On the whole, this set considerably reduces the effective angular aperture of the phase-conjugating element [6, 7]. As a result, diffraction-type distortions (parasitic side peaks) arise in the phase-conjugate beam. The relief located at the liquid–solid interface unifies the transmission conditions for all spectral components incident upon the phase-conjugating element. In this way, by transforming the spatial spectrum of the incident beam, it expands and smoothes out the angular dependence of the transmission coefficient of acoustic waves through the interface. Under such conditions, a greater number of components of the incident wave takes part in the phase-conjugating conversion, and this occurs with approximately equal weights for all components, which improves the quality of phase conjugation. The reconstruction of the initial spatial structure of the incident beam in the process of the transmission of the phase-conjugate wave through the same inhomogeneities is provided by the phase-conjugate character of its front.

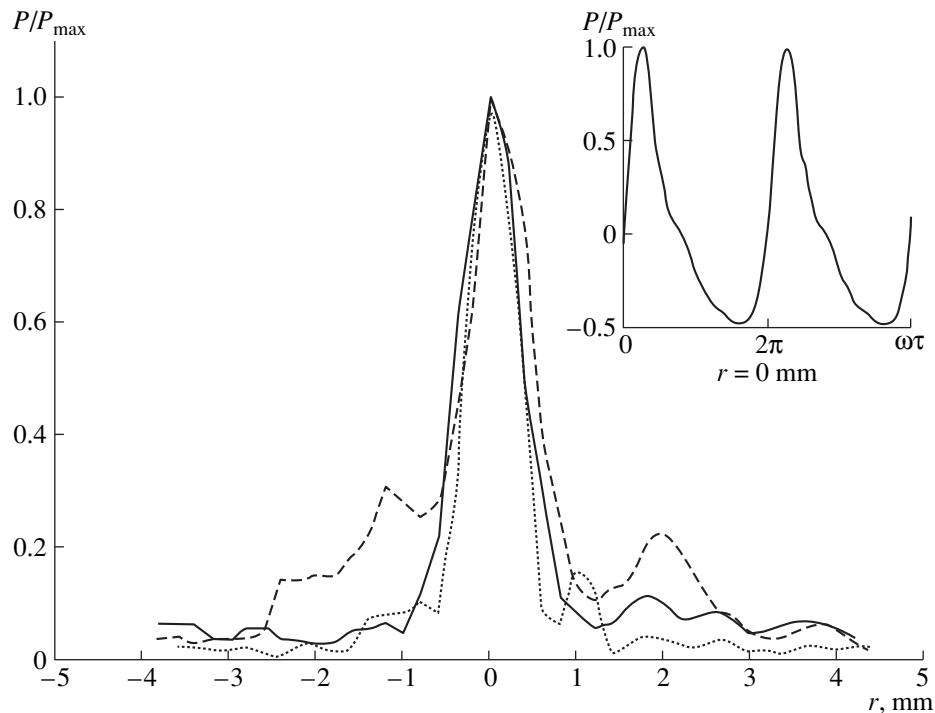


Fig. 2. Normalized distribution of acoustic pressure in the focal plane. The dots indicate the incident beam, and the dashed and solid lines indicate the phase-conjugate beams for the cases of the flat and grooved surfaces of the phase-conjugating element, respectively. The form of the phase-conjugate wave in the focus, which is similar for both cases, is given at the top right of the figure.

The influence of the nonlinearity of the propagation medium on the quality of the parametric phase conjugation of focused ultrasonic beams needs special investigation, and we will consider it in our upcoming publications.

Thus, the conclusion made in our previous paper [7] on the higher quality of the ultrasonic phase conjugation performed by phase-conjugating elements with grooved working surfaces is confirmed experimentally for the case of focused phase-conjugate ultrasonic beams of high intensity.

ACKNOWLEDGMENTS

We are grateful to F.V. Bunkin for supporting our work and A.D. Stakhovskii and N.N. Ryzhov for the assistance in preparation of the experiments.

This study was supported in part by the Russian Foundation for Basic Research, project nos. 99-02-18111, 98-02-16761, and 96-15-96525.

REFERENCES

1. A. P. Brysev, L. M. Krutyanskiĭ, and V. L. Preobrazhenskii, *Usp. Fiz. Nauk* **168**, 877 (1998) [*Phys. Usp.* **41**, 793 (1998)].
2. M. Ohno, *Jpn. J. Appl. Phys., Suppl.* **29**, 299 (1990).
3. K. Yamamoto, A. Kokubo, M. Ohno, *et al.*, in *Proceedings of World Congress on Ultrasonics*, Ed. by K. Takagi (Univ. of Tokyo, Yokohama, 1997), p. 1LP1, 22.
4. M. Tanter, J.-L. Thomas, and M. Fink, in *Proceedings of the 4th Congress on Acoustics*, Ed. by G. Canevet (Teknea, Marseille, 1997), p. 149.
5. A. P. Brysev, F. V. Bunkin, V. L. Krutyanskiĭ, and A. D. Stakhovskii, *Izv. Ross. Akad. Nauk, Ser. Fiz.* **60** (12), 117 (1996).
6. A. P. Brysev, F. V. Bunkin, N. A. Ekonomov, *et al.*, *Phys. Lett. A* **164**, 196 (1992).
7. A. P. Brysev, F. V. Bunkin, V. L. Krutyanskiĭ, *et al.*, *Akust. Zh.* **43**, 244 (1997) [*Acoust. Phys.* **43**, 207 (1997)].

Translated by M. Lyamshev

Field Reconstruction in an Anisotropic Elastic Medium

A. O. Vatul'yan* and A. N. Solov'ev**

*Rostov State University, ul. Zorge 5, Rostov-on-Don, 344090 Russia

**Don State Technical University, pl. Gagarina 1, Rostov-on-Don, 344010 Russia

Received August 28, 1999

Abstract—For steady-state vibrations of an anisotropic elastic body of finite dimensions, a method of the determination of the vibration energy flows in the body is proposed. The method is based on the measurements of the surface values of the stress and displacement vectors at a part of the boundary. The proposed algorithm of the wave field reconstruction is reduced to solving nonclassical boundary integral equations of the first kind with smooth kernels. The formulation of these equations does not require the determination of fundamental solutions, but represents a conditionally well-posed problem. The numerical realization of the proposed method is based on the Tikhonov regularization method and the idea of the boundary element method. Numerical experiments consisting in the reconstruction of the displacements and stresses at the boundary of a rectangular and a circular domains of austenitic steel are performed in the framework of a planar problem of the orthotropic elasticity theory. © 2000 MAIK “Nauka/Interperiodica”.

INTRODUCTION

The problem of field reconstruction in an elastic medium is an important problem of intensimetry, which determines the vibration energy flows in structures from the measured surface values of the stress and displacement vectors. From the viewpoint of applications, the most interesting case is that with the zero components of the stress vector at the boundary of an elastic body. The formulation and the solution of the problem of the wave field reconstruction for an isotropic elastic medium can be found in the literature [1–3]. The problem has been solved on the assumption that, at the free boundary of an elastic body, the components of the displacement vector are known. Such a problem is reduced to a Fredholm integral equation of the first kind with a smooth kernel, and is an ill-posed problem.

In this paper, we consider similar problems for an anisotropic elastic medium. We propose an algorithm of the wave field reconstruction on the basis of a different type of equations. One of the versions of these equations has been proposed in [5] and applied to solving classical boundary-value problems of acoustics and theory of elasticity in [6, 7, 9].

FORMULATION OF THE PROBLEM

Consider steady-state vibrations of an anisotropic simply-connected elastic body V bounded by a smooth surface S . We assume that part of the surface $S_1 \subset S$ is available for the displacement measurements. Then, the problem of the field reconstruction for the body V can be formulated as follows: Determine the components of the displacement vector u_i that satisfy the system of equations [8]

$$c_{ijkl}u_{k,lj} + \rho\omega^2u_i = 0, \quad i = 1, 2, 3 \quad (1)$$

and the boundary conditions at the surface S_1

$$u_i|_{S_1} = u_{i0}, \quad t_i = c_{ijkl}u_{k,l}n_j|_{S_1} = p_{i0}, \quad i = 1, 2, 3, \quad (2)$$

where c_{ijkl} are the components of the elastic constant tensor satisfying the elastic symmetry relations

$$c_{ijkl} = c_{jikl} = c_{ijlk} = c_{klij} \quad (3)$$

and the condition of the positive definiteness of the specific strain energy

$$W(\epsilon) = \frac{1}{2}c_{ijkl}u_{k,l}u_{i,j} \geq 0. \quad (4)$$

Here, n_j are the components of the unit vector of the outer normal to the surface S . The formulation of the boundary-value problem (1), (2) is uncommon for elliptic equations in mathematical physics and, specifically, in the theory of elasticity.

In studying the boundary-value problem with the boundary conditions (2), the main questions to be answered are those about the uniqueness and the stability of the solution under small perturbations.

In the framework of the isotropic elasticity theory, the uniqueness of the problem formulated above has been demonstrated and the stability of this formulation was considered by Bobrovnikskiĭ *et al.* [1, 3]. In solving the system of Fredholm integral equations of the first kind with smooth kernels, the key step was the expansion of the displacement vector in normal modes. The cited papers also determine the criterion relating the accuracy of the field reconstruction to the dimensionality of the approximating model. We note that the boundary-value problem (1), (2) can be easily reduced to the Cauchy problem for equations (1) of the anisotropic elasticity theory. For these equations, the unique-

ness is proved in much the same way as the Holmgren theorem [4].

One of the approaches proposed in the cited papers [1, 3] and leading to the solution of a system of Fredholm equations of the first kind requires knowledge of the Green's matrix function of the problem, which causes mathematical difficulties in solving specific boundary-value problems for bounded bodies. In this paper, we propose another formulation of the operator equations basing on the relation between the known field components and the unknown ones.

REDUCTION OF THE PROBLEM OF THE WAVE FIELD RECONSTRUCTION TO A SYSTEM OF INTEGRAL EQUATIONS

To reduce the formulated nonclassical boundary-value problem for equation (1) with boundary conditions (2), we use the ideas underlying the derivation of the systems of boundary equations for classical boundary-value problems [5-7, 9]. The approach is based on the use of the Fourier integral transform and the following representation of the displacement vector transforms [5]:

$$U_k(\alpha) = \frac{p_{km}(\alpha, \omega)V_m(\alpha)}{p_0(\alpha, \omega)}; \quad k = 1, 2, 3, \quad (5)$$

where

$$U_k(\alpha) = \int_V u_k(x)e^{i(\alpha, x)}dV_x;$$

$$V_m(\alpha) = \int_S [\sigma_{mj}n_j - i\alpha_j c_{mjkl}u_k n_l]e^{i(\alpha, x)}dS_x, \\ m = 1, 2, 3;$$

$$p_0(\alpha, \omega) = \det A, \quad A = \|A_{mk}(\alpha, \omega)\|,$$

$$A_{mk}(\alpha, \omega) = c_{mjkl}\alpha_j\alpha_l - \omega^2 \rho \delta_{mk};$$

$p_{km}(\alpha, \omega)$ are the components of the matrix B adjointed to the matrix A : $BA = p_0(\alpha, \omega)E$ (E is the unit matrix); and

$$\alpha = (\alpha_1, \alpha_2, \alpha_3), \quad (\alpha, x) = \alpha_1 x_1 + \alpha_2 x_2 + \alpha_3 x_3.$$

We note that the set of zeros of the polynomial $p_0(\alpha, \omega)$

for real $\eta_j = \frac{\alpha_j}{|\alpha|}$ is related to the solution of the Christoffel equation [8], whence it follows that $p_0(\alpha, \omega)$ is zero on three real manifolds.

Let us analyze the set of zeros of the polynomial $p_0(\alpha, \omega)$ for complex values of α_j . We introduce the dimensionless variables $\beta_j = k^{-1}\alpha_j$, $k = \omega/c$, and $c = \sqrt{\rho/c_{3333}}$. At fixed values of β_1 and β_2 , the dimension-

less equation $p_0(\alpha, \omega) = k^6 p_0(\beta, 1) = 0$ has six roots $\beta_3 = \beta_{3s}(\beta_1, \beta_2)$, where $s = 1, 2, \dots, 6$. In the case $\text{Im}\beta_1 = \text{Im}\beta_2 = 0$, these roots may include only real ones or pairs of complex conjugate roots because of the real-valued coefficients of the polynomial $p_0(\beta, 1)$. At the next step of our analysis, we divide the set of the roots $P = \{\beta_{3s}(\beta_1, \beta_2)\}$ into two components P_+ and P_- . When $|\beta_1^2 + \beta_2^2| \rightarrow \infty$, the quantities β_{3s} become purely imaginary by virtue of the positive definiteness of the elastic energy (4). We assign the roots, for which $\text{Im}\beta_{3s} > 0$ at $|\beta_1^2 + \beta_2^2| \rightarrow \infty$, to the set P_+ ; in addition, at $\text{Im}\beta_{3s} = 0$, to the set P_+ we assign the roots β_{3s} , for which $\text{Re}\beta_{3s} > 0$. As a result, we have $P_+ = \{\beta_{31}, \beta_{32}, \beta_{33}\}$.

Further analysis of representation (5) for the complex values of α_j leads to the following conclusions. The left-hand member of equation (5) contains the analytical functions of α_j , and the right-hand member contains the functions with poles on the set P . This contradiction is eliminated by the fact that the numerator of the right-hand member of equation (5) vanishes on the set P . This leads to a number of solvability relations, six of them being independent:

$$p_{k1}(\alpha_1, \alpha_2, \pm\alpha_{3s}(\alpha_1, \alpha_2, \omega), \omega) \\ \times V_k(\alpha_1, \alpha_2, \pm\alpha_{3s}(\alpha_1, \alpha_2, \omega)) = 0, \quad s = 1, 2, 3. \quad (6)$$

When relations (6) are valid, the remaining equalities (at $m = 2, 3$) are identically satisfied. If the domain V possesses some symmetry properties, and some boundary conditions are set, the number of independent equations may be reduced to three.

We note that the set of equalities (6) can be interpreted as a system of integral equations relating the known and the unknown quantities at the boundary S (i.e., the quantities $\sigma_{ij}n_j|_{S_1}$, $u_i|_{S_1}$ and $\sigma_{ij}n_j|_{S_2}$, $u_i|_{S_2}$, respectively). Thus, equalities (6) represent a system of integral equations of the first kind with smooth kernels, and their inversion procedure should require a regularization [10]. We note that the right-hand members of these operator equations represent smoothing (integral) operators of the given (measured) functions; therefore, such a problem is a conditionally well-posed one, and the inversion procedure can be efficiently performed with the use of discretization and a transition to a finite-dimensional version.

EXAMPLE: PLANE DEFORMATION OF AN ORTHOTROPIC BODY

As an example, we consider the system of boundary integral equations for an orthotropic body. Such properties are characteristic of austenitic steel [11] and many composite materials in the framework of the effective modulus concept.

The resolving system of integral equations has the dimensionless form

$$\begin{aligned} & p_{11}(\beta_1, \pm\beta_{3s}(\beta_1))V_1(k\beta_1, \pm k\beta_{3s}(\beta_1)) \\ & + p_{13}(\beta_1, \pm\beta_{3s}(\beta_1))V_3(k\beta_1, \pm k\beta_{3s}(\beta_1)) = 0, \\ & \quad s = 1, 2; \\ & p_{11}(\beta_1, \beta_3) = \gamma_5\beta_1^2 + \beta_3^2 - 1, \\ & p_{13}(\beta_1, \beta_3) = -(\gamma_5 + \gamma_7)\beta_1\beta_3, \end{aligned} \quad (7)$$

$$\begin{aligned} V_1(k\beta_1, k\beta_3) &= \int_L (\sigma_{11}n_1 + \sigma_{13}n_3 - ik((\beta_1n_1\gamma_1 \\ & + \beta_3n_3\gamma_5)u_1 + (\beta_1n_3\gamma_7 + \beta_3n_1\gamma_5)u_3)e^{ik(\beta, x)}dL_x, \\ V_3(k\beta_1, k\beta_3) &= \int_L (\sigma_{31}n_1 + \sigma_{33}n_3 - ik((\beta_1n_3\gamma_5 \\ & + \beta_3n_1\gamma_7)u_1 + (\beta_1n_1\gamma_5 + \beta_3n_3)u_3)e^{ik(\beta, x)}dL_x, \end{aligned}$$

where

$$k = \omega\sqrt{\rho/c_{33}}, \quad \gamma_1 = c_{11}/c_{33}, \quad \gamma_5 = c_{44}/c_{33},$$

$$\gamma_7 = c_{13}/c_{33}, \quad \beta_{3s}(\beta_1) = i\mu_s(\beta_1), \quad s = 1, 2,$$

$$\mu_s(\beta_1) = [A_1(\beta_1) - i(-1)^s(A_2(\beta_1))^{1/2}]^{1/2},$$

$$A_1(\beta_1) = (2\gamma_5)^{-1}[(\gamma_1 - 2\gamma_5\gamma_7 - \gamma_7^2)\beta_1^2 - (1 + \gamma_5)],$$

$$A_2(\beta_1) = -(A_1(\beta_1))^2 + (\gamma_5)^{-1}(1 - \gamma_1\beta_1^2)(1 - \gamma_5\beta_1^2).$$

Figure 1 shows the dependences $\beta_{3s}(\beta_1)$ for austenitic steel with the following material constants [11]:

$$\rho = 0.812 \times 10^4 \text{ kg/m}^3, \quad c_{11} = 0.2627 \times 10^{12} \text{ N/m}^2,$$

$$c_{13} = 0.145 \times 10^{12} \text{ N/m}^2, \quad c_{33} = 0.216 \times 10^{12} \text{ N/m}^2,$$

$$\text{and } c_{44} = 0.129 \times 10^{12} \text{ N/m}^2.$$

The system of equations (7) relates the known and unknown components of the displacement vector and the stress vector on the contour $L = L_1 \cup L_2$. We assume that, on the part L_1 , the quantities

$$u_i|_{L_1} = f_i, \quad \sigma_{ij}n_j|_{L_1} = g_i, \quad i = 1, 3 \quad (8)$$

are given, and on the part L_2 , the quantities $u_i|_{L_2}$ and $t_i =$

$\sigma_{ij}n_j|_{L_2}$ ($i = 1, 3$) are unknown. For these unknowns,

equalities (7) represent a system of Fredholm integral equations of the first kind with smooth kernels, and this system is equivalent to the initial boundary-value problem. In fact, these equations are the consequence of the reciprocity theorem formulated in the elasticity theory for true fields and inhomogeneous plane waves in an orthotropic medium.

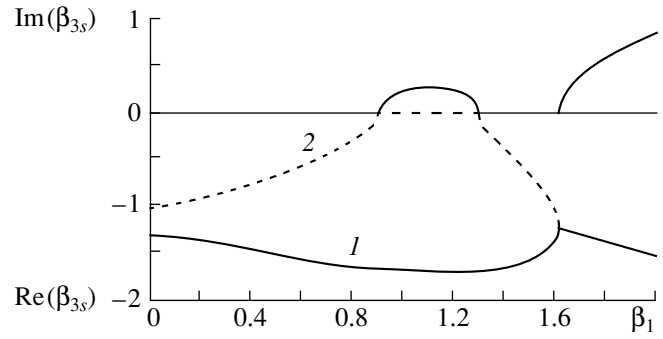


Fig. 1.

For such operator equations, the inversion procedure is ill-defined, and it is based on the combination of the idea of the boundary element method and the Tikhonov regularization method, as was demonstrated earlier for the Helmholtz equations [5] and for the antiplanar problem of the anisotropic elasticity theory [9].

As examples illustrating the proposed approach, we consider two planar problems for a rectangular and a circular domain, for an orthotropic material with the elastic constants specified above.

Field Reconstruction for a Rectangle $S = [0, a] \times [0, b]$

On $L_1 = \{\{x_1 = 0, x_3 \in [b_1, b]\} \cup \{x_3 = b, x_1 \in [0, a]\} \cup \{x_1 = a, x_3 \in [b_2, b]\}\}$, we have the given functions f_i and g_i ($i = 1, 3$) defined by expressions (8); these functions correspond to the displacement and the stress fields calculated on the basis of the generalized Hooke law:

$$\begin{aligned} u_1(x_1, x_3) &= \text{Re}\{-p_{13}(\beta_1, \beta_3)Z(x_1, x_3)\}, \\ u_3(x_1, x_3) &= \text{Re}\{p_{11}(\beta_1, \beta_3)Z(x_1, x_3)\}, \\ \sigma_{11}(x_1, x_3) &= c_{33}\text{Re}\{ik(-\gamma_1p_{13}(\beta_1, \beta_3)\beta_1 \\ & + \gamma_7p_{11}(\beta_1, \beta_3)\beta_3)Z(x_1, x_3)\}, \\ \sigma_{13}(x_1, x_3) &= c_{33}\text{Re}\{ik\gamma_5(-p_{13}(\beta_1, \beta_3)\beta_3 \\ & + p_{11}(\beta_1, \beta_3)\beta_1)Z(x_1, x_3)\}, \\ \sigma_{33}(x_1, x_3) &= c_{33}\text{Re}\{ik(-\gamma_7p_{13}(\beta_1, \beta_3)\beta_1 \\ & + p_{11}(\beta_1, \beta_3)\beta_3)Z(x_1, x_3)\}, \end{aligned} \quad (9)$$

where $Z(x_1, x_3) = \exp[ik(\beta_1x_1 + \beta_3x_3)]$ and $\beta_3 = \beta_{31}(\beta_1)$.

The unknowns to be reconstructed on $L_2 = \{x_1 \in [0, a], x_3 = 0\}$ are the quantities $u_j(x_1, 0)$, $\sigma_{13}(x_1, 0)$, and $\sigma_{33}(x_1, 0)$. Figure 2 shows the plots of the functions $u_1(x_1, 0)$ and $u_3(x_1, 0)$ at the boundary L_2 for $a = 1, b = 1, b_1 = b_2 = 0$,

$$\begin{aligned} ka &= 1.1, \quad k\beta_1 = 3, \\ k\beta_3 &= -2.2507 + 1.7817i. \end{aligned} \quad (10)$$

Curves 1 and 2 in Fig. 2 correspond to the exact solution of system (9), and the dashed lines and stars correspond to the numerically reconstructed values. Figure 3

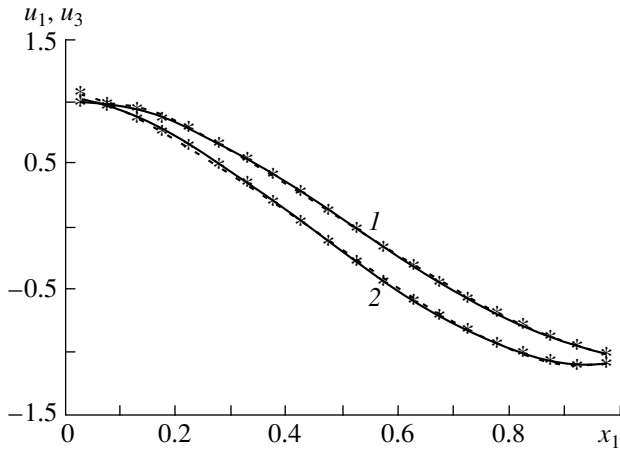


Fig. 2.

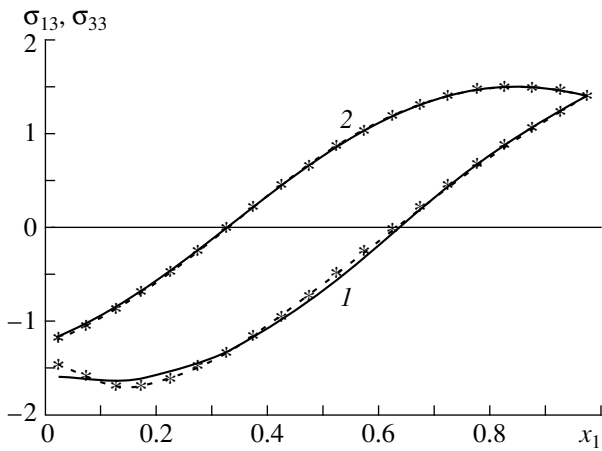


Fig. 3.

presents similar dependences for $\sigma_{13}(x_1, 0)$ and $\sigma_{33}(x_1, 0)$. The calculations were performed by dividing the boundary L_2 into 20 elements. The results of the calculations demonstrate a sufficient accuracy of the field reconstruction in the problem under study in a wide frequency range.

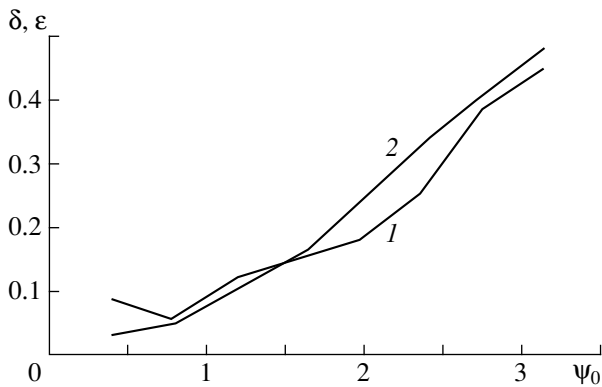


Fig. 4.

Field Reconstruction for a Circle $S = \{x_1, x_3 | (x_1 - R)^2 + (x_3 - R)^2 \leq R^2\}$

We studied the efficiency of the proposed method of the elastic field reconstruction as a function of the size of the boundary part $L_1 = \{x_1 = R + R\cos\psi, x_3 = R + R\sin\psi, \psi \in [\psi_0, 2\pi]\}$ available for the measurements of the elastic field parameters determined by relations (9) and (10). The unknowns are the components of the displacement and stress vectors on $L_2 = \{x_1 = R + R\cos\psi, x_3 = R + R\sin\psi, \psi \in [0, \psi_0]\}$. For $R = 0.5$, Fig. 4 presents the plots of the relative errors δ (curve 1) and ϵ (curve 2)

$$\delta = \sqrt{\delta_1^2 + \delta_2^2}, \quad \delta_1 = \frac{\max_{L_2} |u_1 - u_1^N|}{\max_{L_2} |u_1|},$$

$$\delta_2 = \frac{\max_{L_2} |u_3 - u_3^N|}{\max_{L_2} |u_3|},$$

$$\epsilon = \sqrt{\epsilon_1^2 + \epsilon_2^2}, \quad \epsilon_1 = \frac{\max_{L_2} |\sigma_n - \sigma_n^N|}{\max_{L_2} |\sigma_n|},$$

$$\epsilon_2 = \frac{\max_{L_2} |\sigma_\tau - \sigma_\tau^N|}{\max_{L_2} |\sigma_\tau|}$$

of the reconstruction of the displacement and stress vector components at the boundary L_2 at $\psi_0 \in \{\pi/8, \pi\}$.

(Here, u_i^N , σ_n^N , and σ_τ^N are the reconstructed values, and the number of elements N corresponds to the constant length of a boundary element with the angle $\psi = \pi/40$.) A series of calculations performed for reconstructing the elastic fields testifies to a fairly high accuracy of the field determination when the length of part L_1 is three or more times as great as the length of part L_2 . As the relative length of the part L_2 increases, the accuracy of the reconstruction lowers.

Figure 5 presents the plots of the functions $u_1|_{L_2}$ (curves 1, the dark circles show the reconstructed val-

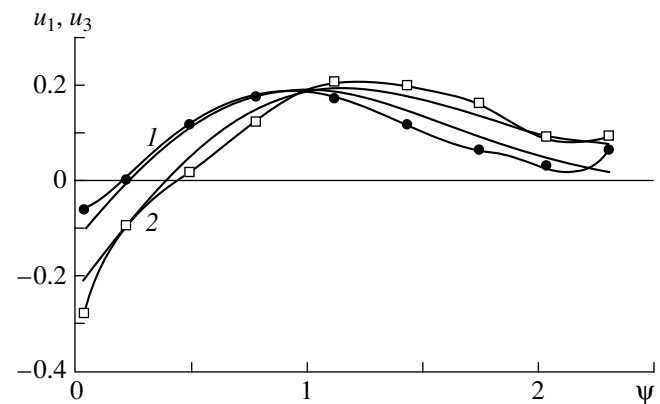


Fig. 5.

ues) and $u_3|_{L_2}$ (curves 2, the empty squares show the reconstructed values) for $\psi_0 = 3\pi/4$. One can see that, with the proposed computational scheme, the maximal error of the reconstruction occurs at the ends of the reconstructed interval. Within the interval, the reconstruction error does not exceed 15%. The bursts of the sought-for values at the edges are typical of the Tikhonov regularization method realized for integrable functions in solving the Fredholm integral equations of the first kind with smooth kernels.

The examples of the elastic field reconstruction considered in this paper demonstrate the efficiency of the proposed numerical algorithm of the field reconstruction.

REFERENCES

1. Yu. I. Bobrovnitskiĭ, *Akust. Zh.* **40**, 367 (1994) [*Acoust. Phys.* **40**, 331 (1994)].
2. S. E. S. Karlson, *J. Sound Vibr.* **196**, 59 (1996).
3. Yu. I. Bobrovnitskiĭ, M. P. Korotkov, A. A. Kochkin, and I. A. Tomilina, *Dokl. Ross. Akad. Nauk* **359**, 190 (1998) [*Dokl. Phys.* **43**, 177 (1998)].
4. S. Mizohata, *The Theory of Partial Differential Equations* (Cambridge Univ. Press, Cambridge, 1973; Mir, Moscow, 1977).
5. A. O. Vatul'yan, *Dokl. Ross. Akad. Nauk* **333**, 312 (1993) [*Phys. Dokl.* **38**, 459 (1993)].
6. A. O. Vatul'yan and E. V. Sadchikov, *Akust. Zh.* **44**, 326 (1998) [*Acoust. Phys.* **44**, 271 (1998)].
7. A. O. Vatul'yan and V. M. Shamshin, *Prikl. Mat. Mekh.* **62**, 112 (1998).
8. V. A. Krasil'nikov and V. V. Krylov, *Introduction to Physical Acoustics* (Nauka, Moscow, 1984).
9. A. O. Vatul'yan and A. N. Solov'ev, in *Integro-Differential Operators and Their Applications* (Donsk. Gos. Tekh. Univ., Rostov-on-Don, 1997), Vol. 2, pp. 30–35.
10. A. N. Tikhonov and V. Ya. Arsenin, *Methods of Solving Ill-Posed Problems* (Nauka, Moscow, 1979).
11. A. Temple and J. Ogilry, in *Proceedings on IUTAM Symposium on Elastic Waves and Ultrasonic Nondestructive Evaluation, University of Colorado, Boulder, 1989* (North-Holland, New York, 1990), pp. 143–149.

Translated by E. Golyamina

Two-Dimensional Phased Arrays for Surgery: Movement of a Single Focus

L. R. Gavrilov* and J. W. Hand**

**Andreev Acoustics Institute, ul. Shvernika 4, Moscow, 117036 Russia*

e-mail: bvp@akin.ru

***Hammersmith Hospital, Imperial College, London,
W12 0HS United Kingdom*

Received October 11, 1999

Abstract—Numerical simulation and comparative analysis of acoustic fields generated by two-dimensional phased arrays designed for ultrasonic surgery is conducted. The case of movement of a single focus by an array with the surface shaped as a part of a spherical shell with the curvature radius 120 mm is considered. The influence of the number of elements (varying from 64 to 1024), their diameter (from 2.5 to 10 mm), frequency (from 1 to 2 MHz), and the degree of sparseness of the elements at the array surface on the field characteristics is studied. The calculations are performed for arrays with elements positioned at the surface both regularly (in square, annular, or hexagonal patterns) and randomly. Criteria for the evaluation of the “quality” of intensity distributions in the field generated by an array in the case of movement of a single focus are suggested. Of all arrays studied, the best quality of distributions is obtained for an array containing 256 elements of diameter 5 mm randomly positioned at the array surface. The quality of the intensity distributions for arrays consisting of 255, 256, and 1024 elements positioned regularly (in square, annular, and hexagonal patterns) is inferior to the corresponding quality for arrays with randomly positioned elements. The irregularity in elements’ positioning considerably improves the distribution quality by suppressing the secondary intensity peaks in the field generated by the array; or, alternatively, it provides an opportunity to obtain the same distribution quality with a fraction of the number of elements in the array. The effects of the number and shape of elements, errors in phase setting, frequency modulation of signals, and non-uniform distribution of amplitudes over the array surface on the distribution quality are analyzed. © 2000 MAIK “Nauka/Interperiodica”.

In recent years, considerable interest has been expressed in developing minimum-injury surgery techniques that should provide better results than common surgery from the viewpoint of reducing the number of lethal outcomes, preventing side effects, and reducing a patient’s hospital stay. Among such techniques, those grounded upon the use of focused ultrasound for the local destruction of in-depth structures of the human body by high-intensity ultrasound are the subject of numerous intensive studies.

Various methods of ultrasonic focusing in biological tissues are discussed in the literature, e.g., the methods based on applying single focusing transducers [1, 2], lenses [3], and phased arrays [4–13]. A simple and rather inexpensive technique is used in practice for a long time. It is based on applying single focusing transducers with the surface shaped as part of a spherical shell and with a continuous distribution of the particle velocity over the transducer surface [1, 2]. However, an essential disadvantage of such focusing systems is their fixed focusing distance. Since the volume of the focal region of a radiator is usually much smaller than the volume of tissues subject to destruction, the means for the mechanical movement of the radiator must be provided. From the practical application of such proce-

dures, it is known that approximately one hour of operation is needed for the destruction of a tissue of volume 2 cm³ (G. ter Haar, private communication, 1998). Then, up to four hours of operation are needed to destruct such comparatively small volume as 8 cm³. Thus, transducers with a fixed focus would hardly be applied widely in clinical practice not only in surgery but also for hyperthermia, which is grounded upon a relatively short-time heating of tissues by high-intensity ultrasound.

Phased ultrasonic arrays have a noticeable advantage in this sense [4–13]. These arrays provide electronic dynamic focusing, i.e., an opportunity to change the place and size of the region of action without moving the array. It is expedient to use arrays with elements positioned at the surface shaped as a part of a sphere, thus combining the opportunities provided by the electronic and geometric focusing [4, 5, 8]. As phased arrays make it possible to simultaneously create several focuses at preset areas [8–11], their application makes it possible to considerably reduce the time of the destruction procedure for a relatively large tissue volume [9]. The disadvantages of arrays are the presence of secondary intensity peaks in their acoustic fields, which are caused, in particular, by the presence of dis-

crete structure in arrays, as well as their complexity, and, therefore, the relatively high cost of an array and the equipment necessary for its operation.

In order to destruct a biological tissue volume acceptable for practice in the depth of a human body ($\geq 10 \text{ cm}^3$), a two-dimensional phased array for use in surgery must provide the focus scanning at the necessary distance in three mutually perpendicular directions and have an acoustic power not smaller than 300–400 W. In addition, it is necessary to have the intensity in undesirable secondary peaks at a level acceptable for practice. The realization of such an array is a compromise between several contradictory requirements. In order to increase the distance for the focus scanning, and therefore to extend the volume of the destruction region, it is necessary to make the elements less directional, i.e., to reduce their size. On the other hand, it is necessary that the active area of the array be not smaller than 50 cm^2 to meet the requirements for the radiated power with not too high values of intensity at the surface of elements. All these considerations lead to designing arrays containing excessively large numbers of elements, and therefore, to an increase in the complexity and costs of an array feeding system.

The safety of the ultrasonic action must be the determining factor in the process of designing phased arrays for surgical applications. Therefore, the minimum level of sidelobes and secondary intensity peaks of ultrasound beyond the focal region becomes one of the basic criteria for the acoustic fields produced by an array. The presence of such peaks can lead to undesirable overheating and even the destruction of structures beyond the preset region of action. In order to reduce the influence of the sidelobes of a directivity pattern, the distance between the centers of the array elements must be less than $< \lambda/2$ [14], where λ is the wavelength, i.e., for example, less than 0.5 mm at the frequency 1.5 MHz. However, with such small elements, it is necessary to use a large number of elements and electronic channels in order to produce an array with a large enough aperture and obtain the acoustic power needed for a therapeutic array. In addition, the “dead” space between elements increases. The known ways of reducing the level of sidelobes in the array directivity pattern are grounded on the reduction of the amplitude at the elements of an array from its center to the periphery [14], and these methods are not always applicable in the specific case under discussion because of the raised requirements for the acoustic power of an array. One more way grounded upon the application of arrays with unequal distances between their elements [14] was tested by Hutchinson, Buchanan, and Hynynen [6, 7], who demonstrated that the reduction of the level of the secondary intensity peaks, which was expected on account of aperiodicity of elements, could attain 30–45% as against arrays with equal distances between elements. Such approaches as the employment of wide-band signals for feeding the array elements [15] and the utilization of only a certain part of the array elements

[16] are known. The approach studied in this paper is grounded upon the application of arrays with sparse elements positioned randomly at the array surface. The basis for this approach is the fact that the level of sidelobes in the field produced by an array depends on the regularity of the array structure [14]. Goss *et al.* [5] demonstrated theoretically that the utilization of elements randomly positioned at the array surface (we will call such arrays randomized for short) provides an opportunity to improve to a certain extent the spatial distribution of intensity in the field. Evidently, the application of arrays with sparse elements may somewhat reduce the complexity and cost of large two-dimensional arrays.

We conducted numerical simulation and comparative analysis of acoustic fields generated by two-dimensional phased arrays with random and regular distributions of elements at their surfaces shaped as parts of spheres. We also analyzed the influence of the dimensions, number, and shape of individual elements, errors in phase setting at the elements, and the frequency modulation of the signal on the quality of the distributions produced by arrays. The work was done for the purpose of clearing out the array designs that provide an opportunity to minimize the influence of secondary intensity peaks using a relatively small number of elements and, hence, to increase the safety of possible applications of such systems in surgery.

The technique used for calculating the acoustic fields produced by arrays is generally similar to the technique described by Goss *et al.* [5]. It consists of three main stages: (i) calculation of the distribution of the complex sound pressure generated by a single radiating element shaped as a disk; (ii) calculation of the distribution of the total complex sound pressure from the given single elements positioned at a part of a spherical shell; and (iii) calculation of the distribution of relative intensity in the field produced by the whole array and the analysis of such distributions with the help of the criteria for the distribution quality evaluation, as described below.

Figure 1 illustrates the calculation technique. The distribution of the complex sound pressure from a flat element shaped as a disk was determined with the help of the method of a point source, according to which the radiating surface of the disk was represented in the form of a set of many elementary radiators [17]. The latter were shaped as squares with a side of 0.25 mm. Assuming the radial symmetry of an element, its three-dimensional acoustic field can be determined by calculating the complex pressure $p(r_s, z_s)$ in the plane as a function of distance in the axial direction z_s and in the radial direction r_s according to the expression [5]

$$p(r_s, z_s) = \frac{j\rho c k u_0 \Delta A}{2\pi} \sum_{\text{surface}} \frac{e^{-(\alpha + jk)R}}{R},$$

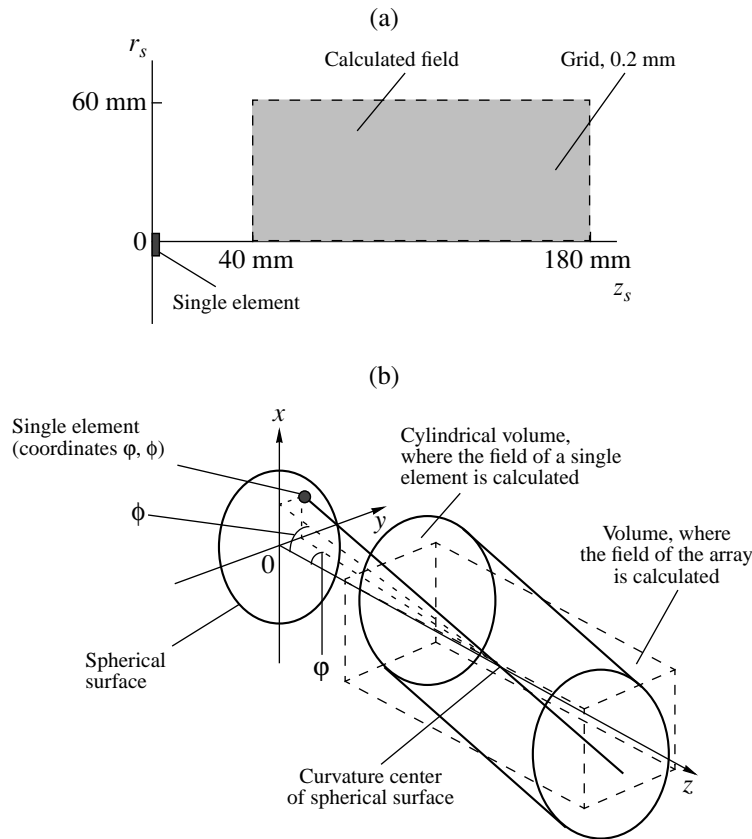


Fig. 1. Illustration of the technique used for the calculations. (a) Calculated field of a single element and (b) calculated field of an array.

where ρ is the tissue density (1000 kg m^{-3}), c is the sound velocity in the tissue (1500 m s^{-1}), k is the wave number, u_0 is the particle velocity at the surface of elementary radiators, ΔA is the area of an elementary radiator, α is the attenuation coefficient in the tissue, and R is the distance from the center of an elementary radiator to the point (r_s, z_s) where the field is calculated. Commonly, the calculation was performed for $40 \leq z_s \leq 180 \text{ mm}$ and $0 \leq r_s \leq 60 \text{ mm}$ at every 0.2 mm in both directions (Fig. 1a). However, in certain cases the field was calculated starting directly from the element surface. The attenuation coefficient in the tissue was taken equal to $10 \text{ Np m}^{-1} \text{ MHz}^{-1}$. This value was used by many researchers for similar calculations [4, 6, 9].

The calculation of the distribution of the total complex sound pressure produced by an array was conducted by the summation of the pressure contributions from all single elements in the three-dimensional region where the resultant distribution was analyzed (Fig. 1b). At first, the complex pressure for each single element with the center determined by the angular coordinates ϕ and φ (the angles from the array center of curvature to the projections of the element coordinates onto the vertical and horizontal axes) was determined in a cylindrical volume (Fig. 1b) as a function of distance in the axial and radial directions. The phase dis-

tribution at the elements, which is necessary for the array focusing, was calculated by the determination of the paths from the element centers to the place of the focus. Then, the values of the complex pressure were transferred from each individual cylindrical volume into the region of analysis that was a parallelepiped with the grid spacing 0.2 mm (Fig. 1b). The dimensions of the region of analysis, in which the summation of the values of complex pressure was performed, were from 50 to 160 mm in the direction of the acoustic axis of the array and from 0 to $\pm 30 \text{ mm}$ (to $\pm 40 \text{ mm}$ in some cases) in two other orthogonal directions. Finally, the intensity in each cell of the grid was calculated and the intensity distribution normalized with respect to the maximum value of intensity in the region of analysis was determined.

The calculation of the sound pressure and intensity distributions were conducted using (i) a computer Silicon Graphics Onyx2 with computer codes written in Fortran 77 and (ii) a Pentium II PC using Microsoft Fortran PowerStation 4.0 based on the Fortran 90 standard. The obtained distributions were analyzed using the AVS v5 (Advanced Visual Systems Inc. Waltham, MA), MATLAB 5.2.1, and Axum 5.0. The three-dimensional distributions of intensity were analyzed qualitatively in order to evaluate the field on the whole

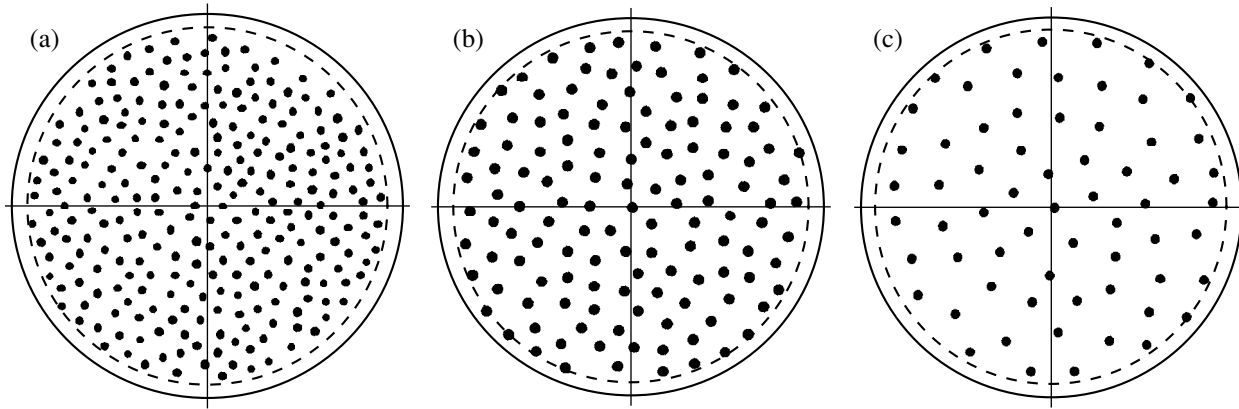


Fig. 2. Schematic representation of arrays consisting of flat elements shaped as disks and randomly positioned at a spherical surface. (a) 256 elements 5 mm in diameter; (b) 128 elements 7 mm in diameter; and (c) 64 elements 10 mm in diameter.

and check for the potential “hot spots” or regions requiring special attention. Two-dimensional boundary distributions in selected planes were basically used for the quantitative analysis of the intensity distributions.

The two-dimensional distributions presented in this paper corresponded as a rule to the data in the y - z plane (Fig. 1b). This plane always contained the focus when the position of the latter did not coincide with the array center of curvature, and, therefore, the secondary peaks of intensity connected with the discrete structure of the array had to be present in this plane. In some cases (see below), the calculation was conducted for the case when the focus scanned in the x - z plane.

We studied the influence of the number of elements (64, 128, 255, 256, and 1024), their diameter (2.5, 5, 7, and 10 mm), frequency (1, 1.5, and 2 MHz), and the sparseness of elements at the array surface on the characteristics of the ultrasonic fields produced by arrays. The calculation was conducted for the arrays with the surface shaped as a part of a spherical shell with the curvature radius 120 mm and elements positioned at the surface both randomly (Fig. 2) and regularly in the square, annular, and hexagonal patterns (Fig. 3). Only the positions of elements are shown in the figures, but not their size. All arrays had the same diameter of 110 mm.

A schematic representation of an array of 256 elements that are shaped as disks with diameters of 5 mm and installed quasi-randomly at a surface in the form of a part of a sphere (the true random distribution was modified in such way that the minimum distance between the element centers was 5.5 mm) is given in Fig. 2a. The distance between the centers of the most distant elements was 100 mm. The calculation was conducted for three operational frequencies: 1, 1.5, and 2 MHz. Several quasi-random distributions of elements at the array surface were studied, but the difference between results obtained for the same array was insignificant. The calculation was also conducted for randomized arrays of 128 elements of diameter 7 mm (Fig. 2b) and of 64 elements of diameter 10 mm

(Fig. 2c). In both cases, the frequency was 1.5 MHz, and the minimum distance between the centers of elements was 7.5 and 10.5 mm, respectively.

Figure 3 shows the investigated arrays with regular positioning of elements at the surface. A schematic picture of an array of 256 elements shaped as disks with diameters of 5 mm that are installed at the surface in square patterns is given in Fig. 3a. The minimum distance between the element centers was 5.5 mm. Figure 3b demonstrates the same array of 1024 elements with diameters of 2.5 mm and the distance between the centers of elements being 2.75 mm. Figure 3c shows an annular array containing 255 elements and consisting of the central element and nine concentric rings with radii from 5.5 to 49.5 mm (with a step of 5.5 mm). The rings consisted of 5, 11, 17, 23, 28, 33, 40, 46, and 51 elements, respectively. The distance between the centers of the elements was 6 mm. An array of 255 elements positioned at the surface in hexagonal patterns with the distance between the element centers 5.5 mm is shown in Fig. 3d. All arrays given in Figs. 2 and 3 have approximately the same (with the precision within 1.5%) total area of all elements (about 50 cm²), and, therefore, must radiate approximately the same acoustic power.

Four criteria were proposed for the evaluation of the normalized intensity distributions calculated for various arrays. The best quality (the criterion A) was assigned to an intensity distribution with the values of intensity larger than $0.1I_{\max}$ (where I_{\max} is the maximum intensity in the focus) being present only around the focal region and absent in other regions of the studied field. This criterion agrees with the common opinion that the level of secondary intensity peaks in the field radiated by an array must be at least by 8–10 dB lower than the maximum intensity in the focal region in order to provide the safety of ultrasonic action on tissues [4–6]. Three other criteria were used to evaluate fields of lower quality. The quality B was assigned to the distribution when less than 10 points or small areas

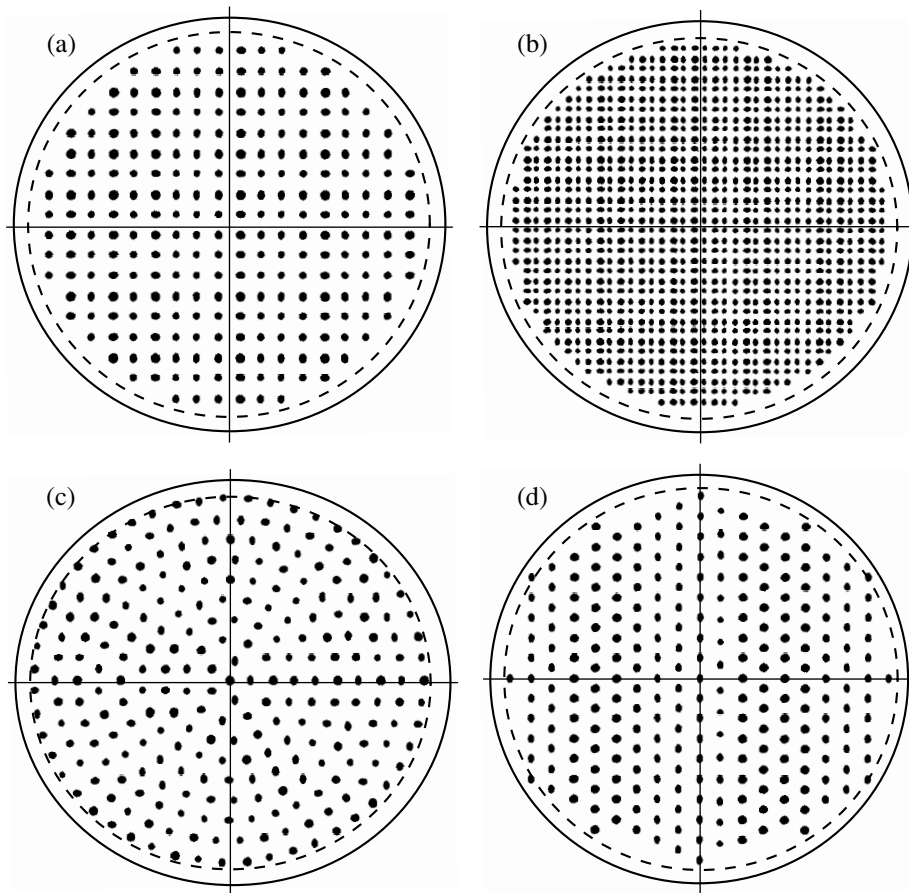


Fig. 3. Schematic representation of arrays consisting of flat elements regularly positioned at a spherical surface. (a) 256 elements of diameter 5 mm positioned in square patterns; (b) 1024 elements of diameter 2.5 mm positioned in square patterns; (c) 255 elements of diameter 5 mm positioned in annular patterns; and (d) 255 elements of diameter 5 mm positioned in hexagonal patterns.

with intensity within the interval $0.1 \leq I \leq 0.15I_{\max}$ were present beyond the focal region. The distribution, in which more than 10 points or small areas with the intensity within the interval $0.1 \leq I \leq 0.15I_{\max}$ were present beyond the focal region, was evaluated as the distribution of the quality C. Finally, the quality D was assigned to distributions having at least one point or small area with the intensity $I \geq 0.2I_{\max}$ in the considered plane beyond the focal region.

Figure 4 demonstrates examples of intensity distributions for a randomized array of 256 elements with the diameter 5 mm, which is excited at the frequency 1.5 MHz for the case of the movement of a single focus. The dependence of the quality of intensity distribution on the position of the shifted focus is shown for the distance from the array surface $z = 110$ mm. One can see that in the case of the focus shift from 10 to 16 mm from the acoustic axis, the quality of the intensity distributions changes from grade A to grade D. The dimensions of the analysis region were 110 mm in the direction along the acoustic axis and 60 mm in the direction perpendicular to it. Nine contours (from 10 to 90% of I_{\max} with the step $10\% I_{\max}$) are present within

the focal region (Fig. 4). The distribution of intensity in the field beyond the focal region was evaluated with the help of contours within the interval 10–20% I_{\max} with the step $5\% I_{\max}$, or $2\% I_{\max}$ when necessary.

The evaluation of the quality of the intensity distributions produced by this array at the frequencies 1, 1.5, and 2 MHz is given in Fig. 5. Here, as in Figs. 6 and 7 below, the data corresponding to scanning in the direction of positive values of y are presented. In the case of randomized arrays, the calculation was conducted for negative values of y as well. The results were qualitatively analogous. As distinct from the study by Goss *et al.* [5], we analyzed the ratios of the secondary and main intensity peaks not only in the focal plane, but also in a relatively large region of analysis before and behind the focus. It turned out that a randomized array of 256 elements with a diameter of 5 mm excited at the frequency 1 MHz provided an opportunity to scan the focus within the distance ± 20 mm from the acoustic axis, within the interval of the values of z from 50 to 130 mm, with the highest quality criterion (A) (Fig. 5a). In the case of the frequency 1.5 MHz, the distances, within which the focus could be shifted from the acous-

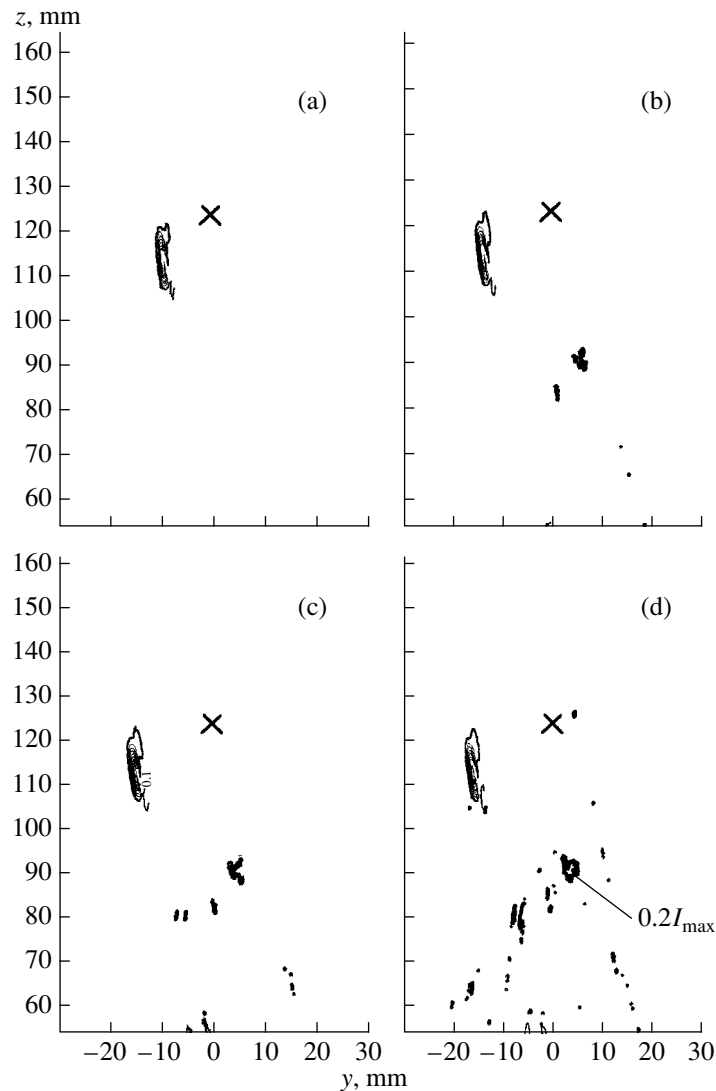


Fig. 4. Examples of the intensity distributions produced by an array of Fig. 2a and the criteria used for the evaluation of the distribution quality. (a) Criterion A; (b) criterion B; (c) criterion C; and (d) criterion D. The cross indicates the position of the curvature center of the array. The focus coordinates: (a) (0, -10, 100 mm); (b) (0, -14, 110 mm); (c) (0, -15, 110 mm); and (d) (0, -16, 110 mm). The analysis region is 110×60 mm.

tic axis with the quality A and B, were ± 10 mm within the interval of the values of z from 70 to 120 mm and ± 15 mm within the interval of the values of z from 50 to 130 mm, respectively (Fig. 5b). The volume of the region of action with the quality A and B constitutes 63 (106) cm^3 (the figures for B are given in parentheses) for the frequency 1 MHz (Fig. 5a) and 16 (49) cm^3 for the frequency 1.5 MHz (Fig. 5b). In the case of the frequency 2 MHz, this volume falls to 12.5 (16) cm^3 (Fig. 5c).

The characteristics of the spatial intensity distributions, which are evaluated using the selected quality criteria, depend on the distance at which the focus is shifted from the array center of curvature and on the attenuation in the medium. Figure 5 shows that, when the focus is shifted from the center of curvature, the

quality of distributions deteriorates sharply. One can also see that the largest interval of the focus shift from the axis of an array of the A quality can be attained not in the focal plane, but at a distance of 1–2 cm from it toward the array.

The ratio of the total area of elements (the active area) in an array of 256 elements with a diameter of 5 mm to the area of the array surface is approximately equal to 51%. Figure 6a illustrates the influence of an increase in the degree of sparseness of elements for the aforementioned randomized array of 256 elements with a diameter of 5 mm (Fig. 2a) when its 128 elements are turned off in an arbitrary way. The operating frequency is 1.5 MHz. Comparing Figs. 6a and 5b, one can see that an increase in the degree of sparseness of elements leads to a deterioration in the quality of the

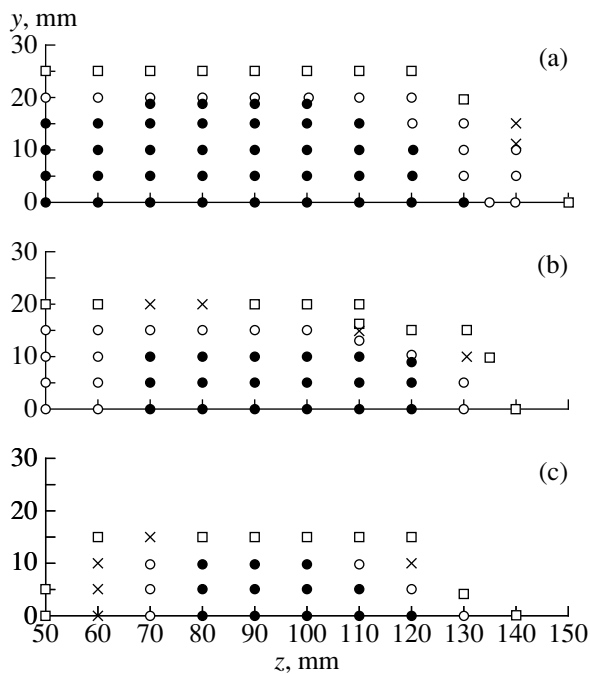


Fig. 5. Summary of the calculation results and the evaluation of the quality of intensity distributions at different ultrasonic frequencies for a randomized array of 256 elements with a diameter of 5 mm (Fig. 2a). The frequencies are (a) 1; (b) 1.5; and (c) 2 MHz. The quality criteria: (●) A; (○) B; (×) C; and (□) D.

intensity distributions. In this case, the useful volume of action upon tissues not only decreases noticeably, but also shifts toward the array. Here, the maximum distance from the array at which it is possible to focus an A grade array is 100 mm (Fig. 6a).

Figure 6b demonstrates the intensity distributions produced at the frequency 1.5 MHz by a randomized array of 128 elements with a diameter of 7 mm (Fig. 2b). Figure 6c presents similar data for a randomized array of 64 elements with the diameter 10 mm (Fig. 2c). The reduction of the number of randomly positioned elements from 256 to 128 and then to 64, which is accompanied by an increase in the diameter (from 5 to 7 and 10 mm, respectively) in order to keep constant the active area of the array, also leads to progressive deterioration of the quality of the intensity distributions (compare Fig. 5b with Figs. 6b and 6c). The difference between the quality of the intensity distributions of a randomized array of 128 elements with a diameter of 5 mm and a similar array with 7-mm diameter elements turned out to be small despite a certain difference in the directivity of the elements (Figs. 6a, 6b). The data shown in Figs. 5 and 6 correspond to focus scanning in the y - z plane. The calculations performed for the x - z plane yield qualitatively analogous results and are not presented here.

The results of the evaluation of the intensity distributions produced at the frequency 1.5 MHz by arrays

with regular positioning of elements in square, annular, and hexagonal patterns (Fig. 3) are given in Figs. 7 and 8. One can see that the quality of the intensity distributions from arrays of 255 and 256 regularly positioned elements with the diameter 5 mm (Figs. 7a, 7c, and 8) is inferior to that for a randomized array of 256 elements with the diameter 5 mm (Fig. 5b). As we have indicated above, the calculation is conducted for the case of the focus moving in both the y - z plane and the x - z plane. The intensity distributions in these planes were almost the same for the arrays with the elements positioned in square (Figs. 3a, 3b) or annular (Fig. 3c) patterns. Therefore, Fig. 7 presents the distributions obtained only in the y - z plane. However, when the pattern of the array structure observed from the place of the focus in the case of scanning along the x and y axes is essentially different, as it takes place in the case of a hexagonal array (see Fig. 3d), the intensity distributions in the y - z and x - z planes are also different (Figs. 8a, 8b). The best quality of distributions among the regular arrays of 255 and 256 elements was observed in the case of annular arrays (Fig. 7c), and the lowest quality was observed for square arrays (Fig. 7a) and hexagonal arrays in the case of scanning in the y - z plane (Fig. 8a).

The quality of the intensity distributions for an array of 1024 elements with the diameter 2.5 mm positioned at the surface in square patterns (Fig. 7b) was much lower than for a randomized array of 256 elements with a 5 mm diameter (Fig. 5b), but comparable to that of a randomized array of 128 elements with a 7 mm diameter (Fig. 6b). This suggests that the randomization of the elements positions at the array surface leads to six- to sevenfold economy in the number of elements and channels exciting them with approximately the same quality of intensity distributions. Nevertheless, from the literature available to us and devoted to the analysis of two-dimensional phased arrays for surgery, it follows that only regular arrays have been discussed, except for the studies by Goss *et al.* [5]. In these regular arrays, the most popular way of positioning the elements at the surface is that in square patterns [4, 8, 10–12].

There is a noticeable difference in the character of intensity distributions produced by arrays with random and regular positioning of elements. The former are characterized by distributions with secondary peaks of intensity observed mainly along the path of a converging ultrasonic beam to the focal region (Fig. 4) and occurred in the focal region only in the case of the lowest quality of distributions (the data are not presented). For arrays with regular positioning of elements, the situation was opposite. The secondary peaks connected with the discrete character of the array structure were observed precisely in the focal plane.

The data obtained show that the positive effect of randomization of the array elements can be attained when the sparseness of elements in an array with random distribution of elements lies within a certain interval (approximately from 40 to 70%). An increase in the

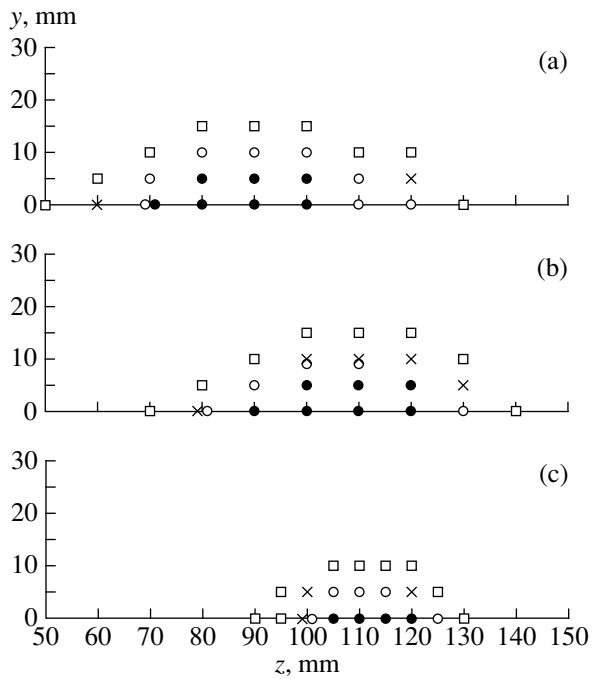


Fig. 6. Evaluation of the quality of intensity distributions produced by randomized arrays: (a) an array of 128 elements randomly selected from a randomized array consisting of 256 elements of diameter 5 mm (Fig. 2a); (b) an array of 128 elements of diameter 7 mm (Fig. 2b); and (c) an array of 64 elements of diameter 10 mm (Fig. 2c). Notations are the same as in Fig. 5.

sparseness (when the active area occupies less than 40% of the array surface) leads to a reduction of radiated power and a deterioration of the distribution quality. On the other hand, a decrease in the sparseness of elements (when the active area occupies more than 70% of the array surface) will inevitably lead to the ordering of the array structure, with all its consequences.

The developed approach to the evaluation of the quality of the intensity distributions was used for investigating the influence of various parameters and geometric characteristics of arrays with a random distribution of elements on the quality of the acoustic fields generated by them. Below, we summarize the main results of our study.

(1) The results testify that the dimensions of individual elements have a decisive effect on the capability of randomized arrays to move the focus with the quality acceptable for practical applications. If the diameter of elements is too large (e.g., 10 mm) and the directivity pattern is too narrow, then even an extremely large number of elements in the array does not allow one to move the focus with the quality of intensity distribution admissible for practice. For example, the calculations show that, in the case of using an array of 256 elements with a diameter of 10 mm (we should note that such an

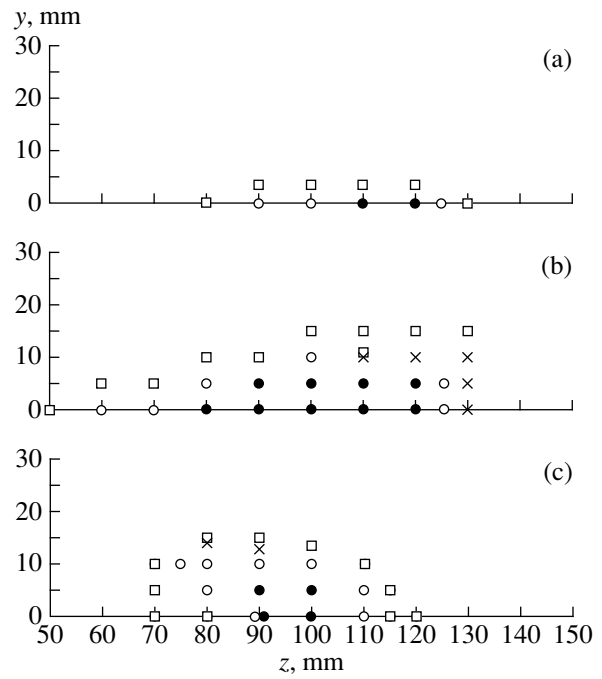


Fig. 7. Evaluation of the quality of intensity distributions produced by arrays with elements positioned regularly at a spherical surface: (a) an array of 256 elements of diameter 5 mm positioned in square patterns (Fig. 3a); (b) an array of 1024 elements of diameter 2.5 mm positioned in square patterns (Fig. 3b); and (c) an array of 255 elements of diameter 5 mm positioned in annular patterns (Fig. 3c). Notations are the same as in Fig. 5.

array is impossible, because the total area of elements exceeds almost twice the area of its surface), it is impossible to move the focus away from the axis to the distance greater than 10 mm with an acceptable quality.

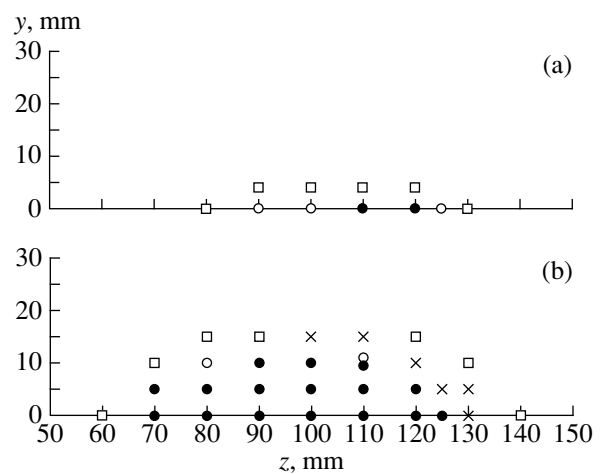


Fig. 8. Evaluation of the quality of intensity distributions produced by an array of 256 elements of diameter 5 mm with the elements positioned at a spherical surface in hexagonal patterns. (a) The focus shift is in the y - z plane and (b) in the x - z plane. Notations are the same as in Fig. 5.

It follows from the obtained data that, in order to scan at a distance of 10–15 mm with acceptable quality, it is necessary for the diameter of elements not to exceed five wavelengths. If this condition is satisfied, the increase in the number of elements and, therefore, in the total active area of the array leads to an increase in the maximum intensity in the focus and to an improvement of the quality of intensity distributions.

(2) The shape of an individual element (concave, flat, or convex) almost does not influence the quality of intensity distributions produced by an array. For example, the evaluation patterns of the quality of distributions for an array, which has the radiation frequency 1.5 MHz and consists of 64 elements with the diameter 10 mm and have different shapes (concave elements with the curvature radii 6 and 12 cm and convex elements of the same radii), barely differ from each other and from the characteristic of an analogous array consisting of flat elements (Fig. 6c). This result is predictable, because, despite a significant difference between the intensity distributions immediately near the surface of the elements of different shape ($z = 0\text{--}5$ cm), the distributions in the focal region ($z = 8\text{--}14$ cm) are essentially the same. It follows from here that there is no need to use more expensive nonflat elements in the design of such arrays.

(3) The shapes of the apertures of randomized arrays (square or circular) do not noticeably affect the quality of intensity distributions. For example, the intensity distributions of arrays of 256×5 mm elements (1.5 MHz) with the apertures shaped as a circle (Fig. 2a) and a square and with equal active areas and sparseness of elements almost did not differ from each other.

(4) Errors in setting the necessary distribution of signal phases at individual elements, for example, because of errors in the element positioning at the surface, can lead to a deterioration of quality of intensity distributions. The calculation of intensity distributions was conducted for a randomized array of 256×5 mm elements (1.5 MHz) with three different phase distributions at the elements: (a) the calculated phase distribution corresponding to the ideally precise positioning of elements; (b) random numbers selected within the interval from -0.4 to 0.4 radian were added to the values of phases from case (a); and (c) random numbers from the interval between -1.0 and 1.0 radian were added to the values of phases from case (a). It turned out that the deterioration of the quality of distributions for case (b) as against case (a) was relatively small. These data agree with the results obtained by Hutchinson *et al.* [6] and Wang *et al.* [13] who demonstrated that a discrete phase setting in 4 bit (22.5°) is sufficient for the satisfactory operation of arrays in practice. A further increase in the phase setting error (case (c)) leads to a sharp deterioration in the quality of intensity distributions.

(5) The utilization of such distributions of the amplitudes of particle velocity at the surface of a randomized

array, when the amplitude values decrease from the array center to the periphery, does not lead to an improvement of the quality of intensity distributions. In particular, the calculations were performed for the distributions of the type $[1 - (r/r_0)^2]^n$ (where $n = 1, 2$, and r_0 is the array radius) used by Skolnik [14] for regular arrays with circular apertures. This approach, which is effective for regular arrays, in the case of randomized arrays leads only to an increase in the relative intensity values in the secondary peaks, because the maximum intensity value in the focus, which is used for the normalization of these values, considerably decreases.

(6) The utilization of the frequency modulation of signals at the elements of a randomized array provides an opportunity to improve to some extent the quality of intensity distributions. For example, calculations were performed for the intensity distributions of a randomized array of 256×5 mm elements for different frequencies ($0.9; 0.95; 1.0; 1.05; \text{ and } 1.1$) f , where f is the central frequency (1.5 MHz). The averaged distribution for the five indicated frequencies turned out to be better than all the others, including the distribution for the central frequency.

The quality of the intensity distributions of the arrays that we studied can be compared with the corresponding quality for the sparse array described by Goss *et al.* [5]. This array consisted of 108 elements with the diameter 8 mm (only 64 of them were excited simultaneously). The frequency was 2.1 MHz. The elements were arranged in hexagonal patterns at a part of a spherical shell with a diameter of 100 mm and a curvature radius of 102 mm. The sparseness of elements was about 45%. The calculations performed by Goss *et al.* [5] demonstrated that, in the case of the array focusing at its curvature center, the predicted intensity level in the secondary peaks in the focal plane was $0.13I_{\max}$. When the focus was shifted by 5 mm from the axis, this level increased to $0.6I_{\max}$. In the measured distributions, these levels increased to $0.38I_{\max}$ and $0.9I_{\max}$, respectively, which is unacceptable for practical purposes. Goss *et al.* [5] estimated the possible role of a random distribution of elements over the array surface and predicted theoretically that, in this case, the expected intensity level in the secondary peaks in the focal plane should be $0.04I_{\max}$ without the focus shift and $0.16I_{\max}$ with the focus shift by ± 5 mm. Such a small effect of randomization obtained by Goss *et al.* [5] was apparently caused by the fact that the ratio of the element diameter to the wavelength was 11.2. As we have already noted, one should only expect a considerable improvement in the quality of intensity distributions when this ratio is selected from the interval $0.5\text{--}5\lambda$.

In conclusion, we note that the results obtained in this paper demonstrate that the irregularity in positioning the elements at the array surface leads to a noticeable improvement in the quality of intensity distributions produced by an array as against a regular positioning of elements (in square, annular, or hexagonal

patterns). The calculations testify that a randomized array that has a diameter of 110 mm and consists of 256 elements with a diameter of 5 mm, which are excited at the frequency 1–1.5 MHz and positioned on a part of a spherical shell with a curvature radius of 120 mm, provides an acceptable quality of intensity distributions according to the criterion of the presence of secondary intensity peaks in the generated field. It is demonstrated that randomized arrays make it possible to provide approximately the same quality of distributions as regular arrays with much greater numbers of elements (greater by a factor of 6 to 7 in the considered case). The number of elements and, especially, their diameter strongly affect the capability of a randomized array to scan the space by the focal region. The shapes of individual elements (flat, concave, and convex elements) barely influence the quality of the fields produced by a randomized array. An error in setting the signal phases at the elements within ± 0.4 radian almost does not deteriorate the quality of the intensity distributions. The frequency modulation of signals within $\pm 10\%$ of the central frequency leads to a certain improvement in the quality of intensity distributions.

The results of the conducted numerical simulation may be useful for designing of such arrays.

REFERENCES

1. F. J. Fry, in *Ultrasound: Its Applications in Medicine and Biology*, Ed. by F. J. Fry (Elsevier, New York, 1978), Part II, pp. 689–736.
2. C. R. Hill and G. R. ter Haar, *Br. J. Radiology* **68** (816), 1296 (1995).
3. R. J. Lalonde, A. Worthington, and J. W. Hunt, *IEEE Trans. Ultrason. Ferroelectr. Freq. Control* **40**, 592 (1993).
4. E. S. Ebbini and C. A. Cain, *IEEE Trans. Biomed. Eng.* **38**, 634 (1991).
5. S. A. Goss, L. A. Frizzell, J. T. Kouzmanoff, *et al.*, *IEEE Trans. Ultrason. Ferroelectr. Freq. Control* **43**, 1111 (1996).
6. E. B. Hutchinson, M. T. Buchanan, and K. Hynynen, *Med. Phys.* **23**, 767 (1996).
7. E. B. Hutchinson and K. Hynynen, *IEEE Trans. Ultrason. Ferroelectr. Freq. Control* **43**, 1032 (1996).
8. H. Wan, P. van Baren, E. S. Ebbini, and C. A. Cain, *IEEE Trans. Ultrason. Ferroelectr. Freq. Control* **43**, 1085 (1996).
9. X. Fan and K. Hynynen, *Ultrasound Med. Biol.* **22**, 471 (1996).
10. D. R. Daum and K. Hynynen, *IEEE Trans. Ultrason. Ferroelectr. Freq. Control* **45**, 208 (1998).
11. X. Fan and K. Hynynen, *Phys. Med. Biol.* **41**, 591 (1996).
12. R. J. McGough, M. L. Kessler, E. S. Ebbini, and C. A. Cain, *IEEE Trans. Ultrason. Ferroelectr. Freq. Control* **43**, 1074 (1996).
13. H. Wang, E. Ebbini, and C. A. Cain, *IEEE Trans. Ultrason. Ferroelectr. Freq. Control* **38**, 521 (1991).
14. M. I. Skolnik, *Introduction to Radar Systems* (McGraw-Hill, New York, 1962; Mir, Moscow, 1965).
15. F. Dupenloup, J. Y. Chapelon, D. J. Cathignol, and O. A. Sapozhnikov, *IEEE Trans. Ultrason. Ferroelectr. Freq. Control* **43**, 991 (1996).
16. L. R. Gavrilov, J. W. Hand, P. Abel, and C. A. Cain, *IEEE Trans. Ultrason. Ferroelectr. Freq. Control* **44**, 1010 (1997).
17. K. Ocheltree and L. Frizzell, *IEEE Trans. Ultrason. Ferroelectr. Freq. Control* **36**, 242 (1989).

Translated by M. Lyamshev

Spatial Correlation of Hydroacoustic Signals in a Biaxial Underwater Sound Channel

O. P. Galkin and S. D. Pankova

Andreev Acoustics Institute, Russian Academy of Sciences, ul. Shvernika 4, Moscow, 117036 Russia

e-mail: bvp@akin.ru

Received July 24, 1999

Abstract—In the hydrological conditions of a biaxial sound channel, the cross-correlation between acoustic signals received at points spatially separated (from 10 to 63 km) along the sound propagation track is investigated. The signals are received by a narrow-beam array scanning in the vertical plane. The beam width is $\sim 2^\circ$ at the mean frequency (1 kHz) of a pseudo-noise signal. It is noted that, as the distance between the points of reception increases, the correlation decreases. This is mainly caused by the effect of the multipath propagation with an incomplete resolution of signals in arrival angles, rather than by changes in the “water” signal spectrum due to the attenuation. © 2000 MAIK “Nauka/Interperiodica”.

The study of the spatial correlation of hydroacoustic signals in a real ocean is of both theoretical and applied significance. The evaluation of the effect of various oceanological factors on the cross-correlation of wide-band signals received at different distances from the sound source allows one to reveal the reasons of the correlation changes and, therefore, to introduce the necessary corrections into the models of an acoustic waveguide. In practice, these studies are especially important for estimating the possibility of constructing wide-aperture arrays, as well as for determining the efficiency of a combined processing of hydroacoustic data received from spatially separated hydroacoustic systems. In a series of recent papers [1–5], the problems of spatial correlation were partly considered. However, the investigations described in these papers were performed with omnidirectional sound receivers and, in most cases, at small distances from the sound source (up to several kilometers). Dahl [1] presented the results obtained by studying the effect of sea surface scattering on the spatial correlation in the experiments with the separation of the points of reception along the signal propagation track up to 15 sound wavelengths (the frequencies ≥ 20 kHz), at distances from 500 to 1000 m. In studying the spatial coherence as a function of the central frequency of broad-band acoustic signals propagating in a shallow-water region ($H = 15$ m), Badiy, Simmen, and Forsythe [2] observed a high coherence for frequencies from 0.6 to 7 kHz. However, the maximum separation of the receivers did not exceed 2 m, and the distance to the source was no more than 214 m. Westwood and Knobles [3] considered the problem of determining the track of a continuous broad-band acoustic source moving in an oceanic waveguide in the case of a good resolution of rays within a multi-ray signal and a high spatial correlation of signals received by horizontally separated receivers. The

experiments were carried out with an above-water source moving at a distance of 2 km from two receivers separated by 438 m. Tielburger, Finette, and Wolf [4] presented the results concerning the influence of internal waves on the spatial (and temporal) coherence of 400-Hz signals in a shallow sea. Siderius *et al.* [5] studied the possibility of using a vertical chain of hydrophones for localizing inhomogeneities in shallow-water regions with the help of a spatial-temporal cross-correlation function.

This paper continues the investigations of the spatial correlation of acoustic signals propagating in complicated hydrological conditions of the deep ocean [6]. The experiments were performed using a conventional procedure: the research vessels passed at a given distance and heaved aback to the drift with transmitting and receiving systems lowered in water. As a sound source, we used an omnidirectional transmitter of a continuous pseudo-noise signal with the mean frequency 1 kHz in the one-octave band. The signals were received by a 40-m vertical array with the angular beam width $\sim 2^\circ$ at the mean signal frequency.

The experiments were carried out in mid-December 1991, in the Atlantic Ocean, not far from the Gibraltar Strait. The geometry of the experiment was as follows: the omnidirectional source was located at a depth of 150 m, the center of the vertical array was at a depth of 180 m, and the water depth along the whole track was equal to ~ 4800 m. The spatial correlation was measured between the signal received by the array at a distance of 72 km from the source and the signals received (at other time) at distances of 62, 95, and 135 km. The sound velocity profile $c(z)$ corresponded to a biaxial underwater channel, one axis being located at a depth of ~ 450 m ($c_{\min 1} = 1503.2$ m/s), and the other axis at a depth of ~ 2000 m ($c_{\min 2} = 1502.9$ m/s). Figure 1

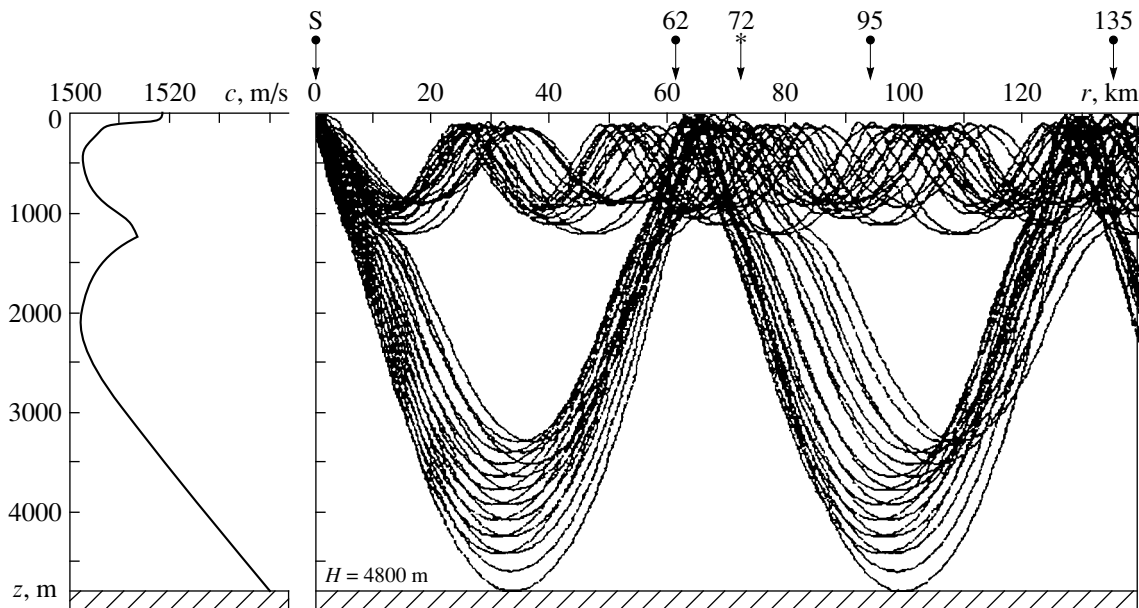


Fig. 1. Sound velocity profile $c(z)$ (left) in the test region (the Atlantic Ocean) and the ray pattern with the source (S) at a depth of 150 m (right).

exhibits the ray pattern for the measured profile $c(z)$ with the source located at a depth of 150 m. The arrows at the top show the positions of the source and the points of reception during the correlation measurements. From this ray pattern, it follows that signals can propagate between the source and the receiving array along two paths: over rays passing only through the upper channel, or over rays occupying the whole waveguide thickness. Thus, we have a superposition of the sound field zone structure with large ray cycle lengths ($\sim 60\text{--}80$ km), which is determined by the deep-water channel, and the zone structure with smaller ray cycle lengths (~ 30 km), which is formed by the upper channel. In the deep-water channel, the first convergence zone begins at a distance of ~ 60 km and ends at a distance of ~ 75 km; the beginning of the second zone is at a distance of ~ 125 km from the source. Therefore, (with consideration for the deep-water channel only), the spatial correlation was measured between the signal received at the middle of the first convergence zone (the reference signal) and the signals received at the origin of the first zone (62 km), in the shadow zone (95 km), and in the second convergence zone (135 km). The separations of the points of reception along the distance were, $\Delta r = 10, 23,$ and 63 km, respectively. Evidently, the signals propagating within the upper channel also arrived at all points of reception.

Consider now the experimental results presented in Fig. 2. This figure exhibits: (top) the angular spectra (the array response versus the vertical angle of signal arrivals) obtained by the array beam scanning in the range of arrival angles $\pm 23^\circ$; (center) the frequency-energy spectra of the signal received from the direction indicated by the arrow in the upper plot; and (below) the autocorrelation functions obtained in the mode of

the array aiming at a chosen angle. Along the ordinate axis, we plotted: for the angular spectra, the amplitudes of the received signals A (on the linear scale) versus the grazing angles α (in deg); for the energy spectra, the spectral density S in dB versus the frequency f (in kHz); and for the correlation functions, the autocorrelation coefficient R versus the time delay τ (in ms). The angular and energy spectra presented in Fig. 2 were averaged over 12 s, and the autocorrelation functions were obtained by averaging over 1.024 s.

Figure 2a characterizes the reference signal propagating without reflections from the waveguide boundaries and received at a distance of 72 km. Its arrival angle equals $\alpha = -6^\circ$ (see $A(\alpha)$). The minus and plus signs mean the arrivals of rays at the point of reception from below and from above, respectively. The aforementioned signal was chosen as a reference one, because it had the highest intensity, and it was well resolved by the array beam in the vertical plane. However, one can observe a modulation of its energy spectrum S with the frequency $f_m \approx 250$ Hz. This is caused by the fact that the signal arrived at the point of reception over two rays with the time difference $\tau = 1/f_m \approx 4$ ms, which corresponds to the position of the second peak (marked by the arrow) on the delay axis τ for the autocorrelation function R .

Figure 2b presents the characteristics of the signal received at the origin of the first convergence zone (for the deep-water channel) at a distance of 62 km. The maximum of the array beam was aimed at the angle $\alpha = +12^\circ$. In this case, the array beam spanned the signals arriving over a small number of rays, as demonstrated by the angular width of the array response A and the lack of modulation in the energy spectrum S . Some

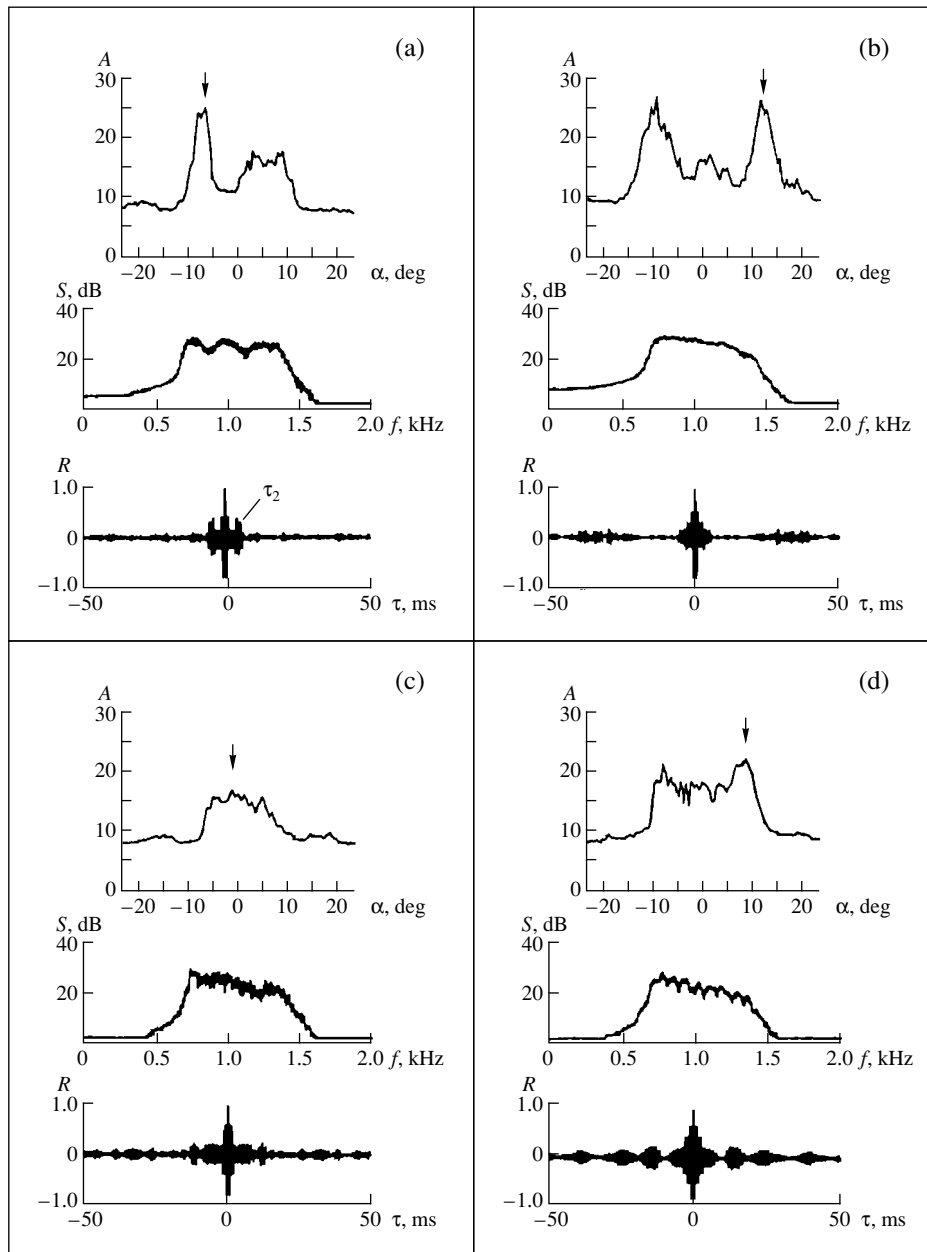


Fig. 2. Angular spectra A (top), frequency–energy spectra S (center), and autocorrelation functions R (bottom) at the points of reception: (a) at the middle of the first convergence zone caused by the lower channel (distance 72 km); (b) at the origin of the first convergence zone (distance 62 km); (c) in the shadow zone (distance 95 km); (d) in the second convergence zone (distance 135 km).

broadening of the main peak is observed in the autocorrelation function R , which indicates the arrival of relatively weak signals with delays τ less than the correlation interval determined by the frequency band of the radiated signal.

From Fig. 1b it follows that the distance 95 km corresponds to the shadow zone for the signals propagating through the deep-water channel. To this distance, only the signals can arrive that propagate through the upper channel in the range of the grazing angles $\pm 6.5^\circ$. The angular spectrum of the received signals A pre-

sented in Fig. 2c is continuous, because separate rays could not be resolved even with the use of the narrow-beam array. The array beam was aimed at the angle $\alpha = -2^\circ$ which corresponds to the received signal of the highest amplitude. From the irregularity of the energy spectrum S and the multitude of small peaks in the autocorrelation function R , we can conclude that a great number of rays were spanned by the array beam.

Figure 2d refers to the case of the receiving array located at a distance of 135 km. Signals can arrive to this distance through both the upper and the lower

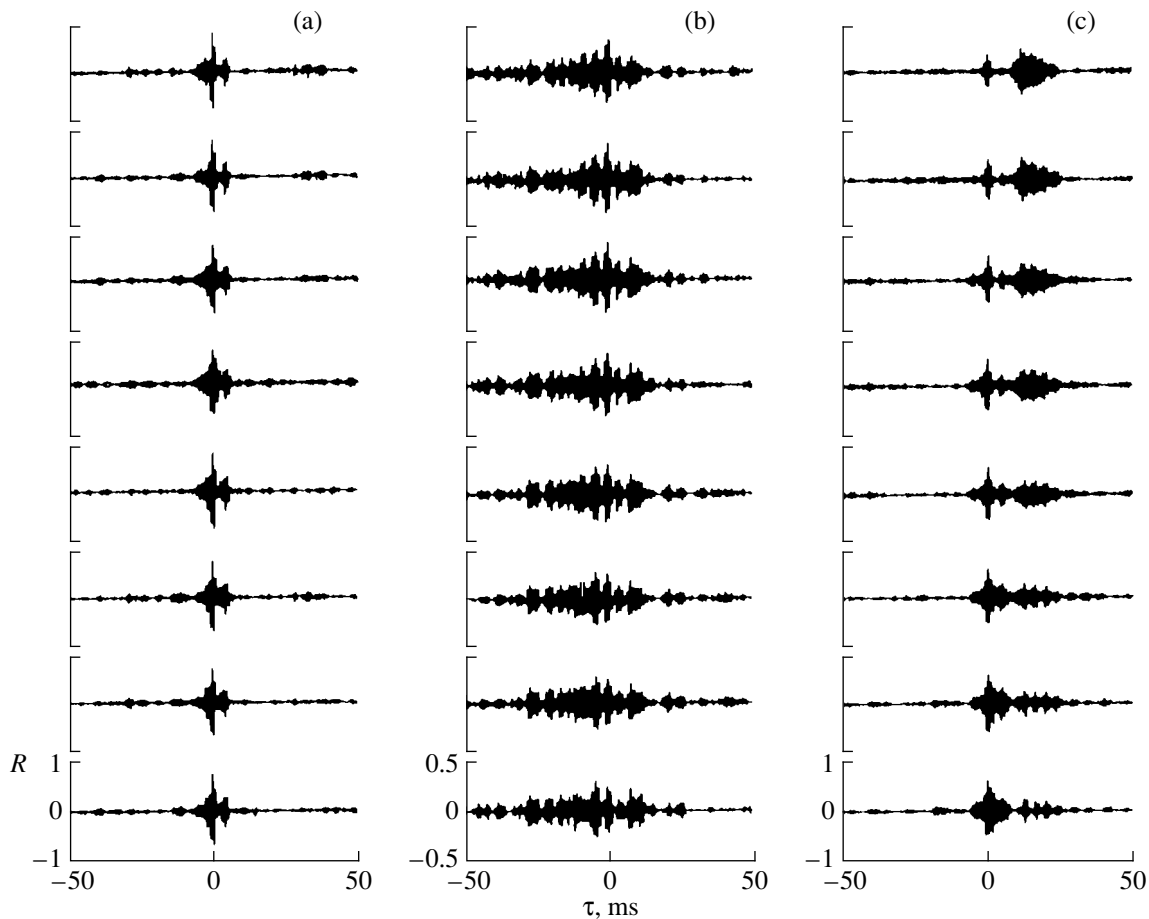


Fig. 3. Normalized cross-correlation functions R for different spatial separations $\Delta r =$ (a) 10; (b) 23 (the scale for R is doubled); and (c) 63 km.

channels (see Fig. 1b). The angular spectrum A is continuous in the range of angles $\pm 10^\circ$. However, the amplitude of the signals with the arrival angles $\alpha \approx -8.5^\circ$ and $\alpha \approx +9^\circ$ was somewhat greater than that of other signals. Therefore, the maximum of the array beam was aimed at an angle of $+9^\circ$. We can see a well-defined modulation in the energy spectrum S and the secondary correlation peaks in the autocorrelation function R , which, as in the previous case, is the consequence of a simultaneous reception of several signals spanned by the array beam.

Having analyzed the characteristics of the sound fields recorded at the chosen distances, we proceed to the main issue, namely, to the cross-correlation of the received signals. The results of measurements of the spatial correlation function $R(\tau)$ are shown in Fig. 3, which illustrates the variations of the normalized cross-correlation functions R within 3 min. The averaging time for each realization was 1.024 s, with the interval between the realizations being 25.5 s, which equals the period of the pseudo-noise signals. The measurement procedure was described in detail in [6]. Since the function $R(\tau)$ was calculated between the signals received at

different spatial points and at different instants of time, the scale of delays τ in Fig. 3 is a conditional one. The zeroth delay corresponds to one of the correlation peaks: in most cases, to the maximum peak.

The temporal variability of the cross-correlation function $R(\tau)$ between the signals received in the first convergence zone (in the deep-water channel) at distances of 62 and 72 km is shown in Fig. 3a. In the curves $R(\tau)$, we can see two main correlation peaks whose values vary from 0.70 to 0.83 and from 0.30 to 0.36, and several weak peaks with smaller values of the correlation coefficients. This testifies to several signal arrivals at the point of reception over different rays with slightly different angles, which fall into the main lobe of the array directional pattern. These signals, especially at time delays exceeding the time correlation interval of the radiated signal, represent an interference with respect to one another. Therefore, it is expedient to estimate the value of the spatial correlation coefficient $|R_s|$ in the absence of multipath propagation. The corrected correlation coefficient allowing for the interaction of the signals arriving over different rays and unre-

Table

Position of the receiving array	Δr , km	α_r/α_s	$ \bar{R}_{\max} $	σ_R	k	$ \bar{R}_s $	σ_{R_s}
In the first convergence zone	10	$-6^\circ/+13^\circ$	0.77	0.05	3	0.89	0.05
First zone–shadow zone	23	$-6^\circ/-2^\circ$	0.31	0.06	12	0.67	0.03
First zone–second zone	63	$-6^\circ/+9^\circ$	0.54	0.10	9	0.84	0.03

solved by the array beam can be found from the following expression [7]

$$|\bar{R}_s| = \sum_{i=1}^N \left(\sum_k |R_{ki}|^2 \right)^{1/2} / N,$$

where k is the number of the correlation peaks and N is the number of independent measurements of the correlation coefficient. In the considered case (with a 10-km separation of the points of reception), the value of the corrected correlation coefficient $|R_s|$ falls in the range 0.81–0.93, and its value averaged over 8 measurements is $|\bar{R}_s| = 0.89 \pm 0.05$.

Figure 3b shows the cross-correlation functions $R(\tau)$ between the reference signal (the distance 72 km) and the signals received at a distance of 95 km from the source, i.e., for the spatial separation of the points of reception 23 km. At this distance, the angular spectrum in the range $\pm 6.5^\circ$ (see Fig. 2c) was totally caused by signals arriving over rays that were not resolved by the array beam. As a result, the functions $R(\tau)$ at the chosen angle $\alpha = -2^\circ$ (see Fig. 3b) exhibit a large number (~ 12) of correlation peaks with small correlation coefficients. For this reason, the scale in Fig. 3b was doubled. Because of the large number of signals spanned by the main lobe of the directional pattern and because of the temporal variability of their amplitudes, the values of the correlation coefficients R_{ki} for separate peaks vary from 0.09 to 0.14 (for peaks with minimum values of the correlation coefficients) and from 0.23 to 0.39 (for peaks with maximum values). The corrected spatial correlation coefficient $|R_s|$ varies from 0.63 to 0.72 with the mean value $|\bar{R}_s| = 0.67 \pm 0.03$. The reduction of the value of the correlation coefficient $|R_s|$ at $\Delta r = 23$ km as compared to that $\Delta r = 10$ km is explained by the incomplete allowance made for the interaction of many signals simultaneously falling within the array beam, rather than by the increasing spatial separation of the points of reception. In particular, this is confirmed by the results obtained for large separations of the points of reception ($\Delta r = 63$ km) with a smaller number of rays.

Figure 3c shows the correlation functions $R(\tau)$ for the spatial separation of the points of reception $\Delta r = 63$ km, for the same reference signal received at a distance of 72 km in the first convergence zone (in the deep-water channel) and the signals with the arrival angles $\alpha \approx +9^\circ$ (see Fig. 2d) recorded in the second convergence zone at a distance of 135 km. These functions exhibit approximately nine correlation peaks $|R_{ki}|$, the value of

the minimum peak varying from 0.07 to 0.13, and the value of the maximum one, from 0.36 to 0.64. The correlation coefficient $|R_s|$ (summed over all peaks) corrected for each realization varied from 0.78 to 0.87, which exceeds $|R_s|$ for $\Delta r = 23$ km, as was noted above.

The results obtained are presented in the table, where the following data are given: the position of the receiving array (relative to the sound field structure caused by the lower channel only); the spatial separation of the points of reception Δr ; and the arrival angles α of the reference signal (α_r) and the spatially-separated signal (α_s) at which the array beam was aimed. The table also gives the greatest correlation coefficients $|\bar{R}_{\max}|$ averaged over the observation time for separate, resolved in arrival times, signals with the standard deviations σ_R ; the average values of the corrected correlation coefficients $|\bar{R}_s|$ with their standard deviations σ_{R_s} ; and the number of the correlation peaks k .

These experimental data show that an increase in the spatial separation of the points of reception from 10 to 63 km leads to a reduction of the cross-correlation coefficient. This reduction is mainly a consequence of the interaction between the simultaneously received signals, which are an interference to one another, rather than a consequence of the increase in distance. Thus, the cross-correlation of signals propagating over purely water paths is predominantly affected by the varying number of received signals falling into the relatively narrow ($\sim 2^\circ$) main lobe of the directional pattern, rather than by the spectrum variation with increasing distance due to the sound attenuation.

REFERENCES

1. P. H. Dahl, *J. Acoust. Soc. Am.* **100**, 748 (1996).
2. M. Badiy, J. Simmen, and S. Forsythe, *J. Acoust. Soc. Am.* **101**, 3361 (1997).
3. E. K. Westwood and D. P. Knobles, *J. Acoust. Soc. Am.* **102**, 2645 (1997).
4. D. Tielburger, S. Finette, and S. Wolf, *J. Acoust. Soc. Am.* **101**, 789 (1997).
5. M. Siderius, D. R. Jackson, D. Rouseff, and R. Porter, *J. Acoust. Soc. Am.* **102**, 3439 (1997).
6. O. P. Galkin and S. D. Pankova, *Akust. Zh.* **45**, 479 (1999) [*Acoust. Phys.* **45**, 426 (1999)].
7. O. P. Galkin and S. D. Pankova, *Akust. Zh.* **44**, 57 (1998) [*Acoust. Phys.* **44**, 44 (1998)].

Translated by Yu. Lysanov

Propagation of Fast Leaky Surface Waves in a System of Metal Electrodes on a Lithium Tetraborate Crystal

V. I. Grigor'evskii and Yu. V. Gulyaev

*Institute of Radio Engineering and Electronics, Russian Academy of Sciences,
pl. Akademika Vvedenskogo 1, Fryazino, Moscow oblast, 141120 Russia*

e-mail: vig286@ire216.msk.su

Received August 28, 1999

Abstract—Dispersion curves are calculated for fast leaky surface acoustic waves in a periodic system of metal electrodes on a lithium tetraborate crystal. The periodic Green's function analysis is applied to the piezoelectric halfspace. To allow for the mechanical properties of the electrodes, a perturbation method is developed that is accurate to within the first order of the electrode thickness-to-period ratio, and the finite-element method is used to investigate the higher-order effects. The reflection factor of a system of two open electrodes is shown to have a minimum at a certain electrode thickness. The fast leaky-to-Rayleigh wave conversion factor and the Rayleigh wave reflection factor are studied as functions of the electrode thickness. © 2000 MAIK "Nauka/Interperiodica".

In recent years, interest has grown considerably in the so-called leaky surface acoustic waves (SAW), which are described by inhomogeneous equations of motion of an elastic medium. The leaky waves experience attenuation along the propagation path due to conversion into bulk waves. At present, the well-known types of leaky waves are those in quartz, lithium niobate, and lithium tantalate. These waves belong to the so-called quasi-shear leaky waves [1, 2], because their shear component predominates. Their velocity is close to that of the fast shear wave, and the attenuation is caused by the conversion into the slow shear wave. Crystal orientations are known for which the attenuation of these waves is very small; in particular, in 36°YX-cut LiTaO₃, it equals 0.0003 decibel per wavelength. The leaky waves have found a wide application in high-frequency SAW filters with low insertion loss, because the propagation velocity of these waves is about 1.5 times higher and the electromechanical coupling factor, which determines the excitation efficiency, is much higher than the corresponding values for the Rayleigh waves.

Low-loss fast surface acoustic waves were discovered not long ago [3, 4]. Their longitudinal displacement component is the predominant one; the velocity is close to that of the longitudinal bulk wave, i.e., it is almost twice as high as that of the Rayleigh wave. Thus, it is possible to further increase the operating frequency of the SAW filters.

Fast leaky surface acoustic waves in a periodic system of metal electrodes on a tetraborate lithium crystal (Li₂B₄O₇) with the orientation specified by the Euler angles (0°, 47.3°, 90°) were theoretically and experi-

mentally studied in [5]. The reflection factor was shown to increase with the electrode thickness-to-wavelength ratio. The dispersion curves were also calculated for the zero-thick electrodes near the Rayleigh wave stopband and near the band where the fast leaky wave is converted into the Rayleigh wave.

In this paper, we study the reflection of the fast leaky surface acoustic waves in a periodic system of metal electrodes on a lithium tetraborate crystal. To describe the piezoelectric halfspace, the periodic Green's function method [6] is applied, which is particularly suitable for studying the SAW propagation in periodic structures on crystals. To describe the effect of mechanical properties of the electrodes, a perturbation method is developed, which is accurate to within the first order of the electrode thickness-to-period ratio (h/p), and the finite-element method is used in order to overcome the limitation that this ratio be small. In contrast to the results reported in [5], the reflection factor of two open electrodes is shown to vary nonmonotonically with increasing ratio h/p . The fast leaky-to-Rayleigh wave conversion factor and the Rayleigh wave reflection factor are studied as functions of the electrode thickness.

Consider a piezoelectric halfspace $z < 0$ on whose surface a system of electrodes with a period p is arranged; the electrode width and height are l and h , respectively; the electrodes are parallel to the Y -axis. It is known that, when sources of elastic stresses and electric charges are present on a piezoelectric surface, they cause particle displacements and induce an electric potential on the surface. The latter quantities can be

expressed in terms of the Fourier transform of the Green's function as follows:

$$\begin{bmatrix} U_i(k, \omega) \\ \varphi(k, \omega) \end{bmatrix} = [G(k, \omega)] \begin{bmatrix} T_{3i}(k, \omega) \\ \sigma(k, \omega) \end{bmatrix}, \quad (1)$$

where k is the wave number; ω is the circular frequency; $U_i(k, \omega)$, $T_{3i}(k, \omega)$, $\varphi(k, \omega)$, and $\sigma(k, \omega)$ ($i = 1, 2$, or 3 refer to the X -, Y -, or Z -axis) are the Fourier transforms of the particle displacements, stress tensor, electric potential, and charge, respectively. In the general case, $[G(k, \omega)]$ is a 4×4 matrix and is called the generalized or matrix Green's function of the linear piezoelectric halfspace [7].

The procedure of calculating the Green's matrix elements involves the solution of the eigenvalue problem for the equations of motion of the piezoelectric medium; this problem can be reduced to finding the attenuation factor characterizing the wave attenuation in the bulk of the crystal in the direction normal to its surface from an octic equation. When the wave number k is real and there are no wave sources in the bulk of the piezoelectric, only four of the eight roots correspond to waves that are confined to the surface or carry the energy away from the surface into the crystal bulk. However, the wave number of the leaky wave is complex. In this case, according to [8], the four attenuation factors should be selected using the analytical expansion of the Green's function elements from the real axis to the complex plane. The poles displaced from the real wave number axis correspond to waves whose amplitude decreases along the propagation path and increases depthward, which testifies to the energy transfer to the bulk waves; therefore, they correspond to the leaky waves. This method for selecting the eigenvalues was used in this paper.

In the presence of a periodic system of electrodes, according to Floquet's theorem, the elastic stress and charge density on the surface can be represented as the functions of the x coordinate in the form

$$\begin{bmatrix} T_{3i}(x, \omega) \\ \sigma(x, \omega) \end{bmatrix} = \exp(iqx) \begin{bmatrix} t_{3i}(x, \omega) \\ s(x, \omega) \end{bmatrix}, \quad (2)$$

where the unknown wave number q describes the dispersion of the system's eigenwaves and the functions $t_{3i}(x, \omega)$ and $s(x, \omega)$ are periodic with the period p .

Strictly speaking, the leaky waves are not the eigenwaves of the piezoelectric halfspace, because their amplitude tends to zero at a long distance from the source. However, when the leaky wave pole on the complex wave number plane is sufficiently close to the real axis, a space region always exists where this wave dominates [9]. In this region, the propagation of the leaky wave can be considered as the eigenwave propagation problem.

Expanding the right-hand side of (2) into the Fourier series yields

$$\begin{bmatrix} T_{3i}(x, \omega) \\ \sigma(x, \omega) \end{bmatrix} = \exp(iqx) \sum_{m=-\infty}^{+\infty} \begin{bmatrix} t_{3i}(m, \omega) \\ s(m, \omega) \end{bmatrix} \exp(imQx), \quad (3)$$

where $t_{3i}(m, \omega)$ and $s(m, \omega)$ are the Fourier series coefficients and $Q = 2\pi/p$ is the "wave number" or the inverse vector of the periodic structure. Formulas (1) and (3) can be used to find the Fourier coefficients for the particle displacements and the electric potential on the surface. The dependences of these quantities on the coordinate can be obtained as a sum of the Fourier series:

$$\begin{bmatrix} u_i(x, \omega) \\ \varphi(x, \omega) \end{bmatrix} = \exp(iqx) \times \sum_{m=-\infty}^{+\infty} [G(q + mQ, \omega)] \begin{bmatrix} t_{3i}(m, \omega) \\ s(m, \omega) \end{bmatrix} \exp(imQx). \quad (4)$$

This expression shows that the response of the piezoelectric halfspace can be calculated in terms of the Green's function

$$[G^p(q, \omega)] = \exp(iqx) \times \sum_{m=-\infty}^{+\infty} [G(q + mQ, \omega)] \exp(imQx), \quad (5)$$

which is the response to a periodic δ -function-type excitation.

The Green's function completely describes the piezoelectric substrate; however, to calculate the eigenwaves of the periodic structure, one should specify additional relationships between the excitations and the responses. These relationships can be obtained by taking into account the mechanical characteristics of the electrode structure.

We study two types of electric connections in the electrode system: all electrodes are either connected (short-circuited) or open (isolated from each other). In both cases, the electric potential is constant within an electrode. We assume that the charge resides at the lower electrode surface, which is adjacent to the piezoelectric. From the viewpoint of electric characteristics, this means that the electrode is treated as an infinitesimally thin one. The charge distribution across the electrode width is represented by the expression

$$s(x) = [1 - (2x/l)]^{-1/2} \sum_{n=0}^N A_n T_n(2x/l), \quad (6)$$

where A_n is an unknown coefficient of the n th-order Chebyshev polynomial $T_n(y)$. This formula gives a correct description of the singularities at the electrode edges; therefore, only a small number of Chebyshev polynomials is needed to provide an adequate description of the charge distribution [6]. Calculating the Fourier transform of (6) yields the amplitudes of the spatial harmonics of charge

$$s_m = \frac{l}{2p} \sum_{n=0}^N (-i)^n \pi J_n \left(\pi \frac{l}{p} m \right) A_n, \quad (7)$$

which are involved in the right-hand member of (4). Here, $J_n(y)$ is the n th-order Bessel function of the first kind.

In a system of connected electrodes, all their potentials are zero. Dividing an electrode into N intervals, setting the potential at each interval equal to zero, and using formula (4), we obtain a system of N linear equations in the amplitudes of the spatial harmonics of charge s_m , which, in turn, are represented by formula (7).

In a system of open electrodes, the potential of each electrode is unknown; an additional equation is given by the condition that the total electrode charge be zero. We multiply expression (7) by $\exp(iqx)$ (see (2)) and integrate the result to obtain

$$\sum_{n=0}^N A_n (i)^n J_n \left(q \frac{l}{2} \right) = 0. \quad (8)$$

Expressions (7) and (8) and the second equation in (4) relate the electric characteristics of the piezoelectric halfspace to those of the electrode structure.

We employ two approaches to describe mechanical properties of the electrodes. The first one uses the perturbation theory, and the second uses the finite element method. In both cases, the particle displacements and the normal stresses must be matched at the interface between the two elastic media.

The approach based on the perturbation theory assumes that the upper medium is a layer whose thickness varies with the period p and is described by the function $\zeta(x)$. At the upper irregular boundary of the layer, the normal elastic stress must be zero:

$$t_{ij} n_j = 0, \quad (9)$$

where n_j ($j = 1, 2, 3$) are the components of the outer normal to the surface $z = \zeta(x)$. When $h = \max |\zeta(x)| \ll p$, one can expand equations (9) into a power series in the small parameter $\varepsilon = h/p$ and restrict it to the first-order term [10, 11]:

$$t_{i3} - t_{i1} \zeta'_x + t'_{i3,z} \zeta = 0. \quad (10)$$

Here, $i = 1, 2, 3$ and the upper prime and the subscripts x or z mean the differentiation with respect to the coordinate x or z , respectively. The elements of the stress tensor and their z -derivatives in (10) are calculated at

the surface $z = 0$. By virtue of (10), the condition that the elastic stresses in the two media be matched at the interface $z = 0$ can be reduced to the form

$$T_{i3} = t_{i1} \zeta'_x - t'_{i3,z} \zeta. \quad (11)$$

Expanding $z = \zeta(x)$ and (11) into the Fourier series yields the expressions for the Fourier coefficients of the elastic stress at the surface of the piezoelectric:

$$T_{i3}^{(n)} = \frac{h}{p} \sum_{m=-\infty}^{+\infty} A_{n-m} \left[i t_{i1}^{(m)} (n-m) - \frac{1}{Q} \frac{\partial t_{i3}^{(m)}}{\partial z} \right], \quad (12)$$

where n and m are the numbers of the Fourier harmonics and A_m are the Fourier coefficients of the function $z = \zeta(x)$. When the electrode cross-section is rectangular, we have

$$A_m = \frac{h}{p} l \sin \left(m \pi \frac{l}{p} \right) / \left(m \pi \frac{l}{p} \right). \quad (13)$$

The assumption that the layer is thin can be used to derive a relationship between the Fourier components of stress t_{i1} , the derivatives $\partial t_{i3}/\partial z$, and the particle displacements at $z = 0$ [12]. For this purpose, one should expand the particle displacements in the layer into a power series

$$u_i = [u_i^{(0)} + u_i^{(1)} z + u_i^{(2)} z^2 + \dots] e^{ikx} \quad (14)$$

and substitute it into the equations of motion of the elastic material of the layer. Then, the condition that the stress at the upper layer boundary be zero yields

$$t_{11}(k, \omega) = ik \frac{c_{11}^2 - c_{12}^2}{c_{11}} u_1^{(0)}, \quad (15)$$

$$t_{13}(k, \omega) = 0, \quad (16)$$

$$\frac{\partial t_{13}}{\partial z}(k, \omega) = \left(\frac{c_{11}^2 - c_{12}^2}{c_{11}} k^2 - \rho \omega^2 \right) u_1^{(0)}, \quad (17)$$

$$\frac{\partial t_{33}}{\partial z}(k, \omega) = -\rho \omega^2 u_3^{(0)}, \quad (18)$$

where c_{11} , c_{12} , and c_{44} are the elastic moduli and ρ is the density of the electrode material. Relationships (12) together with (15)–(18) completely describe the mechanical properties of the electrode structure.

To remove the limitation that the parameter h/p be small, we use the finite element method [13, 14]. In this method, the continuous medium is divided into individual small elements called the finite elements. The elastic displacement distribution within the elements is interpolated by a linear combination of polynomials whose coefficients are equal to the displacements at the nodes of the individual elements. Then, the conditions for minimizing the Lagrangian of the elastic body are imposed, or Galerkin's procedure is applied directly to the differential equations of motion of the elastic medium to derive equations for the elastic displace-

ments at the element nodes. Combining the equations that describe individual elements with the conditions that the particle displacements and stresses at the element interfaces be continuous yields an inhomogeneous system of linear equations in the displacements of all nodes in the region occupied by the finite body. This system can be written in the matrix form

$$\{[S] - \omega^2[M]\}[U] = [T]. \quad (19)$$

Here, matrices $[S]$ and $[M]$ describe the elastic and inertial properties of the medium and are called the elasticity and inertia matrices, respectively; the elements of the vector $[U]$ are the particle displacements at the nodes of all finite elements; and the elements of the external stress vector $[T]$ are given by the expression

$$T_j = \int_e N(x, z) T_{3i} d\Gamma, \quad (20)$$

where the polynomial $N(x, z)$ interpolates the elastic displacements within an individual finite element, and the integral is calculated over the finite element boundaries that approximate the boundary of the elastic body.

The elastic displacements and stresses must be continuous at the interface between the electrode and the piezoelectric crystal. We write the elastic displacements at the surface of the piezoelectric as a superposition of spatial harmonics and use the condition that the displacements at the nodes at the interface between the electrode and piezoelectric crystal be equal to represent the elements of the vector $[U]$

$$U_j = \sum_{n=-\infty}^{+\infty} \exp(ik_n x_j) \sum_{m=1}^4 A_{nm} U_i(k_n, m), \quad (21)$$

where $U_i(k_n, m)$ are the weighting factors, A_{nm} are the partial wave amplitudes, and j and x_j are the number and the coordinate of the node at the interface between the electrode and the piezoelectric crystal.

The elastic stresses at the piezoelectric surface are nonzero under the electrode and zero elsewhere. Introducing the unknown stresses at the nodes that lie at the interface between the electrode and the piezoelectric crystal and approximating the stresses within individual finite elements by interpolation polynomials, one can calculate the elements of the vector $[T]$ in (19) and the Fourier components of the stresses at the piezoelectric surface

$$T_{3i}(k, \omega) = \frac{1}{p} \int_{-l/2}^{l/2} \exp(-ikx) \sum_{m=1}^M T_{3i}^{(m)} N_m(x) dx, \quad (22)$$

where M is the total number of nodes on the electrode–piezoelectric interface, $T_{3i}^{(m)}$ are the elastic stresses at these nodes, and $N_m(x)$ are the interpolation polynomials.

Expressions (19), (21), and (22) provide a complete finite-element description of the system of electrodes and give additional relationships between the sources and the responses to them, which are necessary for solving the eigenwave problem for the structure.

In our calculations, we assume that the electrodes are made of aluminum, which is mostly used in practice. On $(0^\circ, 47.3^\circ, 90^\circ)$ -cut lithium tetraborate, the fast leaky wave has a zero Y -component of displacement; therefore, the matrix $[G(k, \omega)]$ reduces to a 3×3 matrix. Combining equations (4) and relationships that describe the electric and mechanical properties of the electrode structure yields a system of homogeneous linear equations whose determinant depends on the unknown wave number q . The condition that the determinant be zero at the given frequency ω gives the dispersion relationship for the periodic structure.

When M spatial harmonics of the fast leaky wave are taken into account, the perturbation method applied to the system of connected electrodes yields a system of $3M + N$ equations in $3M$ unknown amplitudes of the spatial harmonics and N unknown coefficients of the Chebyshev polynomials in (7). For a system of open electrodes, with allowance for (8), the dimension of the system increases by one. The finite-element method requires more computations. When an electrode is simulated by P_x nodes in the x direction and P_y nodes in the y direction, the number of equations involved in the system is $2P_x P_y + 2P_x + 3M + N$ for connected electrodes and greater by one for open electrodes. Here, the additional unknowns are two stress components at the electrode–piezoelectric interface.

Numerical calculations were performed for $M = 10$, $N = 6$, $P_x = 7$, and $P_y = 3$. A common steepest descent procedure was used to find the minimum of the determinant of the system of equations at a given frequency ω .

Figure 1 shows the imaginary part of the wave number q for a system of connected electrodes versus frequency near Bragg's stopband for the fast leaky wave. The imaginary part of the wave number determines the reflection factor in the stopband. The normalized frequency is specified by the structure period. If $p = 2\pi$, Bragg's reflection condition $\pi/p = q$ gives $q = 0.5$, and the central frequency of the stopband is $\omega \approx V_L/2$, where V_L is the velocity (in km/s) of the fast leaky wave on a free surface of the crystal. The plots are given for $h/p = 0$ to 0.04 with 0.01 intervals. With an increase in this parameter, the stopband broadens and the attenuation increases at the center of the band.

Figure 2 shows the real part of the wave number, which determines the phase velocity, for the system of connected electrodes at the same values of h/p . It can be seen that the wave number remains almost constant (about 0.5) within the stopband. This means that two fast leaky waves propagating in opposite directions are transformed into each other in as a result of reflection.

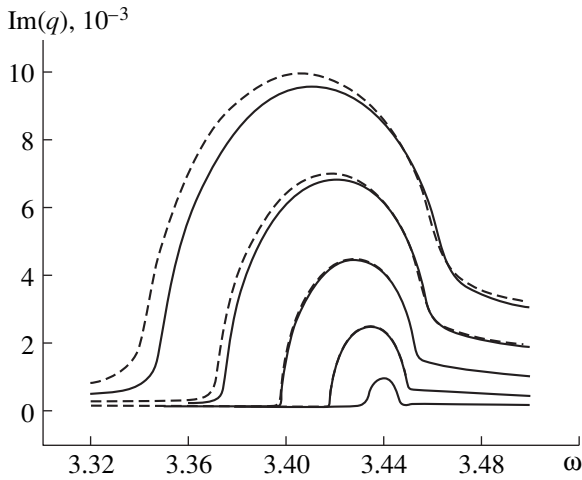


Fig. 1. Imaginary part of the wave number for a system of connected electrodes versus frequency. The parameter h/p varies from 0 to 0.04 at a step of 0.01. The solid lines are calculated by the perturbation method, and the dashed lines by the finite element method.

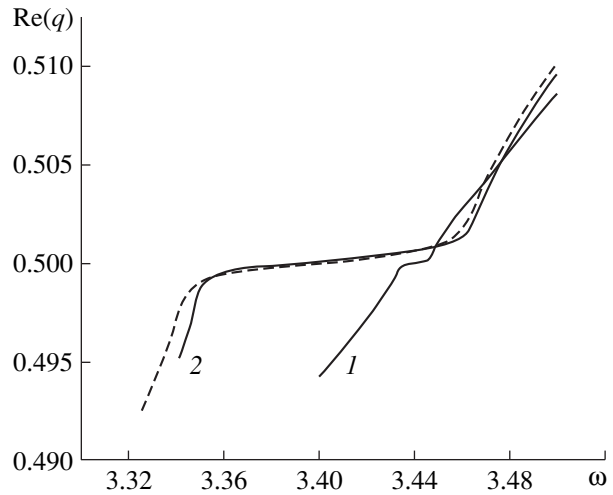


Fig. 2. Real part of the wave number for a system of connected electrodes versus frequency for $h/p = (1) 0$ and $(2) 0.04$.

In the system of open electrodes (Fig. 3), the central frequency of the stopband is shifted toward higher frequencies, which is caused by a lower electric shielding than in the system of connected electrodes. The important feature of this case is that the reflection factor varies nonmonotonically with h/p . This behavior is explained by the fact that the electric reflection factors have opposite signs in systems with connected and open electrodes. When the electrodes are sufficiently thick, the reflection due to the mechanical perturbation predominates over the reflection due to the electric perturbation of the surface, and the resulting reflection factor increases.

Solid lines in Figs. 1–3 refer to the perturbation method; dashed lines, to the finite element method. It can be seen that the results obtained by the perturbation method and the finite element method are very close for small h/p . A noticeable disagreement appears for $h/p > 0.02$. The greatest difference is less than 5%.

Immediately on the right of the stopband (Figs. 1, 3), a high attenuation appears due to the conversion into the longitudinal bulk wave. A similar effect is observed for quasi-transverse leaky waves, e.g., in 36°YX -cut LiTaO_3 [6]. The attenuation on the left of the stopband is associated with the nature of the wave and is related to the conversion into the longitudinal bulk wave. This attenuation also takes place on an unperturbed surface. However, in the system of connected electrodes, the attenuation has a 0.006-dB/wavelength minimum at $h/p = 0.015$ on the left side of the stopband, which is twice as low as the attenuation on an unperturbed metallized surface.

This cut of lithium tetraborate can also support the Rayleigh wave whose velocity V_R is by a factor of 2.1 lower than that of the fast leaky wave V_L . When the con-

dition $Q = q_L + q_R$ is met, where q_L and q_R are the wave numbers of the leaky and Rayleigh waves, the reflection of the fast leaky wave accompanied by the conversion to the Rayleigh wave takes place; at $Q = 2q_R$, the Rayleigh wave is reflected. For open electrodes (Fig. 4), the maximum leaky-to-Rayleigh wave conversion factor varies nonmonotonically with the electrode thickness, as in the case of the fast leaky wave reflection. However, the Rayleigh wave reflection factor in systems of open or connected electrodes varies monotonically with thickness because of the lower electromechanical coupling for the Rayleigh waves. The Ray-

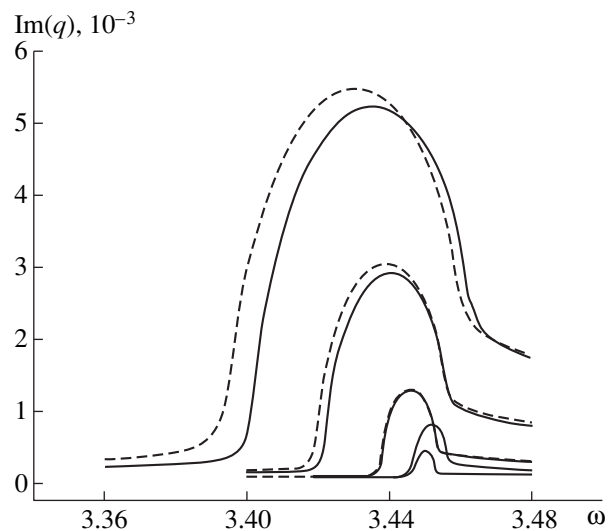


Fig. 3. Imaginary part of the wave number for a system of open electrodes versus frequency. The parameters are the same as in Fig. 1.

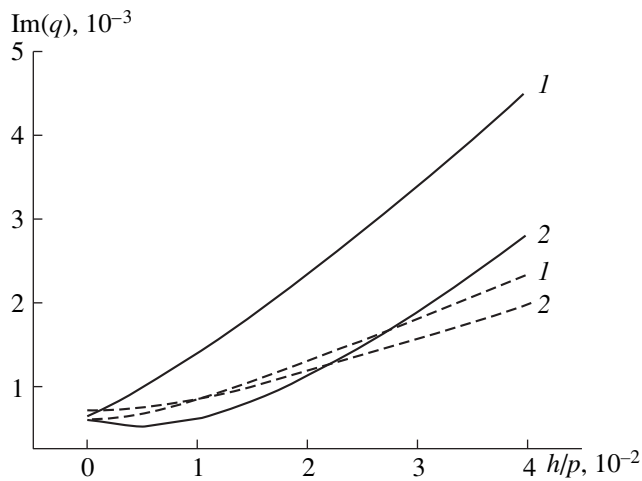


Fig. 4. Imaginary part of the wave number at the center of the stopband versus h/p for (1) connected and (2) open electrodes. The solid lines refer to the fast leaky-to-Rayleigh wave conversion, and the dashed lines to the Rayleigh wave reflection.

leigh wave is also an eigenwave of the piezoelectric halfspace. Therefore, it is more stable to perturbations of the surface, and the leaky-to-Rayleigh wave conversion factor and the Rayleigh wave reflection factor are lower than the fast leaky wave reflection factor.

On the whole, our results are in good agreement with the results reported in [5]. The data obtained by the perturbation method developed above and by the finite element method are in close agreement. The theoretical dispersion curves can be used to calculate the parameters of the coupling mode technique, which is widely used in designing SAW filters.

ACKNOWLEDGMENTS

This work was supported by the INTAS, project no. 96-0441.

REFERENCES

1. Y. V. Gulyaev, *IEEE Trans. Ultrason. Ferroelectr. Freq. Control* **45**, 935 (1998).
2. K. Nakamura, M. Kazumi, and H. Shimizu, *IEEE Ultrason. Symp. Proc.*, 1977, pp. 819–822.
3. N. F. Naumenko, *Kristallografiya* **37**, 979 (1992) [*Sov. Phys. Crystallogr.* **37**, 520 (1992)].
4. T. Sato and H. Abe, *IEEE Ultrason. Symp. Proc.*, 1994, pp. 287–292.
5. T. Sato and H. Abe, *IEEE Ultrason. Symp. Proc.*, 1995, pp. 305–315.
6. V. P. Plessky and T. Thorvaldsson, *IEEE Trans. Ultrason. Ferroelectr. Freq. Control* **42**, 280 (1995).
7. R. C. Peach, *IEEE Ultrason. Symp. Proc.*, 1995, pp. 221–225.
8. S. V. Biryukov and M. Weihnacht, *IEEE Ultrason. Symp. Proc.*, 1996, pp. 221–224.
9. S. V. Biryukov and M. Weihnacht, *J. Appl. Phys.* **83**, 3276 (1998).
10. L. M. Brekhovskikh, *Akust. Zh.* **5**, 282 (1959) [*Sov. Phys. Acoust.* **5**, 288 (1959)].
11. S. V. Biryukov, *Akust. Zh.* **31**, 296 (1985) [*Sov. Phys. Acoust.* **31**, 174 (1985)].
12. B. A. Auld, *Acoustic Fields and Waves in Solids* (Wiley, New York, 1973).
13. R. Lerch, *IEEE Trans. Ultrason. Ferroelectr. Freq. Control* **37**, 233 (1990).
14. M. Koshiba, S. Mitobe, and M. Suzuki, *IEEE Trans. Ultrason. Ferroelectr. Freq. Control* **34**, 472 (1987).

Translated by A. Khzmalyan

Simulation of the Vector Wave Field of a Low-Frequency Sound Source in the Ocean: Some Important Features

A. M. Derzhavin, O. V. Kudryavtsev, and A. G. Semenov

Andreev Acoustics Institute, Russian Academy of Sciences, ul. Shvernika 4, Moscow, 117036 Russia

e-mail: bvp@akin.ru

Received December 15, 1997

Abstract—An approach to the simulation of low frequency vector wave fields in stratified media (mainly in the ocean) is considered. The approach is characterized by an improved stability with respect to dividing the medium into many layers of arbitrary thickness. The model for the sound field of a point source is based on an integral representation of two-dimensional, cylindrically symmetric vector wave fields in inhomogeneous media, so that the contributions of all types of waves are included automatically. The model medium is subdivided into N horizontally homogeneous layers for which $4(N-1)$ equations are formulated to satisfy the boundary conditions between adjacent layers. The method of the generalized Schmidt matrix is used to obtain the coefficients of the equations; these coefficients are substituted into the expressions (of the Fourier–Bessel integral type) for the local parameters of the field. The latter are calculated according to the numerical procedure, and the results are used to model the distributions of the acoustic pressure and the horizontal and vertical components of the particle velocity in liquid and elastic media. The instability of the calculation procedure may result in a disagreement between the model and the exact solution. However, the disagreement is shown to occur mainly in models containing excessively thick layers. A way for improving the stability of the numerical model is suggested. The simulation results are compared with the exact analytical solution for the simplest example and with the results obtained according to the commonly used generalized matrix procedure (the benchmark problem). The examples of the practical application of the model for investigating more complex seismoacoustic wave fields in the ocean are presented. © 2000 MAIK “Nauka/Interperiodica”.

The simulation of wave fields in stratified media is a classical problem of acoustics and, specifically, ocean acoustics. This problem is considered in a number of recent papers [1–11], the well-known monograph [12], and fundamental works [13–19]. Recent activities in such areas as oil exploration and investigation of the sea bottom in the shelf zone are based on applied acoustics, and this fact makes the development of numerical approaches to the wave field simulation an urgent problem, especially when one or several layers of the bottom bulk are characterized by depth-dependent elastic properties, so that waves of different types (including longitudinal, shear, and surface seismoacoustic waves) can propagate in such layers and along their boundaries.

A numerical procedure based on a number of known techniques for calculating the wave fields was developed [6, 15] to simulate seismoacoustic fields in the oceanic medium when the source and the receiver are located at arbitrary depths in the vertically inhomogeneous water or bottom bulk. Each of these techniques (e.g., [11]), as applied to the simulation problem, has disadvantages that are partially discussed below. We suggest a procedure that takes into account our experience in numerical simulations of vector wave fields in elastic media and has a number of new features, partic-

ularly, in the choice of the thickness of elastic layers used in modeling.

We describe the wave fields in elastic media on the basis of the vector wave equations for local the displacements u and the stress tensor σ_{ik} or their components [13] along the coordinate axes. The propagation velocities c_l and c_t of longitudinal and transverse waves are related to the medium density ρ and Lamé coefficients λ and μ through the relationships $c_l^2 = (\lambda + 2\mu)/\rho$ and $c_t^2 = \mu/\rho$ [13]. In this case, a liquid medium appears to be a particular case of an elastic medium, if one sets the coefficient $\mu = 0$ and requires the stress tensor to be composed of only diagonal elements equal to the components of the local acoustic pressure p [12, 13].

The majority of existing models consider the ocean, including its bottom, as a horizontally stratified, cylindrically symmetric medium whose properties may only slightly vary in the horizontal (radial) direction and are independent of the azimuth angle. Here, we will not compare the known procedures of solving the wave equation and formally finding the parameters of wave fields in the stratified ocean. We note only that most of these procedures are reduced to the Green’s function technique [12, 13, 15]. The corresponding calculation models and procedures, their advantages, disadvantages, and limitations are reviewed in detail in papers [6, 15].

Two approaches appear to be most convenient for numerical simulations of low frequency fields. In the first approach, the solution is represented in the form of an expansion in the eigenmodes of the equation. In the second approach, the vector wave field (solution) at every local point is represented as an integral—the convolution with the Green's function, over its domain of definition. In the first approach, the expansion in modes may be unstable if the velocity of shear waves in the ground does not exceed the velocity of sound waves in water. Without additional improvement, this approach is adequate only for simulating the field in the water column [5, 20], and it is much less useful in a more general case, including the simulation of the vector fields in elastic sediments and the underlying bottom bulk.

Because of a direct estimate of the field, the second approach avoids these difficulties and naturally takes into account not only the discrete spectrum of solutions (including decaying modes), but also the continuous spectrum. As a result, the wave field everywhere is a superposition of all types of waves occurring in the water medium and the bottom bulk under the given conditions, namely, the longitudinal, shear, surface, propagating, and inhomogeneous waves [14]. In the absence of external sources, the equations for the displacement potentials in a homogeneous elastic medium have the form [13]

$$\Delta\Phi - c_l^{-2}\partial^2\Phi/\partial t^2 = 0; \quad \Delta\Psi - c_t^{-2}\partial^2\Psi/\partial t^2 = 0, \quad (1)$$

where the scalar Φ and vector Ψ potentials are related to the displacement vector \mathbf{u} through the relationship

$$\mathbf{u} = (\nabla\Phi) + [\nabla, \Psi], \quad (\nabla\Psi) = 0. \quad (2)$$

In the case of cylindrical symmetry, the solution to the problem on the field of an external harmonic source, i.e., the particular solution to equations of type (1) with specified boundary conditions is representable in the form of the Fourier–Bessel integrals of the Green's function of the inhomogeneous equation for both scalar and vector potentials Φ and Ψ [12]:

$$\begin{aligned} \Phi(r, z) &= \int_0^\infty G(z, z_s, \xi) \xi J_0(\xi r) d\xi, \\ \Psi(r, z) &= \int_0^\infty \mathbf{G}^*(z, z_s, \xi) \xi J_1(\xi r) d\xi, \end{aligned} \quad (3)$$

where ξ is the horizontal wave number; r is the horizontal component of the observation point measured relative the source; z_s and z are the vertical coordinates of the source and the observation point (receiver), respectively; $J_0(x)$ and $J_1(x)$ are the zero- and first-order Bessel functions that are the solutions to the homogeneous equations (1); and $G(z, z_s, \xi)$ and $\mathbf{G}^*(z, z_s, \xi)$ are the Green's functions of the boundary-value problem for the scalar and vector potentials. In the layer with the

source, these Green's functions satisfy the inhomogeneous ordinary differential equations

$$\begin{aligned} d^2G/dz^2 + [\omega^2/c_l^2(z) - \xi^2]G &= \delta(z - z_s), \\ d^2\mathbf{G}^*/dz^2 + [\omega^2/c_t^2(z) - \xi^2]\mathbf{G}^* &= \delta(z - z_s), \end{aligned} \quad (4)$$

where $\delta(z - z_s)$ is the Dirac delta-function and ω is the angular frequency of the harmonic source. We considered the case in which the source of compression waves (a monopole) is located within some layer of the considering system of layers, e.g., within the water layer. With this assumption, only the first of equations in (1) is actually inhomogeneous. Nevertheless, equations (4) give us a possibility of finding the Green's function of the system composed of equations (1) and the boundary conditions even for this case. The corresponding equations for Φ and Ψ remain homogeneous for other layers, and, for the particular case of the source of compression, the equation for Ψ is homogeneous even in the layer with the source (e.g., the water layer). The same consideration is true for the equations for Green's functions; unlike equations (4), these equations appear to be homogeneous. In the cylindrical coordinate system, expressions for the horizontal (u_r) and vertical (u_z) displacements can be found immediately from expression (2) with the scalar azimuth component of the potential Ψ taken to be equal to $-\partial\Theta/\partial r$ [12], where the function $\Theta(r, z)$ satisfies the scalar equation of type (1) for transverse waves: $\Delta\Theta + (\omega/c_t)^2\Theta = 0$. This choice of the vector potential component fits the requirement that the transverse component of the displacement vector also satisfies an equation of type (1). As in [12], we proceed from the cylindrical symmetry of the problem and the solenoidal property of vector Ψ and assume that $\Theta(r, z)$ is the unique, azimuth-independent component of the vector potential. In this case, the displacement components u_r and u_z lying in the (r, z) plane are also independent of the azimuth, and the normal σ_{zz} and tangential σ_{rz} components of the stress tensor are determined from the classical Hooke law relating the stresses and the displacements in an elastic medium [13]. Upon simple rearrangement, we obtain:

$$u_r = \partial\Phi/\partial r + \partial^2\Theta/\partial r\partial z, \quad (5a)$$

$$u_z = \partial\Phi/\partial z + \partial^2\Theta/\partial z^2 + (\omega/c_t)^2\Theta, \quad (5b)$$

$$\begin{aligned} \sigma_{zz} &= -\lambda(\omega/c_t)^2\Phi \\ &+ 2\mu\frac{\partial}{\partial z}[\partial\Phi/\partial z + (\omega/c_t)^2\Theta + \partial^2\Theta/\partial z^2], \end{aligned} \quad (5c)$$

$$\sigma_{rz} = \mu\frac{\partial}{\partial r}[2\partial\Phi/\partial z + (\omega/c_t)^2\Theta + 2\partial^2\Theta/\partial z^2]. \quad (5d)$$

Clearly, the scalar potential Φ alone is sufficient to describe the case of a liquid medium, where the dis-

placement components u and the acoustic pressure p are given by the formulas

$$\mathbf{u} = \nabla\Phi, \quad (6a)$$

$$p = -\rho\partial^2\Phi/\partial t^2. \quad (6b)$$

The structure and the behavior of Green's functions (solutions to equations of type (4)) depend on the position and the type of the source, the type of waves, and the corresponding distribution of velocities of the longitudinal and transverse waves along the z axis.

In numerical field simulations, the vertically inhomogeneous ocean and bottom bulk is subdivided into layers whose number N is sufficient to consider their parameters to be homogeneous (invariable) within every particular layer. In other words, the actual distribution of parameters is replaced by a step function. The upper boundary of the system (the water–air boundary) is considered a perfectly soft one, and the lower layer is usually assumed to be a homogeneous elastic half-space. Each layer is specified by thickness h , velocities of the longitudinal c_l and transverse c_t waves, coefficients of their spatial decay, and medium density ρ in the layer. The upper layer is labeled by the index 1, and the lower layer (halfspace), by the index N .

In an arbitrary layer labeled by index n , the potentials can be represented as a superposition of the incident (direct) waves and the reflected (inverse) plane waves:

$$\begin{aligned} \Phi_n(z) &= \Phi_n^+(z) + \Phi_n^-(z) \\ &= a_n^+ \exp(\alpha_n z) + a_n^- \exp(-\alpha_n z), \end{aligned} \quad (7a)$$

$$\begin{aligned} \Theta_n(z) &= \Theta_n^+(z) + \Theta_n^-(z) \\ &= b_n^+ \exp(\beta_n z) + b_n^- \exp(-\beta_n z), \end{aligned} \quad (7b)$$

where a_n^+ , a_n^- , b_n^+ , and b_n^- are the amplitudes of the corresponding waves in the expressions for the scalar and vector potentials; the superscripts “+” and “-” correspond to the direct and inverse waves, respectively; α_n and β_n are the projections of the wave numbers of the corresponding waves on the z axis,

$$\alpha_n = \sqrt{\xi^2 - k_n^2}, \quad \beta_n = \sqrt{\xi^2 - \kappa_n^2}; \quad (8)$$

and $k_n = \omega/c_{l,n}$ and $\kappa_n = \omega/c_{t,n}$ are the wave numbers of longitudinal and transverse waves in the n th layer. The attenuation of waves in the layer is governed by the imaginary part of the complex wave numbers k_n and κ_n . For example, in the case of the longitudinal wave, we have

$$\begin{aligned} k_n &= \omega/\bar{c}_{l,n} = \omega/c_{l,n}/(1 - i\eta_n) \cong \omega/c_{l,n}(1 + i\eta_n) \\ &= \omega/c_{l,n} + i\omega\eta_n/c_{l,n} = k_n' + ik_n'', \end{aligned}$$

where the attenuation coefficient k_n'' is measured either in Neper per meter ($k_n'' = \eta_n\omega/c_{l,n}$), or in decibel per meter ($\alpha_{l,n}'' \cong 8.68\eta_n\omega/c_{l,n}$).

To find the solution for the system of N layers, the fields at the interlayer boundaries are sewed together, which is carried out by satisfying the boundary conditions for every interlayer boundary. At the interface between solid layers, the boundary conditions consist in the continuity of the vertical and horizontal displacements (conditions (5a) and (5b)) and the normal and tangential stresses (conditions (5c) and (5d)). At the interface between liquid layers, they are the continuity of the vertical displacements and the pressure. At the upper free boundary, the pressure formed by the superposition of all waves is set to zero. At the interface between solid (elastic) and liquid layers, the exact boundary conditions are usually reduced to simplified (approximate) conditions, which require that the vertical displacements coincide in both layers ($u_z = (1/\rho\omega^2)\partial p/\partial z$), the total normal stress in the solid layer be equal to the pressure in the liquid layer taken with the inverse sign ($\sigma_{zz} = -p$), and the tangential stress in the solid layer be equal to zero ($\sigma_{rz} = 0$), because the viscosity of liquid is usually neglected.

The conditions at the boundary between the liquid and solid layers require additional consideration. Here, the condition of the coincidence of the horizontal displacements is usually not set, although, strictly speaking, the liquid adheres to the boundary of the elastic layer due to the viscosity, and horizontal displacements actually coincide. However, such a condition would essentially complicate the structure of the equation to be solved. Namely, for the liquid layer, one would be forced to solve the Navier–Stokes equations [13] instead of equations (1). At the same time, the thickness of the corresponding boundary layer is about $\sqrt{\nu/\omega}$, and this value appears to be relatively small because of the low kinematic viscosity of water ($\nu \cong 10^{-6}$ m²/s). Indeed, this thickness measures about 4 mm even for a frequency of 0.01 Hz and decreases with increasing frequency. Outside this thin layer, the flow of liquid is a potential one, and the requirement of the coincidence of the horizontal displacements becomes unnecessary. Thus, the above boundary conditions at the liquid–solid interface are justified, if the liquid motion within the thin boundary layer can be neglected [1].

It should be noted that, in numerical field simulations, we use the boundary conditions in their natural form requiring the coincidence of acoustic displacements and stresses, rather than in the form of the balance between the coefficients of reflection and refraction of separate wave parameters, as is often done. This approach offers us an opportunity to do away with additionally checking the energy fluxes of elastic longitudinal and transverse waves for the continuity at the layer interfaces [2], because this continuity is automatically

retained for the interfaces between elastic layers. However, for the liquid–solid interfaces, the note in the previous passage should be taken into consideration. Neglecting the liquid motion within the boundary layers (i.e., the use of the approximate boundary conditions) results in discontinuities in the wave energy flux because of irreversible viscous losses (heat release) in these layers [13]. One can evaluate the corresponding energy losses E_v from the horizontal displacements of the boundary $u_r(u_{rz})$ on the side of the elastic medium (in essence, we assumed that these displacements can take on arbitrary values). It can be easily shown that these neglected energy losses are small and measure about $E_v \approx i\rho v^{3/2}\omega^{1/2}u_r^2$ per unit area of the boundary. These losses increase with the viscosity of liquid (in proportion to $v^{3/2}$) and the frequency of the wave field (in proportion to $\omega^{1/2}$); however, they can be neglected in numerical simulations of low-frequency wave fields. Here, it is appropriate to recall the known result obtained by B.P. Konstantinov and revised by Savel'ev [23] for elastic boundaries. According to Savel'ev [23], for waves arriving at the interface between two media with different densities at small grazing angles, the reflection coefficient essentially varies and becomes minimal at a certain (quite small) grazing angle. In this conditions, the major part of the reflected energy (to 83% at the interface between liquid and a perfectly rigid halfspace) transforms to the energy of viscous or heat waves propagating along the boundary predominantly within the mentioned viscous layer. For higher frequencies, the neglect of the Konstantinov effect results in errors, especially in simulating the spatial losses of the field; however, the contribution of viscous waves to the energy balance of the wave field decreases with decreasing frequency, and the boundary can be considered as an ideal one even for small grazing angles [23].

At every boundary, the boundary conditions and potentials (7) form the so-called local system of equations. All local systems appear interrelated [10] and together form a generalized (global) system of equations. In such a system, the contributions of sources at the boundaries are simply added up. As a result, we can obtain the generalized system of algebraic equations in the coefficients a_n^\pm and b_n^\pm . If the medium is subdivided into N layers, the generalized system is the system of $4(N-1)$ equations in $4(N-1)$ unknowns in the general case (all layers are elastic). For liquid layers, we have only half of the equations (and unknowns). The obtained system is usually solved according to a numerical procedure of Gaussian exclusion of unknowns with partial permutations; the details of this procedure are described in the literature [9, 19].

Unfortunately, this generalized (global) system is hardly solvable analytically, especially for a large number of layers. Therefore, it is convenient to rewrite the system in matrix form and solve it using matrix algebra

techniques. In this context, the techniques most widely used in recent years are the method of the Thomson–Haskell matrix [10] and the method of the generalized Schmidt matrix [11], the latter including the former as a particular case.

We obtain the final solution for the displacements and stresses (5) by integrating expressions (3) for the potentials represented in the form (7):

$$\begin{aligned}
 u_r &= \int_0^\infty \{-\xi[a_n^+ \exp(\alpha_n z) + a_n^- \exp(-\alpha_n z)] \\
 &+ \beta_n \xi[b_n^+ \exp(\beta_n z) - b_n^- \exp(-\beta_n z)]\} J_1(\xi r) \xi d\xi, \\
 u_z &= \int_0^\infty \{\alpha_n[a_n^+ \exp(\alpha_n z) - a_n^- \exp(-\alpha_n z)] \\
 &- \xi^2[b_n^+ \exp(\beta_n z) + b_n^- \exp(-\beta_n z)]\} J_0(\xi r) \xi d\xi, \\
 \sigma_{zz} &= \int_0^\infty \{(-\lambda_n k_n^2 + 2\mu_n \alpha_n^2) \\
 &\times [a_n^+ \exp(\alpha_n z) + a_n^- \exp(-\alpha_n z)] \\
 &+ 2\mu_n \beta_n \xi^2 [b_n^+ \exp(\beta_n z) - b_n^- \exp(-\beta_n z)]\} J_0(\xi r) \xi d\xi, \\
 \sigma_{rz} &= \int_0^\infty \{-2\mu_n \xi \alpha_n [a_n^+ \exp(\alpha_n z) - a_n^- \exp(-\alpha_n z)] \\
 &- \mu_n \xi (\xi^2 + \beta_n^2) [b_n^+ \exp(\beta_n z) \\
 &+ b_n^- \exp(-\beta_n z)]\} J_1(\xi r) \xi d\xi.
 \end{aligned} \tag{9}$$

Thus, the determination of the parameters of the seismoacoustic field in the horizontally stratified medium breaks up into two steps. The first step consists in the numerical evaluation of the unknown coefficients a_n^\pm and b_n^\pm in equations (7) for every discrete wave number ξ by using the generalized Schmidt matrix that takes into account the interlayer boundary conditions. The second step consists in computing the integral transforms (9) for the specified reception depth z from the determined coefficients a_n^\pm and b_n^\pm . This computation can be accomplished, for example, using the fast Fourier transform and the asymptotic expressions for the Bessel functions of large arguments.

Note several features that must be taken into account in numerical simulations of wave fields. First of all, the evaluation of integral expressions (9) assumes that one must take into account the oscillating behavior of the Bessel functions appearing in the integrand and, especially, the features of the complex Green's function (4), such as singularities, branch points, and oscillations. The distance-dependent oscillation period, the peak widths, and the law of the spatial

decay of Green's function immediately determine the admissible mesh width and limits of integration in expressions (9).

Another feature is associated with the so-called masking effect occurring in thick layers. In an arbitrary layer with index n , one of the two fundamental solutions usually increases with depth z , and the other decreases. This behavior follows from the fact that exponents appearing in linear equations (7) are characterized by significant real parts when ξ in (8) considerably exceeds k_n and κ_n in this layer. In these conditions, the amplitude ratio of the solutions increases as the waves propagate from the source predominantly along the layer, and, for thick layers, this ratio may often fall beyond the digital possibility of a computer. As a result, the decreasing solution seemingly disappears against the background of the increasing solution (the masking effect). The neglect of this effect inevitably results in instabilities of the numerical model. In addition, the boundary conditions cease to be satisfied, because one fundamental solution (decreasing in z) is actually lost.

To overcome this difficulty, we suggest [21] to represent the solutions in the layer as a superposition of transmitted and reflected waves and use recursion relationships [16] for a layer-by-layer calculation of the partial reflection and refraction coefficients of longitudinal, transverse, and exchange (i.e., corresponding to transformations of longitudinal waves to transverse waves and vice versa) waves at the interfaces between elastic layers. This representation excludes the increasing fundamental solution, because the expressions for the partial reflection and refraction coefficients contain only factors with the exponents $2\alpha_n h_n$, $2\beta_n h_n$, and $(\alpha_n + \beta_n)h_n$, where h_n is the thickness of the n th layer. If these exponents have negative real parts and if these real parts are sufficiently large in magnitude, the reflection coefficients necessarily approach the reflection coefficients for the corresponding layers of infinite thickness, and all subsequent layers can be excluded from consideration for the mentioned types of waves.

For example, the reflection coefficient V_n from the n th liquid layer is related to the reflection coefficient V_{n+1} from the subsequent layer by the recursion relationship

$$V_n = \frac{R_n + V_{n+1} \exp(2\alpha_n h_n)}{1 + R_n V_{n+1} \exp(2\alpha_n h_n)}, \quad (10)$$

where R_n is the Fresnel reflection coefficient from the interface between two semi-infinite media of numbers $(n-1)$ and n . For $\text{Re}[\exp(2\alpha_n h_n)] \rightarrow 0$, the reflection coefficient $V_n \rightarrow R_n$, and the wave incident on the upper boundary does not reach the lower boundary of the layer. In this case, the reflected wave formally disappears, and the layer can be considered as a halfspace.

As was shown earlier [22], the optimum mesh width h_n in the subdivision of an inhomogeneous liquid layer into homogeneous sublayers is determined from the

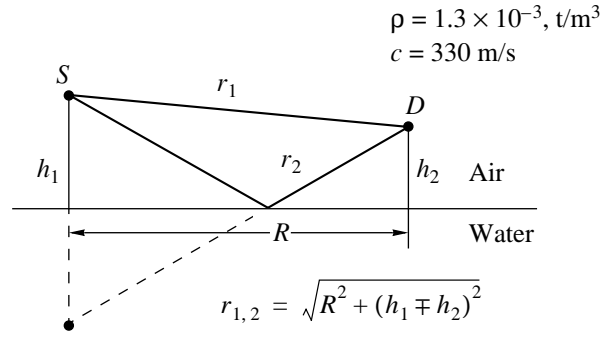


Fig. 1. Geometry of the simple problem on the wave field in the halfspace overlying a rigid boundary (the benchmark problem). The source is located at the point S , the receiver is located at the point D , R is the horizontal distance between the points S and D , and h_1 and h_2 are the heights of these points above the rigid boundary.

condition $|h_n \Delta k_n| < \pi$, where $\Delta k_n = k(z_{n+1}) - k(z_n)$ is the difference between the wave numbers at the sublayer boundaries. For elastic layers, the quantity Δk_n should be replaced by the maximum of the wave number differences for longitudinal and transverse waves. This maximum depends on the vertical gradient of the velocity of the corresponding elastic wave χ_n , which results in the relation for the sublayer thickness in the form $h_n < c_n \pi^{1/2} \omega^{-1/2} |\chi_n|^{-1/2}$, where c_n is the propagation velocity of the chosen type of waves. Clearly, the thickness h_n should be additionally checked for the masking effect in accordance with formulas similar to (10).

In terms of wave numbers, the above criterion additionally determines the maximum horizontal wave number ξ for which the slowest wave originating at the source height ceases to arrive at the height of the reception point. One can replace the infinite upper limit in integrals (9) by this maximum ξ_{\max} , and this maximum must be redetermined every time when constructing a particular numerical model. Besides, such a procedure offers the possibility of creating an essentially faster code.

To illustrate the efficiency of the suggested numerical model, we compare our simulations for one of the simplest cases (which allows an analytical solution) with the known exact analytical solution and the simulations based on the method of the generalized Schmidt matrix [11]. Such an approbation procedure for simulations by comparing the simulated results with the known ones has been called the benchmark problem. To implement this procedure, we choose the wave (sound) field of a source in the halfspace above a perfectly rigid boundary (halfspace). Figure 1 schematically shows the geometry of the problem (positions of the source and the observation point) along with the corresponding notation, and Fig. 2 shows the simulated results [21].

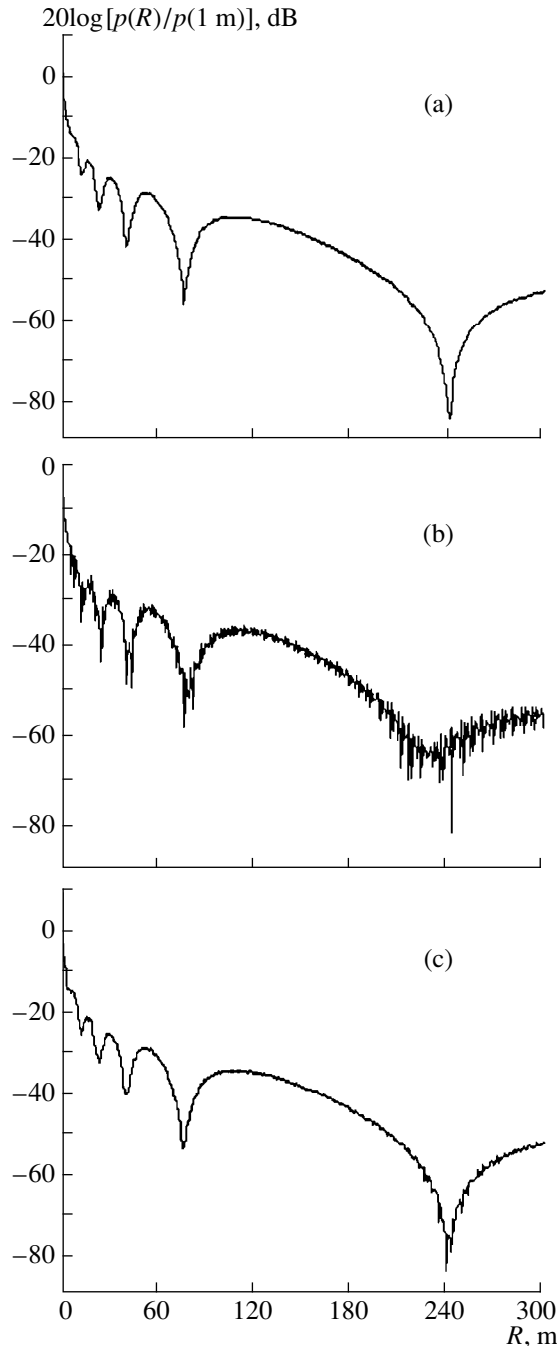


Fig. 2. Pressure $p(R)$ (normalized by the pressure generated by the source at a distance of 1 m, $p(1 \text{ m})$) versus the horizontal distance R . The calculations were performed for $h_1 = h_2 = 20 \text{ m}$ and the source frequency 50 Hz. The curves $p(R)$ were obtained according to (a) the exact solution, (b) the method of the generalized matrix, and (c) the proposed stable procedure.

As is known, the exact solution for the acoustic pressure p in the wave field of a source of unit amplitude has the form

$$p = e^{ikr_1}/r_1 + e^{ikr_2}/r_2, \quad (11)$$

where r_1 and r_2 are the distances travelled by the direct and reflected waves to the observation point and k is the wave number of the sound wave in the upper halfspace.

A comparison of the curves $p(R)$ constructed according to the exact solution (Fig. 2a), the method of the generalized matrix (Fig. 2b), and the proposed procedure (Fig. 2c) shows that the latter gives the best agreement with the exact solution. At the same time, simulations based on the method of the generalized matrix may essentially (and sometimes unacceptably) deviate from the exact solution. These deviations follow from the fact that the commonly accepted simulation procedure becomes unstable for an arbitrary subdivision of the calculation region into layers parallel to the rigid boundary.

From the practical standpoint, the simulated results given in Figs. 3–6 are more informative. They give an example of simulating the seismoacoustic field of a source located in the ocean water layer. The calculations were carried out for the frequencies 0.01, 0.10, 1.00, and 10.0 Hz with the use of two different models for the bottom structure. Model 1 was composed of the water layer 1 overlying a sand halfspace 2; model 2 was composed of the water layer 1 overlying a finite sand layer 2 and a limestone halfspace 3. Every layer is characterized by a thickness h_n and geoacoustic parameters: density ρ_n , velocities of longitudinal and transverse waves $c_{l,n}$ and $c_{t,n}$, and attenuation coefficients of longitudinal and transverse waves per unit frequency $\delta_{l,n}$ and $\delta_{t,n}$, e.g., $\delta_{l,n} \cong 54.5\eta_n/c_{l,n}$.

We used the following parameters of the layers:

1. Water layer: $h_1 = 150 \text{ m}$, $\rho_1 = 10^3 \text{ kg/m}^3$, $c_{l,1} = 1450 \text{ m/s}$, and $\delta_{l,1}$ is virtually zero for the frequencies used in the simulation ($f \leq 10 \text{ Hz}$).

2. Loose sediments (sand): $h_2 = \infty$ (for model 1) or $h_2 = 50 \text{ m}$ (for model 2), $\rho_2 = 2 \times 10^3 \text{ kg/m}^3$, $c_{l,2} = 1800 \text{ m/s}$, $c_{t,2} = 700 \text{ m/s}$, $\delta_{l,2} = 0.10 \text{ dB/m kHz}$, and $\delta_{t,2} = 6.0 \text{ dB/m kHz}$.

3. Petrified sediments (limestone): $h_3 = \infty$ (for model 2), $\rho_3 = 2.2 \times 10^3 \text{ kg/m}^3$, $c_{l,3} = 2400 \text{ m/s}$, $c_{t,3} = 1000 \text{ m/s}$, $\delta_{l,3} = 0.03 \text{ dB/m kHz}$, and $\delta_{t,3} = 0.20 \text{ dB/m kHz}$.

For frequencies $f \leq 10 \text{ Hz}$, the attenuation coefficient is linear in frequency, $(\alpha_{l,t}) \text{ dB/m} = \delta_{l,t}$, for all types of rock and loose sediments.

The point source (monopole) creating an alternating pressure of amplitude 1 Pa at a distance of 1 m in the infinite water medium was located in the water layer at a depth $z_s = 100 \text{ m}$. The reception point was located either at the bottom of the water layer, or in the bottom bulk, at a depth of 50 m in the sand layer. Thus, the reception was carried out either in the bulk of the sand halfspace (model 1), or in the bottom bulk, at the interface between the sand layer and the limestone halfspace (model 2).

The curves in Figs. 3–6 are the horizontal sections of the simulated field of the source. Figures 3a–6a cor-

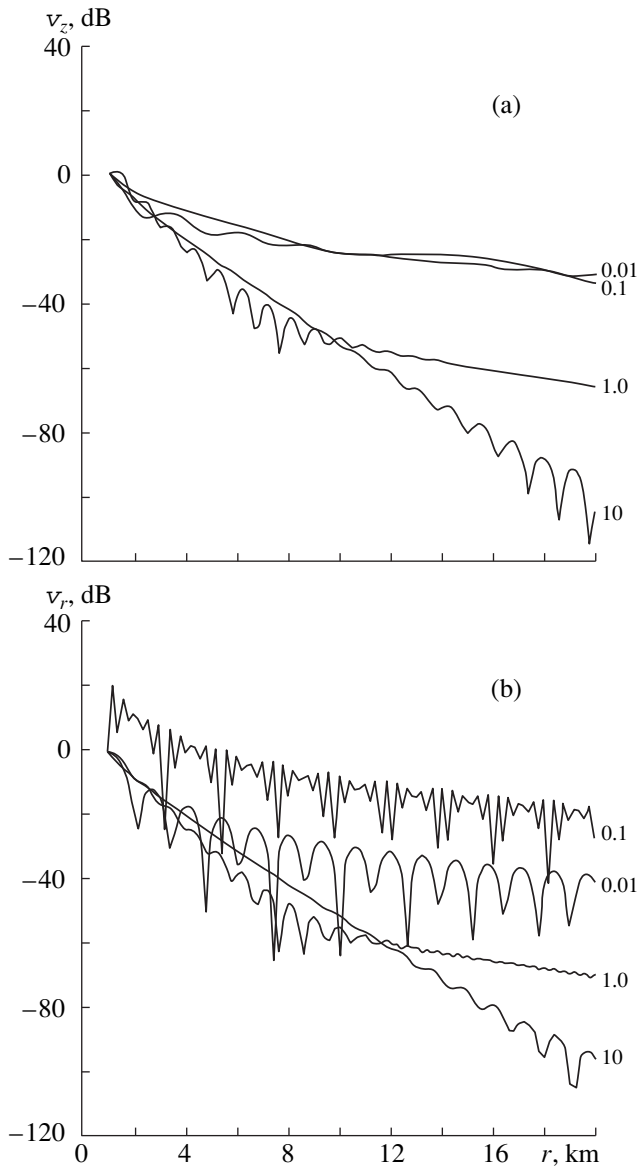


Fig. 3. The horizontal sections of the seismoacoustic field of particle velocities for the source frequencies 0.01, 0.10, 1.00, and 10.0 Hz. The particle velocities are normalized by their values at a distance of 1 km. The observation point is located at the bottom of the water layer. The medium is composed of the water layer overlying a sand halfspace (model 1). (a) Vertical components v_z . (b) Horizontal components v_r .

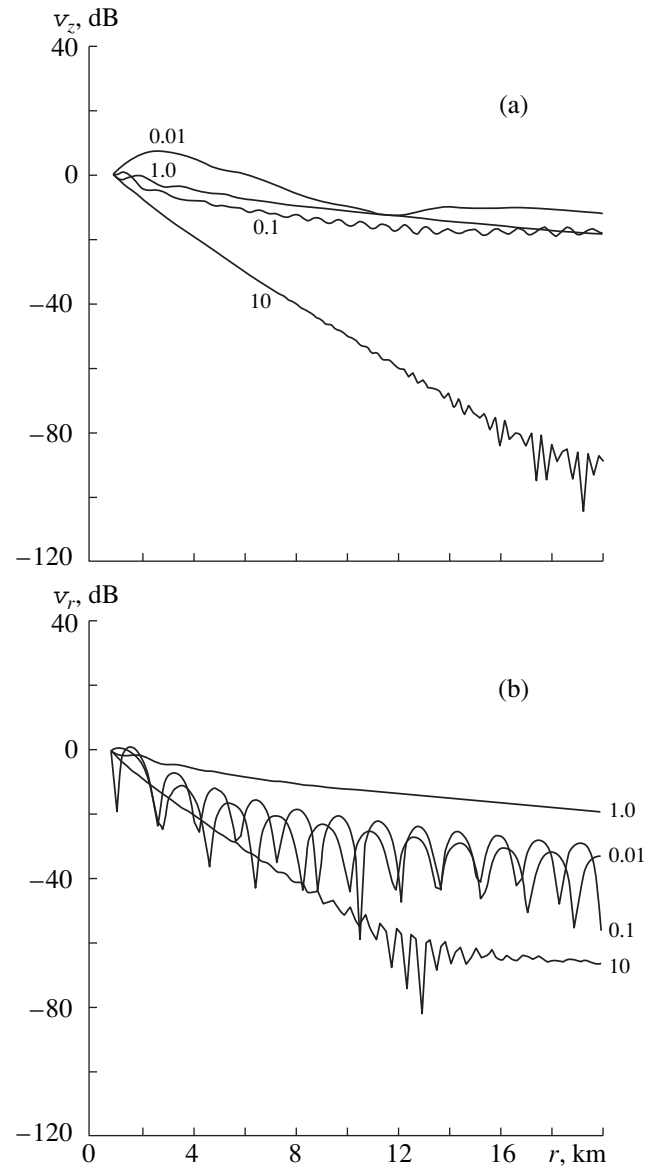


Fig. 4. The horizontal sections of the seismoacoustic field of particle velocities for the source frequencies 0.01, 0.10, 1.00, and 10.0 Hz. The particle velocities are normalized by their values at a distance of 1 km. The observation point coincides with that in Fig. 3. The medium is composed of the water layer overlying a sand layer and a limestone halfspace (model 2). (a) Vertical components v_z . (b) Horizontal components v_r .

respond to the vertical component of the local particle velocity v_z , and Figs. 3b–6b correspond to the horizontal component v_r . The parameter distinguishing the curves is the frequency of the source. On the ordinate, the components of the particle velocity, v_z and v_r , normalized by their values $v_{z,0}$ and $v_{r,0}$ at a horizontal distance of 1 km from the source are plotted in decibels. The table presents the magnitudes of the velocities $v_{z,0}$ and $v_{r,0}$ and the corresponding predictions for the

decay of the field of particle velocities at a distance of 20 km.

From the analysis of the above simulated field, it follows that, near the bottom of the water layer, the vertical components of the velocity v_z and the acoustic pressure p decrease with distance steeper than by the cylindrical decay law (proportionally to $R^{-1/2}$). This is immediately seen from latter two columns of the table where the decay of the field essentially exceeds the value 13 dB expected for a cylindrical wave. The reason

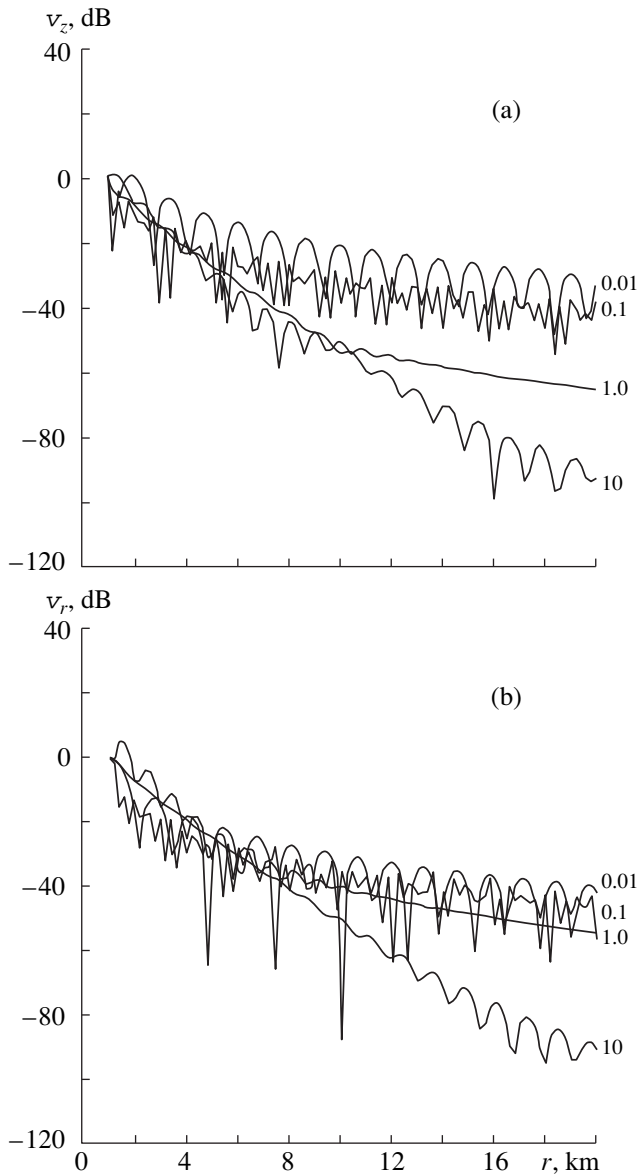


Fig. 5. The horizontal sections of the seismoacoustic field of particle velocities for the source frequencies 0.01, 0.10, 1.00, and 10.0 Hz. The particle velocities are normalized by their values at a distance of 1 km. The observation point is located in the bottom bulk, 50 m below the lower water boundary. The medium is composed of the water layer overlying a sand halfspace (model 1). (a) Vertical components v_z . (b) Horizontal components v_r .

is that shear waves are strongly attenuated in sand. As may be shown using a thin water layer overlying a homogeneous elastic halfspace as the model (similar to model 1), the majority of the wave energy (about 68%) of the point source (monopole) propagates along the water–bottom interface in the form of surface waves [7], and their attenuation is mainly governed by losses in the elastic halfspace (sand). Note that paper [7], unfortunately, does not take into account the additional

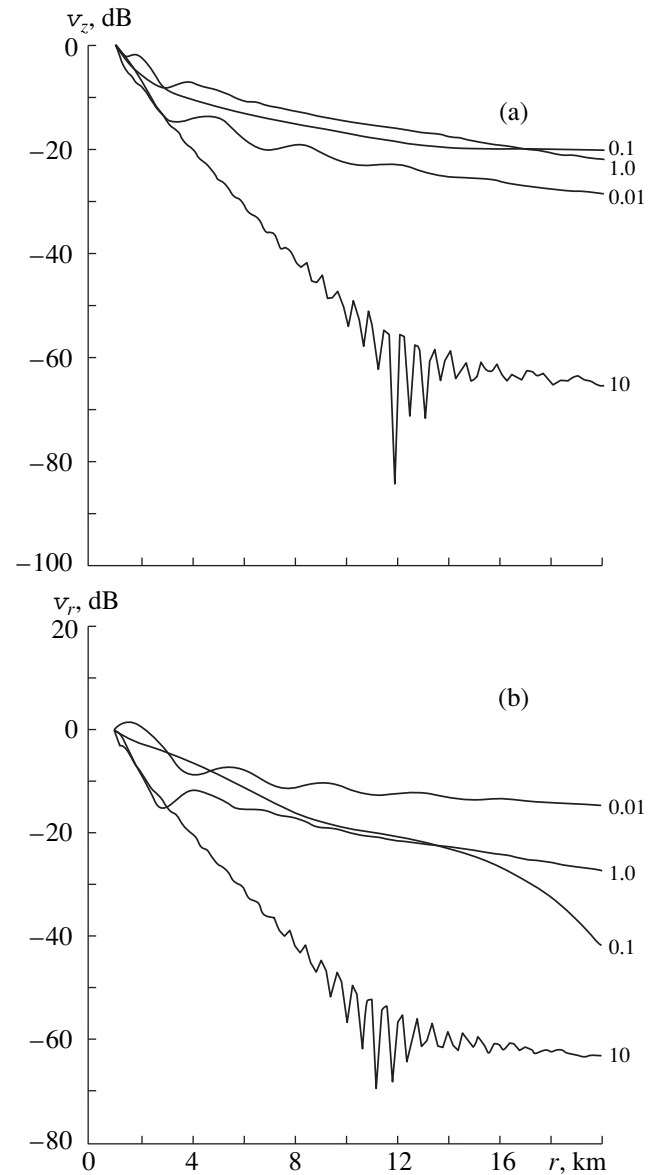


Fig. 6. The horizontal sections of the seismoacoustic field of particle velocities for the source frequencies 0.01, 0.10, 1.00, and 10.0 Hz. The particle velocities are normalized by their values at a distance of 1 km. The observation point coincides with that in Fig. 5. The medium is composed of the water layer overlying a sand layer and a limestone halfspace (model 2). (a) Vertical components v_z . (b) Horizontal components v_r .

loss mechanisms discussed above and the conclusions of paper [23].

The replacement of the sand halfspace by a comparatively thin layer and the introduction of a new interface between sand and limestone (model 2) results in a considerable increase in the velocity components v_z and v_r . Indeed, for frequencies 1 and 10 Hz, the respective velocity components at a distance of 20 km exceed the corresponding components obtained in model 1 by

The magnitudes of the components $v_{z,0}$ and $v_{r,0}$ of particle velocities at a distance of 1 km and the corresponding forecasts for an additional decay of the field of particle velocities at a distance of 20 km ($p_1 = 1\text{Pa}$, $z_s = 100\text{ m}$, and $h_1 = 150\text{ m}$)

Location of the reception point	Model	Frequency, Hz	$v_{z,0} \times 10^{10}$, m/s	$v_{r,0} \times 10^{10}$, m/s	$v_z/v_{z,0}$, dB	$v_r/v_{r,0}$, dB
At the bottom of water layer	1	0.01	0.11	80.0	-29.2	-40.3
		0.10	0.74	2.80	-32.0	-26.5
		1.00	3.80	3.90	-64.0	-68.9
		10.0	5.40	9.40	-102.6	-95.8
	2	0.01	0.0089	30.0	-12.3	-33.2
		0.10	0.27	15.0	-18.3	-56.4
		1.00	4.30	3.40	-18.8	-19.3
		10.0	5.10	9.10	-89.0	-66.5
At a depth of 50 m in the bulk of the bottom	1	0.01	2.50	68.0	-32.7	-40.8
		0.10	9.70	1.80	-38.0	-55.2
		1.00	4.30	0.78	-64.8	-53.1
		10.0	2.70	6.40	-92.0	-89.5
	2	0.01	0.046	0.0022	-28.3	-13.7
		0.10	0.34	0.55	-19.7	-40.8
		1.00	6.90	7.50	-21.6	-26.3
		10.0	4.10	5.70	-65.1	-61.9

50 and 30 dB for the reception near the bottom, and by 27 and 28 dB for the reception at the interface between sand and limestone. For the frequencies 0.01 and 0.10 Hz, the observation point, even if it is located at a distance of 20 km from the source, falls in the near (Fresnel) zone of the source, where all field parameters, including the particle velocities v_z and v_r , strongly fluctuate, and this fact determines the structure of the simulated field.

Our recent papers [24–27] describe the proposed numerical model of the bottom bulk in more detail.

ACKNOWLEDGMENTS

We are grateful to Prof. S.A. Rybak for useful discussions.

This work was supported by the Russian Foundation for Basic Research, project nos. 96-02-16560, 97-02-16087a, 99-02-16618-a and 00-02-17858-a.

REFERENCES

- N. Favretto-Anres, *Acust.—Acta Acust.* **82**, 829 (1996).
- M. A. Ainslie and P. W. Burns, *J. Acoust. Soc. Am.* **98**, 2836 (1995).
- S. M. Grudskii, S. S. Mikhalkovich, and A. I. Hilko, *Akust. Zh.* **43**, 630 (1997) [*Acoust. Phys.* **43**, 542 (1997)].
- M. S. Fokina, V. N. Fokin, and G. A. Sharonov, *Akust. Zh.* **43**, 688 (1997) [*Acoust. Phys.* **43**, 596 (1997)].
- N. S. Ageeva, V. D. Krupin, V. P. Perelygin, and N. V. Studenichnik, *Akust. Zh.* **40**, 181 (1994) [*Acoust. Phys.* **40**, 159 (1994)].
- M. J. Buckingham, *J. Acoust.* **5**, 223 (1992).
- A. D. Lapin, *Akust. Zh.* **38**, 364 (1992) [*Sov. Phys. Acoust.* **38**, 198 (1992)].
- Formation of Acoustic Fields in Oceanic Waveguides*, Ed. by V. A. Zverev, et al. (Inst. Prikl. Fiz., Nizhni Novgorod, 1991).
- A. E. Mudrov, *Numerical Methods for Personal Computers in BASIC, FORTRAN, and Pascal Languages* (RASKO, Tomsk, 1991).
- F. R. Di Napoli and R. L. Deavenport, *J. Acoust. Soc. Am.* **67**, 92 (1980).
- H. Schmidt and F. B. Jensen, *Comput. Math. Appl.* **11**, 669 (1985).
- L. M. Brekhovskikh, *Waves in Layered Media* (Nauka, Moscow, 1973).
- L. D. Landau and E. M. Lifshitz, *Theory of Elasticity* (Nauka, Moscow, 1965; Pergamon, New York, 1986).
- W. M. Ewing, W. S. Jardetzky, and F. Press, *Elastic Waves in Layered Media* (McGraw-Hill, New York, 1957).
- W. A. Cooperman and F. B. Ensen, *Underwater Acoustics and Signal Processing*, Ed. by L. Bjørnø (Plenum, New York, 1982; Mir, Moscow, 1985).
- V. Yu. Zavadskii *Calculation of Wave Fields in Open Regions and Waveguides* (Nauka, Moscow, 1972).
- L. A. Molotkov, *The Matrix Method in the Theory of Wave Propagation in Elastic and Fluid Layered Media* (Nauka, Leningrad, 1984).

18. K. Aki and P. Richards, *Quantitative Seismology: Theory and Methods* (Freeman, San Francisco, 1980; Mir, Moscow, 1983).
19. A. A. Samarskiĭ and A. V. Gulin, *Numerical Methods* (Nauka, Moscow, 1982).
20. V. D. Krupin, *Sudostr. Prom. Ser. Akust.*, No. 4, 82 (1989).
21. A. G. Semenov and O. V. Kudryavtsev, in *Proceedings of OCEAN OSATES Conference, Brest, France, 1994*.
22. O. V. Kudryavtsev and N. A. Grubnik, *Sudostr. Prom. Ser. Akust.*, No. 3, 80 (1986).
23. A. Ya. Savel'ev, *Akust. Zh.* **19**, 231 (1973) [*Sov. Phys. Acoust.* **19**, 154 (1973)].
24. L. A. Bespalov, A. M. Derzhavin, O. V. Kudryavtsev, and A. G. Semenov, in *Ocean Acoustics: Proceedings of the Advanced-Study School of Academician L. M. Brekhovskikh* (GEOS, Moscow, 1998), pp. 104–108.
25. A. G. Semenov, A. M. Derzhavin, and O. V. Kudryavtsev, in *Proceedings of Marine Technology Society Annual Conference, Baltimore, 1998*, Vol. 1, pp. 457–461.
26. L. A. Bespalov, A. M. Derzhavin, O. V. Kudryavtsev, and A. G. Semenov, *Akust. Zh.* **45**, 25 (1999) [*Acoust. Phys.* **45**, 19 (1999)].
27. A. G. Semenov, A. M. Derzhavin, and O. V. Kudryavtsev, *J. Acoust. Soc. Am.* **105**, 1266 (1999).

Translated by A. Vinogradov

Interpretation of a Layer Mechanical Impedance Measured Using a Hard Round Die

E. V. Eremin and E. M. Timanin

*Institute of Applied Physics, Russian Academy of Sciences,
ul. Ul'yanova 46, Nizhni Novgorod, 603600 Russia
e-mail: eugene@appl.sci-nnov.ru*

Received June 17, 1999

Abstract—Theoretical expressions for the impedance characteristics of a layer bound to a rigid base are obtained for various profiles of the normal pressure under a die that vibrates on the layer surface without producing any shear stresses. The frequency dependences of the impedance characteristics of a homogeneous gelatin layer and their variation with changes in the die diameter are measured by means of a specialized software–hardware system. The impedance characteristics are calculated for the models with “uniform,” “parabolic,” and “hyperbolic” pressure profiles under the die, and the results are compared with the experimental data. The model with a uniformly distributed pressure under the die is found to be the most adequate one. © 2000 MAIK “Nauka/Interperiodica”.

The development of mathematical models of impedance characteristics of soft biological tissues is not only of purely scientific interest, but is also important in connection with the modern advances in the method of continuously monitoring the mechanical parameters of tissues with high time resolution on the basis of the data of single-frequency impedance measurements [1] and in the method of reconstructing the mechanical parameters of layered tissues from the data of spectral impedance measurements (i.e., from the frequency dependences of the impedance characteristics) [2–4]. Today, there exist a number of models of the impedance properties of biological tissues [3–9]. The most complete one is the three-layer model developed by Skovoroda and Aglyamov [3] on the basis of the data of experiments with human forearm tissues. However, using this model for interpreting the experimental data on the impedance characteristics of other parts of human body, which are very different in their structure and mechanical properties, or for selecting the optimal conditions for such studies is difficult due to the complexity of the identification of the model parameters. Such an identification demands specialized software tools. It seems possible to use other less rigorous but essentially less labor-intensive computational models, namely, “models with a power source of vibrations,” which are grounded on the approximations used for solving the Lamb problem [4, 10–12]. This paper demonstrates such opportunities by comparing the calculations for a single-layer model of the aforementioned type with the experimental data obtained for a homogeneous gelatin layer.

The development of such models, as well as the model by Skovoroda and Aglyamov [3], utilizes a known approach [10]. This approach is as follows:

(i) consideration is restricted to the axially-symmetric case and a general solution to the equations for an acoustic field in a linear elastic medium is determined in terms of the Hankel transforms; (ii) the boundary conditions corresponding to the layered object under consideration are set; and (iii) the stiffness K (the impedance Z) of the object is determined as the ratio between the force P applied to a die and the die displacement U (velocity V) by using the inverse Hankel transform. The distinctive feature of the “models with a power source of vibrations” is the fact that simplified boundary conditions are set at the outer surface of the object, namely, the condition of the known normal pressure and the condition of the absence of tangential stress over the whole surface including the surface under the die. The last condition is interpreted as the condition of die slip, and, basically, it can be provided in the experiment by special means. The pressure profile under the die $p(r)$ in the models of this class must be selected so as to fit the experiments.

Omitting here relatively simple calculations corresponding to this approach (see the paper by Timanin [4] for details), we give the final expression for the complex stiffness of the layer with the lower surface $z = H$ rigidly bound to the rigid base and the upper surface $z = 0$ driven in the region $r \leq a$ by a vibrating flat round die of radius a :

$$K = \frac{P}{U} = \frac{1}{\int_0^{\infty} \frac{\kappa_r(D_{13} + D_{14}) - k^2(D_{11} - D_{12})R(k)}{(k^2 + \kappa_r^2)(D_{13} - D_{14}) - 2k^2\kappa_r(D_{11} + D_{12})} dk} dk. \quad (1)$$

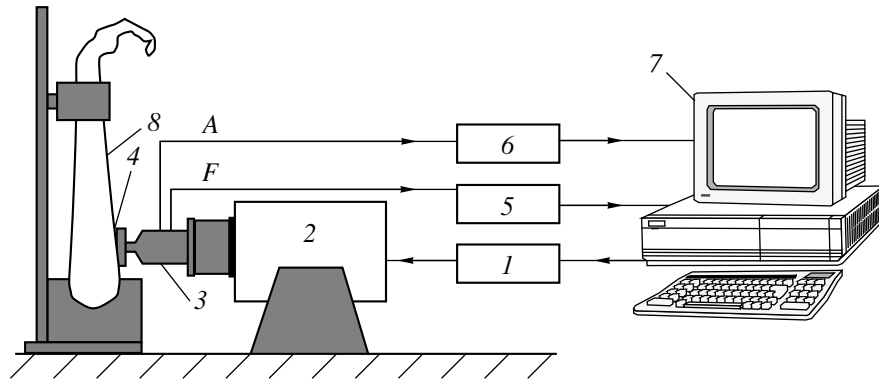


Fig. 1. Block diagram of the software–hardware system for the investigation of spectra of the impedance characteristics of soft biological tissues. (1) A power amplifier (type 2707); (2) a vibration test bench (type 4801T); (3) an impedance head (type 8001); (4) a removable die; (5), (6) amplifiers for the sensor signals (type 2626); (7) a computer with a CT4170 sound card; and (8) the object under investigation.

Here, k is the parameter of the Hankel transform; the parameters $\kappa_t^2 = k^2 - k_l^2$ and $\kappa_l^2 = k^2 - k_t^2$ are determined by the wave numbers of shear and longitudinal waves $k_t^2 = \omega^2/c_t^2$ and $k_l^2 = \omega^2/c_l^2$, where ω is the circular frequency of die vibrations and $c_t^2 = \mu/\rho$ and $c_l^2 = (\lambda + 2\mu)/\rho$ are the velocities of shear and longitudinal waves determined by the density ρ and the Lamé constants λ and μ . The determinants of the third order D_{1j} in expression (1) are the cofactors of the elements of the first line in the principal determinant of the set of equations that corresponds to the boundary conditions of the problem:

$$\begin{aligned}
 & -2\mu k^2 \kappa_t A_1 + 2\mu k^2 \kappa_t A_2 + \mu(k^2 + \kappa_t^2) B_1 \\
 & + \mu(k^2 + \kappa_t^2) B_2 = -p(k), \\
 & \mu k(k^2 + \kappa_t^2) A_1 + \mu k(k^2 + \kappa_t^2) A_2 - 2\mu k \kappa_t B_1 \\
 & + 2\mu k \kappa_t B_2 = 0,
 \end{aligned} \tag{2}$$

$$-k^2 e^{\kappa_t H} A_1 - k^2 e^{-\kappa_t H} A_2 + \kappa_t e^{\kappa_t H} B_1 - \kappa_t e^{-\kappa_t H} B_2 = 0,$$

$$k \kappa_t e^{\kappa_t H} A_1 - k \kappa_t e^{-\kappa_t H} A_2 - k e^{\kappa_t H} B_1 - k e^{-\kappa_t H} B_2 = 0.$$

The function $p(k)$ on the right-hand side of the first equation of set (2) is the Hankel transform of the pressure profile at the outer surface of the layer $p(r)$. This quantity also determines the function $R(k)$ involved in expression (1). In the determination of die displacement from the averaged over its area displacement of the layer surface under it [10], $U = \frac{1}{\pi a^2} \int_0^a u_z(r, 0) 2\pi r dr$,

the function $R(k)$ has the form:

$$R(k) = -\frac{2J_1^2(ka)}{k\pi a^2 \mu}, \tag{3}$$

when the pressure under the die is uniformly distributed according to the formula $p(r) = P/\pi a^2$,

$$R(k) = -\frac{8J_1(ka)J_2(ka)}{k^2 \pi a^3 \mu}, \tag{4}$$

when the pressure under the die is distributed according to the “parabolic” law $p(r) = 2[1 - (r/a)^2]P/\pi a^2$, and

$$R(k) = -\frac{J_1(ka) \sin(ka)}{k\pi a^2 \mu}, \tag{5}$$

when the pressure under the die is distributed according to the “hyperbolic” law [10] $p(r) = P/2\pi a \sqrt{a^2 - r^2}$. At the surface outside the die area, the pressure is absent in all cases.

Expression (1), in which the determinants correspond to the set of equations (2) for various types of the function $R(k)$ determined by expressions (3)–(5), will be used below for numerical calculations and the approximation of experimental data in order to select the best model. The model modifications corresponding to different functions $R(k)$ will be called A-models, PA-models, and GA-models, respectively.

A specialized software–hardware system has been constructed for the experimental investigation of the frequency dependences (spectra) of the impedance characteristics of biological tissues and their physical models (for example, a gelatin layer) [4]. This system provides the spectra of the impedance characteristics in a digital form already in the course of the experiment. These spectra can be easily used for further processing, and, in particular, for the identification of the model of a specific object. The experimental system based on Bruel & Kjaer equipment for the generation and measurement of vibrations and described earlier [7] formed the main part of the new system. The distinctive feature of the latter (Fig. 1) is the fact that the signal processing is conducted not by a spectrum analyzer, but by a computer using specialized software for Windows 95/98.

The signal input is performed with the help of the CT4170 Creative card. The software provides an opportunity to detect at the monitor screen and save to a disk the frequency dependences of the impedance characteristics of the studied object within the band up to 512 Hz. The time of the data acquisition for one spectrum is one second, and the frequency resolution is 1.22 Hz. There is an opportunity to average a given number of spectra of the impedance characteristics. The compensation of the mass associated with the force transducer, i.e., the compensation of its accelerometer sensitivity, is performed in each experiment before the measurements. In order to do this, the signals from the sensors, which correspond to the die vibrations in the air, are stored to the computer memory, and necessary corrections to them are introduced in the measurement procedure. Moreover, the calibration of the system is conducted before the measurements by putting a load of a known mass upon the operating die. The corresponding signals are also stored in the computer memory and then used to normalize the impedance characteristics to be determined. The frequency dependences of the real ($\text{Re}M$) and imaginary ($\text{Im}M$) parts of the complex inertia in grams, or the frequency dependences of the real parts of the complex stiffness ($\text{Re}K$) in N/m and the complex impedance ($\text{Re}Z$) in N s/m, are displayed in the program windows in the measurement mode. These values can be saved to a disk and used for further processing. The correctness of the operation of the new system has been tested in several special experiments [4]. First, the impedance characteristics corresponding to the verifying load of known mass connected to the die have been recorded. Second, simultaneous measurements of the impedance properties of a limp human forearm have been conducted using the new system and a 2034 spectrum analyzer connected to the computer in parallel.

A special series of measurements were conducted on a homogeneous gelatin layer of thickness 30 mm with the help of the system described above. The values of $\text{Re}K$ and $\text{Re}Z$ were detected with the help of three dies with diameters of 6, 10, and 16 mm. Each measurement was performed for the static impression of the die into the object to 1 mm. Averaging over 20 realizations was performed in the process of each impression. The gelatin density $\rho \approx 1008 \text{ kg/m}^3$ was determined by additional measurements of the sample mass and volume, and the velocity of longitudinal waves in the gelatin sample $c_l \approx 1500 \text{ m/s}$ was determined by measuring the time of propagation of an ultrasonic pulse from the surface to the base and back. The stored experimental data were read into the files for calculating the impedance characteristics with the help of the Matcad software. Fitting of the rheological parameters of the models for the best approximation of the experimental data was performed. The experimental curves are given below, together with the results of numerical calculations.

Numerical calculations in the models were performed using the Matcad software directly according to formula (1) with setting the determinants from the set of equations (2). The viscous properties of the layer material were taken into account by the change of its elastic parameters for the complex operators corresponding to the viscoelastic type, which can be done for each problem of fully-developed vibrations of linear viscoelastic bodies [14]. The simplest model, i.e., the Voigt body, was selected as the model of the viscoelastic behavior. According to this model, the Lamé constants must be set in the form $\mu = \mu_0 + i\omega\eta$ and $\lambda = \lambda_0 + i\omega\xi$, where μ_0 and λ_0 are the static moduli and η and ξ are the moduli of shear and bulk viscosity, respectively. Just this expression for μ was taken as the initial one for numerical calculations of c_l and k_l , which turned out to be complex in the result. A purely real experimental value of $c_l \approx 1500 \text{ m/s}$ was taken as initial for calculating k_l . Analyzing the complex expression for $c_l = \sqrt{(\lambda + 2\mu)/\rho}$, it is possible to determine that, in the case of the reduction of frequency, its real part tends to the value $c_l = \sqrt{(\lambda_0 + 2\mu_0)/\rho}$, and its imaginary part tends to zero. The validity condition for the passage to the limit is the condition $\omega \ll \omega_{cr} = (\lambda_0 + 2\mu_0)/(\xi + 2\eta)$, which should apparently be satisfied at a frequency lower than 1 kHz, at which the measurements were conducted.

The investigation of the integrands was performed before calculating the integral in (1), and the region where they were essentially nonzero was determined. The upper limit of integration was selected to be of the order of 7500 to 10500, which lies beyond this region. Since the integrands have a singularity at small k (a sufficiently sharp peak, if the material viscosity is small), it is necessary to break the interval of integration into two parts: the first part is relatively short (up to $k = 500\text{--}2000$) and contains a peak, and the second one is longer (the function slowly attenuates within it). The independence of the results from the upper integration limit and the way of division of the integration interval into parts was verified in the process of calculation.

The identification of the model parameters, which provide the best approximation of the experimental data, was conducted by fitting, i.e., by the multiple repetition of the following steps: setting of the model parameters; numerical calculation of the impedance characteristics; and visual comparison of the calculated results and experimental data displayed in one plot on the monitor screen. In all cases, the coincidence of the calculated and experimental data within the area of the low-frequency plateau of stiffness $\text{Re}K$ was attained, first of all, by selecting the modulus of elasticity, and, then, the coincidence of the calculated and experimental data on the impedance $\text{Re}Z$ in the range of medium and high frequencies was attained by selecting the modulus of viscosity.

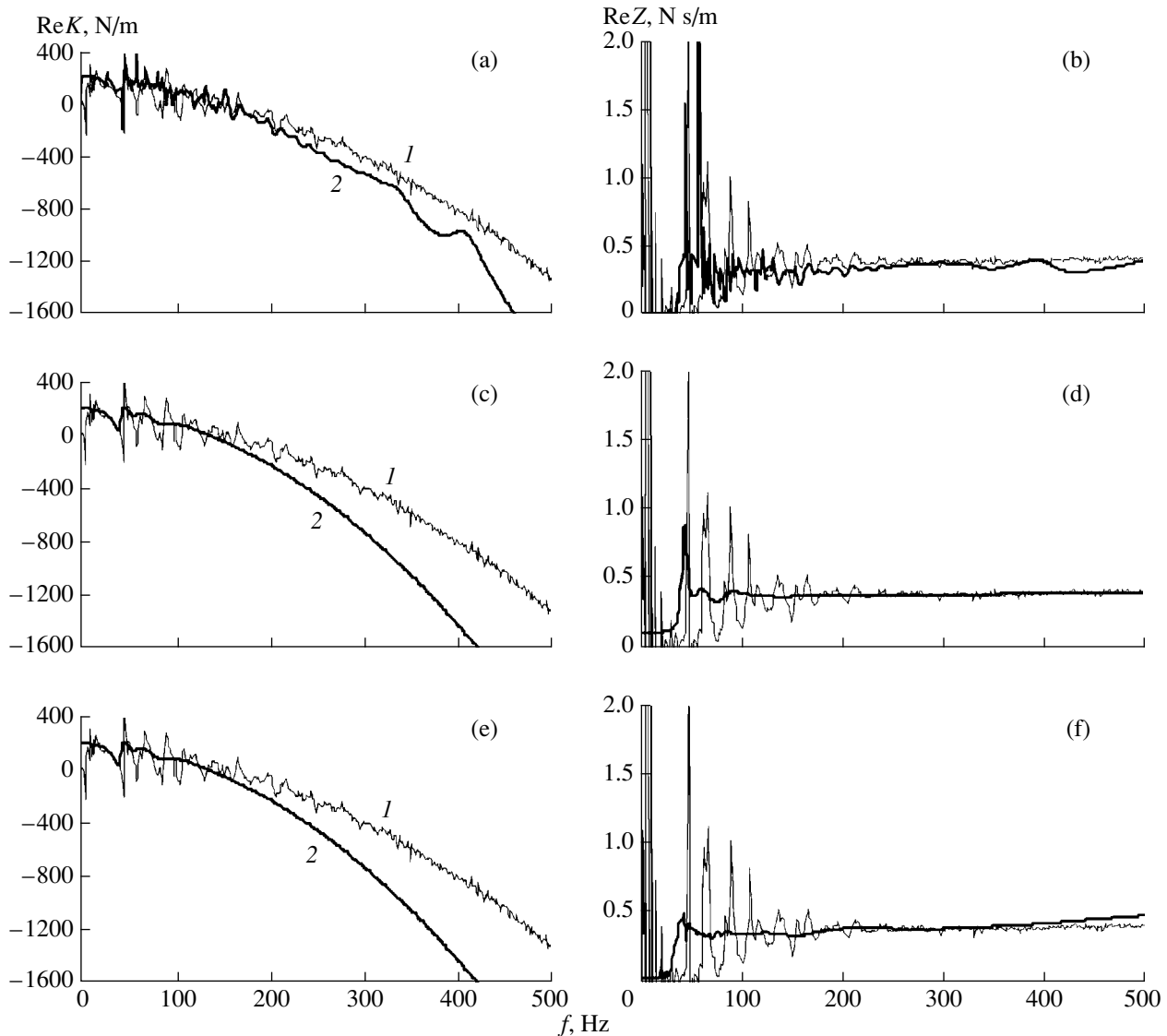


Fig. 2. (1) Experimental and (2) calculated impedance characteristics of a gelatin layer: (a), (b) A-model, $\mu = 5$ kPa, $\eta = 0.2$ Pa s; (c), (d) PA-model, $\mu = 5$ kPa, $\eta = 3$ Pa s; and (e), (f) GA-model, $\mu = 4$ kPa, $\eta = 0.8$ Pa s. The model parameters are $d = 10$ mm, $H = 3$ cm, $\rho = 1008$ kg/m³, and $c_l = 1500$ m/s.

The comparison of different models in their capability to determine the properties of a homogeneous gelatin layer gives the following results. The best correlation of the calculated and experimental data is observed for the A-model (Fig. 2). The model reproduces the low-frequency plateau of the curve $\text{Re}K(f)$, the high-frequency plateau of the curve $\text{Re}Z(f)$, and the qualitative pattern of the layer resonance. In addition, the reproduction of all these characteristics of curves at fixed model parameters remains the same for different diameters of the die (Fig. 3). The high-frequency drop in the curve $\text{Re}K(f)$ in this model, as well as in all other models, is reproduced as a steeper one in comparison with the experiment. Apparently, this is connected with the adopted approximation of the “power source of vibrations.” An important property of the A-model is

the fact that the agreement with the experiment in the level of loss $\text{Re}Z(f)$ in the upper and middle parts of the utilized range is attained automatically after setting very small values of viscosity η and selecting the modulus of elasticity of the layer μ for the reproduction of the level of the low-frequency stiffness plateau in the curve $\text{Re}K(f)$. The variation of viscosity within the range 0.1–1.0 Pa s almost does not influence the loss level and determines only the forms of the resonances of the viscoelastic layer. In order to obtain a qualitative agreement with the experiment in these resonances, it is necessary to set $\eta \approx 0.2$ Pa s. Thus, this model describes the loss in the gelatin layer in the case of the radiation in the frequency range after the resonances as mainly “elastic” loss. Since, in the case of a change in the die diame-

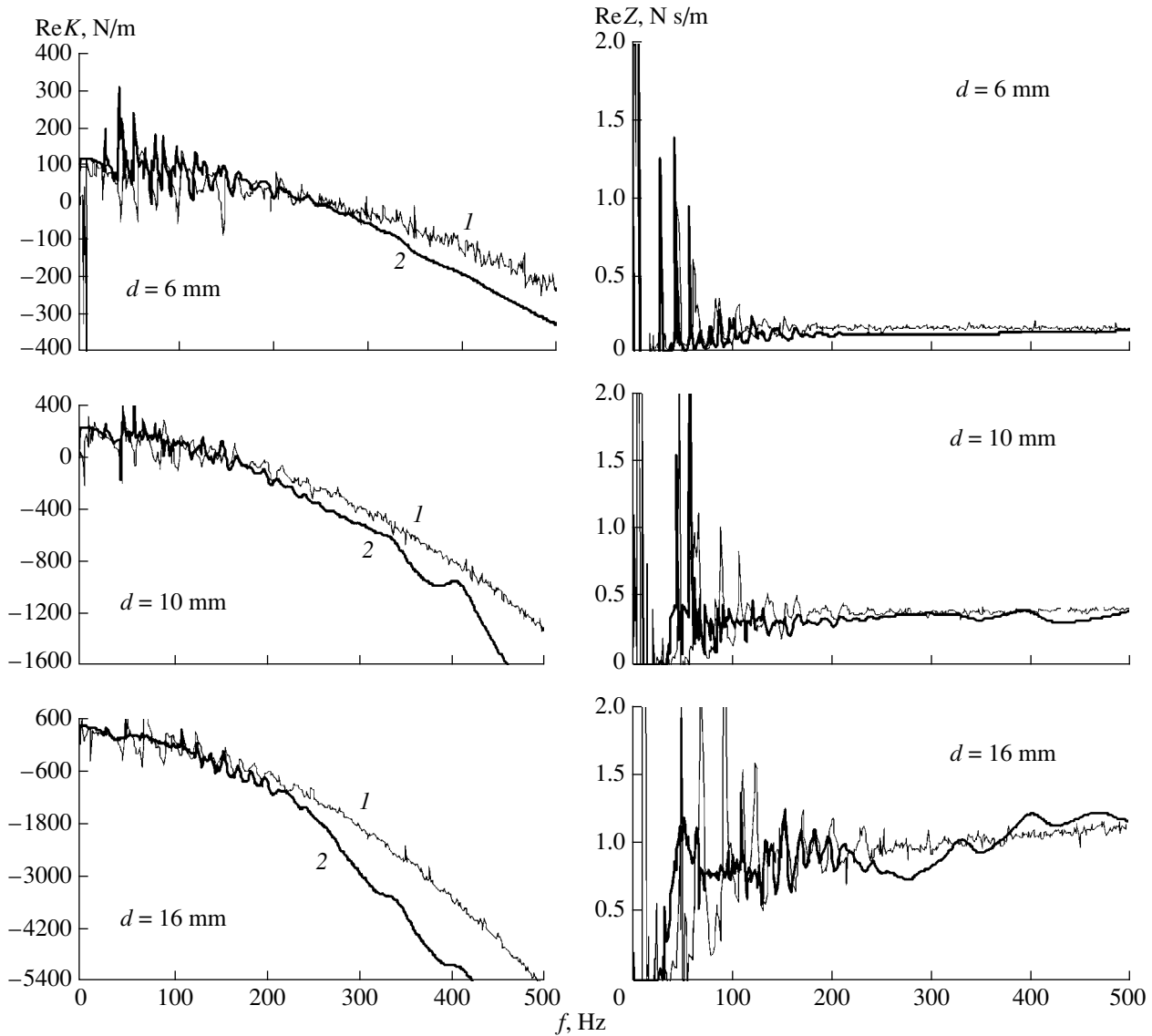


Fig. 3. (1) Experimental and (2) calculated (according to the A-model) frequency dependences of the impedance characteristics of a gelatin layer for different diameters of the die. The model parameters are $H = 3$ cm, $\rho = 1008$ kg/m³, $\mu = 5$ kPa, $\eta = 0.2$ Pa s, and $c_l = 1500$ m/s.

ter, the model reproduces the change in the loss (Fig. 3), this representation is apparently close to reality.

The PA- and GA-models provide less agreement with the experiments, even in the case of a single die diameter (Fig. 2). In the PA-model in the case of a small viscosity, the radiation loss is determined as too small, and it is necessary to considerably increase the value of viscosity η in order to reproduce their level. This deteriorates the reproduction of the form of the layer resonances, and, what is more important, leads to the description of the radiation loss in the gelatin layer as a sum of the comparable “elastic” and “viscous” components. However, if the die diameter is changed, the change of loss in the model does not correspond to the loss observed experimentally, and it is necessary to

select a new value of viscosity to reproduce the loss level corresponding to the new die. In the GA-model, the radiation loss is given correctly “on the average” in the case of low viscosity, but slow variations are reproduced here around this average level. It is possible to smooth off these variations in the curves corresponding to the dies with the diameters $d = 6$ mm and 10 mm on account of an increase in the viscosity, but they remain in the curve corresponding to the die with the diameter $d = 16$ mm.

Thus, in describing the impedance properties of a homogeneous layer in the framework of models with power sources of vibrations, the results that best fit the experiment are provided by the model with a uniform distribution of pressure under the die (excluding the

description of the behavior of stiffness ReK at high frequency). It is impossible to improve the correlation between theory and experiment by using the “parabolic” or “hyperbolic” pressure profiles. On the grounds of this conclusion, one can recommend to use mainly the models with a uniform distribution of pressure under a die for describing the properties of biological tissues.

REFERENCES

1. E. M. Timanin, *Med. Tekh.* (Moscow), No. 2, 39 (1998).
2. H. Oka and T. Irie, *Med. Prog. Technol., Suppl.* **21**, 1 (1997).
3. A. R. Skovoroda and S. R. Aglyamov, *Biofizika* **43**, 348 (1998).
4. E. M. Timanin, Preprint No. 488, IPF RAN (Institute of Applied Physics, Russian Academy of Sciences, Nizhni Novgorod, 1999).
5. H. Oestraeicher, *J. Acoust. Soc. Am.* **23**, 707 (1951).
6. G. I. Arvin, *Med. Tekh.* (Moscow), No. 3, 26 (1972).
7. E. M. Timanin, in *Methods of Vibration Diagnostics of Rheological Characteristics of Soft Materials and Biological Tissues* (Inst. Prikl. Fiz. Akad. Nauk SSSR, Gorki, 1989).
8. E. V. Glushkov, N. V. Glushkova, and E. M. Timanin, *Akust. Zh.* **39**, 1043 (1993) [*Acoust. Phys.* **39**, 551 (1993)].
9. R. Zhang, *J. Sound Vibr.* **229**, 1193 (2000).
10. W. Nowacki, *Theory of Elasticity* (PWN, Warszawa, 1970; Mir, Moscow, 1975).
11. E. V. Glushkov and N. V. Glushkova, *Prikl. Mat. Mekh.* **54**, 474 (1990).
12. B. N. Klochkov and A. V. Sokolov, *Akust. Zh.* **40**, 270 (1994) [*Acoust. Phys.* **40**, 244 (1994)].
13. L. D. Landau and E. M. Lifshitz, *Theory of Elasticity* (Nauka, Moscow, 1982; Pergamon, New York, 1986).
14. P. M. Ogibalov, V. A. Lomakin, and B. P. Kishkin, *Mechanics of Polymers* (Mosk. Gos. Univ., Moscow, 1975).

Translated by M. Lyamshev

Nonlinear Interaction of Acoustic Emission Pulses with a Harmonic Test Wave

S. N. Zaitsev, I. A. Soustova, and A. M. Sutin

*Institute of Applied Physics, Russian Academy of Sciences,
ul. Ul'yanova 46, Nizhni Novgorod, 603600 Russia*

e-mail: soustova@hydro.appl.sci-nnov.ru

Received May 5, 1998

Abstract—Phase modulation of weak, high-frequency, monochromatic waves interacting with strong pulsed signals is investigated. Some estimates are obtained for the interaction between the acoustic emission pulses caused by the crack formation in the Arctic ice cover and a high-frequency test wave. © 2000 MAIK “Nauka/Interperiodica”.

Much attention is currently given to studying the phenomenon called acoustic emission (AE), to which many theoretical and experimental studies are devoted [1–3]. The importance of these investigations follows from the nature of the phenomenon.

The acoustic emission is defined as the generation of elastic waves that accompanies the deformation processes in stressed materials and is related to the crack formation and growth; in other words, the acoustic emission can be considered as a sort of deformation noise emitted by the material. It is this definition that governed the choice of the AE method as the main method of monitoring the fracture processes in materials. It is used for controlling the state of high-pressure pipes, nuclear reactors [1], various types of mines, and rock masses [2, 3]. This method is now recognized as appropriate for investigating the seismic conditions and predicting earthquakes and rock bursts. In these problems, the earthquake zones are considered from the standpoint of physics and mechanics of fracture. In this context, a model of large-scale fracture, the so-called cumulatively unstable model of crack formation [2], was developed. According to this model, the formation and development of the fracture zone can be reliably revealed from the variations of the AE parameters, which is confirmed by experiments [2, 3].

However, the commonly used procedure of recording the AE signals encounters a number of difficulties. First, the receivers of signals are usually located outside the object under investigation (for example, in the case of microseism recording, they lie on the earth's surface). As a result, reflections from the boundary, reflections caused by multiray propagation, and the presence of several types of propagating waves essentially distort the received AE signals. Second, the AE signals have a broadband frequency range. For example, the growing cracks in a reactor housing produce signals with frequencies ranging from 500 kHz to 2 MHz, and

the sample fracture in laboratory conditions produces signals in the frequency range from 3 to 30 kHz [1]. It is also known that the spectrum of the rock mass cave-in differs from the spectrum of a rock bump or burst by the predomination of low frequencies [2]. These features make it difficult to select the frequency range of the required equipment. Today, this choice can be made solely on an experimental basis.

In addition, almost all methods of active acoustic control are based on linear acoustics, because nonlinear effects appearing in interacting acoustic waves are fairly small; in most cases, signals caused by nonlinear effects do not exceed fractions of a percentage point. However, it should be noted that these signals are governed by entirely different, namely, nonlinear acoustic parameters of the medium, and these parameters are more sensitive to the defects and structure variations occurring in the medium as compared to the linear parameters (the sound velocity and the absorption and scattering coefficients), which is of particular importance for diagnostic purposes.

This paper considers the possibility of using the nonlinear interactions between acoustic waves for receiving the AE signals. The acoustic signal reception due to the signal interaction with a pump wave of higher frequency is called the parametric reception of sound [4, 5]. The theory of parametric receivers considers the situations in which the received wave arrives at the interaction region from afar and assumes that this wave can be considered as a plain wave with a constant amplitude. In this paper, we deal with the parametric reception of the AE signals and consider the situations in which the interaction can occur near the emission source, which means that the received signal can widely vary in amplitude within the interaction zone.

It is common practice to introduce nonlinear acoustic parameters of liquids and gases by considering the

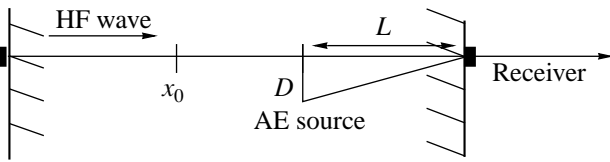


Fig. 1. Scheme of the method of acoustic tomography.

expansion of the pressure in terms of the density to the quadratic terms:

$$p = p_0 + A[(\rho - \rho_0)/\rho_0] + B/2[(\rho - \rho_0)/\rho_0]^2, \quad (1)$$

where $A = \rho_0(\delta p/\delta \rho)_{\rho_0}$, $B = \rho_0^2(\delta^2 p/\delta \rho^2)_{\rho_0}$, c_0 is the linear sound velocity in the medium, and p_0 and ρ_0 are the pressure and density at the equilibrium state.

With this representation of $p(\rho)$, the nonlinearity of the medium is characterized by the ratio $B/2A$.

The equation of state of a liquid or gas medium is sometimes given by an empirical relationship of the form

$$p = p_0(\rho/\rho_0)^\gamma. \quad (2)$$

For a gas, we have $\gamma = C_p/C_v$, and the relationship (2) is reduced to the equation for the adiabatic curve. The parameter γ is also a commonly accepted characteristic of the medium nonlinearity; however, the parameter $\epsilon = 1 + B/2A = (\gamma + 1)/2$ is used more frequently. This parameter includes both the nonlinearity of the equation of state and the nonlinear terms in the equations of motion. Below, we will deal with the media characterized by high values of nonlinear acoustic parameters ($\epsilon \gg 1$) with the physical nonlinearity predominating in these media, i.e.,

$$\epsilon \approx B/2A \approx \gamma/2 = \rho_0 c_0 (\delta c/\delta p)_{\rho_0, p_0}. \quad (3)$$

The introduction of the nonlinear parameter for solids is a more complicated problem, because different kinds of waves can propagate and interact in this case. For solids, we restrict ourselves to considering solely longitudinal waves, because they are most similar to the acoustic waves in liquids and gases. In this case, we can use formula (3) for media with high values of the nonlinear acoustic parameter.

Compare the nonlinear parameters for media of different types. For the majority of homogeneous materials, such as water and most metals, the characteristic values of the quadratic nonlinear parameter do not exceed $\epsilon \sim 3-10$ [6]. By contrast, this parameter can exceed 10^3-10^4 for inhomogeneous media, such as water with gas bubbles [7] and some types of rock [8, 9, 12], which clearly demonstrates the sensitivity of the nonlinear acoustic parameter to the inhomogeneities of the medium.

This paper presents an alternative method of recording the AE pulsed signals. The method is based on the known properties of the nonlinear interaction of a low-frequency pumping pulse with a high-frequency monochromatic wave along its propagation path that passes near the emission source. As a result, we obtain a virtual receiver located near the source, and the effect of the signal distortions along the path on the parameters of the received signal are considerably reduced.

In this paper, we derive the general formulas relating the parameters of the AE pulses to the parameters of the high-frequency (HF) test wave transmitted through the medium under study. Additionally, we obtain some estimates allowing definite conclusions to be made on whether or not the obtained results can actually be used for a particular case of measuring the AE caused by the crack formation in the Arctic ice cover. Figure 1 shows the scheme of the suggested method. The scheme is as follows. The plane monochromatic test wave of frequency ω propagates through the material under study (along the x axis). The receiver is located at the point $x = L$. The source of the signal (the AE pulse) lies at the point $(0, D)$. Due to the nonlinearity of the medium, the signal affects the propagation velocity of the HF test wave. We will assume that the amplitude of the AE pulse far exceeds the amplitude of the HF signal. Then, for media with the quadratic nonlinearity, the variation in the propagation velocity of the test wave can be determined from the expression [5]

$$\Delta c = \epsilon p/\rho_0 c_0 \ll c, \quad (4)$$

where p is the pressure in the AE pulse; ϵ is the nonlinear parameter; and ρ_0 and c_0 are the equilibrium density and velocity, respectively.

Thus, for the variation of the phase of the HF wave at the reception point, we can write the expression

$$\Delta \varphi = \int \omega(\Delta c)/(c^2) dx = \omega \int [\epsilon p(x, t)]/(\rho_0 c_0^3) dx. \quad (5)$$

Consider a portion of the wave that has the coordinate x_0 at the instant corresponding to the beginning of the AE pulse ($T = 0$). This portion arrives at the reception point $x = L$ at the instant

$$t = (L - x_0)/c.$$

We will assume that the source generates a pressure pulse in the form of a spherical wave

$$p = A(t - r/c)/r.$$

Then, the phase shift will be given by the expression

$$\Delta \varphi(t) = \omega N \int_{x_0}^L [A(t - r/c)/r] dx, \quad (6)$$

where $r = \sqrt{D^2 + x^2}$; $N = \epsilon/\rho_0 c^3$; and one must set $t = (x - x_0)/c$, which is the instant the wave with the ini-

tial coordinate x_0 arrives at the point x . Then, we have

$$\Delta\varphi(t) = \omega N \int_{x_0}^L \{ A[1/c((x-x_0) - \sqrt{D^2+x^2})] \} / \sqrt{D^2+x^2} dx. \quad (7)$$

Now, we substitute the integration variable with the new variable $\xi = x - x_0 - \sqrt{D^2+x^2}$ that characterizes the time within which the considered portion of the test wave interacts with the AE pulse. After a simple rearrangement, we obtain

$$\Delta\varphi(x_0) = \omega N \int_0^{\xi_1} A(\xi/c)/(-x_0-\xi) d\xi. \quad (8)$$

We set the lower limit of integration $\xi = 0$ (not $\xi = \xi(x=x_0) = -\sqrt{D^2+x_0^2}$), because negative values of ξ correspond to $x-x_0 < \sqrt{D^2+x^2}$, which means that the HF wave will arrive at the point x prior to the emission pulse, and, consequently, no interaction will occur. The upper limit $\xi_1 = \xi(x=L) = L - x_0 - \sqrt{D^2+L^2}$ corresponds to the termination of the interaction (at the instant the considered portion of the wave arrives at the receiver).

The quantity x_0 cannot take on arbitrary values. It is required that $x_0 < 0$; otherwise, the portion of the wave will arrive at the receiver without any interaction with the pulse. Consequently, we have $x_0 < L - \sqrt{D^2+L^2} < 0$, which means that the denominator in expression (8) varies from $-x_0$ at $\xi = 0$ ($-x_0 > 0$) to $\sqrt{D^2+L^2} - L > 0$ at $\xi = \xi_1$ and always remains positive and nonzero. The only exclusion is the case $D = 0$ corresponding to the AE pulse source located at the x -axis. This case must be considered in greater detail separately.

Let $D = 0$. In this case, the denominator in the integral formula (8) vanishes, and the integrand becomes singular. The singularity is caused by the spherical property of the considered pulsed signal. Note that, in this case, the new variable ξ is a constant that coincides exactly with the parameter x_0 . As a result, we cannot use formula (8), where this variable plays the role of the integration variable. Instead, we will use the initial relationship (6). To avoid the singularity in the integrand, we surround the source of the AE pulse by a sphere of radius r_0 , i.e., we take into account the fact that actual

AE pulses cannot have an unbounded amplitude. Then, we obtain from (8):

$$\Delta\varphi(t) = \omega N \left[\int_{-x_0}^{-r_0} A(t-r/c)/rdx + \int_{r_0}^L A(t-r/c)/rdx \right]. \quad (9)$$

Since we are interested in the solution at the x axis, we define r_0 as follows:

$$r = x \text{ for } x > 0, \quad r = -x \text{ for } x < 0; \quad (r = |x|).$$

Then, the integral formula (9) takes the form

$$\begin{aligned} \Delta\varphi(x_0) \\ = \omega N \left[\int_{-r_0}^L A(x_0/c)/xdx - \int_{-x_0}^{-r_0} A((2x+x_0)/c)/xdx \right]. \end{aligned}$$

Performing the corresponding calculations, we obtain

$$\begin{aligned} \Delta\varphi(x_0) = \omega N A(x_0/c) \ln(L/r_0) \\ - \omega N \int_{-x_0}^{-r_0} A((2x+x_0)/c)/xdx. \end{aligned} \quad (10)$$

It is clear that the magnitude of the received signal depends on the introduced parameter r_0 and becomes infinite at $r_0 = 0$.

Now, we return to the general case (6). To demonstrate the use of the obtained results, we consider the rectangular pulse as a simple example (needless to say that the actual AE pulses are characterized by much more complex shapes):

$$A(\xi/c) = \begin{cases} A_0, & 0 < \xi \leq c\tau \\ 0, & \xi > c\tau. \end{cases}$$

Omitting the constant factor ωN in formula (8) and using for the parameter x_0 its absolute value, we obtain

$$f(x_0) = \int_0^{\xi_1} A(\xi/c)/(x_0-\xi) d\xi. \quad (11)$$

The result of integration in (11) depends on the relationship between ξ_1/c and the pulse duration τ (the upper limit equals $c\tau$ for $\xi_1 > c\tau$ and ξ_1 for $\xi_1 < c\tau$). Thus, we obtain

$$f(x_0) = A_0 \begin{cases} \ln[x_0/(x_0-c\tau)], & \xi_1 \geq c\tau \\ \ln[x_0/(\sqrt{d^2+L^2}-L)], & 0 < \xi_2 \leq c\tau. \end{cases} \quad (12)$$

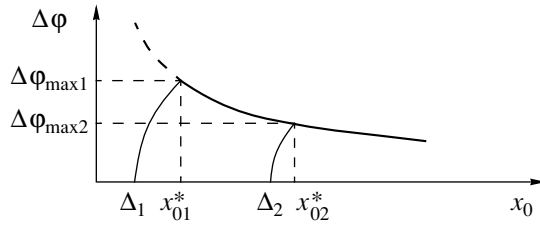


Fig. 2. Phase shift of the test wave for different values of the parameter Δ .

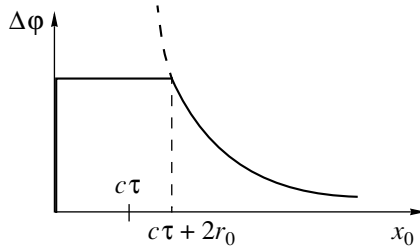


Fig. 3. Phase shift of the test wave with allowance made for the radius of the AE source.

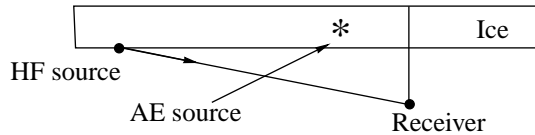


Fig. 4. Scheme of the method of acoustic tomography for the case of ice cracking.

Note that the condition $\xi_1 > c\tau$ corresponds to $x_0 > x_0^*$, where $x_0^* = c\tau + L - \sqrt{D^2 + L^2} = c\tau - \Delta$. Going back to the phase variation $\Delta\phi$, we obtain from (12):

$$\Delta\phi(x_0) = \omega N A_0 \begin{cases} \ln[x_0/(x_0 - c\tau)], & x_0 \geq x_0^* \\ \ln[x_0/(\sqrt{D^2 + L^2} - L)] & \sqrt{D^2 + L^2} - L \leq x_0 \leq x_0^* \end{cases} \quad (13)$$

Let us trace the variations in the obtained solution with distance D (or the parameter $\Delta = \sqrt{D^2 + L^2} - L$, which additionally includes the variations of x_0^*). This behavior may be of interest in tomographic applications, which use several receivers located at different points. Formula (13) gives the following behavior of $\Delta\phi(x_0)$ for different Δ .

It is clear that the above parameter x_0^* uniquely related to Δ affects only the maximum phase variation and determines the effective duration of these variations.

In the case $\Delta \gg c\tau$, we can determine the maximum value of $\Delta\phi$ according to the approximate formula

$$\Delta\phi_{\max} \approx \omega N A_0 c\tau / \Delta. \quad (14)$$

For $D = 0$, we must use formula (10) for a pulse of such a shape. Consider the second term in this formula. It can be rearranged to the form

$$-\omega N A_0 \int_{-x_0/c}^q dx/x = \omega N A_0 \ln(x_0/-2q), \quad (15)$$

where the upper limit of integration depends on the relationship between the quantity $(c\tau - x_0)/2$ (because $(2x + x_0)/2 = c\tau$ corresponds to $x = (c\tau - x_0)/2$) and the parameter r_0 :

$$q = \begin{cases} (c\tau - x_0)/2 & \text{for } (c\tau - x_0)/2 < r_0 \\ -r_0 & \text{for } (c\tau - x_0)/2 > r_0. \end{cases} \quad (16)$$

Thus, from formula (10), we finally obtain the following relationship:

$$\Delta\phi(x_0) = \omega N A_0 \left[\ln L/r_0 \text{ (for } 0 < x_0 < c\tau) + \begin{cases} \ln[x_0/(x_0 - c\tau)], & x_0 > c\tau + 2r_0 \\ \ln[x_0/(2r_0)], & 2r_0 < x_0 < c\tau + 2r_0 \end{cases} \right]. \quad (17)$$

It is clear that introduction of the small parameter r_0 makes it possible to obtain the results that agree well with the earlier results (see Fig. 3 where the dashed line represents the solution obtained from (13) for D approaching to zero, and the smallness of the parameter r_0 is taken into account).

As was mentioned above, the actual AE pulses are characterized by fairly complex shapes. Because of this fact, there are no simple and clear solutions, as in the above example with the rectangular pulse.

Let us try to derive some approximate estimates for an arbitrarily shaped pulse.

Taking the derivative of (11) with respect to the parameter x_0 , we obtain

$$f'(x_0) = A(\xi_1/c)/(x_0 - \xi_1) + \int_0^{\xi_1} A(\xi/c)/(x_0 - \xi)^2 d\xi. \quad (18)$$

In this relationship, the terms may be of the same order of magnitude within the whole region of integration. However, for sufficiently short pulses satisfying the condition $\xi_1/x_0 \ll 1$, this formula makes it possible to easily obtain the relationship between the derivative of the phase of the HF wave and the corresponding parameters of the pulse:

$$\Delta\phi'(x_0) \approx \omega N [A(\xi_1/c)/(x_0 - \xi_1)] = \omega N A(\xi_1/c)/\Delta. \quad (19)$$

It can be readily shown that formula (19) is applicable only to the HF test wave portions corresponding to sufficiently small initial coordinates x_0 , which corresponds to the earlier instants of observation of the phase modulations at the receiver: $t \sim \Delta/c$. This fact makes it possible to simplify the initial formula (8) for $\Delta\varphi(x_0)$. Indeed, we can easily obtain from (8) the following relationship:

$$\Delta\varphi(x_0) = \omega N/x_0 \int_0^{\xi_1} A(\xi/c) d\xi. \quad (20)$$

This formula is valid for sufficiently short pulses and clearly shows that the phase of the HF wave is determined by the pulse area (in the case of pulsed signals that do not satisfy the condition of shortness, the relationship between the phase and the integral over the pulse envelope will be valid for the initial portion of the pulse).

The relationship obtained above offers us a possibility to consider an additional example more consistent with actual practice. In this example, we use the AE signal in the form of a harmonic, exponentially decaying pulse: $A = A_0 \sin(\Omega t) \exp(-\alpha t)$. The calculations by formula (20) yield

$$\begin{aligned} \Delta\varphi(x_0) &= (\omega N A_0/x_0)(c/(\alpha^2 + \Omega^2)\Omega) \\ &- \exp(-\alpha \xi_1/c)(\alpha \sin(\Omega \xi_1/c) + (\Omega \cos(\Omega \xi_1/c))). \end{aligned} \quad (21)$$

Here, the phase variations have alternating signs.

This result can be significantly simplified. Consider the following approximation: $\alpha/c\xi_1 \ll 1$ and $\Omega/c\xi_1 \ll 1$. This approximation is consistent with the conditions of the problem under consideration and agrees well with the assumption $\xi_1/x_0 \ll 1$ used in the derivation of the initial formulas (20) and (21). In this case, we obtain

$$\begin{aligned} \Delta\varphi(x_0) &= (\omega N A_0/x_0)(c\Omega)/(\alpha^2 + \Omega^2)(1 - (\alpha \xi_1/c)). \end{aligned} \quad (22)$$

If we recall the relationship between ξ_1 and the parameter x_0 (corresponding to the current reception time $t = (L + x_0)/c$ in our consideration), we obtain

$$\Delta\varphi = (\omega N A_0 \Omega)/(\alpha^2 + \Omega^2)((c + \Delta\alpha)/x_0 - \alpha). \quad (23)$$

To evaluate the quantity $\Delta\varphi$, we consider expression (19) in more detail. For the characteristic scale of variations $\Delta x = c\Delta t = c2\pi/\Omega$ (where Ω is the frequency of oscillations in the pulse), as a result of simple rearrangement we obtain

$$\Delta\varphi(x_0) = 2\pi c N A(\xi_1/c)\omega/(\Omega\Delta). \quad (24)$$

The comparison of the approximate expression (23) with the case of the rectangular pulse (17) shows a good quantitative agreement, which is not unexpected, as both these formulas were derived for sufficiently short emission pulses. Namely, formula (24) was derived

under the assumption that $\xi_1/x_0 \ll 1$, and formula (17) was derived under a more strict requirement $\Delta \gg c\tau$.

Recall the relationship between the amplitude $A(\xi_1/c)$ and the pressure in the pulse $P = A(\xi_1/c)/R$ (here, one must set $r = R$, where R is the distance from the AE source to the receiver) and the expression for the parameter $N = \epsilon/\rho_0 c^3$. Then, we obtain an estimator for an arbitrarily shaped pulse:

$$\Delta\varphi = 2\pi\epsilon\omega R M/\Omega\Delta, \quad (25)$$

where $M = P/\rho_0 c^2$ is the Mach number.

To illustrate the possibility of actually using the suggested method, we consider a particular experimental scheme. We consider such an AE source as ice cracking. In the recent years, this problem became urgent because of the increasing interest in Arctic explorations. The suggested scheme is shown in Fig. 4.

The receiver is a hydrophone located in water and receiving spherical acoustic waves of AE (because these are the waves characterized by the lowest attenuation in the case under consideration [10]).

In formula (25), we will use the following parameters: $\epsilon \approx 3$, $\rho_0 = 1000 \text{ kg/m}^3$, and $c = 1500 \text{ m/s}$ for water; $P \sim 1 \text{ Pa}$ at distances $R \sim 100 \text{ m}$ and $\Omega \sim 100 \text{ Hz}$ for the characteristic sources of AE in ice [10, 11]. For small values of D , we estimate the parameter Δ as $\Delta = D^2/2L$ and, according to the suggested scheme, set $D \sim 1 \text{ m}$ and $L \sim 100 \text{ m}$. Then, if we use the frequency of the HF wave $\omega \sim 100 \text{ kHz}$, we obtain the value of the phase shift

$$\Delta\varphi \sim 4 \times 10^{-2},$$

which is quite measurable. Note that, for rocks with $\epsilon \approx 10$ and the AE signals with the parameters $2\pi/\Omega \approx 5 \text{ s}$ and $P = 5 \times 10^{-2} \text{ Pa}$, the quantity $\Delta\varphi$ estimated for the HF wave propagating in the ground (with the parameters $\rho = 10^3 \text{ kg/m}^3$, $c \approx 10^3 \text{ m/s}$, $R = 100 \text{ m}$, and $\Delta \approx 10^{-2} \text{ m}$) reaches the value 10^{-1} and greater for the frequencies $\omega \approx 10^5 \text{ Hz}$.

In the foregoing, we considered only media with the quadratic nonlinearity. As follows from (8), the phase variation $\Delta\varphi$ is determined as an integral over the pulse. At the same time, it should be noted that the form of the AE pulses is generally alternating in sign. For this reason, we take into account the cubic nonlinearity of the medium. In this case, the phase variation $\Delta\varphi$ will be governed by the energy parameters of the AE pulse. The inclusion of the cubic nonlinearity of the medium results in an additional phase modulation of the HF test wave [4, 5]:

$$\Delta\varphi_{\text{cub}} = \omega B \int_{x_0}^L [A^2(t - r/c)]/[(D^2 + x^2)] dx, \quad (26)$$

where $B = \beta/\rho^2 c^5$ and β is the cubic nonlinear parameter.

Going to the variable ξ , we obtain the expression

$$\Delta\varphi_{\text{cub}} = \omega B \int_0^{\xi_1} \frac{A^2(\xi/c)}{(x_0 + \xi)^2 + D^2} d\xi.$$

Under the condition $\xi_1/x_0 \ll 1$, the relationship between $\Delta\varphi$ and the intensity of the pulsed signal becomes more obvious:

$$\Delta\varphi_{\text{cub}} = \omega B \left[\int_0^{\xi_1} A^2(\xi/c) d\xi \right] / (x_0^2 + D^2). \quad (27)$$

Recall that the new variable ξ prevents us from using the obtained relationship for the case of the source located at the x -axis (for $D = 0$). In this case, we are again forced to return to the initial formula (26) and to introduce the parameter r_0 . Carrying out the calculations similar to those described above for the case of the quadratic nonlinearity, we obtain the final expression

$$\Delta\varphi = \omega B A^2(x_0/c) \times \left[(L - r_0)/Lr_0 + \omega B \int_{-x_0}^{-r_0} A^2((2x + x_0)/c)/x^2 dx \right]. \quad (28)$$

As can be seen, the result again essentially depends on the parameter r_0 .

Consider the example with the rectangular pulse once again. Using the line of reasoning similar to that used for the quadratic nonlinearity, we obtain the following relationship for the case of an arbitrary location of the source of signal (i.e., for $D \neq 0$):

$$\Delta\varphi = (\omega B A^2)/D \begin{cases} \arctan(x_0 + c\tau)/D - \arctan x_0/D, & \xi_1 \geq c\tau \\ \arctan(x_0 + \xi_1)/D - \arctan x_0/D, & 0 < \xi_1 \leq c\tau. \end{cases} \quad (29)$$

Note that this result is similar to that obtained previously for the rectangular pulse in the medium with the quadratic nonlinearity.

In the case of the source located at the x axis, for the rectangular pulse, we use the formula (28) to obtain the expression

$$\Delta\varphi = \omega B A^2 [((L - r_0)/Lr_0) (\text{for } 0 \leq x_0 \leq c\tau) + \begin{cases} 2c\tau/x_0(x_0 - c\tau), & x_0 > c\tau + 2r_0, \\ (x_0 - 2r_0)/(x_0 r_0), & 2r_0 < x_0 < c\tau + 2r_0. \end{cases} \quad (30)$$

Thus, this paper suggests a new method of monitoring the AE signals. The method is based on the nonlin-

ear interaction between the monochromatic HF test wave and the emission pulses. The estimates show that the suggested method is suitable for practical applications.

ACKNOWLEDGMENTS

This work was supported by the Russian Foundation for Basic Research, project nos. 96-05-64459 and 97-05-64711.

REFERENCES

1. *Application of the Acoustic Emission Method in Reactor Materials Science* (Inst. Atomn. Energ. im. I.V. Kurchatova, Moscow, 1974).
2. V. M. Sboev, *Development of the Scientific and Engineering Foundations of Microseismic Monitoring, Diagnostics, and Prediction of the State of a Rock Mass in the Conditions of Underground Mines and Structures* (Inst. Fiziki Zemli im. O.Yu. Shmidta, Moscow, 1990).
3. V. A. Mansurov, *Dilatancy and Acoustic Emission in the Formation and Development of Microfracture Centers in Rock* (Inst. Fiziki Zemli im. O.Yu. Shmidta, Moscow, 1990).
4. I. Yu. Belyaeva, V. Yu. Zaitsev, and A. M. Sutin, *Fiz. Zemli*, No. 12, 44 (1994).
5. O. V. Rudenko and S. I. Soluyan, *Theoretical Foundations of Nonlinear Acoustics* (Nauka, Moscow, 1975; Plenum, New York, 1977).
6. L. K. Zarembo and V. A. Krasil'nikov, *Introduction to the Nonlinear Acoustics* (Nauka, Moscow, 1966).
7. Yu. A. Kobelev and L. A. Ostrovskii, in *Models of Gas-Liquid Mixtures as Nonlinear Dispersive Media* (Inst. Prikl. Fiz. Akad. Nauk SSSR, Gorki, 1980), pp. 143-160.
8. A. L. Gromkov, R. R. Kalimulin, and G. M. Shalashov, *Dokl. Akad. Nauk SSSR* **315**, 14 (1991).
9. A. V. Nikolaev, *Problems of Nonlinear Seismic Processes* (Nauka, Moscow, 1987).
10. P. J. Stein, *J. Acoust. Soc. Am.* **83**, 617 (1988).
11. H. Schmidt, *J. Acoust. Soc. Am.* **91**, 1734 (1993).
12. R. A. Guyer and P. A. Johnson, *Phys. Today* **52** (4), 30 (1999).

Translated by A. Vinogradov

Frequency Shift of Rayleigh Waves Excited by a Source Moving Perpendicularly to the Interface between Two Media

Yu. M. Zaslavskii

*Institute of Applied Physics, Russian Academy of Sciences,
ul. Ul'yanova 46, Nizhni Novgorod, 603600 Russia
e-mail: strom@hydro.appl.sci-nnov.ru*

Received June 8, 1999

Abstract—Characteristic features of the Doppler frequency shift of Rayleigh and bulk waves excited in an elastic halfspace by a source vertically moving in a contacting gaseous halfspace (atmosphere) are studied. © 2000 MAIK “Nauka/Interperiodica”.

In the seismology and acoustics of vibrations, one frequently encounters the phenomenon of the generation of elastic waves by moving sources. A higher level of high-frequency seismic background in the regions of the passage of atmospheric fronts with the development of catastrophic or fast atmospheric processes is one of the examples of their manifestation. It is possible to give many other facts that testify to the connection of seismic vibrations with the fast-moving atmospheric perturbations of natural origin generating them. Hurricane movement of atmospheric masses, thunderstorm phenomena, and, specifically, the lightning discharge, which is accompanied by vertical movement of the so-called “leader” to the Earth surface, is an example of a moving thermal source of sound, both in the atmosphere and in the surface layers of the Earth medium. It is interesting to study the characteristics of seismic vibrations excited in the Earth medium and affecting its surface and deep layers due to such phenomena. In this case, the Rayleigh surface waves and waves similar to them are excited together with longitudinal and transverse bulk waves. The generation of acoustic waves in gaseous and liquid media by supersonic and subsonic moving sources has been studied in detail and described in many papers [1–4]. The analysis of the characteristics of elastic seismic fields generated by moving sources is presented in the literature to a much lesser extent. Meanwhile, such type of sources is known in seismology, and they manifest themselves, for example, in the realization of the “ripping” mechanism in the seismic center [5]. Model numerical simulations have demonstrated that movement may introduce certain peculiarities into the spectrum and may lead to anisotropy in the generation of these waves, since a moving source is an analog of a source distributed in space, and it can be characterized by an imaginary aperture VR/c , where V is the velocity of source movement, R is the distance between the source and the receiver, and c is the velocity of wave propagation. All

specific features of the radiation characteristics, which are caused by the source movement, are interrelated. The simplest feature is the frequency shift of a wave. The manifestation of this shift becomes noticeably more complex in the propagation through a medium with an inhomogeneous layered structure, which causes reflection and refraction at the interfaces.

By now, the dependence of the frequency shift of Rayleigh waves in an elastic medium upon the velocity of the source movement is not sufficiently investigated. The purpose of this paper is to analyze this dependence for a surface wave excited by a source vibrating with the frequency Ω and moving in the upper gaseous medium perpendicularly to the boundary of the elastic halfspace with a subsonic velocity, i.e., when $V/c < 1$. It is assumed that the density of the upper medium is very small as against the density of the lower medium, the sound velocity in the upper medium is noticeably less than the velocity of compression and shear waves in the lower medium, and the height of the source position over the boundary is much less than the sound wavelength. If the two first conditions are met, the excited surface wave is an almost Rayleigh one [6]. The general scheme of source positioning with respect to the interface and the system of coordinates is given in Fig. 1.

It should be noted that the problem of the determination of the frequency and amplitude of the Rayleigh wave was already considered earlier [7] for the case of an oscillating force acting on the boundary of a solid halfspace and moving uniformly along the horizontal boundary. The solution provided an opportunity to reveal certain features specific to both the frequency shift and the azimuth distribution of amplitude in this wave. The case of a static load applied to the boundary of a solid halfspace and moving with acceleration was also considered in the literature [8]. However, it is impossible to use the data obtained in the cited publications in the case of a vertical movement of the source because of the different geometry of the problem,

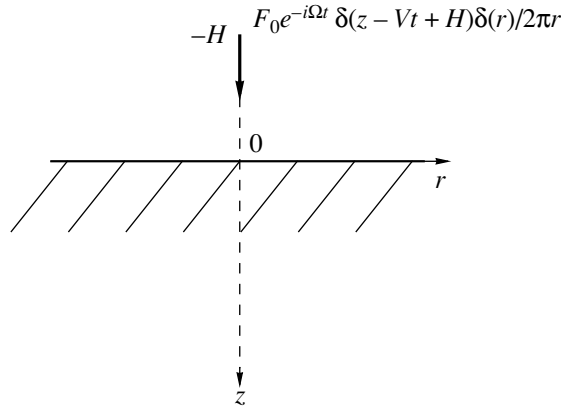


Fig. 1. Schematic representation of a source moving in the air close to the boundary of an elastic halfspace.

which in the case under study is characterized by axial symmetry. This fact calls for a special analysis of the frequency shift of the Rayleigh wave in the specific generation conditions.

Since the movement and not the type of action on the upper medium is essential, we can use any type of the source (monopole or dipole) for our calculations. A point source of oscillating force F normal to the boundary, which moves in the upper medium, can be represented in the form of the following spatial-time function:

$$F = F_0 \exp\{-i\Omega t\} \delta(z - Vt + H) \delta(x) \delta(y). \quad (1)$$

Then, we proceed to the Fourier transforms of the considered force acting on the medium. An explicit expression for its Fourier transform with respect to space and time can be written in the form

$$\bar{F}(\omega, k) = \frac{F_0}{16\pi^4} \int_{-\infty}^{\infty} dx \int_{-\infty}^{\infty} dy \int_{-\infty}^{\infty} dz \int_{-\infty}^{\infty} dt \delta(x) \delta(y) \times \delta(z + H - Vt) e^{-i(\Omega - \omega)t - ik_x x - ik_y y - ik_z z}, \quad (2)$$

where $k^2 = k_x^2 + k_y^2$.

Using the properties of the delta-function, we can obtain an explicit expression for transform (2)

$$\bar{F}(\omega, k) = \frac{F_0}{8\pi^3} e^{iH\sqrt{\frac{\omega^2}{c^2} - k^2}} \delta\left(\omega - \Omega - V\sqrt{\frac{\omega^2}{c^2} - k^2}\right), \quad (3)$$

where c is the sound velocity in the upper medium.

We conduct further consideration under the assumption of not too high source velocity when $V \ll c$, which provides an opportunity to simplify the argument of the delta-function. The integration variable ω under the radical sign can be changed for the constant value of the force frequency Ω . In this case, the argu-

ment of the delta-function is simplified, and the latter takes the form

$$\delta\left(\omega - \Omega - V\sqrt{\frac{\Omega^2}{c^2} - k^2}\right). \quad (4)$$

We will describe the acoustic field in the upper medium by the scalar potential φ_1 and the elastic field in the lower medium by the scalar potential φ_2 and by the azimuth component of the vector potential ψ_2 . As the force, these fields can be represented in the form of the Fourier-Bessel expansions in the spatial and time frequencies by virtue of the axial symmetry of the problem. An expression for the acoustic potential in the upper medium can be readily derived using the following considerations: the displacements at the points belonging to an infinitely narrow region (slightly higher and slightly lower than the horizontal line passing through the source) are equated, while the pressure difference is set equal to the acting alternating force.

The corresponding elementary intermediate transformations allow us to express the primary incident field through the source parameters. In addition, it is necessary to take into account the fact that the acoustic field in the upper medium also contains the component reflected by the media interface. The amplitude of this component is *a priori* unknown. Therefore, the following expression is valid for the acoustic potential:

$$\varphi_1 = \frac{-F_0}{8^2 \pi^2 \rho_a} \int_{-\infty}^{\infty} H_0^{(1)}(kr) k dk \int_{-\infty}^{\infty} \delta\left(\omega - \Omega - V\sqrt{\frac{\Omega^2}{c^2} - k^2}\right) \times \exp i \sqrt{\frac{\omega^2}{c^2} - k^2} |z + H| \frac{e^{-i\omega t}}{\omega^2} d\omega + \int_{-\infty}^{\infty} H_0^{(1)}(kr) k dk \times \int_{-\infty}^{\infty} Q(\omega, k) \exp -i \sqrt{\frac{\omega^2}{c^2} - k^2} |z - H| e^{-i\omega t} d\omega. \quad (5)$$

According to aforesaid, the potentials describing the elastic field of the wave in the lower medium (the scalar potential and the azimuth component of the vector potential) are represented by the relationships

$$\varphi_2 = \int_{-\infty}^{\infty} H_0^{(1)}(kr) k dk \int_{-\infty}^{\infty} B(\omega, k) \exp iz \sqrt{\frac{\omega^2}{c_l^2} - k^2} e^{-i\omega t} d\omega, \quad (6)$$

$$\psi_2 = \int_{-\infty}^{\infty} H_0^{(1)}(kr) k dk \int_{-\infty}^{\infty} C(\omega, k) \exp iz \sqrt{\frac{\omega^2}{c_t^2} - k^2} e^{-i\omega t} d\omega,$$

where $Q(\omega, k)$, $B(\omega, k)$, and $C(\omega, k)$ are the unknown functions, which are the complex amplitudes of the reflected wave in the upper medium and the compression and shear waves in the lower medium, respectively, and ρ_a is the density of the acoustic medium.

It is easy to write down the expressions for the wave displacements and elastic stresses or the acoustic pressure in both media on the basis of the given expansions of fields (5) and (6) [9]. For example, the z -component of the displacements in the upper and lower halfspaces can be determined by the formulas

$$\begin{aligned}
 u_{z1} = & -i \frac{F_0}{8^2 \pi^4 \rho_a} \int_{-\infty}^{\infty} H_0^{(1)}(kr) k dk \int_{-\infty}^{\infty} \sqrt{\frac{\omega^2}{c^2} - k^2} \\
 & \times \delta \left(\omega - \Omega - V \sqrt{\frac{\Omega^2}{c^2} - k^2} \right) e^{-i\omega t + i|z + H| \sqrt{\frac{\omega^2}{c^2} - k^2}} d\omega \\
 & + i \int_{-\infty}^{\infty} H_0^{(1)}(kr) k dk \\
 & \times \int_{-\infty}^{\infty} \sqrt{\frac{\omega^2}{c^2} - k^2} Q(\omega, k) e^{-i\omega t - i|z - H| \sqrt{\frac{\omega^2}{c^2} - k^2}} d\omega, \quad (7) \\
 u_{z2} = & -i \int_{-\infty}^{\infty} H_0^{(1)}(kr) k dk \\
 & \times \int_{-\infty}^{\infty} \sqrt{\frac{\omega^2}{c_l^2} - k^2} B(\omega, k) e^{-i\omega t + i \sqrt{\frac{\omega^2}{c_l^2} - k^2} z} d\omega \\
 & - \int_{-\infty}^{\infty} H_0^{(1)}(kr) k^3 dk \int_{-\infty}^{\infty} C(\omega, k) e^{-i\omega t + i \sqrt{\frac{\omega^2}{c_l^2} - k^2} z} d\omega.
 \end{aligned}$$

Analogously, we can represent the expressions for the wave stresses σ_{zz} and σ_{zr} in the lower medium and the acoustic pressure p in the upper medium. The latter is directly related to the potential in this medium; therefore, the expression $p(\omega, k) = \omega^2 \rho_a \phi_1(\omega, k)$ is valid for the Fourier components. In this connection, there is no need to write down the explicit expression for pressure. Further, we give the corresponding expressions for stresses under the assumption that the Lamé constants of the elastic medium are equal: $\lambda = \mu$:

$$\begin{aligned}
 \sigma_{zz} = & \mu \int_{-\infty}^{\infty} H_0^{(1)}(kr) k dk \int_{-\infty}^{\infty} B(\omega, k) \left(2k^2 - \frac{\omega^2}{c_l^2} \right) \\
 & \times e^{-i\omega t + i \sqrt{\frac{\omega^2}{c_l^2} - k^2} z} d\omega + 2i\mu \int_{-\infty}^{\infty} H_0^{(1)}(kr) k^3 dk
 \end{aligned}$$

$$\begin{aligned}
 & \times \int_{-\infty}^{\infty} C(\omega, k) \sqrt{\frac{\omega^2}{c_l^2} - k^2} e^{-i\omega t + i \sqrt{\frac{\omega^2}{c_l^2} - k^2} z} d\omega, \quad (8) \\
 \sigma_{zr} = & -2i\mu \int_{-\infty}^{\infty} H_1^{(1)}(kr) k^2 dk \int_{-\infty}^{\infty} B(\omega, k) \sqrt{\frac{\omega^2}{c_l^2} - k^2} \\
 & \times e^{-i\omega t + i \sqrt{\frac{\omega^2}{c_l^2} - k^2} z} d\omega - \mu \int_{-\infty}^{\infty} H_1^{(1)}(kr) k^2 dk \\
 & \times \int_{-\infty}^{\infty} C(\omega, k) \left(2k^2 - \frac{\omega^2}{c_l^2} \right) e^{-i\omega t + i \sqrt{\frac{\omega^2}{c_l^2} - k^2} z} d\omega.
 \end{aligned}$$

It is evident that now to solve the excitation problem it is sufficient to satisfy the boundary conditions at $z = 0$, i.e., along the interface plane. This leads to the necessity to satisfy a set of equations that express the condition of the equality of normal displacement components and the equality of the stress σ_{zz} to the negative pressure value p . In addition, the condition of the zero nondiagonal component of stress σ_{zr} at $z = 0$ should be satisfied. Thus, we obtain a set of three equations connecting the spectral amplitudes $Q(\omega, k)$, $B(\omega, k)$, and $C(\omega, k)$ with the parameters of the specified force:

$$\begin{aligned}
 & \mu \left(2k^2 - \frac{\omega^2}{c_l^2} \right) B(\omega, k) + 2i\mu k^2 \sqrt{\frac{\omega^2}{c_l^2} - k^2} C(\omega, k) \\
 & + \omega^2 \rho_a e^{-iH \sqrt{\frac{\omega^2}{c^2} - k^2}} Q(\omega, k) = \frac{F_0}{8^2 \pi^4} e^{iH \sqrt{\frac{\omega^2}{c^2} - k^2}} \\
 & \times \delta \left(\omega - \Omega - V \sqrt{\frac{\Omega^2}{c^2} - k^2} \right), \\
 2i \sqrt{\frac{\omega^2}{c_l^2} - k^2} B(\omega, k) + \left(2k^2 - \frac{\omega^2}{c_l^2} \right) C(\omega, k) = 0, \quad (9) \\
 & i \sqrt{\frac{\omega^2}{c_l^2} - k^2} B(\omega, k) + k^2 C(\omega, k) \\
 & - i \sqrt{\frac{\omega^2}{c^2} - k^2} e^{-iH \sqrt{\frac{\omega^2}{c^2} - k^2}} Q(\omega, k) \\
 & = -i \frac{F_0}{8^2 \pi^4 \rho_a \omega^2} e^{-iH \sqrt{\frac{\omega^2}{c^2} - k^2}} \delta \left(\omega - \Omega - V \sqrt{\frac{\Omega^2}{c^2} - k^2} \right).
 \end{aligned}$$

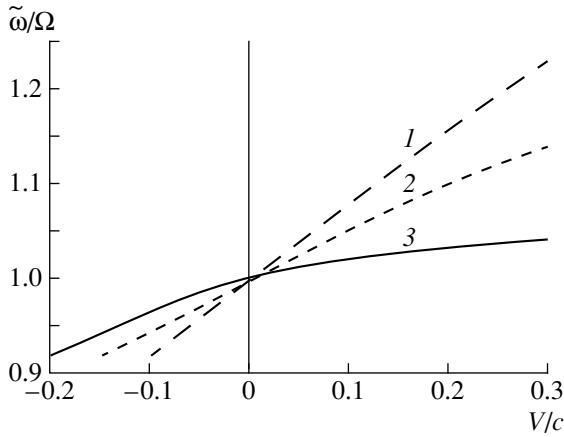


Fig. 2. Frequency shift of the Rayleigh wave as a function of the Mach number V/c for three values of the ratio of the propagation velocities: $c/c_R = (1) 0.6$; (2) 0.8; and (3) 0.95.

Here, since the delta-function is involved on the right-hand sides of the first and the last equations (9),

the quantity ω is replaced by $\Omega + V \sqrt{\frac{\Omega^2}{c^2} - k^2}$. It is

known [5, 6, 9] that the real root of the dispersion equation resulting from the condition of the zero determinant of the set of equations (9) is the pole point, the half-residue at which determines the amplitude of the Rayleigh wave excited by the source under consideration. If we take into account the above assumption on the negligibly small density of the upper medium as against that of the lower medium, we arrive at the conclusion that the determinant of the set of equations virtually depends only on the coefficients at the amplitudes $B(k)$ and $C(k)$ (the index ω in the argument is omitted by virtue of the assumption on convolution with delta-function) in the first two equations (9). Now,

the wave number k must be treated as $k = \frac{\tilde{\omega}}{c_R}$, where c_R is the Rayleigh wave velocity in the solid halfspace, and $\tilde{\omega}$ must be treated as the unknown wave frequency, the dispersion equation for this frequency being given by the expression

$$\begin{aligned} & \left(2 \frac{\tilde{\omega}^2}{c_R^2} - \frac{1}{c_t^2} \left(\Omega + V \sqrt{\frac{\Omega^2}{c^2} - \frac{\tilde{\omega}^2}{c_R^2}} \right)^2 \right)^2 \\ & - 4 \frac{\tilde{\omega}^2}{c_R^2} \sqrt{\frac{\tilde{\omega}^2}{c_R^2} - \frac{1}{c_t^2} \left(\Omega + V \sqrt{\frac{\Omega^2}{c^2} - \frac{\tilde{\omega}^2}{c_R^2}} \right)^2} \\ & \times \sqrt{\frac{\tilde{\omega}^2}{c_R^2} - \frac{1}{c_t^2} \left(\Omega + V \sqrt{\frac{\Omega^2}{c^2} - \frac{\tilde{\omega}^2}{c_R^2}} \right)^2} = 0. \end{aligned} \tag{10}$$

One can see from equation (10) that, independently of the Mach number V/c , the sought-for frequency of the Rayleigh wave detected in a fixed coordinate system lies within the interval

$$\frac{c_R}{c} > \frac{\tilde{\omega}}{\Omega} > \frac{c_R}{c_t}, \tag{11}$$

which is determined only by the ratio of the propagation velocities of elastic waves in the contacting media. The solution of equation (10) is obtained numerically with both directions of motion being considered, i.e., for positive values of the velocity $V > 0$ and for negative values $V < 0$. The results of the calculations are given in Fig. 2, where curves 1, 2, and 3 correspond to the cases $c/c_R = 0.6$; 0.8; and 0.95, respectively. The curves testify that the positive values of the velocity of the source motion (toward the interface) cause a monotonic increase in frequency, which corresponds to the growth of the velocity of the source motion, at least for relatively small values of the Mach number V/c used for the calculation. A steeper increase corresponds to a smaller ratio c/c_R . Conversely, in the case of the source moving away from the interface, i.e., for $V < 0$, the frequency shift is negative with the frequency decrease rate also increasing with decreasing ratio c/c_R . Moreover, in the latter case of the source motion, when the source velocity exceeds in the absolute value some critical value depending on c/c_R , the excitation of the Rayleigh wave becomes impossible at all frequencies. It is easy to see that the interval of the frequency shift is fairly small in comparison with the value of the frequency itself in the case of the motion along the perpendicular to the interface. This feature distinguishes the Doppler shift in the Rayleigh surface wave from the frequency shifts of compression and shear waves. The Doppler shift is also opposite in sign to the frequency shift of waves refracted at critical angles at the interface between two acoustic media [10]. It is necessary to stress the opportunity of a total suppression of Rayleigh waves when the velocity of the source motion exceeds a certain value constituting a small fraction of the velocity of the Rayleigh wave, which has not been noticed in earlier studies. Explaining this statement, we should note that the displacement amplitude in the Rayleigh wave is determined by the half-residue at the specified pole point. The differentiation of the left-hand side of expression (10) with respect to k gives the denominator of the fraction that in fact determines the half-residue and, therefore, the amplitude of oscillations in the surface wave in integral expressions (7) and (8). We do not give the result of differentiation in this paper, as it is rather cumbersome. However, the conducted analysis shows that the excitation amplitude of the studied wave vanishes at the edges of the admissible frequency range (11). Thus, the suppression of the Rayleigh wave is not

a consequence of a large distance from the source to the interface, when the excitation amplitude of the wave is affected by the exponential factor on the right-hand side of system (9), but is explained by another reason.

If we establish a correspondence between a certain departure angle of the ray of the primary wave at the point of the instantaneous position of the source and each value of the Rayleigh wave frequency in the case of a moving source, we can construct the dependences of the ray incidence angle on the Mach number (in reality, we mean the surface of a cone with the vertex at the source; the surface is intersected by the interface, and its vertical section forms two symmetric inclined segments—rays). These dependences are obtained using the fact that the oscillation frequency of a moving source is uniquely related to the frequency of the acoustic wave at the reception point by the relationship $\tilde{\omega} = \Omega/[1 - (V/c)\cos\theta]$, where the angle θ is counted from the direction of source motion [4]. In our case, the angle is counted from the positive direction of the z axis. Figure 3 shows the curves corresponding to Fig. 2 and characterizing the dependence of the inclination angles of rays, which are counted from the vertical line, on the Mach number; the primary field in the upper medium is incident upon the boundary along these rays and excites the Rayleigh wave. Here, the case of source motion toward the interface corresponds to the curves with the positive Mach numbers $V/c > 0$, and the case of the source moving away from the interface corresponds to $V/c < 0$. The set of curves for positive values of $V/c > 0$ is limited by the condition $V/c \ll 1$ and can be extended to the right in the general case, whereas for negative values of $V/c < 0$, the termination of the curves corresponds to the fundamental impossibility of the Rayleigh wave excitation, as its amplitude vanishes and the requirement of real values of frequency is violated when the velocity exceeds some threshold value. It should be noted that each ratio c/c_R at $V/c = 0$ corresponds to its own angle of excitation of the surface wave, and this angle decreases with the decrease in this ratio.

Let us demonstrate that the longitudinal and transverse bulk waves excited in the lower medium by the same moving source have a frequency shift that differs from that of the Rayleigh wave. Evidently, in the calculation of the far fields of bulk waves in the lower medium with the help of expansions (7) and (8), these waves correspond to the contribution to the full integral with respect to the spatial frequency k , which results from the integration over a certain interval on the wave number axis near the point of stationary phase corresponding to this wave type [3]. The complete phase in

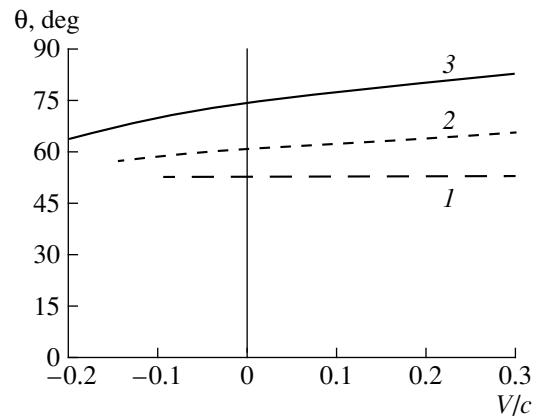


Fig. 3. Inclination angle of the ray of the initial incident wave exciting the Rayleigh wave as a function of the Mach number V/c for $c/c_R = (1) 0.6; (2) 0.8; \text{ and } (3) 0.95$.

the spectrum of, e.g., shear waves is given by the expression

$$\exp i \left\{ kr + z \sqrt{\frac{\left(\Omega + V \sqrt{\frac{\Omega^2}{c^2} - k^2} \right)^2}{c_t^2} - k^2} \right\}. \quad (12)$$

We change over to the spherical system of coordinates R, Θ (the radius-vector R and the angle Θ originate from the zero point at the interface and the z axis in the lower medium) in order to designate the observation point in the elastic medium: $r = R \sin \Theta, z = R \cos \Theta$, and we set the derivative of the complete phase with respect to the variable k equal to zero. In the first approximation with respect to the Mach number V/c , for the point of stationary phase we have the value

$$\bar{k} = \frac{\Omega}{c_t} \left(1 + \frac{V}{c} \right) \sin \Theta. \quad (13)$$

The substitution of this value in expression (12) yields

$$\exp i \left\{ 1 + \frac{V}{c} \right\} \frac{\Omega}{c_t} R. \quad (14)$$

Expression (14) demonstrates that the shear wave detected in the elastic medium must be received in all directions at the shifted frequency $\Omega(1 + V/c)$. An analogous conclusion is valid for longitudinal waves. The interpretation of the obtained result consists of the fact that, in the case of small wave distances from the source in the upper medium to the interface, only the ray nor-

mal to the interface excites compression and shear waves in the lower medium with the angle-independent frequency determined by a common Doppler shift. This provides the frequency shift for the bulk waves in the lower medium, and this shift is equal in all directions.

In conclusion, we note that a dedicated reception of the Rayleigh-type seismic surface waves and the set of bulk and refracted waves generated by natural phenomena mentioned above should make it possible to refine the vertical seismic profile at the site of experiment in the case of further spectral and correlation analysis of acoustic and seismic signals detected by a microphone and a geophone simultaneously, because each type of waves refracted or captured by an interface between layers provides a frequency shift of known value and a corresponding amplitude of response.

ACKNOWLEDGMENTS

The work is supported by the Russian Foundation for Basic Research, project no. 99-02-16957.

REFERENCES

1. V. E. Ostashev, *Sound Propagation in Moving Media* (Nauka, Moscow, 1992).
2. D. I. Blokhintsev, *Acoustics of a Moving Inhomogeneous Medium* (Nauka, Moscow, 1981).
3. L. M. Brekhovskikh and O. A. Godin, *Acoustics of Layered Media* (Nauka, Moscow, 1989).
4. P. M. Morse and K. U. Ingard, *Theoretical Acoustics* (McGraw-Hill, New York, 1968).
5. K. Aki and P. Richards, *Quantitative Seismology: Theory and Methods* (Freeman, San Francisco, 1980; Mir, Moscow, 1983), Vol. 1.
6. I. A. Viktorov, *Surface Acoustic Waves in Solids* (Nauka, Moscow, 1981).
7. Yu. M. Zaslavskii, *Akust. Zh.* **34**, 536 (1988) [*Sov. Phys. Acoust.* **34**, 310 (1988)].
8. V. V. Krylov, *Acta Acustica* **82**, 642 (1998).
9. W. Nowacki, *Theory of Elasticity* (PWN, Warszawa, 1970; Mir, Moscow, 1975).
10. Yu. M. Zaslavskii, *Akust. Zh.* **45**, 274 (1999) [*Acoust. Phys.* **45**, 239 (1999)].

Translated by M. Lyamshev

Photoacoustic Study of the Transmission of Wide-Band Ultrasonic Signals through Periodic One-Dimensional Structures

A. A. Karabutov, V. V. Kozhushko, I. M. Pelivanov, and N. B. Podymova

International Laser Center, Moscow State University, Vorob'evy gory, Moscow, 119899 Russia

e-mail: ivan@gpwpl.phys.msu.su

Received June 8, 1999

Abstract—The propagation of wide-band acoustic pulses in one-dimensional periodic structures consisting of alternating plexiglas and water layers is studied theoretically and experimentally. The experiment is carried out with the use of the wide-band photoacoustic spectroscopy based on the laser excitation of ultrasound and a wide-band signal detection. The fact that the transmission spectrum of a periodic structure has alternating pass and stop bands is confirmed experimentally. The width and localization of the stop bands strongly depend on the thickness of the layers and on the phase velocity of ultrasound in them. It is demonstrated that defects of the structure periodicity give rise to one or several local transmission maxima in the stop band and to a modification of the pass band. The amplitude and position of a local maximum in the stop band strongly depend on the position of the defective layer. The experimental data agree well with the results of numerical simulation.
© 2000 MAIK “Nauka/Interperiodica”.

Studies of the structure and condition of composite materials and items made of them is of great scientific and practical interest. One of the basic methods of non-destructive testing of composites is the ultrasonic technique. The majority of composite materials have periodic structures, and, therefore the study of acoustic properties of periodic structures is quite topical. It is easy to calculate the elastic moduli and the attenuation coefficient for ultrasound in transversely isotropic and orthotropic composite materials in the long-wave approximation. These studies were reviewed in our previous papers [1, 2]. In the general case, the spectrum of the ultrasound transmission through a periodic structure consists of alternating pass and stop bands. Such stop bands were observed experimentally in glass-reinforced plastic composites [3].

Experimental studies of ultrasonic propagation in periodic structures are few in number. Basically, such investigations are restricted to considering one-dimensional periodic structures. This is connected with the fact that multidimensional periodic systems have different characteristic periods of their structure in different directions, and sources of wide-band acoustic signals are necessary for their investigation. Conventional piezoelectric radiators are of little use for this purpose.

Scott and Gordon [4] studied both theoretically and experimentally the ultrasonic propagation in a periodic structure consisting of six periodically arranged glass and water layers of thickness 1.22 and 1 mm, respectively. For this structure, the presence of stop and pass bands for ultrasound in the range 1–8 MHz was demonstrated.

Existence of pass and stop bands in the transmission spectrum of a periodic structure was also demonstrated theoretically and experimentally by James *et al.* [5]. It was found that the presence of defects in a periodic structure gives rise to a local transmission maximum in the stop band of the transmission spectrum. Thus, James *et al.* [5] demonstrated an opportunity for the diagnostics of a periodic structure with defects.

Kushwacha [6], Young-Sang Joo *et al.* [7], and Maidanic and Becker [8] theoretically analyzed the band structure of ultrasonic transmission spectra for a system consisting of metal cylindrical rods positioned in parallel in the air or in a liquid. A theoretical study of ultrasonic propagation in two- and three-dimensional periodic structures was conducted by Kushwacha *et al.* [9, 10]. The corresponding problem is solved using the Bloch theorem and the Fourier transform, and the solution is reduced to the determination of the eigenvalues of the wave vectors of acoustic waves propagating in periodic structures. Papers devoted to the investigation of the ultrasonic wave propagation in composite structures in the case of the acoustic wavelength being close to the structure period were reviewed by Nayfeh [11], who analyzed various theoretical models of one- and three-dimensional ordered composite structures.

The frequency spectrum of ultrasonic transmission through a two-dimensional structure in the form of a system of 36 metal rods of diameter 2.34 cm positioned in the nodes of a square grid with the period 3.7 cm was studied by Robertson and Rudi [12]. The existence of stop bands for the ultrasonic transmission in the frequency range up to 10 kHz was proved experimentally.

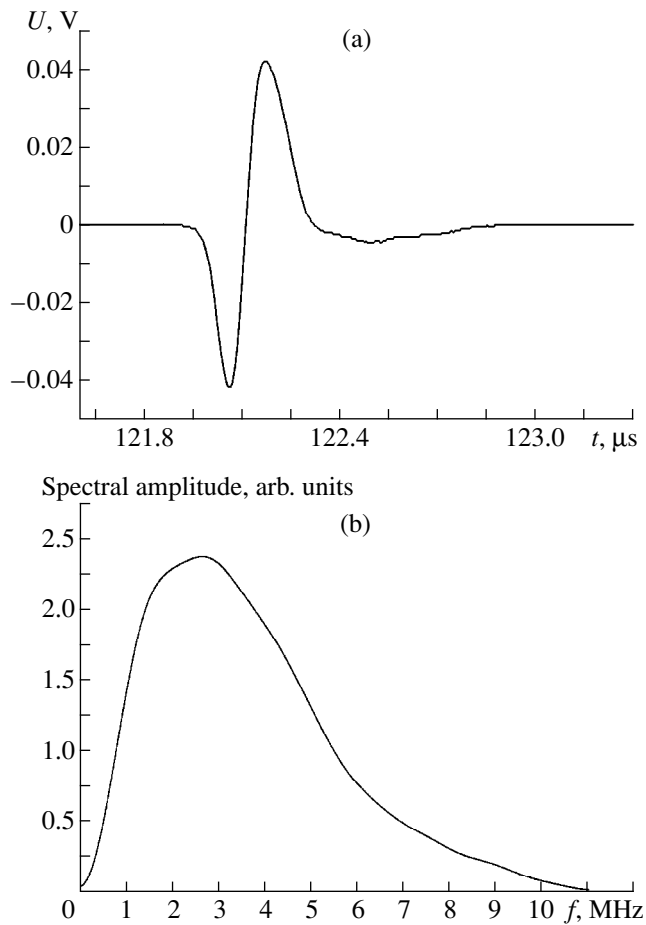


Fig. 1. Reference acoustic signal in distilled water: (a) the time profile and (b) the spectrum.

However, the absence of comparison of the experimental results with numerical simulation, a small number of experimental points in the spectrum, and a strong irregularity of the latter do not provide enough evidence to judge about the validity of the results.

In the majority of papers on the acoustic waves propagation in periodic structures, only the structures with a small number of layers were studied. This is connected with the reduction of the transmission in periodic structures with the increase in the number of layers and with the limitation of the frequency range due to the use of piezoelectric transducers. The employment of wide-band thermo-optical ultrasonic sources provides an opportunity to overcome these difficulties. Thus, the investigation of the ultrasonic propagation in model one-dimensional periodic structures with known characteristics and the comparison of the experimental data with the theoretical calculations remain being topical. Hopefully, the study of the transmission spectra of composites in a wide frequency range will make it possible to reveal their structure.

The purpose of this study is the experimental investigation of the propagation of wide-band acoustic sig-

nals in one-dimensional periodic structures by the wide-band acoustic spectroscopy using a laser ultrasonic source; the determination of the stop bands in the spectra of one-dimensional periodic structures with various periods; and the experimental study of the influence of defects of the structure periodicity on the spectrum of ultrasonic transmission.

According to the theory, the transmission coefficient T of a one-dimensional periodic structure containing n layers is determined by solving $2(n + 1)$ coupled linear equations, which are the relationships for pressures and particle velocities in the i th and $(i + 1)$ th layers. Similar calculations were performed by Scott and Gordon [4] and James *et al.* [5]. In our case, in order to determine the coefficient T , we have solved the problem numerically using Matlab software. If we introduce a complex value of the propagation velocity of longitudinal acoustic waves, it is possible to investigate the absorbing layered structures as well.

The experimental study of the transmission coefficient of acoustic waves in a layered periodic structure was conducted using the method of the laser photoacoustic spectroscopy [13, 14]. This method provides an opportunity to investigate the coefficients of transmission, reflection, and absorption of ultrasonic waves in a wide spectral range, from hundreds of kilohertz to tens of megahertz.

The periodic structure under investigation was placed into a photoacoustic cell filled with an immersion fluid, which in our case was distilled water. Water also filled the unconfined space of the periodic structure and thus formed a water–plexiglas periodic structure. China ink was used as the thermo-optical ultrasonic source. The ink was placed into a cylindrical cell contacting with the immersion liquid (the cell bottom was made of a thin polyethylene film matched in its acoustic impedance with ink and water). A YAG-Nd laser was used for the excitation of ultrasonic pulses (pulse length 12 ns, energy 30 mJ, and spot diameter 8 mm). The ink concentration was selected in such a way that the spectral range of the excited pulses extended from 0.5 to 9 MHz (the pulse shape and its spectrum are given in Fig. 1). The detection of acoustic pulses, which were transmitted through the photoacoustic cell in the absence of the periodic structure and when it was present in the ultrasonic beam, was performed by a wide-band piezoelectric receiver made of a PVDF film (thickness 30 μm). As one can see from Fig. 1, the receiver could detect signals within the aforementioned frequency range. The electric signal was recorded by a digital oscilloscope of the Tektronix TDS220 type with the analog band 100 MHz. The oscilloscope was connected with a computer of the IBM PC type. In the experiment, the signal-to-noise ratio exceeded 10^2 .

The frequency dependence of the transmission coefficient of the periodic structure was determined as the absolute value of the ratio between the spectrum of the

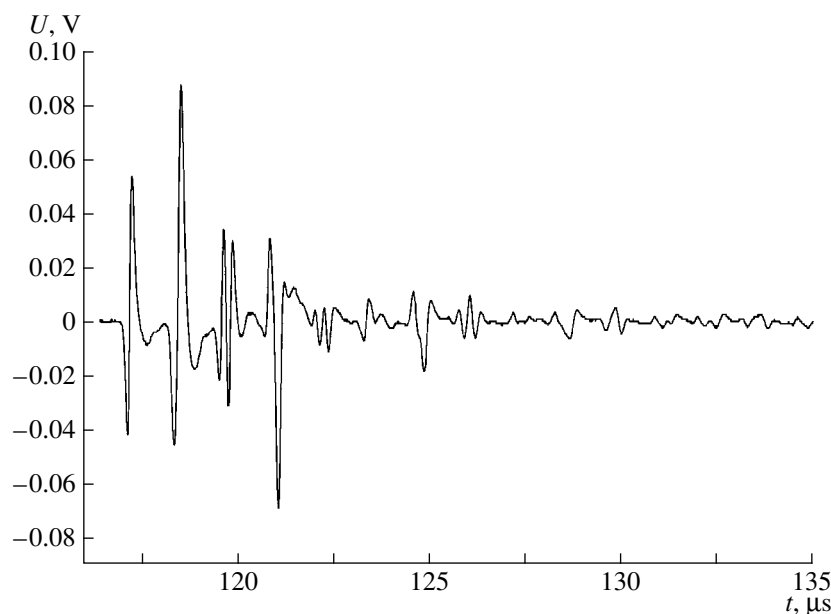


Fig. 2. Acoustic signal in a periodic structure consisting of ten equivalent plexiglas layers ($d_1 = 1.655$ mm and $c_1 = 2.67$ mm/ μ s) and nine equivalent water layers ($d_2 = 0.94$ mm and $c_2 = 1.482$ mm/ μ s).

ultrasonic signal transmitted through the periodic structure placed in the cell (see Fig. 2) and the spectrum of the reference signal transmitted through the cell in the absence of the periodic structure (Fig. 1b). The width and position of the stop bands strongly depend on the thickness of the plexiglas and water layers. Therefore, we studied two structures with equal numbers of plexiglas layers, but with slightly different thicknesses of these layers.

The form of the signal transmitted through the periodic structure (see Fig. 2) contains a “head” pulse, which corresponds to a single passage of a wave through the layers, and a series of attenuating oscillations related to the reverberation of the initial pulse in the multilayer system. In the case under study, the system consisted of ten 1.65 mm thick plexiglas layers positioned at a distance of 0.95 mm from each other. The travel times of ultrasound through the plexiglas layer and the water layer were approximately the same and constituted 0.63 μ s. Since the length of the initial pulse was less than the time of travel through the layer, reverberations were separated in time from the direct transmitted signal. The complete track of the detected signal contained over 10^4 points (Fig. 2 gives only the initial part of the record), which provided the opportunity to study the signal spectrum with necessary details. The transmission spectrum of this periodic structure is given in Fig. 3a (the dotted curve). In the same figure, we present for comparison the transmission spectrum calculated for this periodic structure according to the matrix technique (the solid curve). Naturally, this spectrum consists of alternating pass and stop bands. The positions of the stop bands measured experimentally agree well with the calculations. The main discrepancy

between the amplitudes of the narrow minima in theory and experiment is related to the error in the measurement of the phase velocity of longitudinal acoustic waves in plexiglas, which constitutes 1% of the velocity value, as well as to the small difference in the thickness of the plexiglas plates making up the periodic structure (about 1%). The thin solid line in Fig. 3a represents the numerical simulation of the ultrasonic transmission through a one-dimensional periodic structure with the values of the phase velocity in plexiglas and the layer thickness changed by 1%. As one can see from the plot, there is almost no frequency shift in the pass and stop bands. However, the amplitudes of the narrow minima decrease almost by half. This is caused by the fact that the narrow transmission minima in the pass bands represent newly formed stop bands. Since the system is resonant, small changes in its parameters lead to considerable changes in the transmission coefficient for the forming bands.

The difference between the absolute values of the transmission maxima in the pass bands in theory and experiment may be connected with the one-dimensionality of the model used for the calculations. The finiteness of the acoustic beam leads to the generation of shear acoustic waves at the fluid–solid interface even in the case of normal incidence [15, 16], which may affect the transmission spectrum of longitudinal acoustic waves. However, taking into account such effects in the utilized theoretical model lies beyond the framework of this study.

The spectrum of ultrasonic transmission changes, if one or several plexiglas layers are removed, i.e., if a “defective” layer is created in the periodic structure. In this case, one or several local transmission maxima

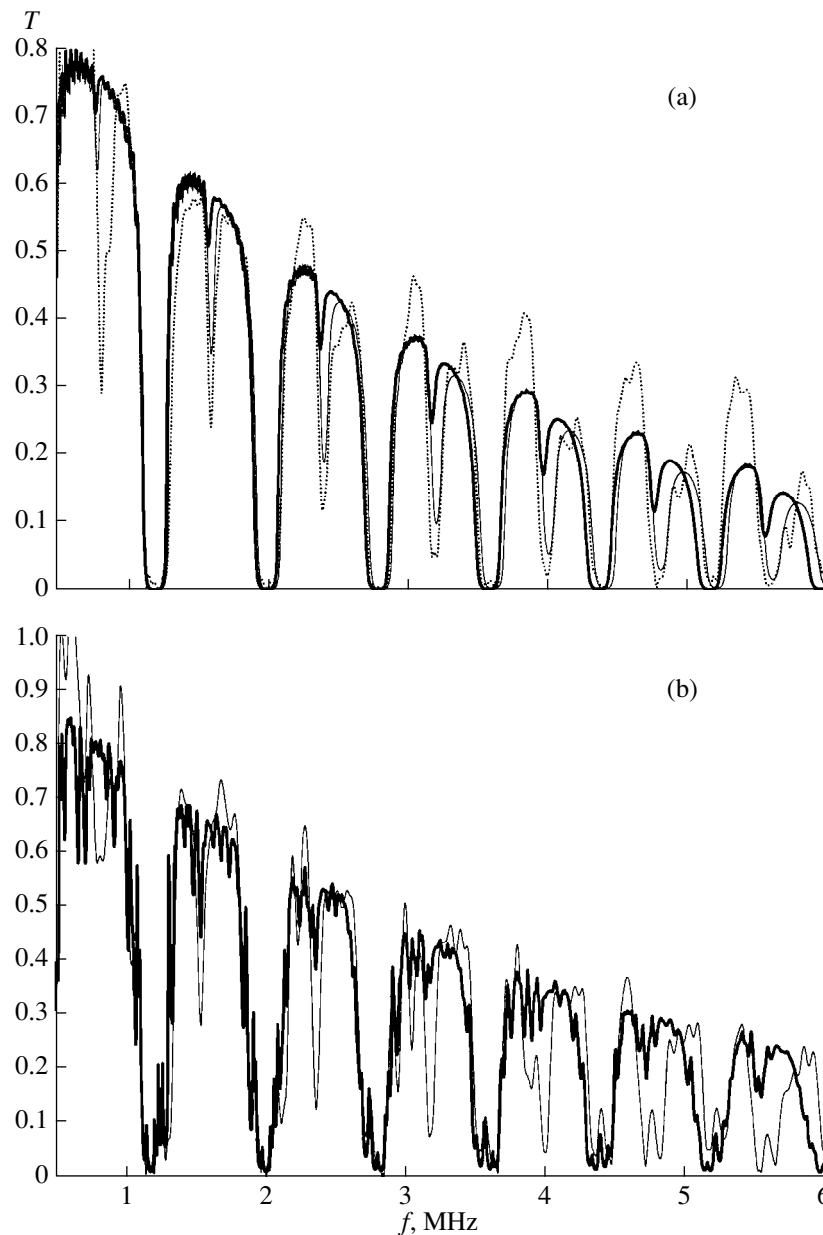


Fig. 3. Transmission spectra of a periodic structure consisting of ten plexiglas layers and nine water layers: (a) $d_1 = 1.655$ mm, $c_1 = 2.67$ mm/ μ s, $d_2 = 0.94$ mm, and $c_2 = 1.482$ mm/ μ s (the thick line represents the calculation and the thin line shows the experiment); the calculation performed for $d'_1 = 1.64$ mm, $c'_1 = 2.7$ mm/ μ s, $d'_2 = 0.955$ mm, and $c_2 = 1.482$ mm/ μ s (the thin line); (b) the fifth and eighth plexiglas layers are replaced by water (the thick line refers to the calculation and the thin line refers to the experiment).

arise in the stop band, and the pass band becomes more irregular (Fig. 3b), the position and amplitude of the local maximum in the stop band depending on the position of the defective layer. The closer the defective layer is to the system center, the greater the amplitude of the local maximum, and the closer this maximum is to the center of the stop band. The presence of defects in the system can also lead to shifts of the narrow stop bands, which is illustrated by Fig. 4a. A narrow minimum that is close to the frequency 1.5 MHz in the

defective periodic structure shifts to the low-frequency range.

As we have noted above, the transmission spectrum of a periodic structure is very sensitive to a change in layer thickness. To illustrate this fact, the spectrum of ultrasonic transmission for a periodic structure consisting of ten 1.5 mm thick plexiglas layers and nine 1.1 mm thick water layers is given in Fig. 4b. One can see that the stop bands are less dense. The thick line in the same figure represents the transmission spectrum of a peri-

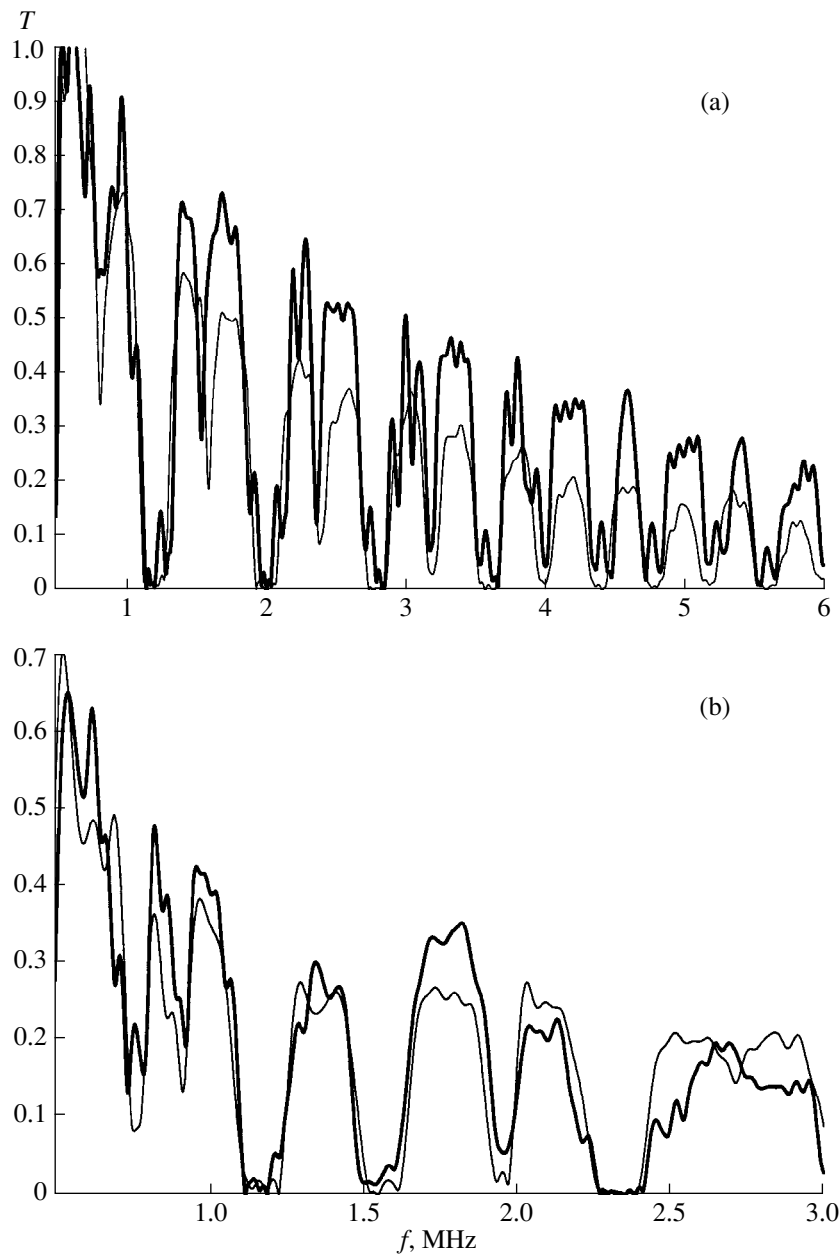


Fig. 4. Experimental dependences of the transmission spectra for two different periodic structures: (a) a periodic structure consisting of ten plexiglas layers ($d_1 = 1.65$ mm) and nine water layers ($d_2 = 0.94$ mm) (the thin line) and the same periodic structure, where the fifth and eighth plexiglas layers are replaced by water (the thick line); (b) a periodic structure consisting of ten plexiglas layers ($d_1 = 1.47$ mm) and nine water layers ($d_2 = 1.1$ mm) (the thin line) and the same periodic structure with the eighth plexiglas layer being replaced by water (the thick line).

odic structure with the removed eighth plexiglas layer. One can readily see that, in contrast to the periodic structure considered earlier (Figs. 3a–4a), a noticeable local transmission maximum is observed in the stop band only near 0.75 MHz, and the amplitudes of other local maxima are much less.

Thus, the propagation of ultrasonic waves in one-dimensional periodic structures of plexiglas and water has been studied using wide-band photoacoustic spectroscopy with a laser ultrasonic source. It has been

demonstrated that the transmission spectrum of such systems consists of pass and stop bands. The width and localization of the stop bands depend heavily on the values of the layer thickness and the phase velocity of ultrasound in the layers. It has been shown that, when one or several plexiglas layers is replaced by water, one or several local transmission maxima arise in the stop band, and the pass band is modified. The position and amplitude of the local maximum in the stop band depend heavily on the position of the defective layer. It

should be noted that the transmission spectra of one-dimensional periodic structures can be obtained in real-time. The frequency range of the investigation is determined only by the width of the spectrum of the photoacoustic generator. The results presented above can be used for nondestructive testing of various periodic structures and composite materials.

REFERENCES

1. A. A. Karabutov, I. M. Kershtein, I. M. Pelivanov, and N. B. Podymova, *Akust. Zh.* **45**, 86 (1999) [*Acoust. Phys.* **45**, 76 (1999)].
2. A. A. Karabutov, V. V. Murashov, and N. B. Podymova, *Mekh. Kompoz. Mater.* **35**, 125 (1999).
3. A. A. Karabutov and N. B. Podymova, *Mekh. Kompoz. Mater.* **31**, 405 (1995).
4. W. R. Scott and P. F. Gordon, *J. Acoust. Soc. Am.* **62**, 108 (1977).
5. R. James, S. M. Woodley, C. M. Dyer, and V. F. Humphrey, *J. Acoust. Soc. Am.* **97**, 2041 (1995).
6. M. S. Kushwacha, *Appl. Phys. Lett.* **70**, 3218 (1997).
7. Young-Sang Joo, Jeong-Guon Ih, and Myoung-Seon Choi, *J. Acoust. Soc. Am.* **103**, 900 (1998).
8. G. Maidanic and K. J. Becker, *J. Acoust. Soc. Am.* **104**, 700 (1998).
9. M. S. Kushwacha, P. Halevi, L. Dobrinski, and Djafari-Rouchani, *Phys. Rev. Lett.* **71**, 2022 (1993).
10. M. S. Kushwacha and P. Halevi, *J. Acoust. Soc. Am.* **101**, 619 (1997).
11. A. Nayfeh, *J. Acoust. Soc. Am.* **89**, 1521 (1991).
12. W. M. Robertson and J. F. Rudi, *J. Acoust. Soc. Am.* **104**, 694 (1998).
13. V. É. Gusev and A. A. Karabutov, *Laser Optoacoustics* (Nauka, Moscow, 1991).
14. A. A. Karabutov, M. P. Matrosov, N. B. Podymova, and V. A. Pyzh, *Akust. Zh.* **37**, 311 (1991) [*Sov. Phys. Acoust.* **37**, 157 (1991)].
15. D. A. Hutchins, R. J. Dewhurst, S. B. Pulmer, and C. B. Scruby, *Appl. Phys. Lett.* **38**, 677 (1981).
16. D. A. Hutchins, R. J. Dewhurst, S. B. Pulmer, and C. B. Scruby, *J. Appl. Phys.* **53**, 4064 (1982).

Translated by M. Lyamshev

Correlation Reception of a Diffraction Sound Field in an Oceanic Waveguide

V. M. Kuz'kin

Wave Research Center, General Physics Institute, Russian Academy of Sciences,
ul. Vavilova 38, Moscow, 117942 Russia

e-mail: petniko@kapella.gpi.ru

Received September 14, 1999

Abstract—Intensity matched processing is considered for a diffracted signal when the object is detected by the main lobe of the shadow scattered sound field. The consideration is based on the few-parameter model that adequately describes the characteristics of the desired signal. It is shown that, in the absence of noise and fluctuations in the parameters of the medium, the proposed algorithm provides the determination of the exact parameters of the signal and the moving object. © 2000 MAIK “Nauka/Interperiodica”.

Earlier, a simple physical model has been proposed [1, 2] that provided adequate estimates for the frequency-temporal parameters of a diffracted signal in an oceanic waveguide when the object is detected by the “shadow” field scattered by it. This model is important, because it allows one to predict the results of numerical calculations and makes it possible to reveal the stable signs of the signal. Such signs are known to afford the detection of weak signals against the background of strong interference, if sufficiently long data acquisition is used. By using the few-parameter model for the signal scattered by a moving object and imposing constraints on the possible range of changes in its characteristics, one can adjust the parameters of the reference signal (namely, those of the transfer function of the matched filter) to obtain the maximum correlation response. With such an algorithm of acoustical monitoring of localized inhomogeneities, a quality of detection can be achieved that is close to the potential limit, and the object parameters can be predicted to a given accuracy. This approach based on matched filtering is a version of the method known as Matched Field Processing (MFP) [3, 4].

In this paper, we consider the problem of reconstructing the parameters of a moving object from the shadow scattered field processed with the correlation algorithm [5, 6]. We estimate the domain of strong correlation where the maximum in the envelope of the normalized cross-correlation function between the model and reference signals is no lower than a given value. Thereby, the maximum step in digitizing the parameters of the reference signal can be estimated to select reliable parameter values. To reconstruct the object parameters from the measurements of the received signal, a two-point reception scheme is proposed with receivers spaced in the horizontal plane.

After [1, 2], we restrict ourselves to considering a monochromatic transmitted signal and a horizontal motion of the object with a constant speed, perpendicularly to the base-line connecting the source and the receiver. Then, the signal scattered by the moving object is a pulse whose envelope is determined by the shadow contour and whose carrier is a sinusoidal oscillation with a linearly varying frequency. In practice, the shape of the object is usually unknown. At the same time, from physical considerations and in accordance with [7], the shape of the envelope is of no importance, if matched filtering oriented at the expected signal parameters is used. This result can be explained by the fact that the sound energy is mainly concentrated within the main lobe of the shadow scattered field for a convex object. Therefore, for simplicity we assume that the signal envelope has the Gaussian form. Then, the diffracted signal can be written [2] as

$$u(t) = U_0 \exp(-2t^2/\vartheta^2) \cos(\omega_0 t + \alpha t^2/2 + \theta_0), \quad (1)$$

where $\alpha = 2\pi v^2/L^2$; $\vartheta = L^2/\sqrt{2}lv$; $L = (R_1 R_2 \lambda/R)^{1/2}$ is the size of the first Fresnel zone; R is the horizontal distance between the fixed point source S and the fixed receiver A_1 ; R_1 and R_2 are the distances from the point where the object crosses the base line to S and A_1 , respectively (Fig. 1); $2l$ and v are the characteristic horizontal size and speed of the object; ω_0 and λ are the acoustic frequency and wavelength; and U_0 and θ_0 are the amplitude and initial phase that depend on the propagation conditions. The pulse duration is specified as the width $\sqrt{2}\vartheta$ of its envelope at the level $1/e$ relative to the maximum.

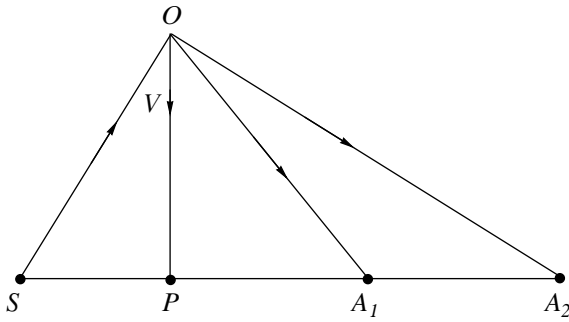


Fig. 1. Measurement geometry: S , source; O , object; $A_{1,2}$, receivers; $SP = R_1$; $PA_1 = R_2$; $SA_1 = R$; $A_1A_2 = R_3$.

Let us consider the autocorrelation function of signal (1):

$$\Psi(\tau) = \int_{-\infty}^{\infty} u(t)u(t + \tau)dt.$$

Usually, the deviation of the instantaneous frequency within the time interval ϑ is small in comparison with ω_0 ($\alpha\vartheta \ll \omega_0$), and ϑ far exceeds the mean period $2\pi/\omega_0$ ($\omega_0\vartheta \gg 2\pi$). Then, in the entire significant domain τ , the function $\Psi(\tau)$ can be quite accurately described by the expression [8]:

$$Y(\tau) = \frac{\sqrt{\pi}}{4} U_0^2 \vartheta \exp(-s\tau^2/\vartheta^2) \cos \omega_0 \tau, \quad (2)$$

where $s = 1 + \kappa$, $\kappa = \alpha^2\vartheta^4/16 = (\pi m/4)^2$, and $m = (L/l)^2$ is the signal base that characterizes its complexity [2]. The width $\Delta\tau$ of the autocorrelation function, when measured at the level $1/e$ of the maximum (energy) value $\Psi(0)$, is equal to

$$\Delta\tau = \frac{2\vartheta}{\sqrt{s}} = \frac{2\vartheta\tau_*}{\sqrt{\vartheta^2 + \tau_*^2}},$$

where $\tau_* = 4/\alpha\vartheta = 2\sqrt{2}l/\pi v$ is the correlation time for the frequency-modulated carrier. This quantity is reciprocal of the deviation $\alpha\vartheta/4$ of the instantaneous frequency $\omega(t) = \omega_0 + \alpha t$ within the envelope width $\vartheta/4$. For a pulse of high complexity, $\tau_* \ll \vartheta(4/\pi \ll m)$ and $\Delta\tau \approx 2\tau_* = (4\sqrt{2}/\pi)(l/v)$. In contrast, if α decreases and the carrier changes to a harmonic oscillation with an infinite correlation time τ_* , the pulse becomes “simple,” and $\Delta\tau \approx 2\vartheta = \sqrt{2}L^2/lv$. Thus, the ratio $\sqrt{2}\vartheta/\Delta\tau$, which determines the compression coefficient, is equal to $\sqrt{[1 + (\pi m/4)^2]}/2$. The width of $\Psi(\tau)$ is equal to $\delta\tau = 2\vartheta\sqrt{\ln 2/s}$ at the level $\Psi(0)/2$.

Suppose that the received and reference signals, $u_1(t)$ and $u_2(t)$, belong to the class of functions (1), and their carrier frequencies coincide ($\omega_1 = \omega_2 = \omega_0$), but

they have different amplitudes $U_{1,2}$, durations $\vartheta_{1,2}$, rates $\alpha_{1,2}$ of frequency variations, and initial phases $\theta_{1,2}^{(0)}$. Let us consider the effect of such a mismatch on the cross-correlation coefficient $K_{12}(\tau)$ of the signals $u_{1,2}(t)$:

$$K_{12}(\tau) = \frac{\Psi_{12}(\tau)}{\sqrt{\Psi_1(0)\Psi_2(0)}} = |K_{12}(\tau)| \exp(i\theta_{12}(\tau)),$$

$$\Psi_{12}(\tau) = \int_{-\infty}^{\infty} u_1(t)u_2(t + \tau)dt,$$

where $\Psi_{1,2}(0)$ is the maximum value of the autocorrelation function for the signals $u_{1,2}(t)$. By substituting expression (1) for $u_{1,2}(t)$ and performing the integration, we obtain

$$|K_{12}(\tau)| = \frac{2}{\sqrt{\vartheta_1\vartheta_2^4\sqrt{a^2 + p^2}}}$$

$$\times \exp\left\{\frac{a(b^2 - ac) - (aq^2 - 2bpq + cp^2)}{a^2 + p^2}\right\}, \quad (3)$$

$$\theta_{12}(\tau) = \frac{1}{2} \arctan \frac{p}{a}$$

$$- \frac{p(q^2 - pr) - (b^2p - 2abq + a^2r)}{a^2 + p^2}.$$

Here, the following notation is used:

$$a = \frac{2(\vartheta_1^2 + \vartheta_2^2)}{\vartheta_1^2\vartheta_2^2}, \quad b = \frac{\tau(\vartheta_1^2 - \vartheta_2^2)}{\vartheta_1^2\vartheta_2^2},$$

$$c = \frac{\tau^2(\vartheta_1^2 + \vartheta_2^2)}{2\vartheta_1^2\vartheta_2^2}, \quad (4)$$

$$p = \frac{\alpha_2 - \alpha_1}{2}, \quad q = \frac{\tau(\alpha_1 + \alpha_2)}{4},$$

$$r = \omega_0\tau + \frac{\tau^2(\alpha_2 - \alpha_1)}{8} + \theta_2^{(0)} - \theta_1^{(0)}.$$

Thus, if the mismatch takes place, the distribution $K_{12}(\tau)$ is a modulated oscillation with the carrier frequency $\hat{\theta}_{12}(\tau)$, initial phase $\theta_{12}^{(0)} = (1/2) \arctan(p/a) + a^2(\theta_2^{(0)} - \theta_1^{(0)})/(p^2 + a^2)$, and envelope $|K_{12}(\tau)|$.

Further, we assume that the processing procedure is based on the envelope of the cross-correlation function, i.e., the intensity matched processing is used. Then, the effect of the frequency-modulated carrier and the initial phase is ruled out. Let us derive the expression that determines the domain of permissible deviations of the

parameters ϑ_2 and α_2 from ϑ_1 and α_1 , where the following condition is met:

$$|K_{12}(0)| = \frac{2}{4\sqrt{a^2 + p^2}} \frac{1}{\sqrt{\vartheta_1 \vartheta_2}} \geq H, \quad 0 < H \leq 1. \quad (5)$$

This expression serves as a closeness criterion for the signals $u_1(t)$ and $u_2(t)$. The value of H is chosen according to the requirements on the level of the correlation response. If $\vartheta_2 = \vartheta_1$ and $\alpha_2 = \alpha_1$, we have $|K_{12}(0)| = \max = 1$.

Let us specify

$$\begin{aligned} \vartheta_1 &= \vartheta_2 + \Delta\vartheta; & \alpha_1 &= \alpha_2 + \Delta\alpha; & x &= \Delta\vartheta/\vartheta_2, \\ y &= \Delta\alpha/\alpha_2. \end{aligned} \quad (6)$$

In the notation of (6), inequality (5) takes the form:

$$\frac{\sqrt{1+x}}{\sqrt[4]{\left(1+x+\frac{x^2}{2}\right)^2 + \frac{\kappa y^2}{4}(1+x)^4}} \geq H, \quad \kappa = \frac{\alpha_2^2 \vartheta_2^4}{16}. \quad (7)$$

If one converts expression (7) to new coordinates $X = x + 1$, $Y = y$ in the Oxy plane, an equation can be obtained for the curve of constant level for the envelope maximum of the cross-correlation coefficient, this curve separating the domains of weak and strong correlations:

$$4X^2 = H^4[(1+X^2)^2 + \kappa Y^2 X^4]. \quad (8)$$

The curve (8) of the sixth order splits into two closed lines that are symmetric about the X and Y coordinate axes. The entire right-hand line lies in the right-hand

half-plane of the O_1XY plane, and the entire left-hand line lies in the left-hand one. Only the line that is located to the right of the Y axis ($X > 0$) has a physical meaning. Let us consider the characteristic values of curve (8).

1. Points of intersection with the O_1X axis:

$$\begin{aligned} X_{1,2} &= \frac{1}{H^2}(1 \pm \sqrt{1-H^4}), & X_{3,4} &= -X_{2,1}, \\ X_{2,1} &> 0, & X_{3,4} &< 0 \end{aligned}$$

(for $0 < H \leq 1$, we have $1 \leq X_1 < \infty$, $0 < X_2 \leq 1$).

2. Extremum points:

$$X_{5,6} = \pm \frac{H^2}{\sqrt{2-H^4}}$$

$$\text{with } Y_{1,2} = Y(X_5) = Y(X_6) = \pm \frac{2\sqrt{1-H^4}}{H^4\sqrt{\kappa}}$$

(for $0 < H \leq 1$, we have $0 < X_5 \leq 1$, $-1 \leq X_6 < 0$, $0 \leq Y_1 < \infty$, $-\infty < Y_2 \leq 0$).

When the level H and the parameter κ increase, the strong-correlation domains become narrower, and, in the limiting case $H = 1$, they shrink to the points with the coordinates $X = \pm 1$, $Y = 0$. Figure 2 shows the curves $Y(X)$ (8) for the domain of positive values of X and for different values of H and κ .

According to (3), the width $\delta\tau_{1,2}$ measured at half the level of $|K_{12}(0)|$ is $\delta\tau_{12} = 2\sqrt{\ln 2/\rho}$, where

$$\rho = \frac{H^4 \left\{ \left(1+x+\frac{x^2}{2}\right) + \kappa(1+x)^2 \left[\left(1+x+\frac{x^2}{2}\right) \left(1+y+\frac{y^2}{2}\right) + xy \left(1+\frac{x}{2}\right) \left(1+\frac{y}{2}\right) \right] \right\}}{\vartheta_2^2(1+x)^2}.$$

As follows from this expression, the signal mismatch leads to an increase in the duration of the correlation response, as compared to the case of no mismatch. For $x = y = 0$ ($H = 1$), the result is evident: $\delta\tau_{12} = \delta\tau$.

Assume that *a priori* information exists on the available range of changes in the object parameters v , l , and L : $v_{\min} \leq v \leq v_{\max}$, $l_{\min} \leq l \leq l_{\max}$, $L_{\min} \leq L \leq L_{\max}$. Then one can define the domain of realistic values for the parameters ϑ_2 and α_2 of the reference signal: (ϑ_{\min} , ϑ_{\max})

and (α_{\min} , α_{\max}), where $\vartheta_{\min, \max} = L_{\min, \max}^2 / \sqrt{2} (lv)_{\max, \min}$

and $\alpha_{\min, \max} = 2\pi v_{\min, \max}^2 / L_{\max, \min}^2$. By exhausting these values, a combination of the parameters can be found that meets condition (5). The parameters ϑ_2 and α_2 selected in such a way can be treated as the desired ones

that correspond to the parameters ϑ_1 and α_1 of the received signal.

To exhaust the parameters in the minimum number of steps, it is sufficient to digitize the aforementioned domains into segments $\Delta\vartheta_i = \Delta x \vartheta_i$ ($i = 1, 2, \dots, n$) and $\Delta\alpha_j = \Delta y \alpha_j$ ($j = 1, 2, \dots, m$) whose length is equal to the maximum absolute errors. In other words, one should specify:

$$\begin{aligned} \Delta x &= X_2 - X_1 = \frac{2\sqrt{1-H^4}}{H^2}, \\ \Delta y &= Y_1 = \frac{2\sqrt{1-H^4}}{H^4\sqrt{\kappa}}, \end{aligned} \quad (9)$$

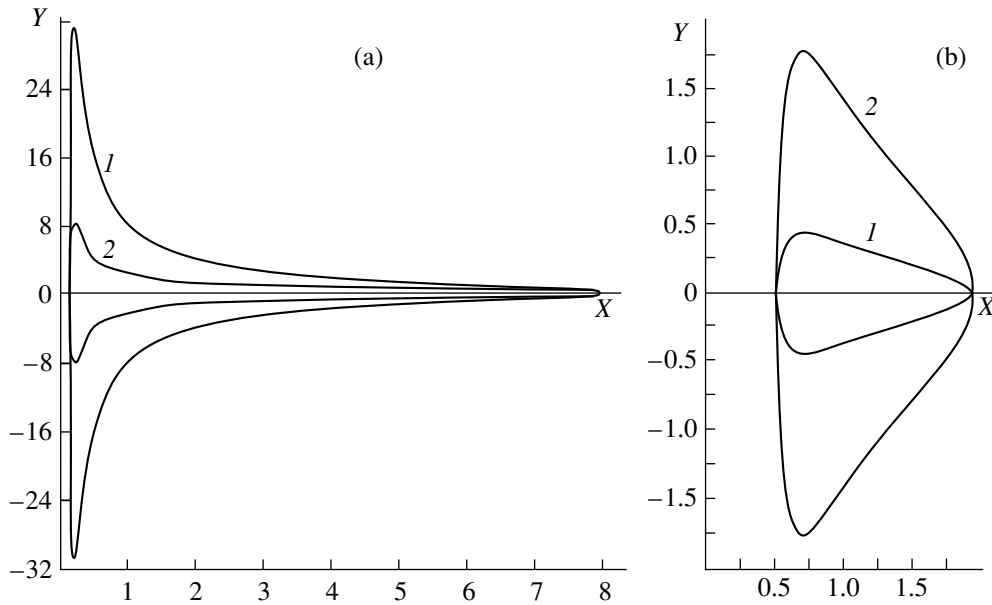


Fig. 2. Curves of constant level for the maximum in the envelope of the cross-correlation coefficient (l , $\kappa = 1$; 2 , $\kappa = 16$): (a) $H = 0.5$; (b) $H = 0.9$.

where $\Delta\vartheta_i = \vartheta_{i+1} - \vartheta_i$ and $\Delta\alpha_j = \alpha_{j+1} - \alpha_j$. Here, $\vartheta_{1,n} = \vartheta_{\min, \max}$ and $\alpha_{1,m} = \alpha_{\min, \max}$. The sequence $\{\vartheta_i\}$ is a geometric progression: $\vartheta_i = \vartheta_1(1 + \Delta x)^{i-1}$. Hence, the number of increments is

$$n = \left[\frac{\log(\vartheta_{\max}/\vartheta_{\min})}{\log(1 + \Delta x)} + 1 \right].$$

Here the square brackets mean the integer part of a number. According to (9), the quantity $\Delta\alpha_j$ equals to

$$\Delta\alpha_j = \frac{8\sqrt{1-H^4}}{H^4\vartheta_j^2}.$$

Thus, the length of the segment $\Delta\alpha_j$ depends on both the level H and the selected value of the duration ϑ_i . Condition (5) will be met if the domain of the values of the parameter α_2 is broken into equidistant segments of length

$$\Delta\alpha = \frac{8\sqrt{1-H^4}}{H^4\vartheta_{\max}^2}.$$

As a result, we have for the number of increments:

$$m = \left[\frac{\alpha_{\max} - \alpha_{\min}}{\Delta\alpha} \right].$$

Thus, the minimum number of combinations is estimated as

$$\min Q = n \times m. \tag{10}$$

For numerical calculations by formula (10), we use the following values: $l_{\min, \max} = 30$ and 75 m; $v_{\min, \max} = 3$ and 12 m/s; $R_{l\min, \max} = 10$ and 60 km; $R = 120$ km; and

$\lambda = 10$ m. Then, for the reference signal, the domain of the parameter values is estimated as follows: $7.20 \times 10 \leq \vartheta_2 \leq 2.36 \times 10^3$ s, $1.88 \times 10^{-4} \leq \alpha_2 \leq 9.87 \times 10^{-3}$ s⁻². For $H = 0.5$, we have $\min Q = 2 \times 434$; for $H = 0.9$, we have $\min Q = 4 \times 8066$.

Exhausting the values of ϑ_2 and α_2 with selecting their most reliable combinations according to criterion (5) leads to uncontrolled errors in the parameters ϑ_1 and α_1 of the received signal. With the specified digitization, these relative errors are limited from above by relation (9), and one can see that they are rather high, even at large H . For instance, if $H = 0.9$, we obtain $\Delta x \approx 1.45$ and $\Delta y \approx 7.15/\alpha_2\vartheta_2^2$. To reduce the errors, one can increase the threshold level of H and/or increase the number of combinations Q .

However, with the considered processing method, the parameters of the desired signal can be reconstructed exactly. Let $\{\vartheta_i, \alpha_j\}$ and $\{\vartheta_\rho, \alpha_\gamma\}$ be the combinations of the parameters ϑ_2 and α_2 at which the maxima in the cross-correlation coefficient envelope are H_1 and H_2 , respectively. Note that their values may coincide. Using the notation of (6), in view of relation (8), we obtain a system of equations

$$\begin{cases} \alpha_1 = \alpha_j + \frac{8\sqrt{(\vartheta_1/\vartheta_i)^2 - (H^4/4)[1 + (\vartheta_1/\vartheta_i)^2]}}{H^2\vartheta_1^2} \\ \alpha_1 = \alpha_\gamma + \frac{8\sqrt{(\vartheta_1/\vartheta_\rho)^2 - (H^4/4)[1 + (\vartheta_1/\vartheta_\rho)^2]}}{H^2\vartheta_1^2} \end{cases} \tag{11}$$

for the parameters ϑ_1 and α_1 of the received signal. It is clear that the signal level is also completely reconstructed in this case.

The considered monostatic reception scheme does not allow the object parameters v , L , l to be reconstructed from the measured signal parameters ϑ_1 and α_1 . To eliminate this ambiguity, one can implement a bistatic reception with the receiving points being spaced by a certain distance from each other along the base line (Fig. 1). Note that a vertical separation of the receivers does not solve the problem under discussion [2].

Let $\vartheta_{2,3}$ and $\alpha_{2,3}$ be the parameter values for the diffracted signals at the reception points $A_{1,2}$, these values being determined by the system (11). Then, the object parameters will be determined by the following system of equations:

$$\begin{cases} \vartheta_{2,3} = L_{2,3}/\sqrt{2}lv \\ \alpha_{2,3} = 2\pi v^2/L_{2,3}^2, \end{cases} \quad (12)$$

where $L_2^2 = R_1(R - R_1)\lambda/R$ and $L_3^2 = R_1(R + R_3 - R_1)\lambda/(R + R_3)$. From the first equation of (12), we find

$$R_1 = \frac{(1 - \gamma)R(R + R_3)}{R(1 - \gamma) + R_3}, \quad \gamma = \vartheta_2/\vartheta_3.$$

Assuming that L_2 is known, from (12) we obtain

$$v = \frac{L_2}{\sqrt{2\pi}}\sqrt{\alpha_2}, \quad l = \frac{\sqrt{\pi}L_2}{\sqrt{\alpha_2}\vartheta_2}.$$

Hence, the bistatic measuring scheme allows one to eliminate the ambiguity in determining the distance R_1 between the source and the point at which the object crosses the base line, and the object parameters can be completely reconstructed.

Thus, this paper considers the algorithm for an acoustic monitoring of a moving object with the use of the shadow scattered field. The algorithm is based on the *a priori* information on the object parameters that

form the diffracted signal and on the intensity matched processing. As the closeness criterion for the parameters of the received and reference signals, that of the maximum in the envelope of the normalized cross-correlation function is chosen. It is shown that, in the absence of noise and fluctuations in the oceanic medium, the algorithm provides the exact values of the parameters of the desired signal and the moving object.

ACKNOWLEDGMENTS

This work was supported by Russian Foundation for Basic Research, project no. 99-02-17671.

REFERENCES

1. S. M. Gorskiĭ, V. A. Zverev, A. L. Matveev, and V. V. Mityugov, *Akust. Zh.* **41**, 223 (1995) [*Acoust. Phys.* **41**, 190 (1995)].
2. V. M. Kuz'kin, *Akust. Zh.* **43**, 514 (1997) [*Acoust. Phys.* **43**, 440 (1997)].
3. A. B. Baggeroer and W. A. Kuperman, in *Acoustic Signal Processing for Ocean Exploration*, Ed. by J. M. F. Moura and L. M. G. Lourtie (Kluwer, Dordrecht, 1992), pp. 79–114.
4. J. V. Candy and E. J. Sullivan, in *Proceedings of the 4th European Conference on Underwater Acoustics, Rome, 1998*, Vol. 1, pp. 3–8.
5. P. M. De Kooter, Master's Thesis (Naval Postgraduate School, Monterey, CA, 1997).
6. K. B. Smith, J. Brune, and C. S. Chiu, in *Proceedings of the 4th European Conference on Underwater Acoustics, Rome, 1998*, Vol. 1, pp. 9–14.
7. V. A. Zverev, A. L. Matveev, and V. V. Mityugov, *Akust. Zh.* **41**, 591 (1995) [*Acoust. Phys.* **41**, 518 (1995)].
8. S. M. Rytov, *Introduction to Statistical Radiophysics* (Nauka, Moscow, 1976), Chap. 1.

Translated by E. Kopyl

Effect of the Bulk Viscosity on the Sound Propagation in Nonequilibrium Suspensions of Microparticles in Gas

N. E. Molevich and V. E. Nenashev

Korolev State Aerospace University, Samara, Moskovskoe sh. 34, Samara, 443086 Russia

e-mail: molevich@mb.ssau.ru

Received September 27, 1999

Abstract—The sound propagation in a mixture of gas with uniformly dispersed solid particles, whose temperature is maintained above that of the gas by an external source, is considered. The dispersion properties of this kind of suspensions are studied, and expressions for the second viscosity and the sound velocity in such suspensions are derived. It is shown that, in a nonequilibrium suspension, the second viscosity may be negative. The ranges of the suspension parameters, for which the propagation of low-frequency sound is impossible, are determined. © 2000 MAIK “Nauka/Interperiodica”.

It is well known that one of the mechanisms of sound absorption in relaxing media is related to the presence of the bulk (second) viscosity in these media. In a number of nonequilibrium media, the bulk viscosity may be negative [1–4]. Examples of such media are molecular ones with a nonequilibrium excitation of the internal degrees of freedom, as well as nonisothermic plasma or media with heat release. A negative bulk viscosity leads to an acoustic instability of the medium and to considerable changes in its dispersion properties. Specifically, the low-frequency sound velocity u_0 may exceed the high-frequency sound velocity u_∞ . Such media are also characterized by the presence of nonequilibrium regions where low-frequency sound cannot propagate. This opens up possibilities to use these media for low-frequency noise control. Besides, these media exhibit considerable changes in the conditions of the laminar-to-turbulent transition [4].

In recent years, much attention has been given to studying the sound propagation in nonequilibrium multiphase media, e.g., in dust-ion plasma [5, 6]. In this paper, we consider the sound propagation in a mixture of gas with uniformly dispersed solid microparticles (a gaseous suspension) with the temperature of the microparticles being maintained at a level above the gas temperature by an external source of energy. We show that the dispersion properties of such suspensions can be described by the second viscosity introduced in an explicit form. We specify the conditions at which the second viscosity of such a medium can be negative, and we determine the regions within which the transmission of low-frequency sound is impossible.

We assume that the size of the solid particles far exceeds the molecular one and is much less than the sound wavelength. In this case, we can use a continuous

medium model and write the gas dynamics equations for the case of a low concentration of the solid phase $\varepsilon \ll 1$ in the form of equations of continuity and linear momentum conservation:

$$\frac{\partial \rho_s}{\partial t} = -\frac{\partial(\rho_s v_s)}{\partial x},$$

$$\frac{\partial \rho_g}{\partial t} = -\frac{\partial(\rho_g v_g)}{\partial x},$$

$$\frac{\partial(\rho_s v_s)}{\partial t} = -\frac{\partial(\rho_s v_s^2)}{\partial x} - f,$$

$$\frac{\partial(\rho_g v_g)}{\partial t} = -\frac{\partial(p + \rho_g v_g^2)}{\partial x} + f;$$

we also use the heat transfer equations

$$c_{v\infty} \frac{dT_g}{dt} - \frac{T_g}{\rho_g} \frac{d\rho_g}{dt} = \frac{\rho_s m_0}{\rho_g m_{\text{par}}} Q_s - I + v_g f \frac{m_0}{\rho_g},$$

$$c_{\text{par}} \frac{dT_s}{dt} = Q - Q_s - v_s f \frac{m_{\text{par}}}{\rho_s}$$

and the equation of state for the gas

$$p = \frac{\rho_g T_g}{m_0}.$$

Here, the subscripts s and g correspond to the solid and gaseous phases of the mixture; ρ , v , and T are the density, sound velocity, and temperature characterizing

these phases; p is the gas pressure; m_0 is the molecular mass of gas; m_{par} is the particle mass; ρ_{par} is the particle density;

$$f = \frac{\rho_s(v_s - v_g)}{\tau_v}$$

is the volume force applied to the gas from the side of the solid phase;

$$Q_s = \frac{(T_s - T_g)c_{\text{par}}}{\tau_T}$$

is the heat flux from the solid phase to the gaseous one per particle; and τ_v and τ_T are the characteristic times of the dynamic and thermal interactions between the phases. For the Stokes flow conditions in a gas flowing about the solid particles of radius R_{par} , the relaxation times τ_v and τ_T can be expressed through the dynamic viscosity η and the thermal conductivity χ of gas [7]:

$$\tau_v = \frac{m_{\text{par}}}{6\pi R_{\text{par}}\eta}, \quad \tau_T = \frac{m_{\text{par}}c_{p\infty}}{m_0 4\pi R_{\text{par}}\chi}.$$

In normal conditions, for most gases, the following relations are valid:

$$\frac{\tau_T}{\tau_v} = \frac{3\eta c_{p\infty}}{2m_0\chi} \approx 1, \quad \tau_{Tp} = \frac{\rho_g \partial \tau_T}{\tau_T \partial \rho} \approx 0,$$

$$\tau_{TT} = \frac{T_g \partial \tau_T}{\tau_T \partial T_g} \approx -0.5 \dots -1.$$

At other flow conditions, which are not considered in this paper, these quantities may noticeably deviate from the values given above. Other notations in the initial equations are as follows: c_{par} is the specific heat of the solid component, and $c_{v\infty}$ and $c_{p\infty}$ represent the specific heat of the gaseous component at constant volume and at constant pressure. The heat transfer equation and the equation of state for the gas are presented in energy units. The quantities Q and I represent the heat source power and the heat release rate, which provide the constant temperature difference $\Delta T = T_s - T_g$. In our model, we do not take into account the origin of the heat source; it can be the electromagnetic energy absorbed by the solid particles, or the plasma electron energy transferred to the solid particles through collisions, or other. We also neglect the possible dependence of Q and I on the temperature and density of the phases. According to the previous publications [1–3], the inclusion of such a dependence may give rise to additional second viscosity coefficients (both positive and negative).

Applying the linearization and some simple transformations, we reduce the initial system of equations to a single equation

$$\begin{aligned} & \tau_T \tau_v c_{p\infty} \frac{\partial^2 A_\infty}{\partial t^2} + \tau_T c_{pT} \frac{\partial A_T}{\partial t} \\ & + \tau_v c_{pv} \frac{\partial A_v}{\partial t} + c_{p0} A_0 = 0, \end{aligned} \quad (1)$$

where

$$\begin{aligned} A_i &= \frac{\partial^2 v'_g}{\partial x^2} - \frac{1}{u_i^2} \frac{\partial^2 v'_g}{\partial t^2}; \\ u_i^2 &= \frac{c_{pi} T_g}{c_{vi} m_0}, \quad i = \{\infty, T, v, 0\}; \\ c_{pT} &= c_{p\infty}; \quad c_{vT} = (1 + \alpha) c_{v\infty}; \\ c_{pv} &= c_{p\infty} + \alpha v c_{p\infty} [1 + S(\tau_{TT} - \tau_{Tp} - 1)]; \\ c_{vv} &= c_{v\infty} + \alpha v c_{p\infty} (1 + S\tau_{TT}); \\ c_{p0} &= c_{p\infty} + \alpha v c_{p\infty} [1 + S(\tau_{TT} - \tau_{Tp} - \tau_v/\tau_T)]; \\ c_{v0} &= [c_{v\infty} + \alpha v c_{p\infty} (1 + S\tau_{TT})] (1 + \alpha); \\ S &= \Delta T/T_g; \quad v = m_0 c_{\text{par}}/m_{\text{par}} c_{p\infty}; \end{aligned}$$

$\alpha = \rho_s/\rho_g = \varepsilon \rho_{\text{par}}/\rho_g$ is the mass content of the solid phase, and v'_g is the gas velocity disturbance.

At $S = 0$ (an equilibrium suspension), equation (1) coincides with that obtained by Clarke [7].

We consider a disturbance u'_g in the form of a monochromatic plane wave

$$u'_g = \tilde{u}_g e^{ikx - i\omega t}, \quad k = k' + ik''$$

and substitute it into equation (1). As a result, we obtain the dispersion relation

$$\frac{\omega^2}{k^2} = \frac{c_p T_g}{c_v m_0} = \text{Re} + i\text{Im}, \quad (2)$$

where

$$\begin{aligned} c_p &= c_{p0} - i\omega \tau_T c_{pT} - i\omega \tau_v c_{pv} - \omega^2 \tau_T \tau_v c_{p\infty}, \\ c_v &= c_{v0} - i\omega \tau_T c_{vT} - i\omega \tau_v c_{vv} - \omega^2 \tau_T \tau_v c_{v\infty} \end{aligned}$$

are the complex specific heats of the suspension at constant pressure and constant volume, and Re and Im denote the real and imaginary parts of the quantity ω^2/k^2 . Their form is typical of a medium with two relaxation processes [2, 3]. The imaginary part of the wave vector determines the acoustic decrement δ (or increment for $k'' < 0$), and the real part determines the sound velocity $u = \omega/k'$.

In the absence of reciprocal phase transformations, the fairly cumbersome dispersion relation obtained by Nigmatulin [8] for a two-phase equilibrium mixture can be reduced to relation (2). Nigmatulin [8] did not

provide the explicit form of the decrement δ and the sound velocity u because of the cumbersome form of his formulas. Earlier [2, 3] it was shown that, for $k' \gg k''$ and $\text{Re} > 0$, dispersion relation (2) provides relatively simple expressions for the aforementioned quantities:

$$\delta = k'' = \frac{\omega^2 \zeta(\omega)}{2u^3(\omega)\rho_g}, \quad (3)$$

$$u = \frac{\omega}{k'} = \left(\frac{T_g(ab + cd\omega^2\tau_T^2)}{m_0(a^2 + \omega^2\tau_T^2c^2)} \right)^{\frac{1}{2}} = \sqrt{\text{Re}}, \quad (4)$$

where

$$\zeta(\omega) = -\frac{\rho_g}{\omega} \text{Im} \left(\frac{\omega^2}{k^2} \right) = \frac{\tau_T p(ad - bc)}{a^2 + \omega^2\tau_T^2c^2}$$

is the bulk viscosity, $a = c_{v0} - \omega^2\tau_T\tau_v c_{v\infty}$; $b = c_{p0} - \omega^2\tau_T\tau_v c_{p\infty}$; $c = c_{vT} + \tau_v c_{vv}/\tau_T$, and $d = c_{pT} + \tau_v c_{pv}/\tau_T$.

In the high- and low-frequency limits (relative to the relaxation times τ_T and τ_v), the coefficient δ determined by expression (3) can be represented in the form of the superposition of partial coefficients [2]: $\delta_{jk}^T + \delta_{em}^v$ ($\{j, k, l, m\} = \{0, \infty, T, v\}$), where for high frequencies we have

$$\delta_{jk}^i = \delta_{jk}^{i\infty} = \frac{\zeta_{jk}^i c_{vk}^2}{2\tau_i^2 u_j^3 c_{vj}^2 \rho_g}, \quad i = \{T, v\}$$

and for low frequencies

$$\delta_{jk}^i = \delta_{jk}^{i0} = \frac{\zeta_{jk}^i \omega^2}{2u_k^3 \rho_g}.$$

Here,

$$\zeta_{jk}^i = \frac{\tau_i c_{vj}(u_j^2 - u_k^2)\rho_g}{c_{vk}}$$

is the low-frequency bulk viscosity, which has the form similar to that of the bulk viscosity in a medium with a single relaxation process [9]. This quantity may be negative in nonequilibrium media when $c_{pk}/c_{pj} - c_{vk}/c_{vj} > 0$, i.e., in the presence of a positive feedback between the acoustic disturbances and the rate of the heat release from the nonequilibrium excited degrees of freedom [1–3].

We consider four limiting cases.

1. The low-frequency limit $\omega^2\tau_T\tau_v \ll (c_{v0}/c_{v\infty})^2$. Here, the sound velocity is $u = u_0$, and the acoustic decrement has the form

$$\delta_0 = \delta_{T0}^{T0} + \delta_{v0}^{v0} = \frac{\omega^2 \zeta_0}{2u_0^3 \rho_g},$$

where the viscosity coefficient ζ_0 is determined as a sum of the partial low-frequency second viscosity coefficients

$$\zeta_0 = \zeta_{T0}^T + \zeta_{v0}^v,$$

$$\zeta_{T0}^T = \frac{\tau_T c_{vT}(u_T^2 - u_0^2)\rho_g}{c_{v0}}, \quad \zeta_{v0}^v = \frac{\tau_v c_{vv}(u_v^2 - u_0^2)\rho_g}{c_{v0}}.$$

2. The high-frequency limit $\omega^2\tau_T\tau_v \gg (c_{v0}/c_{v\infty})^2$. Here, the sound velocity in the gaseous suspension coincides with the sound velocity in gas $u = u_\infty$, and the decrement has the form

$$\delta_\infty = \delta_{\infty T}^{T\infty} + \delta_{\infty v}^{v\infty} = \frac{1}{2u_\infty^3 c_{v\infty}^2 \rho_g} \left(\frac{\zeta_{\infty T}^T c_{vT}^2}{\tau_T^2} + \frac{\zeta_{\infty v}^v c_{vv}^2}{\tau_v^2} \right),$$

where

$$\zeta_{\infty T}^T = \frac{\tau_T c_{v\infty}(u_\infty^2 - u_T^2)\rho_g}{c_{vT}}, \quad \zeta_{\infty v}^v = \frac{\tau_v c_{v\infty}(u_\infty^2 - u_v^2)\rho_g}{c_{vv}}.$$

3. In the case $\omega\tau_T \ll c_{v0}/c_{vT}$, $\omega\tau_v \gg c_{v0}/c_{vv}$, the sound propagation occurs with the velocity $u = u_v$, and the damping decrement is determined by the expression

$$\delta = \delta_{\infty v}^{T0} + \delta_{v0}^{v\infty} = \frac{\omega^2}{2\rho_g u_v^3} \left(\zeta_{\infty v}^T + \frac{\zeta_{v0}^v c_{v0}^2}{\omega^2 \tau_v^2 c_{vv}} \right),$$

where

$$\zeta_{\infty v}^T = \frac{\tau_T c_{v\infty}(u_\infty^2 - u_v^2)\rho_g}{c_{vv}}.$$

4. In the case $\omega\tau_T \gg c_{v0}/c_{vT}$, $\omega\tau_v \ll c_{v0}/c_{vv}$, the sound propagation velocity is $u = u_T$, and the damping decrement has the form

$$\delta = \delta_{T0}^{T\infty} + \delta_{\infty T}^{v0} = \frac{\omega^2}{2\rho_g u_T^3} \left(\zeta_{\infty T}^v + \frac{\zeta_{v0}^v c_{v0}^2}{\omega^2 \tau_T^2 c_{vT}} \right),$$

where

$$\zeta_{\infty T}^v = \frac{\tau_v c_{v\infty}(u_\infty^2 - u_T^2)\rho_g}{c_{vT}}.$$

For the Stokes conditions of heat transfer in the suspension, we have $\tau_T \sim \tau_v$, and the ‘‘asymmetric’’ limiting cases 3 and 4 are impossible. In the low-frequency limit, we have $\delta_0 \sim \omega^2$, and in the high-frequency limit, the quantity δ_∞ is frequency independent. Such a behavior of $\delta(\omega)$ is characteristic of the sound dispersion in relaxing media. We note that the nonstationary processes of heat transfer between the phases, which are neglected in our consideration, may become significant at high frequencies. According to Nigmatulin [8], these processes lead to an increase in the decrement with increasing frequency in the high-frequency region. Besides, at high frequencies, it is necessary to take into account other mechanisms of sound absorp-

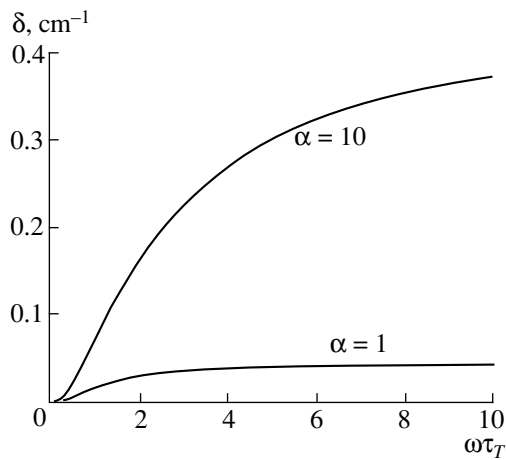


Fig. 1. Frequency dependence of the acoustic decrement in an equilibrium suspension for different mass contents of solid particles.

tion related to the presence of the shear viscosity and heat conduction in the medium.

As an example, we consider the estimates of the decrement, sound velocity, and second viscosity for a

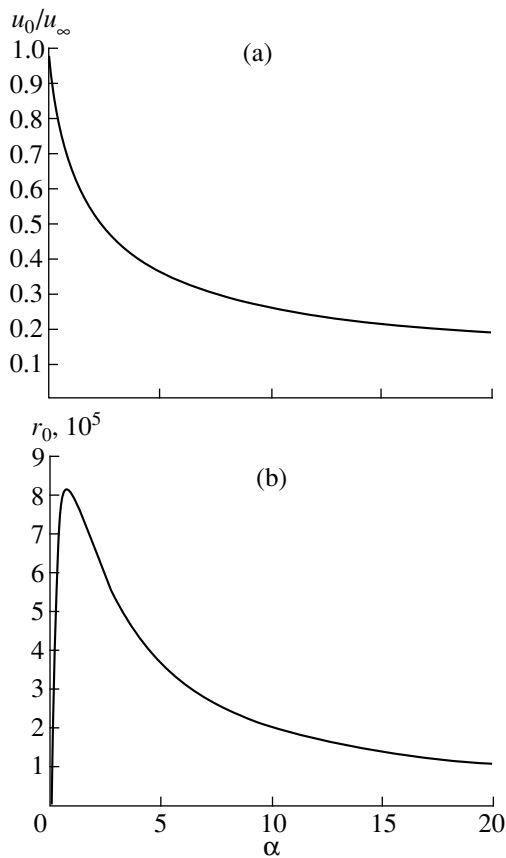


Fig. 2. Dependences of (a) the ratio of the low-frequency and high-frequency sound velocities and (b) the viscosity coefficients on the mass content of particles in an equilibrium suspension.

suspension consisting of steel spherical particles ($R_{\text{par}} = 2 \times 10^{-6}$ m) dispersed in nitrogen at normal conditions. The mass content of particles is assumed to be $\alpha < 60$, which corresponds to their volume content $\varepsilon < 0.01$.

For these conditions, the decrement tends to a constant value δ_{∞} with increasing ω , as is shown in Fig. 1. According to Fig. 2, in an equilibrium suspension at large values of α , the low-frequency sound velocity u_0 is much less than u_{∞} . The ratio $r_0 = \zeta_0/\eta \gg 1$ is reached already at $\alpha \sim 1$. Such large values of the ratio between the bulk and dynamic viscosity coefficients make it necessary to take into account the second viscosity in studying the hydrodynamic stability of flows, including the subsonic ones [10–12]. For coarser suspensions, this ratio may be even greater, because $\tau_T \sim R_{\text{par}}^2$. Evidently, in this case, the low-frequency sound range ($\omega^2 \tau_T \tau_v \ll (c_{v0}/c_{v\infty})^2$) narrows; the high-frequency decrement $\alpha_{\infty} \sim 1/\tau_T$ decreases.

Figure 3 presents the frequency dependences of the dimensionless sound velocity $u(\omega)/u_{\infty}$ and the dimensionless decrement $\bar{\delta}(\omega) = 2\pi k''/k'$ characterizing the attenuation within the wavelength for $\alpha = 1$ and differ-

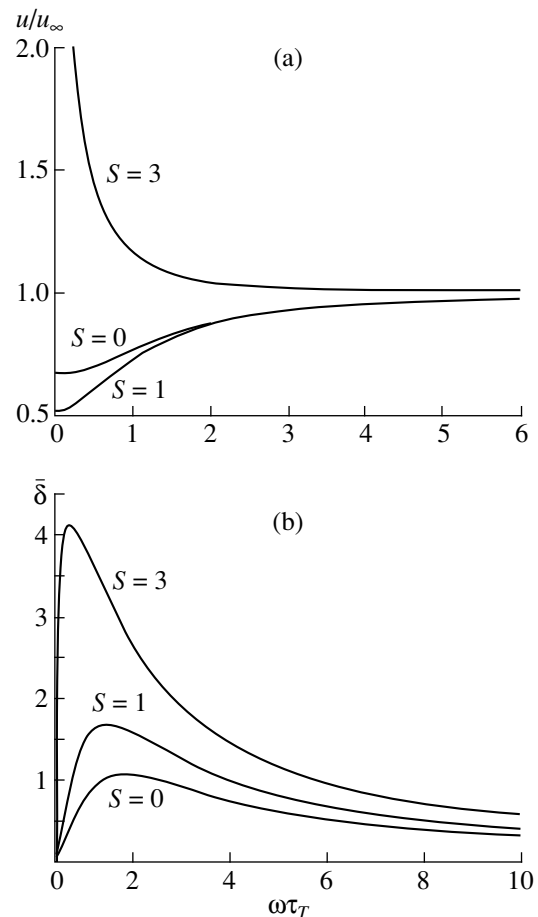


Fig. 3. Frequency dependences of (a) the sound velocity and (b) the dimensionless decrement at $\alpha = 1$.

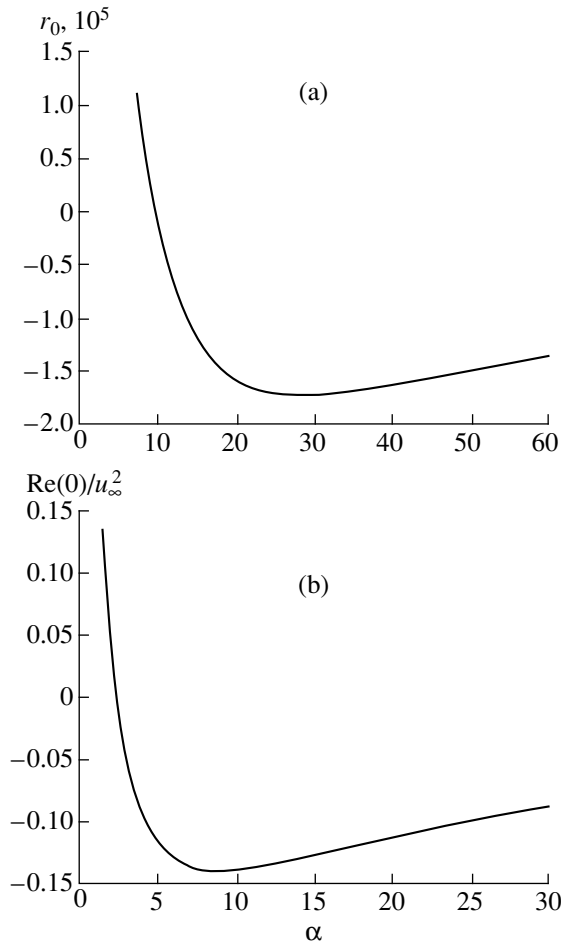


Fig. 4. Dependences of the ratios (a) of the viscosity coefficients and (b) $\text{Re}(0)/u_\infty^2$ on the mass content of particles at $S = 1$.

ent values of S . For large S , the low-frequency sound velocity may exceed the high-frequency one.

Figure 4a shows that the ratio $r_0 = \zeta_0/\eta$ strongly depends on α , and, for α (and S), there exists a range of values within which we have $\zeta_0 < 0$. A negative viscosity leads to $k'' < 0$, i.e., either low-frequency sound is amplified or its propagation is impossible [13]. It can be shown that the amplification of sound corresponds to the conditions $\zeta(\omega) < 0$, $\text{Re}(\omega) > 0$, and the impossibility of sound propagation corresponds to the case $\text{Re}(\omega) < 0$. In the suspension under study, the conditions for the sound amplification cannot be satisfied for any values of S . According to Fig. 4b, the low-frequency viscosity is negative only in the region where the sound propagation is impossible. In addition, from Fig. 5 one can see that the frequency range of negative viscosity is considerably narrower than the frequency range within which $\text{Re}(\omega) < 0$.

Thus, in this paper, we studied the dispersion properties of a suspension of microparticles in gas with the Stokes conditions of interaction between the phases.

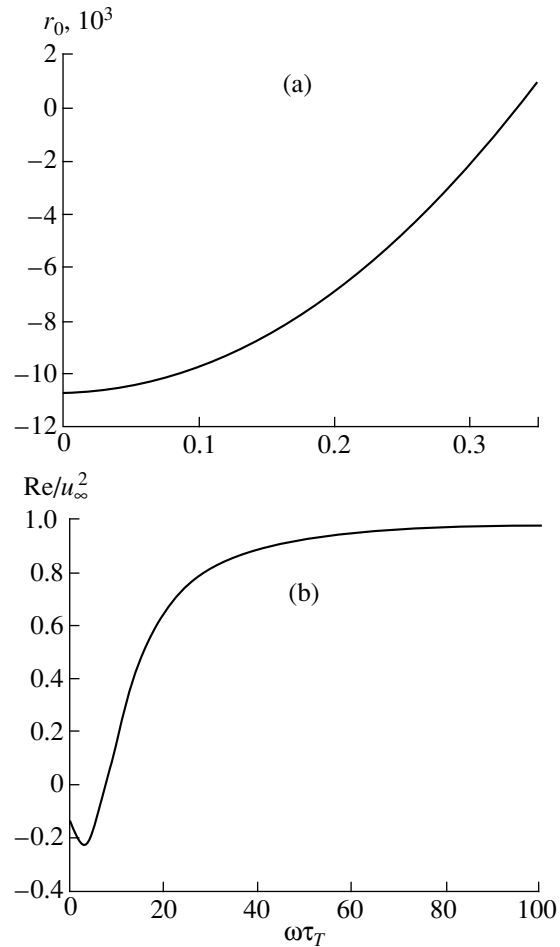


Fig. 5. Frequency dependences of the ratios (a) of the viscosity coefficients and (b) Re/u_∞^2 at $S = 1$, $\alpha = 10$.

We determined the sound velocity and the decrement, as well as the bulk viscosity in the equilibrium and non-equilibrium suspensions. We determined the conditions at which the second viscosity is negative. In closing, we note two facts. First, for other models of phase interactions (and, hence, other dependences $\tau_T(T_g, \rho_g)$, τ_T/τ_v), the existence of conditions corresponding to the sound amplification ($\zeta(\omega) < 0$, $\text{Re}(\omega) > 0$) is possible. Second, whether a suspension of microparticles in gas belongs to the sound amplifying type or to the nontransmitting one, one can expect (by analogy with nonequilibrium media) that the negative second viscosity will considerably affect the conditions of the hydrodynamic stability of flows in a nonequilibrium suspension. These problems require further studies.

REFERENCES

1. N. E. Molevich and A. N. Oraevskii, *Zh. Eksp. Teor. Fiz.* **94**, 128 (1988) [*Sov. Phys. JETP* **67**, 504 (1988)].

2. N. E. Molevich and A. N. Oraevskii, Preprint No. 106, FIAN (Lebedev Institute of Physics, Academy of Sciences of USSR, Moscow, 1990).
3. I. P. Zavershinskiĭ, E. Ya. Kogan, and N. E. Molevich, *Akust. Zh.* **38**, 702 (1992) [*Sov. Phys. Acoust.* **38**, 387 (1992)].
4. N. E. Molevich, *Izv. Ross. Akad. Nauk., Mekh. Zhidk. Gaza*, No. 5, 82 (1999).
5. V. N. Tsytovich, *Usp. Fiz. Nauk* **167**, 57 (1997) [*Phys. Usp.* **40**, 53 (1997)].
6. M. R. Amin, G. E. Morfill, and P. K. Shukla, *Phys. Rev. E* **58**, 6517 (1998).
7. J. F. Clarke, *Ann. Phys. (Paris)* **9**, 211 (1984).
8. R. I. Nigmatulin, *Dynamics of Multiphase Media* (Nauka, Moscow, 1987), Part I.
9. L. D. Landau and E. M. Lifshitz, *Hydrodynamics* (Nauka, Moscow, 1986).
10. G. Emanuel, *Phys. Fluids A* **2**, 2252 (1990).
11. E. Ya. Kogan and N. E. Molevich, *Akust. Zh.* **41**, 613 (1995) [*Acoust. Phys.* **41**, 538 (1995)].
12. O. A. Nerushev and S. A. Novopashin, in *Proceedings of the 4th Siberian Seminar "Stability of Flows of Homogeneous and Heterogeneous Liquids," Novosibirsk, 1997*, pp. 76–77.
13. E. M. Lifshitz and L. P. Pitaevskii, *Physical Kinetics* (Nauka, Moscow, 1979; Pergamon Press, Oxford, 1981).

Translated by E. Golyamina

Rayleigh's Flow near a Boundary between Two Liquids

V. A. Murga

St. Petersburg State Marine Technical University,
ul. Lotsmanskaya 3, St. Petersburg, 190008 Russia
e-mail: rec@mtu-rec.spb.su

Received May 18, 1998

Abstract—The problem of a stationary acoustic flow that occurs in a standing wave field formed by two travelling monochromatic plane waves incident on a plane boundary between two liquids is solved theoretically. It is shown that the flow formed in such conditions noticeably differs from the known Rayleigh's flow that occurs near a rigid plane. © 2000 MAIK "Nauka/Interperiodica".

A stationary flow that occurs in a sound field near a solid body is determined by the viscosity of liquid and the condition that, at the surface of the body, the velocity of the particles of liquid is equal to zero. Such flows represent second-order effects with respect to the acoustic Mach number. In particular, Rayleigh's flow occurs in the field of a standing sound wave in a planar channel [1] or near a single rigid plane. This paper studies Rayleigh's flow in a more general case of two arbitrary liquids with a plane boundary between them. The standing wave field is formed as a sum of the fields produced by two travelling plane harmonic waves propagating in one of these liquids. Considering this wave field, it is necessary to take into account the reflection and refraction of waves at the boundary between two dissipative media. For each of the two media, the solution of the problem depends on the parameter

$$\varepsilon = k_0(\nu/\omega)^{1/2} = k_0\delta/\sqrt{2} \ll 1,$$

where $k_0 = \omega/c$, ω is the angular frequency, c is the sound velocity, ν is the kinematic viscosity coefficient, and $\delta = (2\nu/\omega)^{1/2}$ is the thickness of the acoustic boundary layer. The heat conductivity of liquids is neglected for the sake of brevity. Let the unperturbed boundary between the two media be a horizontal plane, where the y axis is directed upwards, the surface $y = 0$ coincides with the boundary between the liquids, the x axis is directed along the boundary, and the process does not depend on the z coordinate. In the upper liquid, two identical plane waves propagate in the xy plane, and the incidence of these waves on the boundary between the liquids is symmetric about the y axis, i.e., if the phase factor of one wave is $\exp[i(kx - \gamma y)]$, the phase factor of the other wave will be $\exp[i(-kx - \gamma y)]$. Here, $k^2 + \gamma^2 = k_0^2$, and k and γ are positive real numbers related to the angle of incidence of the wave by the formulas $k =$

$k_0 \sin \theta$ and $\gamma = k_0 \cos \theta$; from here on, the time factor $\exp(-i\omega t)$ is omitted.

In the first-order (acoustical) approximation, the problem of the transmission of a single wave through the boundary between two liquids was solved by Savel'ev [2] with allowance for the viscosity (and heat conduction) for small grazing angles. One can easily generalize the solution to arbitrary angles. Then, in order to obtain a standing wave along the x axis, one should combine two solutions that correspond to the two aforementioned waves. The resulting oscillatory particle velocity fields that are formed in the two media will be described by the expressions:

$$u_1 = (e^{-i\gamma y} + Ae^{i\gamma y}) \cos kx,$$

$$v_1 = (Ae^{i\gamma y} - e^{-i\gamma y}) \frac{\gamma i}{k} \sin kx,$$

$$u_2 = Be^{i\sigma y} \cos kx, \quad v_2 = -\frac{Bki}{\sigma} e^{i\sigma y} \sin kx, \quad (1)$$

$$u'_1 = De^{-i\gamma' y} \cos kx, \quad v'_1 = -D \frac{\gamma' i}{k} e^{-i\gamma' y} \sin kx,$$

$$u'_2 = Ce^{i\sigma' y} \cos kx, \quad v'_2 = -\frac{Cki}{\sigma'} e^{i\sigma' y} \sin kx.$$

Here, the quantities marked with the primes refer to the lower liquid ($y < 0$). The oscillatory particle velocity vector \mathbf{v} in liquid is represented by the sum of the potential \mathbf{v}_1 and solenoidal \mathbf{v}_2 components; $u = u_1 + u_2$ and $v = v_1 + v_2$ are the projections of the vector \mathbf{v} on the x and y axes, respectively. The above expressions take into account that $k = k'$; $\gamma'^2 + k'^2 = k_0'^2$, where γ' can be either a positive real quantity or an imaginary one (for angles of incidence exceeding the critical angle); and $\sigma^2 = i\omega/\nu$, where the imaginary part of σ is positive in the upper liquid and negative in the lower one. It is

evident that $k_0/|\sigma| \sim \varepsilon$. In each of the incident waves, the amplitude of the longitudinal (along the x axis) component of the liquid particle velocity is taken to be equal to unity. The quantities A and D are the reflection and transmission coefficients, respectively; the expressions for them and the constants B and C have the form

$$\begin{aligned} A &= \frac{1 - \gamma' \rho / \gamma \rho' - M}{1 + \gamma' \rho / \gamma \rho' + M}, \quad D = \frac{2\rho/\rho'}{1 + \gamma' \rho / \gamma \rho' + M}, \\ M &= \frac{k^2(1 - \rho/\rho')^2}{\gamma \sigma \left(1 + \frac{\rho}{\rho'} \sqrt{\frac{v}{v'}}\right)}, \\ B &= \frac{2(\rho/\rho' - 1)}{(1 + \gamma' \rho / \gamma \rho' + M) \left(1 + \frac{\rho}{\rho'} \sqrt{\frac{v}{v'}}\right)}, \\ C &= \frac{2(1 - \rho/\rho')}{(1 + \gamma' \rho / \gamma \rho' + M) \left(1 + \frac{\rho'}{\rho} \sqrt{\frac{v'}{v}}\right)}, \end{aligned} \quad (2)$$

where ρ is the unperturbed density of liquid.

In the second-order approximation (quadratic in the oscillation amplitude), it is necessary to take into account both the motion and the curvilinearity of the x , y coordinate system, because the surface $y = 0$ coincides with the oscillating boundary between the media. To write the equations and the boundary conditions for the absolute motion of liquid in the moving coordinate system, we introduce an auxiliary fixed Cartesian coordinate system X , Y (where the plane $Y = 0$ coincides with the unperturbed boundary between the media). The x , y and X , Y coordinates are related as follows:

$$x = \int_0^x \sqrt{1 + (\partial \xi / \partial X)^2} dX \approx X, \quad y = Y - \xi,$$

where $\xi(X, t)$ is the deviation of a boundary element from the plane $Y = 0$. Hence it follows that the time derivative $\partial/\partial t$ taken in the fixed coordinate system should be replaced by the operator $\partial/\partial t - v_0 \partial/\partial y$ in the moving coordinate system ($v_0(x, y) = \partial \xi / \partial t$). In addition, we have

$$\begin{aligned} \frac{\partial}{\partial X} &= \frac{\partial}{\partial x} - \frac{\partial \xi}{\partial x} \frac{\partial}{\partial y}, \quad \frac{\partial}{\partial Y} = \frac{\partial}{\partial y}, \\ a_x &= a_x, \quad a_y = a_y + a_x \frac{\partial \xi}{\partial x}, \end{aligned} \quad (3)$$

where \mathbf{a} is an arbitrary vector, and the subscript y indicates its projections on the y -axis of the corresponding coordinate system. It should be noted that the x -axis is not a straight line, and the components of the vector \mathbf{a} in the moving coordinate system are oblique projections of this vector on the y -axis and the tangent to the x -axis, because the x , y coordinate system is not an orthogonal one. Below, we present some differential

relationships expressed in the moving coordinate system and obtained from the corresponding expressions given in the Cartesian system by using formulas (3):

$$\begin{aligned} (\nabla \times \mathbf{a})_z &= \frac{\partial a_y}{\partial x} - \frac{\partial a_x}{\partial y} + \frac{\partial \xi}{\partial x} \left(\frac{\partial a_x}{\partial x} - \frac{\partial a_y}{\partial y} \right) + a_x \frac{\partial^2 \xi}{\partial x^2}, \\ \nabla^2 f &= \frac{\partial^2 f}{\partial x^2} + \frac{\partial^2 f}{\partial y^2} - 2 \frac{\partial \xi}{\partial x} \frac{\partial^2 f}{\partial x \partial y} - \frac{\partial^2 \xi}{\partial x^2} \frac{\partial f}{\partial y}, \\ \nabla \cdot \mathbf{a} &= \frac{\partial a_x}{\partial x} + \frac{\partial a_y}{\partial y}. \end{aligned} \quad (4)$$

In the second-order approximation, the derivation of the equations for a stationary flow in the moving coordinate system is similar to that in a fixed coordinate system [3]. Then, for each of the two liquids, we obtain

$$\begin{aligned} &\langle \boldsymbol{\Omega}(\nabla \cdot \mathbf{v}) - \mathbf{v} \times \nabla(\nabla \cdot \mathbf{v}) + \nabla \times [\boldsymbol{\Omega} \times (\mathbf{v} - \mathbf{v}_0)] \rangle \\ &= \mathbf{v} \left(\frac{\partial^2}{\partial x^2} + \frac{\partial^2}{\partial y^2} \right) (\nabla \times \mathbf{V}) + \mathbf{v} \langle \nabla^2 (\nabla \times \mathbf{v}) \rangle, \end{aligned} \quad (5)$$

$$\nabla \cdot \left[\mathbf{V} + \left\langle \frac{\rho_1}{\rho} (\mathbf{v} - \mathbf{v}_0) \right\rangle \right] = 0,$$

where \mathbf{V} is the time-average velocity of liquid particles at a fixed point of space in the given coordinate system (the Euler velocity), the angular brackets denote the averaging over time, ρ_1 is the acoustic density, \mathbf{v} is the particle velocity (real) in the first-order approximation (the complex amplitudes of the components of this vector are given by expressions (1)), the vector \mathbf{v}_0 is parallel to the y axis, and $\boldsymbol{\Omega} = \nabla \times \mathbf{v}$. The terms containing the factor \mathbf{v}_0 in the system of equations (5), as well as the second term on the right-hand side of the first equation of this system, are caused by the motion and the deformation of the boundary between the media. The aforementioned term of the first equation is much less than the left-hand member of this equation, provided that the limiting case $\rho/\rho' \gg 1$ is excluded from the consideration. To prove this statement, we use relations (4) and obtain the expression

$$\begin{aligned} &\mathbf{v} \langle \nabla^2 (\nabla \times \mathbf{v}) \rangle_z \\ &= \mathbf{v} \left\langle 4 \frac{\partial \xi}{\partial x} \frac{\partial^3 u_2}{\partial x \partial x \partial y^2} + 2 \frac{\partial^2 \xi}{\partial x^2} \frac{\partial^2 u_2}{\partial y^2} \right\rangle. \end{aligned}$$

In order of magnitude, this expression is equal to $\sim k^2 v_0 u_2$, whereas the left-hand member of the equation in question is equal to $\sim k^2 u u_2 / \varepsilon$. The comparison of these two expressions shows that the former is an order of magnitude (in terms of ε) greater than the latter, provided that $u \sim v_0$. The equality fails when $u \ll v_0$. From formulas (1) and (2), it follows that the equality can hold only in the upper liquid on condition that $\rho/\rho' \gg 1$.

From the second equation of system (5), it follows that the vector

$$\mathbf{U} = \mathbf{V} + \left\langle \frac{\rho_1}{\rho} (\mathbf{v} - \mathbf{v}_0) \right\rangle \quad (6)$$

is related to the mass transfer and, therefore, is equal to the average velocity of a given particle (the Lagrange velocity); it is this quantity that is usually observed in experiments. Eliminating the quantity ρ_1 by applying the continuity equation in the first-order approximation, we recast expression (6) to the form

$$\mathbf{U} = \mathbf{V} + \frac{i}{2\omega} (\mathbf{v} - \mathbf{v}_0) \operatorname{div} \mathbf{v}^*. \quad (7)$$

Here, we use the complex amplitudes of the oscillatory particle velocity of the medium and of the boundary between the media (the asterisk denotes complex conjugation). Only the real part of expression (7) has a physical meaning. We introduce the stream function Ψ in such a way that

$$U_x = \frac{\partial \Psi}{\partial y}, \quad U_y = -\frac{\partial \Psi}{\partial x}, \quad (8)$$

where U_x and U_y are the components of the vector U . Finally, we assume that the angle of the wave incidence on the boundary is not too small, so that, in order of magnitude, we obtain $k \sim k_0$. Taking into account everything mentioned above and excluding the case $\rho/\rho' \gg 1$ from our consideration, we obtain a single equation for the stream function (for each of the two media) instead of equations (5):

$$\begin{aligned} \nabla^4 \Psi &= \frac{1}{2v} \left[u \frac{\partial^2 u_2^*}{\partial x \partial y} + (v - v_0) \frac{\partial^2 u_2^*}{\partial y^2} \right] \\ &+ \left(\frac{1}{v} \frac{\partial u_2^*}{\partial y} - \frac{i}{2\omega} \frac{\partial^3 u_2^*}{\partial y^3} \right) \operatorname{div} \mathbf{v}, \quad (9) \\ \nabla^4 &= \left(\frac{\partial^2}{\partial x^2} + \frac{\partial^2}{\partial y^2} \right)^2. \end{aligned}$$

The right-hand member of this equation is expressed through the complex amplitudes (1), and only the real part of the expression has a physical meaning.

Let us consider the conditions at the boundary between the media. The kinematic condition expressed in Cartesian coordinates has the form

$$\frac{\partial \xi}{\partial t} + w_x \frac{\partial \xi}{\partial X} = w_Y \quad (Y = \xi).$$

Here, \mathbf{w} is the liquid particle velocity vector, which includes the stationary and the oscillatory components.

Using relations (3), we represent this expression in the x, y coordinates:

$$\frac{\partial \xi}{\partial t} = w_y \quad (y = 0).$$

By averaging the latter expression over time and assuming that the time-average position of the boundary is constant (i.e., $\langle \partial \xi / \partial t \rangle = 0$), we obtain $\langle w_y \rangle = V_y = 0$. Then, we use the condition of the equality of tangential forces acting on a unit area of the boundary from the side of both liquids. It can be shown that, in the x, y coordinates, the average tangential force is given by the expression

$$v\rho \left[\frac{\partial V_y}{\partial x} + \frac{\partial V_x}{\partial y} + \left\langle u \frac{\partial^2 \xi}{\partial x^2} - \frac{\partial \xi}{\partial x} \left(\frac{\partial u}{\partial x} - \frac{\partial v}{\partial y} \right) \right\rangle \right].$$

We assume that, in this expression, the nonlinear terms can be neglected in comparison with the linear ones. An additional check shows that this assumption is valid for any two liquids excluding the case $\rho/\rho' \gg 1$ (this case was already excluded from our consideration). By adding the equality condition for the tangential components of the average velocity \mathbf{V} of two liquids at the boundary, we finally obtain the boundary conditions (at $y = 0$):

$$\begin{aligned} V_x &= V'_x, \quad V_y = 0, \quad V'_y = 0, \\ v\rho \left(\frac{\partial V_y}{\partial x} + \frac{\partial V_x}{\partial y} \right) &= v'\rho' \left(\frac{\partial V'_y}{\partial x} + \frac{\partial V'_x}{\partial y} \right). \quad (10) \end{aligned}$$

The calculation of the right-hand member of equation (9) yields the equation

$$\begin{aligned} \nabla^4 \Psi &= f(y) \sin 2kx, \\ f(y) &= \frac{B^* k i \sigma^*}{4v} e^{-i\sigma^* y} \left\{ (1 + A) \left(4 + 3 \frac{\gamma^2}{k^2} \right) \right. \\ &\left. + B[(1 - i)e^{i\sigma y} + i] + \frac{\gamma \sigma^*}{k^2} [e^{-i\gamma y} - 1 + A(1 - e^{i\gamma y})] \right\} \quad (11) \end{aligned}$$

for the upper liquid. For the lower liquid, the function $f'(y)$ has a similar form with the following changes being introduced in expression (11): $A = 0$, B should be replaced by C , $(1 \pm A)$ should be replaced by D , and $\exp(-i\gamma y)$ should be replaced by $D \exp(-i\gamma' y)$. These changes of constants can be inferred from formulas (1) by comparing the homogeneous equations for the upper and lower liquids. From expression (7), for the upper medium we obtain:

$$U_x = V_x + \frac{ikB^*}{4\omega} (1 + A) \left(1 + \frac{\gamma^2}{k^2} \right) e^{-i\sigma^* y} \sin 2kx. \quad (12)$$

A similar expression can be obtained for the lower medium. From expression (12), it follows that $U_x = V_x$

outside the acoustic boundary layer ($|\sigma y| \gg 1$) and also at $y = 0$ (in the latter case, the term added to V_x on the right-hand side of (12) is purely imaginary, and, therefore, it should be discarded). The particular solution to equation (11) has the form $\varphi(y)\sin 2kx$, where $\varphi(y)$ is calculated by the fourfold integration of the function $f(y)$ with respect to y . The solution to the homogeneous (biharmonic) equation for the stream function should have the form $\Phi(y)\sin 2kx$, where the function Φ is determined by the equation

$$\Phi^{(4)} - 8k^2\Phi^{(2)} + 16k^4\Phi = 0$$

(the numbers in parentheses indicate the order of the derivative with respect to y). The solution to this equation for both media has the form

$$\Phi = e^{-2ky}(N + Py), \quad \Phi' = e^{2ky}(N' + P'y), \quad (13)$$

where N , P , N' , and P' are unknown constants. The complete solution to equation (11) is represented by the formula

$$\Psi = (\Phi + \varphi)\sin 2kx. \quad (14)$$

Substituting expression (14) in boundary conditions (10) and using relations (7), (8), (12), and (13), we derive the expressions for the sought-for constants:

$$\begin{aligned} N &= \frac{B^*k\delta}{8\omega} \left[(1+A) \left(4 - \frac{\gamma^2}{k^2} \right) - \frac{3}{2}B \right] \\ P &= \frac{BB^*}{16\omega\delta \left(1 + \frac{\rho v}{\rho'v'} \right)} \left[6k\delta - \frac{\rho v}{\rho'v'} \left(1 + \frac{\rho}{\rho'} \sqrt{\frac{v}{v'}} \right) \right], \\ N' &= \frac{C^*k\delta'}{8\omega} \left[D \left(4 - \frac{\gamma'^2}{k'^2} \right) - \frac{3}{2}C \right], \end{aligned} \quad (15)$$

$$P' = \frac{CC^*}{16\omega\delta' \left(1 + \frac{\rho'v'}{\rho v} \right)} \left[6k\delta' - \frac{\rho'v'}{\rho v} \left(1 + \frac{\rho'}{\rho} \sqrt{\frac{v'}{v}} \right) \right]$$

(here, we take into account the relation $\sigma = (1 + i)/\delta$). The expressions for the components of the average velocity vector \mathbf{U} in the upper liquid have the form

$$U_x = \left[e^{-2ky} P(1 - 2ky) + \frac{d\varphi}{dy} \right] \sin 2kx, \quad (16)$$

$$U_y = -[e^{-2ky} P(N + Py) + \varphi] 2k \cos 2kx.$$

For the lower liquid, we have to replace the minus sign before ky by the plus sign (see (13)). Formulas (16) and (15) represent the solution to the problem under study. Let us consider some particular cases.

In the limiting case $\rho/\rho' \rightarrow 0$, from expressions (15) we obtain (see also (2)):

$$P = \frac{3k}{8\omega} BB^*, \quad P' = -\frac{CC^*}{16\omega\delta'} \frac{\rho'}{\rho} \sqrt{\frac{v'}{v}} = 0. \quad (17)$$

In the lower medium the flow is absent (as one would expect). In the upper medium, according to expressions (16) and (17), the average velocity at the boundary of the acoustic layer ($|\sigma y| \gg 1$, $|ky| \ll 1$) is determined by the formula

$$U_x = P \sin 2kx = \frac{3k}{8\omega} |1 + A|^2 \sin 2kx, \quad (18)$$

because, in this case, $B = -(1 + A)$. However, $|1 + A|^2$ is the squared amplitude of the longitudinal oscillatory particle velocity in the resulting sound field formed in the upper medium. Thus, formula (18) coincides with Rayleigh's result [1]. In the other limiting case $\rho/\rho' \rightarrow \infty$, we have

$$\begin{aligned} P &= -\frac{BB^*}{16\omega\delta'} \frac{\rho}{\rho'} \sqrt{\frac{v}{v'}} = 0, \\ P' &= \frac{3k}{8\omega} CC^* = \frac{3k}{8\omega} DD^*. \end{aligned} \quad (19)$$

In the lower liquid, we obtain Rayleigh's solution as before, the quantity DD^* being the squared amplitude of the longitudinal oscillatory particle velocity in the lower medium. In the upper medium, according to expression (19), the flow must be absent. However, the case $\rho/\rho' \rightarrow \infty$ has been excluded from our consideration. In reality, one should expect the appearance of a weak flow in the upper liquid, and the velocity of this flow should be an order of magnitude less (in terms of ε) than the velocity of Rayleigh's flow near a rigid plane.

In the intermediate case determined by the condition

$$\frac{1}{\varepsilon} \gg \frac{\rho}{\rho'} \gg \varepsilon \quad (20)$$

for simplicity we assume that $v/v' \sim 1$, and, from (15) we obtain

$$\begin{aligned} P = P' &= -\frac{BB^* \left(1 + \frac{\rho}{\rho'} \sqrt{\frac{v}{v'}} \right)}{16\omega\delta' \left(1 + \frac{\rho'v'}{\rho v} \right)} \\ &= -\frac{CC^* \left(1 + \frac{\rho'}{\rho} \sqrt{\frac{v'}{v}} \right)}{16\omega\delta' \left(1 + \frac{\rho v}{\rho'v'} \right)}. \end{aligned} \quad (21)$$

Expression (21) can be represented in the form

$$P = P' = -\frac{u_0^2}{16\omega\delta} \frac{\left(1 - \frac{\rho}{\rho'}\right)^2}{\left(1 + \frac{\rho'v'}{\rho v}\right)\left(1 + \frac{\rho}{\rho'}\sqrt{\frac{v}{v'}}\right)}, \quad (22)$$

where $u_0^2 = |1 + A|^2$. In this case, in formulas (16), one should neglect the particular solution ϕ , the derivative $d\phi/dy$, and the constant N . Then, the velocity field of a stationary flow is described by the expressions

$$\begin{aligned} U_x &= Pe^{-2ky}(1 - 2ky)\sin 2kx, \\ U_y &= -Pe^{-2ky}2ky\cos 2kx, \\ U'_x &= Pe^{2ky}(1 + 2ky)\sin 2kx, \\ U'_y &= -Pe^{2ky}2ky\cos 2kx. \end{aligned} \quad (23)$$

In both liquids, the flow patterns are identical and symmetric with respect to the boundary between the liquids. The maximal flow velocity is achieved at the boundary, and it is determined by the formula

$$U_0 = P\sin 2kx. \quad (24)$$

The comparison of formulas (24) and (22) with expression (18) shows that, in this case, the flow velocity exceeds the velocity of Rayleigh's flow that occurs near a rigid plane by a factor of ε^{-1} . Besides, in contrast to Rayleigh's flow with its complex structure (small-scale and large-scale vortices), the flow considered in this paper consists of only large-scale vortices with the characteristic size k^{-1} .

Solution (23) retains its form in the Cartesian coordinate system. The coordinates x, y in expressions (23) determine the liquid particle position averaged over several periods of oscillation; these coordinates approximately coincide with the average coordinates X, Y of the same particle. According to relations (3), we have $U_X = U_x, U_Y = U_y + \langle u\partial\xi/\partial x \rangle$. As one can see from

formulas (22) and (23), the second term on the right-hand side of the expression for U_Y is an order of magnitude less (in terms of ε) than the first term; hence, in the approximation under study, it can be neglected.

Thus, the deformation of the boundary between two liquids does not affect the solution of the problem in the first-order approximation.

In closing, we note that the solution presented above is valid as long as the initial equations (5) are valid. The method of successive approximations used in the derivation of these equations implies a small value of the average velocity of liquid particles as compared to the oscillatory particle velocity; i.e., we should have (see (22))

$$Ma < \varepsilon, \quad (25)$$

where Ma is the acoustic Mach number. In addition, the Reynolds number Re for a stationary flow must be much less than unity, because equations (5) do not take into account the nonlinear terms (quadratic in the average velocity). Therefore, the following condition must be satisfied:

$$Re = \frac{U}{\nu k_0} \sim \frac{Ma^2}{\varepsilon^3} < 1. \quad (26)$$

The latter condition imposes a stronger limitation on the allowable intensity of acoustic field (the acoustic Mach number) than condition (25). Thus, solution (22), (23) is valid when conditions (20) and (26) are met.

REFERENCES

1. J. W. Strutt (Lord Rayleigh), *The Theory of Sound* (Macmillan, London, 1896, 2nd ed.; Gostekhizdat, Moscow, 1955), Vol. 2.
2. A. Ya. Savel'ev, *Akust. Zh.* **19**, 231 (1973) [*Sov. Phys. Acoust.* **19**, 154 (1973)].
3. L. K. Zarembo and V. A. Krasil'nikov, *Introduction to Nonlinear Acoustics* (Nauka, Moscow, 1966).

Translated by E. Golyamina

Acoustic Field of a Point Source in Water with Air Bubbles

G. A. Postnov

Shirshov Institute of Oceanology, Russian Academy of Sciences,
Nakhimovskii pr. 36, Moscow, 117851 Russia

e-mail: nosoff@chip.sio.rssi.ru

Received September 15, 1998

Abstract—A model problem of sound wave propagation from a point source located in water at the center of a spherical bubble cloud is solved. The resulting dependences of wave attenuation on the sound frequency and bubble concentration are compared with those obtained in the approximation of a quasi-homogeneous medium. The validity limits of this approximation are determined. © 2000 MAIK “Nauka/Interperiodica”.

The literature on sound propagation in water with air bubbles is quite extensive. Clay and Medwin [1] considered the propagation of sound in an unbounded medium. Zhen (see, for example, [2]) considered the features of sound propagation in sea water where air bubbles are mainly located near the sea surface. Dean [3] analyzed the sound propagation in a spherical cloud of air bubbles generated by breaking waves. As a rule, the contribution of bubbles to sound propagation is described with the use of the effective complex wave number k . For low bubble concentrations, the wave number is calculated in the single-scattering approximation. For moderate concentrations when

$$\langle r \rangle \ll \lambda, \quad (1)$$

where $\langle r \rangle$ is the mean distance between bubbles and λ is the sound wavelength in the medium, the wave number k is calculated in the approximation of a quasi-homogeneous continuous medium [4]. However, for high bubble concentrations typical of, say, breaking wind waves in the ocean [5], the sound wavelength λ depends on the bubble concentration, which makes it difficult to *a priori* estimate the validity of the quasi-homogeneous approximation (QHA).

The aim of this paper is to estimate the applicability limits of the QHA by comparing the results of the field calculations performed by two methods for a model problem of a point source located at the center of a spherical cloud of air bubbles. The calculations were first carried out on the basis of the QHA and then with allowance for multiple scattering from the bubbles. Our aim is to also obtain an alternative approximate estimate of sound wave attenuation in water with a high bubble concentration.

Assume that all bubbles are spherical in shape and their distribution in size has the form $n(a)$, where a is

the bubble radius. The bubble concentration is described by the parameter V , which is the fraction of the medium volume occupied by bubbles:

$$V = 4\pi/3 \int_0^{\infty} a^3 n(a) da. \quad (2)$$

The wave number k used in the QHA is expressed in terms of the complex sound velocity in water with bubbles, c , by the formula $k = 2\pi f/c$, where f is the frequency of the emitted field. To determine the sound velocity c , we use the known formula $c = (\bar{\rho} K)^{-1/2}$ [1], where $\bar{\rho}$ is the water density and K is the compressibility of water with bubbles. According to [4], we have $\bar{\rho} = (1 - V)\rho_0 + V\rho'$. According to [1], the compressibility K can be represented as $K = \frac{1 - V}{\rho_0 c_0^2} + K'$, where ρ_0 and ρ' are the densities of water and air, respectively; c_0 is the sound velocity in water without bubbles; and K' is the complex additional term caused by the presence of bubbles. Since $\rho' \ll \rho_0$, we can set $\bar{\rho} \approx (1 - V)\rho_0$. Calculating the quantity K' in the same way as in [1], we obtain the following relation for a bubble ensemble described by the distribution $n(a)$:

$$\frac{1}{c} = \left[\frac{(1 - V)^2}{c_0^2} + \frac{1 - V}{\pi f^2} \int_0^{\infty} \frac{an(a) da}{D - i\delta} \right]^{1/2}, \quad (3)$$

where $D = (f_0/f)^2 - 1$, f_0 and δ are the frequency and the attenuation constant of the fundamental radial oscillations of a bubble of radius a . This expression coincides

with that of presented in [4] for $V \ll 1$. Denoting the imaginary part of k by β , we obtain

$$\beta = \sqrt{2\pi}f/c_0[(N^2 + M^2)^{1/2} - N]^{1/2}$$

$$N = (1 - V)^2 + \frac{(1 - V)c_0^2 J r}{\pi f^2},$$

$$M = \frac{(1 - V)c_0^2 J i}{\pi f^2},$$

$$J r = \int_0^\infty \frac{D n a d a}{D^2 + \delta^2}, \quad J i = \int_0^\infty \frac{\delta n a d a}{D^2 + \delta^2}.$$

The expressions for f_0 and δ are presented in [1]. It can be shown that for bubbles at a small depth, $f_0 \approx (300a)^{-1}$ and $\delta \approx 0.014(1 + f_0^{1/2})$, where f_0 is expressed in kilohertz and a in meters.

It is clear that for large values of V , formula (3) is not valid, since it was derived by replacing the instantaneous values of ρ by the time-average ones, which is admissible only for $V \ll 1$. Another restriction on the applicability of formula (3) provides condition (1). Let us estimate the form of the dependence of $\langle r \rangle$ and λ on V . For an arbitrary frequency, this estimate is very cumbersome. It has the most simple form for low frequencies, when the sound velocity in water with bubbles has the form $\text{Re } c = c_0 \left(1 + \frac{1.4\rho_0 c_0^2}{p_0}\right)^{-1/2}$, where p_0

is the hydrostatic pressure [4]. On the other hand, we have $\langle r \rangle \sim \langle a \rangle V^{-1/3}$ and $\langle a \rangle = \int_0^\infty a n(a) da$. Taking into account that $\lambda = \text{Re } c/f$ and substituting these estimates in (1), we obtain the condition of the applicability of the QHA:

$$V^{1/3} \left(1 + \frac{1.4c_0^2 \rho_0 V}{p_0}\right)^{-1/2} \gg \langle a \rangle f/c_0. \tag{5}$$

It is evident that this condition is violated for $V \rightarrow 0$. However, as V increases, the left-hand side of this inequality reaches its maximum and then decreases. Therefore, for some conditions, inequality (1) is no longer valid for large values of V as well. More detailed estimates of the validity of the QHA, in particular, in the presence of the resonance bubbles, can be obtained by comparing the QHA with the exact solution to the problem of wave propagation in water with bubbles.

Consider a model problem of the field of a monochromatic point source located at the center of a spherical homogeneous cloud of air bubbles of radius R . The Green's function of such a source is described by the Dyson equation [6]. To find closed expressions for the mean field and the total intensity, it is necessary to make a number of simplifications. We will use the Twersky equations [7] based on the assumption that the

main contribution to the field (intensity) is provided by single scattering over the paths passing through each bubble.

We start with considering the simplest bubble cloud model in the form of a sphere of radius R filled with passive bubbles whose mean concentration is constant inside the cloud and the density distribution of their radii a is described by the function $n(a)$. Assume that a source of the acoustic field of frequency f is located at the center of the cloud, and the emitted field has the form $p_0(r) = \exp(ik_0 r)/r$, where r is the distance from the cloud center and $k_0 = 2\pi f/c_0$.

The scattered field averaged over an ensemble of bubbles (the coherent field) at the distance r from the cloud center is described by the equation

$$p(r) = p_0(r) + 2\pi \int_0^R \int_0^1 \int_{-1}^1 p(r') r'^2 \sigma \frac{\exp(ik_0 \rho)}{\rho} n(a) da dr' dy. \tag{6}$$

Here, σ is the scattering amplitude of a passive bubble of radius a , $\rho = (r^2 + r'^2 - 2rr'y)^{1/2}$, and y is the cosine of the angle between the vectors \mathbf{r} and \mathbf{r}' . Since, according to [1], $\sigma = a/L$ and $L = D - i\delta$, we obtain

$$p(r) = p_0(r) + 2\pi J_0 \int_0^R \int_{-1}^1 p(r') r'^2 \frac{\exp(ik_0 \rho)}{\rho} dr' dy, \tag{7}$$

where $J_0 = J r + iJ i$.

The integration with respect to y yields

$$p(r) = p_0(r) + M \left[\int_0^r p(r') \frac{r'}{r} \exp(ik_0 r) \sin k_0 r' dr' + \int_r^R p(r') \frac{r'}{r} \exp(ik_0 r') \sin k_0 r dr' \right], \tag{8}$$

where $M = \frac{4\pi J_0}{ik_0}$. This is a Fredholm integral equation of the second kind with the degenerate kernel, which allows an exact solution in the form

$$p(r) = [C_1 \exp(ik_0 r) + C_2 \sin k_0 r]/r, \tag{9}$$

where

$$C_1 = \frac{1 + M\beta_{22}}{1 + M(\beta_{11} + \beta_{22}) + M^2(\beta_{11}\beta_{22} - \beta_{21}\beta_{12})},$$

$$C_2 = \frac{M\beta_{21}}{1 + M(\beta_{11} + \beta_{22}) + M^2(\beta_{11}\beta_{22} - \beta_{21}\beta_{12})},$$

$$\beta_{11} = \frac{1 - \cos 2k_0 r}{2k_0} + \frac{i}{2} \left(r - \frac{\sin 2k_0 r}{2k_0} \right),$$

$$\beta_{12} = \text{Im}\beta_{11}, \quad \beta_{21} = \frac{\exp(2ik_0R) - \exp(2ik_0r)}{2ik_0},$$

$$\beta_{22} = \frac{\cos 2k_0R - \cos 2k_0r}{2k_0}$$

$$+ \frac{i}{2} \left(R - r + \frac{\sin 2k_0R - \sin 2k_0r}{2k_0} \right).$$

Figure 1 shows the dependence of $r|p(r)|$ on r at $R = 0.1$ m, $V = 0.01$, and $f = 3$ kHz (curves 1 and 4 refer to the case when $p(r)$ is described by formula (9)). The calculation was carried out with the use of the standard approximation to $n(a)$ in the form $n(a) = Aa^{-\kappa}$ for $a_{\min} \leq a \leq a_{\max}$, where κ is a constant and A (with allowance

for identity (2)) has the form $A = V \frac{3(1 - \kappa/4)}{\pi(a_{\max}^{4-\kappa} - a_{\min}^{4-\kappa})}$. For

sea water with allowance for the literature data, we set $a_{\max} = 3 \times 10^{-3}$ and $a_{\min} = 3 \times 10^{-5}$ m. The scatter of the estimates reported for κ is large, but most publications provide values in the range 3–5, and these values were used in our calculations. Curve 1 refers to $\kappa = 3$ and curve 4 refers to $\kappa = 5$. Curves 2 and 5 represent the same function calculated without allowance for the bubble scattering at $r > r'$; in this case, $\beta_{21} = \beta_{22} = 0$. Since the error introduced by this assumption is small, we will use it in our subsequent calculations.

Let us show that the expressions obtained for $p(R)$ with the use of the QHA and from equation (9) coincide for small V and R . If V and, therefore, J_0 are small,

expression (3) yields $c = c_0 / \left(1 + \frac{c_0^2 J_0}{2\pi f^2} \right)$. Hence, we

obtain $p(R) = \exp(ikR)/R \approx \exp(ik_0R) \left(1 + i \frac{c_0 J_0 R}{f} \right) / R$

when R/f is small. On the other hand, expression (9) at $r = R$ and a small value of $J_0 R/f$ takes the form $p(R) \approx$

$\frac{\exp(ik_0R)}{R(1 - ic_0 J_0 R/f)} \approx \exp(ik_0R) \left(1 + i \frac{c_0 J_0 R}{f} \right) / R$. Hence,

we determine the criterion of the proximity of the solution based on the QHA to the exact solution:

$$c_0 |J_0| R/f \ll 1. \tag{10}$$

The curves obtained for the quantity $20 \log |Rp(R)|$ calculated on the basis of the QHA (curves 3) and from formula (9) (curves 1) as a function of V at $f = 6$ kHz are shown in Fig 2, and as a function of f at $V = 0.1$ in Fig. 3. It is seen that, for large V , the error of the QHA is large, and the use of this approximation is inexpedient. On the other hand, to find the exact expression for the acoustic field with allowance for multiple scattering is only feasible for a very limited number of configurations of the scattering medium (a plane layer, a circular cylinder,

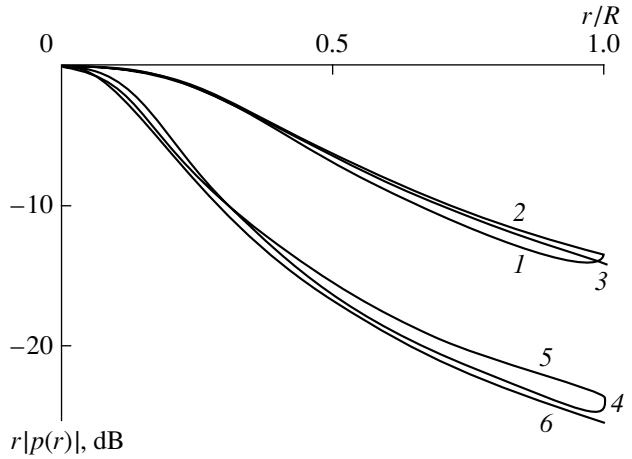


Fig. 1. Dependence of the amplitude of a spherical sound wave of frequency 3 kHz generated in water at the center of a spherical cloud of bubbles of radius R on the distance r from the source. Curves 1 and 4 are calculated from formula (9), curves 2 and 5 from formula (9) at $r = R$, and curves 3 and 6 are obtained from formula (11). Curves 1–3 correspond to $\kappa = 5$ and curves 4–6 correspond to $\kappa = 3$.

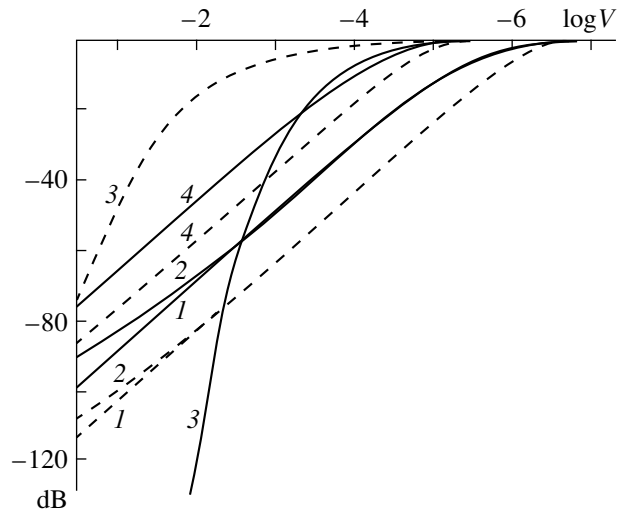


Fig. 2. Dependence of the intensity of the spherical wave intensity on the bubble concentration V at $R = 0.1$ m and $f = 6$ kHz for $\kappa = 3$ (solid lines) and 5 (dashed lines). Curves 1–4 are calculated from formulas (9), (17), (4), and (11), respectively.

and a sphere). Therefore, for practice, it is important to be able to describe the effect of the medium on the sound propagation through a local attenuation coefficient β . If we assume that β weakly depends on the form of the scattering domain and depends only on the wave path length r in this domain, then $\beta = (\ln |rp(r)|)/r$, where $rp(r)$ can be obtained from formula (9) by substituting the estimate of the integral J_0 in this formula and assuming that $k_0 r$ is small (since a high bubble concen-

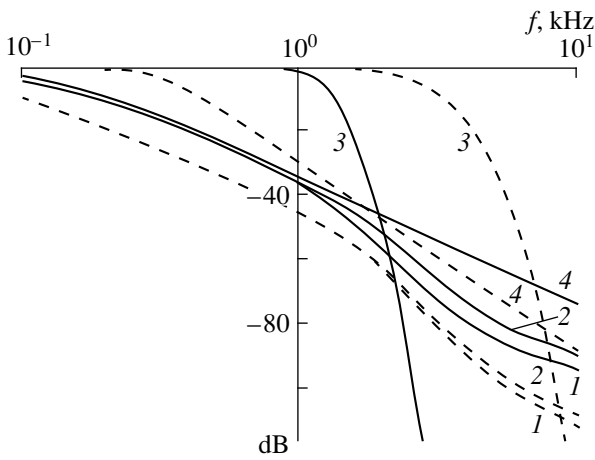


Fig. 3. Dependence of the wave intensity on the source frequency at $V = 0.1$ and $R = 0.1$ m. Other notations are the same as in Fig. 2.

tration in sea water is observed only in small volumes). For $f \geq f_0(a_{\max})$, the estimate J_0 takes the form

$$J_0 \approx 10^5 A f^2 \frac{(300f)^{\kappa-4} - a_{\min}^{4-\kappa}}{4-\kappa} - iA(300f)^{\kappa-2};$$

for $f < f_0(a_{\max})$, we can ignore the imaginary part. Finally, we obtain

$$\beta \approx r^{-1} \ln \left[1 + 15A(300)^{\kappa-2} f^{\kappa-1} R^3 + 2\pi(300)^2 A f^2 \frac{(300f)^{\kappa-4} - a_{\min}^{4-\kappa}}{4-\kappa} R^2 \right], \tag{11}$$

where r and R are expressed in meters and f in kilohertz.

Curves 3 and 6 in Fig. 1 correspond to the solution obtained on the basis of the QHA with β being described by formula (11). It is seen that these curves fit the exact solution well. This is also true for curves 4 in Figs. 2 and 3. It is seen that they lie much closer to curves 1, as compared to curves 3.

The exact calculation of the coherent component of the field scattered within the spherically symmetric bubble cloud can also be carried out when V is an arbitrary function of r . In the previous publication [8], the result of calculations is presented for an exponentially decreasing function $V(r)$.

The calculation of the total intensity I of a point source located at the center of a spherical bubble cloud is much more complicated. Therefore, we use the Twersky equations that were obtained for the same assumptions as equation (6). Then, we have

$$I(r) = |p(r)|^2 + 2\pi \int_0^R \int_{-1}^1 I(r') r'^2 |v(r, r', y)|^2 n(a) da dr' dy. \tag{12}$$

Here, $p(r)$ is expressed by formula (9) and v is determined from the equation

$$v(r, r', y) = \frac{a \exp(ik_0 \rho)}{L \rho} + 2\pi J_1 \int_0^R \int_{-1}^1 v(r, r'', y') r''^2 \frac{\exp(ik_0 \rho')}{\rho'} dr'' dy',$$

where $\rho' = (r^2 + r''^2 - 2rr''y')^{1/2}$ and y' is the cosine of the angle between the vectors \mathbf{r} and \mathbf{r}'' , and

$$J_1 = \int \frac{n(a) a^2 da}{|L|^2}.$$

The solution of equation (12) presents a complicated problem. Therefore, we apply the approach used in [7] and describe the field scattered by a bubble at the point r' by the expression that involves the local wave number k . Then, we obtain

$$v(r, r', y) = a \exp(ik\rho)/(L\rho). \tag{13}$$

As $\beta = \text{Im}k$, we can choose quantity (4) obtained on the basis of the QHA, or any other approximation.

Substituting (13) in (12) and neglecting the field scattered at $r < r' < R$, we obtain

$$I(r) = |p(r)|^2 + 2\pi J_1 \int_{-1}^1 \int_0^r I(r') r'^2 \frac{\exp(-2\beta\rho)}{\rho^2} dy dr'. \tag{14}$$

After integrating with respect to y , we obtain the expression

$$I(r) = |p(r)|^2 + \Lambda \int_0^1 I(\mu) \mu [E_1(2\beta r(1-\mu)) - E_1(2\beta r(1+\mu))] d\mu, \tag{15}$$

where E_1 is the integral exponential function and $\Lambda = 2\pi J_1 r$.

In order to find an approximate solution to this equation, we need to estimate the convergence of the Neumann series. As shown in [9], the convergence condition for equation (15) has the form

$$\Lambda < \left[\int_0^1 \mu E_1(2\beta r(1-\mu)) d\mu \right]^{-1} \approx 2\beta r.$$

Using the estimate for β in the form (4) or (11), we can show that this condition is not always realized in the presence of the resonance bubbles. To provide the convergence of the Neumann series, we use the method of analytical continuation and replace the variable Λ by $\eta = \Lambda/(1 + \Lambda)$. Under this condition, the Neumann series converges everywhere, and the first term of the

series retains its previous form. In the first approximation, solution (15) is finally written as

$$I(r) \cong |p(r)|^2 + \eta \int_0^1 \mu |p(\mu r)|^2 E_1(2\beta r(1-\mu)) d\mu. \quad (16)$$

For $r > R$, the intensity I is found from formula $I = i/r^2$, where

$$i = R^2 \left(|p(R)|^2 + 2\pi J_1 \int_{0-1}^R \int_{-1}^1 I(r) \frac{r^2 \exp(-\beta \rho_1)}{\rho_1^2} dr dx, \quad (17) \right.$$

$$\rho_1 = (R^2 - r^2(1-x^2))^{1/2} - rx.$$

Curves 2 in Figs. 2 and 3 show the results of the calculation of the function $10 \log i$, where β is calculated by formula (11).

As V increases, the validity limits of formula (17) are primarily determined by the condition that the largest bubbles retain their spherical shape, as well as by the fact that the Twersky equations were derived by ignoring the pair correlations between the positions of the scattering bubbles. However, this question requires special consideration.

A general conclusion that results from the analysis of the acoustic field attenuation in water with bubbles is that the approximation of the quasi-homogeneous medium is valid, as a rule, only for V of the order of 10^{-4} and that this approximation can only be used for bubble clouds with fairly low bubble concentrations,

which correspond to their life times of several seconds after the wave breaking, when the number of the active (radiating) bubbles in the cloud rapidly decreases. The first seconds of the existence of the bubble cloud are of particular interest from the standpoint of the bubble contribution to the noise field of the ocean. However, in this case, the noise intensity must be calculated with allowance for multiple scattering.

REFERENCES

1. C. S. Clay and H. Medwin, *Acoustical Oceanography* (Wiley, New York, 1977; Mir, Moscow, 1980).
2. Ye Zhen, *J. Acoust. Soc. Am.* **102**, 788 (1997).
3. G. Dean, *J. Acoust. Soc. Am.* **102**, 2671 (1997).
4. K. A. Naugol'nykh and L. A. Ostrovskii, *Nonlinear Wave Processes in Acoustics* (Nauka, Moscow, 1990).
5. E. Lamarre and W. Melville, *J. Acoust. Soc. Am.* **95**, 1317 (1994).
6. S. M. Rytov, Yu. A. Kravtsov, and V. I. Tatarskiĭ, *Principles of Statistical Radiophysics* (Nauka, Moscow, 1978; Springer, Berlin, 1989), Part 2.
7. A. Ishimaru, *Wave Propagation and Scattering in Random Media* (Academic, New York, 1978; Mir, Moscow, 1982), Vol. 2.
8. G. A. Postnov, *Dokl. Akad. Nauk* **360**, 117 (1998).
9. L. V. Kantorovich and V. I. Krylov, *Approximate Methods of Higher Analysis* (Fizmatgiz, Moscow, 1962).

Translated by Yu. Lysanov

Wide-Band Sound-Absorbing Structures for Aircraft Engine Ducts

A. F. Sobolev

Zhukovskii Central Aerohydrodynamics Institute, ul. Radio 17, Moscow, 107005 Russia

Received June 8, 1999

Abstract—With a view to providing sound absorption in a wide frequency range, one- and two-layer sound-absorbing structures, in which nets are used as absorbing layers, are investigated. A semiempirical theory of calculating the impedance characteristics of these structures is proposed. The theory takes into account the interaction between the net layers for a wide range of their perforation factors. A good agreement between theory and experiment is observed. It is shown that two-layer net structures are vastly superior to two-layer structures with perforated panels from the viewpoint of the sound absorption bandwidth. © 2000 MAIK “Nauka/Interperiodica”.

In recent years, in connection with the expected more stringent international requirements on environmental noise for airliners with high-bypass-ratio engines, growing interest is being shown in various measures intended for reducing the noise of fans and turbines of aircraft engines. As practice shows, the most effective means of reducing this noise are resonant cellular sound-absorbing structures (SAS) with perforated panels. However, one-layer cellular SAS used today will apparently not be able to provide the required additional noise reduction from the viewpoint of both the sound absorption bandwidth and the maximum sound attenuation. In this connection, it is possible to point out several directions of research aimed at developing enhanced SAS. One of these is associated with detailed studies of flows inside the holes of a perforated panel and of the mechanism of sound absorption in a single hole [1–4]. These investigations are aimed at creating improved methods of determining the impedance characteristics of SAS. Another direction of research is connected with the study of the influence of the increase in the number of degrees of freedom of a resonance structure on its acoustic efficiency. The simplest examples of such structures are two-layer [5] and combined [6] SAS. By properly controlling the degrees of freedom, it is possible to provide the broadening of the sound absorption bandwidth without an increase in the SAS area. The third direction of research is represented by the studies of microporous blown-through panels used as sound-absorbing layers. It is experimentally established that the impedance of structures with a microporous inlet element barely depends on the level of sound pressure, and the associated mass is small (at least for sufficiently deep structures). These features make such structures attractive for use in the ducts of aircraft engines in a wide range of operating conditions from landing to takeoff. Current investigations are directed at creating experimental equipment for deter-

mining the impedance and propagation constant of porous sound-absorbing materials [7], as well as at developing new materials [8–11].

For the manufacture of microporous panels, various technological processes are used, in particular, laser boring of aluminum or titanium plates or electrolytic deposition of nickel plates [8]. These processes do not provide sufficiently homogeneous acoustic properties within the panel area. In this paper, as a microporous absorbing layer we use the net panels of so-called serge weave which are commercially produced. Their advantages are the homogeneity of acoustic properties within the panel area and their smoothness. We investigate one- and two-layer structures, which contain air cavities separated by partitions and net panels serving as absorbing layers. Although the net structures have been known for a long time [12], no adequate method of calculating their impedance characteristics has been developed. In spite of the apparent simplicity, the impedance calculations require some complicated mathematics. Figure 1 displays photographs of a dense metal commercially available net of serge weave (no. 450, made according to the standard TU14-4-432-94) at various magnifications. This net has the number of fibers per decimeter of warp 450, and of weft 3640. The thickness of fibers is 0.09 and 0.055 mm, respectively. The mass of 1 m² of the net is 0.97 kg. At high magnification, it is seen that the surface of the net consists of alternating “crests” and “hollows.” The height of crests is approximately equal to the thickness of the weft fiber.

The losses in the net holes depend significantly on their form and size which, in their turn, depend on the type of weave. In many types of weave and, in particular, in the serge weave, smooth inlets and outlets of holes are formed, which prevents the formation of jet flows. This explains in part the weak dependence of the

impedance on the sound pressure level. The real shape of the holes cannot be determined; therefore, in our calculations we approximate them by round openings of small diameter. We also suppose that jet flows are not generated at high sound pressure levels. In this case, for calculating the specific resistance of the net, we can use the equation derived by Krendall [13] to determine the impedance of a narrow tube of the round cross-section of diameter d and length δ :

$$Z_s = \frac{j\omega\delta}{cF} \left(1 - \frac{4 J_1(\chi d/2)}{\chi d J_0(\chi d/2)} \right), \quad (1)$$

where

$$\chi = \sqrt{-j\omega\rho/\mu} = \sqrt{-j\omega/\nu}, \quad (2)$$

ρ is the density of the medium, μ is the coefficient of viscosity, ν is the kinematic viscosity coefficient equal to $\nu = 14.5 \text{ mm}^2/\text{s}$ (for air), F is the net perforation factor (in percent), ω is the angular frequency, and J_0 and J_1 are the Bessel functions. For tubes with metal walls having high thermal conductivity, the internal friction is higher, and, according to Kirchhoff, it is necessary to use the increased value of the coefficient of viscosity from the equation [14]

$$\sqrt{\mu'} = \sqrt{\mu[1 + (\gamma - 1)\sqrt{\kappa/\mu c_p}]}, \quad (3)$$

where $\gamma = c_p/c_v$ and κ is the coefficient of thermal conductivity of gas. If, instead of coefficients of viscosity and thermal conductivity, we introduce the kinematic viscosity coefficient ν and the coefficient of thermal diffusivity at constant pressure $\tau_p = \kappa/\rho c_p = 18 \text{ mm}^2/\text{s}$, equation (3) can be written as

$$\sqrt{\nu'} = \sqrt{\nu(1 + (\gamma - 1)\sqrt{\tau_p/\nu})}. \quad (4)$$

It should be noted that, in the investigated frequency range, the parameter $\chi d/2$ varies within $0 < \chi d/2 < 10$. In these limits, there is no single asymptotic representation of Bessel functions, and, hence, they should be calculated directly. For determining the net perforation factor, one can use the schematic diagram displayed in Fig. 2, which is obtained from Fig. 1. The diameter of holes is taken equal to the thickness of the weft fibers. The perforation factor is determined approximately by the formulas

$$S = lr - \pi r^2/2, \quad V_s = 2SNL,$$

$$F = \left(1 - \frac{P_{sp}/\rho_{sp} + V_s}{V_{sp}} \right) \times 100\%,$$

where l is the distance between the centers of hollows, r is the radius of the inscribed circle, N is the number of hollows, P_{sp} is the weight of the sample, ρ_{sp} is the density of the material, V_{sp} is the volume of the sample, and L is the width of the sample. Thus, for net no. 450, the perforation factor equals 12%.

In calculating the impedance of an air cavity of the structure, one should take into account the sound

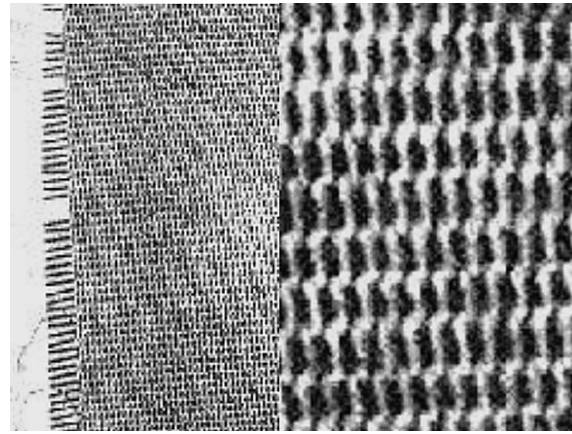


Fig. 1. Photographs of the face layer (net) at various magnifications.

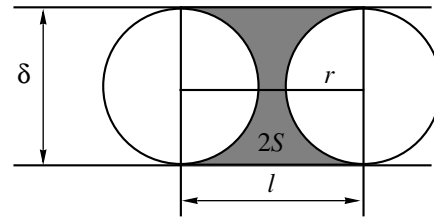


Fig. 2. On estimating the net perforation factor.

absorption on the side and back walls and the appearance of the additional associated mass related to the radiation into the cavity. In most cases, the absorption effect is insignificant; however, for a closely positioned back wall and for narrow resonators, it should be taken into account. The associated mass depends not only on the size and form of the resonator, but also on its load. Specifically, for a two-layer structure, the load is the second internal layer. Therefore, in determining the cavity impedance, we will consider the more general case when the resonator cavity is loaded by some impedance Z_0 .

We consider a resonator $a \times b \times h$ where a and b are the transverse dimensions, and h is the depth. Neglecting the interaction between holes in the face panel, the air oscillations in the holes can be replaced by oscillations of a piston, the area of which is equal to the total area of the holes. The piston can be represented as a set of continuously distributed point sources described by a three-dimensional δ -function with a harmonic dependence on time ($\exp(j\omega t)$). The equation for the pressure p has the form

$$\frac{\partial^2 p}{\partial x^2} + \frac{\partial^2 p}{\partial y^2} + \frac{\partial^2 p}{\partial z^2} + k^2 p = -V_0 \rho c k \delta(x - x_0) \delta(y - y_0) \delta(z), \quad (5)$$

where $k = \omega/c$ is the wave number, ρ is the air density, c is the sound velocity, V_0 is the amplitude of the velocity

of a point source, and x_0, y_0 are the coordinates of a source in the plane $z = 0$. The effect of the viscosity and the heat conduction of the resonator walls can be described by introducing the complex conductivities [15]

$$Y_R = \frac{\xi^2}{k^2}(1+j)\sqrt{\frac{v\omega}{2c^2}}, \tag{6}$$

$$Y_T = (1+j)(\gamma-1)\sqrt{\frac{\tau\omega}{2c^2}}, \tag{7}$$

where ξ is the wave number in the z direction. The field inside the resonator cavity must satisfy the boundary conditions on the side walls

$$\frac{\partial p}{\partial x} = \pm jkYp|_{x=0,a}, \tag{8}$$

$$\frac{\partial p}{\partial y} = \pm jkYp|_{x=0,b}, \tag{9}$$

where

$$Y = Y_R + Y_T,$$

and the condition on the back wall

$$\frac{\partial p}{\partial z} = -jkY_0p|_{z=h}. \tag{10}$$

For determining Green's function, we use the results of the previous paper [16]. In this paper, the expression for Green's function in a two-dimensional lined duct for a uniform flow with velocity V was derived:

$$p = j \sum_{n=1}^{\infty} V_0 \rho c k \frac{\exp(-j\xi_n(z-z_0)) \cos(\alpha_n x_0 - \varphi_n) \cos(\alpha_n x - \varphi_n) F_1(\alpha_n a) (1 + R_n^2)}{\alpha_n \frac{\partial F}{\partial \alpha} \Big|_{\alpha=\alpha_n} \frac{\partial \alpha}{\partial \xi} \Big|_{\xi=\xi_n}}, \tag{11}$$

where ξ_n and α_n are the roots of the set of equations

$$\begin{aligned} F(\xi_n) &= \tan(\chi_n a) (1 - G_{1,n} G_{2,n} / \chi_n^2) \\ &+ (G_{1,n} + G_{2,n}) / \chi_n = 0, \\ \alpha_n^2 &= (k - M\xi_n)^2 - \xi_n^2, \end{aligned}$$

$$G_{i,n} = ikY_i \left(1 - M \frac{\xi_n}{k}\right)^2, \quad i = 1, 2;$$

$$F_1(\alpha_n a) = \frac{\alpha_n^2 + G_{1,n}^2}{\alpha_n^2 - G_{1,n} G_{2,n}}; \quad R_n = G_{2,n} / \alpha_n; \quad M = V/c;$$

$\tan(\varphi_n) = -R_n$; and a is the height of the duct.

In deriving equation (11), we did not assume the local behavior of the conductance Y_i , i.e., its independence of the mode number. Moreover, the actual conductance $G_{i,n}$ becomes dependent on the mode number due to the convection term, and this dependence is accounted for in calculating the derivative in the denominator of expression (11).

In the considered case, we have $Y_1(\xi) = Y_2(\xi) = Y(\xi)$,

$$M = 0, \quad z_0 = 0, \quad \text{and} \quad \frac{\partial F}{\partial \xi} \Big|_{\xi=\xi_n} = \frac{\partial F}{\partial \alpha} \Big|_{\alpha=\alpha_n} \frac{\partial \alpha}{\partial \xi} \Big|_{\xi=\xi_n} +$$

$\frac{\partial F \partial Y}{\partial Y \partial \xi} \Big|_{\xi=\xi_n}$. Performing the necessary calculations, we obtain

$$p = \sum_{n=1}^{\infty} C_n(x_0, x) \exp(-j\xi_n|z|), \tag{12}$$

where

$$\begin{aligned} C_n(x_0, x) &= -V_0 \rho c k \\ &\times \frac{j \cos(\alpha_n x_0 - \varphi_n) \cos(\alpha_n x - \varphi_n)}{a \xi_n U_n}, \end{aligned} \tag{13}$$

$$U_n = \frac{\alpha_n^2 \left(1 + \frac{4(j-1)}{ka} \sqrt{\frac{v\omega}{2c^2}}\right) - (kY_n)^2 + 2jkY_n/a}{\alpha_n^2 - (kY_n)^2}, \tag{14}$$

and Y_n is the value of Y at $\xi = \xi_n$.

Equation (12) defines the field in an infinite duct. For determining the field of a point source in a duct of limited length $0 \leq z \leq h$ with a rigid wall at $z = 0$ and a wall with the conductance Y_0 at $z = h$, we place the source inside the duct and represent the solution inside the duct as a sum of a particular solution of an inhomogeneous equation and a general solution of a homogeneous equation:

$$\begin{aligned} p &= \sum_n C_n(x_0, x) \exp(-j\xi_n|z|) + A_n(x) \exp(-j\xi_n z) \\ &+ B_n(x) \exp(j\xi_n z). \end{aligned} \tag{15}$$

Upon satisfying the boundary conditions, we replace the source on the rigid wall. As a result, the coefficients A_n and B_n can be expressed by the formulas

$$A_n = C_n \frac{1 + Q_n}{1 - Q_n}, \quad B_n = \frac{2C_n Q_n}{1 - Q_n}, \tag{16}$$

where

$$Q_n = \frac{\xi_n - kY_0}{\xi_n + kY_0} \exp(-2j\xi_n h),$$

and the field in the duct $0 \leq z \leq h$ can be written as

$$p = \sum_{n=0}^{\infty} \frac{2C_n(x_0, x)}{(1 - Q_n)} [\exp(-j\xi_n z) + Q_n \exp(j\xi_n z)]. \quad (17)$$

This field corresponds to the point source $V_0 \rho c k \delta(x - x_0) \delta(z)$. Evidently, the field

$$p = \sum_{m=0}^{\infty} \frac{2C'_m(y_0, y)}{(1 - Q_m)} \times [\exp(-j\xi_m z) + Q_m \exp(j\xi_m z)], \quad (18)$$

where $C'_m(y_0, y) = \frac{j \cos(\beta_m y_0 - \phi_m) \cos(\beta_m y - \phi_m)}{b \xi_m V_m}$, β_m and ϕ_m are determined from the boundary conditions (9), and V_m and Q_m from equations (14) and (16), with the replacement of a by b corresponds to the point source $\delta(y - y_0) \delta(z)$. According to [17], we can find a three-dimensional Green's function by combining solutions (17) and (18) for two-dimensional Green's functions and represent it as the following double sum

$$p = \sum_{n=0}^{\infty} \sum_{m=0}^{\infty} \frac{4C_n(x_0, x) C'_m(y_0, y)}{(1 - Q_{n,m})} \times [\exp(-j\xi_{n,m} z) + Q_{n,m} \exp(j\xi_{n,m} z)]. \quad (19)$$

The constant of separation $\xi_n^2 = k^2 - \alpha_n^2$ is replaced in view of the increase in dimension by $\xi_{n,m}^2 = k^2 - \alpha_{n,m}^2 - \beta_{n,m}^2$. The second index of the eigenvalues of α and β appears due to the dependence of the conduction Y on

ξ . Accordingly, all the quantities which depend on ξ become the elements of a two-dimensional matrix. According to the boundary conditions, the eigenvalues $\alpha_{n,m}$ and $\beta_{n,m}$ are determined by solving the following transcendental equations

$$\tan(\alpha_{n,m} a) = \frac{2jk\alpha_{n,m} Y_{n,m}}{\alpha_{n,m}^2 + (kY_{n,m})^2}, \quad (20)$$

$$\tan(\beta_{n,m} b) = \frac{2jk\beta_{n,m} Y_{n,m}}{\beta_{n,m}^2 + (kY_{n,m})^2}, \quad (21)$$

$$\tan(\phi_{n,m}) = \frac{jkY_{n,m}}{\alpha_{n,m}}, \quad \tan(\phi_{n,m}) = \frac{jkY_{n,m}}{\beta_{n,m}}.$$

The total field generated by all sources in the hole is determined by the integration over the hole area $p_S = \iint_S p \, dx_0 dy_0$. For performing the integration, it is convenient to introduce the polar coordinates $x_0 = x_c + r \cos \psi$, $y_0 = y_c + r \sin \psi$, where (x_c, y_c) are the coordinates of the hole center. It can be shown that

$$J = \int_0^{2\pi} d\psi \int_0^{r_0} \cos[\alpha_{n,m}(x_0 + r \cos \psi) - \phi_{n,m}] \times \cos[\beta_{n,m}(y_0 + r \sin \psi) - \phi_{n,m}] r dr \\ = \frac{2\pi r_0}{W_{n,m}} J_1(W_{n,m} r_0) \cos(\alpha_{n,m} x_c - \phi_{n,m}) \times \cos(\beta_{n,m} y_c - \phi_{n,m}),$$

where J_1 is the first-order Bessel function, $W_{n,m} = \sqrt{\alpha_{n,m}^2 + \beta_{n,m}^2}$, and r_0 is the hole radius. Thus, the expression for the total field has the form

$$\frac{p_S}{\rho c} = \sum_{n,m} \frac{8V_0 k \pi r_0 J_1(W_{n,m} r_0) \cos \Phi_{n,m} \cos \Psi_{n,m} (\exp(-j\xi_{n,m} z) + Q_{n,m} \exp(j\xi_{n,m} z))}{ab \xi_{n,m} W_{n,m} (1 - Q_{n,m}) U_{n,m} V_{n,m}} \times \cos(\alpha_{n,m} x - \phi_{n,m}) \cos(\beta_{n,m} y - \phi_{n,m}), \quad (22)$$

where $\Phi_{n,m} = \alpha_{n,m} x_c - \phi_{n,m}$ and $\Psi_{n,m} = \beta_{n,m} y_c - \phi_{n,m}$.

Integrating (22) over the hole area, we obtain the expression for the mean pressure $p = \frac{1}{\pi r_0^2} \iint_S p_S \, dx dy$:

$$p = \sum_{n,m} \frac{16\rho c k V_0 \pi J_1^2(W_{n,m} r_0) \cos^2 \Phi_{n,m} \cos^2 \Psi_{n,m} (\exp(-j\xi_{n,m} z) + Q_{n,m} \exp(j\xi_{n,m} z))}{\xi_{n,m} W_{n,m}^2 (1 - Q_{n,m}) ab U_{n,m} V_{n,m}}. \quad (23)$$

Setting $z = 0$ and using the explicit expression for $Q_{n,m}$ from (16), we derive the expression for the specific impedance of a hole radiating into the cavity:

$$Z_V = \frac{p}{V_0 \rho c F} = \sum_{n,m} \frac{16kJ_1^2(W_{n,m}r_0) \cos^2 \Phi_{n,m} \cos^2 \Psi_{n,m}}{\xi_{n,m} W_{n,m}^2 r_0^2 U_{n,m} V_{n,m}} \times \frac{\xi_{n,m} Z_0 + jk \tan(\xi_{n,m} h)}{j \xi_{n,m} Z_0 \tan(\xi_{n,m} h) + k}, \quad (24)$$

where $F = \pi r_0^2 / ab$ is the perforation factor of the face panel, and $Z_0 = 1/Y_0$. Let us assume that the point (x_c, y_c) is located at the center of the cell, i.e., it has the coordinates $(a/2, b/2)$. Then, $\cos^2 \Phi_{n,m} = \cos^2 \Psi_{n,m} = 1$, and formula (24) reduces to

$$Z_V = \sum_{n,m} \frac{16kJ_1^2(W_{n,m}r_0)}{\xi_{n,m} W_{n,m}^2 r_0^2 U_{n,m} V_{n,m}} \times \frac{\xi_{n,m} Z_0 + jk \tan(\xi_{n,m} h)}{j \xi_{n,m} Z_0 \tan(\xi_{n,m} h) + k}. \quad (25)$$

For the case of low conductivity $Y \ll 1$, from equations (20) and (21) we have $(\alpha_{0,0} a)^2 \approx 2jkaY_{0,0}$ and $(\beta_{0,0} b)^2 \approx 2jkbY_{0,0}$. Then, for the zeroth term of expansion in (25), we obtain

$$Z_V^{(0)} = (R_1 R_2)^{-1} \frac{Z_0 + jk \tan(\xi_{0,0} h) / \xi_{0,0}}{j \xi_{0,0} Z_0 \tan(\xi_{0,0} h) / k + 1}, \quad (26)$$

where

$$R_1 = 1 + (2(j-1)/ka) \sqrt{v\omega/2c^2},$$

$$R_2 = 1 + (2(j-1)/kb) \sqrt{v\omega/2c^2}.$$

This is nothing but the impedance of a layer of thickness h with the load Z_0 with consideration for the absorption at the cavity walls due to the viscosity and heat conductivity. The influence of the boundary walls results in the appearance of the correction factors R_1 and R_2 , which in the case of low wall conductivity are close to unity. In the even more special case of a rigid back wall, when $Z_0 = \infty$, we have

$$Z_V^{(0)} = -j \frac{k}{\xi_{0,0}} (R_1 R_2)^{-1} \cot(\xi_{0,0} h). \quad (27)$$

Expression (25) with the eliminated zeroth term determines the associated mass caused by the radiation into the cavity.

In determining the impedance of a one-layer net structure, one should take into account the effect of both ends of the hole of the face panel on the associated mass [18]. For finding the associated mass corresponding to the second end, it is necessary to set $Z_0 = 0$ and

$h = \infty$ in expression (25). Thus, the expression for the impedance of a one-layer structure has the form

$$Z_1 = Z_S + Z_V(h) + Z_V(\infty) + Z_V^{(0)}(h), \quad (28)$$

where Z_S is given by formula (1), $Z_V(h)$ and $Z_V(\infty)$ are the inertial impedances determined by expression (25) with the eliminated zeroth term, and $Z_V^{(0)}(h)$ is the elastic impedance determined by formula (27).

Now we determine the impedance of a two-layer net structure. Let the depth of the first layer be h_1 and the depth of the second layer be h_2 . For the inner net, the loads are: on one side, a rigid wall at the distance h_2 and, on the other side, the face net at the distance h_1 . The impedance of the second layer is determined by the expression similar to (28):

$$Z_2 = Z_S + Z_V(h_2) + Z_V(h_1) + Z_V^{(0)}(h_2), \quad (29)$$

where $Z_V(h_1)$ is found from formula (25) with the eliminated zeroth term and with the load $Z_0 = Z_S + 1$; $Z_V(h_2)$ is determined by formula (25) with the eliminated zeroth term and with the load $Z_0 = \infty$; and $Z_V^{(0)}(h_2)$ is determined by formula (27). For the outer net, the loads are: on one side, the impedance Z_2 at the distance h_1 and, on the other side, an air column of infinite height. The impedance of a two-layer structure is the sum of the impedance of the face net, the inertial impedance of the face net loaded by Z_2 , the inertial impedance of the face net with the load corresponding to an infinite air column, and the impedance of a layer of thickness h_1 loaded by the impedance $Z_0 = Z_2$ determined from formula (26):

$$Z = Z_S + Z_V(h_1) + Z_V(\infty) + Z_V^{(0)}(h_1). \quad (30)$$

For calculating the inertial impedance by formula (25), it is necessary to know the roots of the dispersion equations (20) and (21). It is seen from these equations that, due to the nonlocal behavior of the admittance Y , the eigenvalues along the x - and y -axes are related to each other through the axial (along the z -axis) wave number. Hence, these two equations should be solved simultaneously. For the case of low conductivity $Y \ll 1$, the roots can be found analytically. Indeed, the dispersion equation along the x -axis can be written in the form

$$\alpha_{n,m} a \tan(\alpha_{n,m} a) = 2ka(j-1) \left[\frac{\xi_{n,m}^2}{k^2} \sqrt{\frac{v\omega}{2c^2}} + (\gamma-1) \sqrt{\frac{\tau\omega}{2c^2}} \right], \quad (31)$$

where

$$\xi_{n,m}^2 = k^2 - \alpha_{n,m}^2 - \beta_{n,m}^2.$$

The dispersion equation along the y -axis can be written similarly by substituting β for α and b for a . The index n corresponds to the mode number along the x -axis, and

the index m corresponds to the mode number along the y axis. For the case of $m = n = 0$ for a zero wave, to a good approximation we obtain

$$\xi_{0,0}^2 = \frac{k^2 \left[1 - 2 \frac{a+b}{kab} (j-1)(\gamma-1) \sqrt{\frac{\tau\omega}{2c^2}} \right]}{1 + 2 \frac{a+b}{kab} (j-1) \sqrt{\frac{v\omega}{2c^2}}}, \quad (32)$$

$$\alpha_{0,0}^2 = \frac{2k}{a} (j-1) \left[\frac{\xi_{0,0}^2}{k^2} \sqrt{\frac{v\omega}{2c^2}} + (\gamma-1) \sqrt{\frac{\tau\omega}{2c^2}} \right]. \quad (33)$$

Replacing a by b in (33), we obtain the expression for $\beta_{0,0}^2$. If n is nonzero and m is zero, we have

$$\alpha_{n,0} = \frac{n\pi}{a} + \frac{2(j-1)k}{n\pi} \left[S_{n,0} \sqrt{\frac{v\omega}{2c^2}} + (\gamma-1) \sqrt{\frac{\tau\omega}{2c^2}} \right],$$

$$S_{n,0} = \begin{cases} 1 - (n\pi/ka)^2 - \beta_{0,0}^2/k^2, & \text{when } n\pi < ka \\ 0, & \text{when } n\pi > ka, \end{cases} \quad (34)$$

$$\xi_{n,0}^2 = k^2 - \alpha_{n,0}^2 - \beta_{0,0}^2.$$

Relations for $\beta_{0,m}$ and $\xi_{0,m}^2$ are derived from (34) by substituting b for a , m for n , and $\alpha_{0,0}^2$ for $\beta_{0,0}^2$. Finally, for $m \neq 0$ and $n \neq 0$, expressions for $\alpha_{n,m}$ and $\xi_{n,m}$ have the form

$$\alpha_{n,m} = \frac{n\pi}{a} + \frac{2(j-1)k}{n\pi} \left[S_{n,m} \sqrt{\frac{v\omega}{2c^2}} + (\gamma-1) \sqrt{\frac{\tau\omega}{2c^2}} \right],$$

$$S_{n,m} = \begin{cases} 1 - (n\pi/ka)^2 - (m\pi/kb)^2 \\ \text{when } (n\pi/ka)^2 + (m\pi/kb)^2 < 1 \\ 0, & \text{when } (n\pi/ka)^2 + (m\pi/kb)^2 > 1, \end{cases}$$

$$\xi_{n,m}^2 = k^2 - \alpha_{n,m}^2 - \beta_{n,m}^2.$$

Expressions for $\beta_{n,m}$ are obtained by replacing a with b .

The formulas obtained above were used for calculating the impedance of one- and two-layer sound absorbing structures with the nets of serge weave as sound absorbers. The depth of the air cavity in the samples of one-layer SAS ranged from 4 to 35 mm. For the two-layer samples, we determined the influence of the distance h_1 between the nets, as well as the depth h_2 of the cavity behind the inner net. The total depth of two-layer SAS varied from 16 to 38 mm. The samples were tested using a high-level interferometer by the standard standing-wave method in the frequency range 0.8–5 kHz. The processing of the test results made it possible to obtain the values of the real X and imaginary Y parts of the impedance Z and the values of the absorption coefficient α .

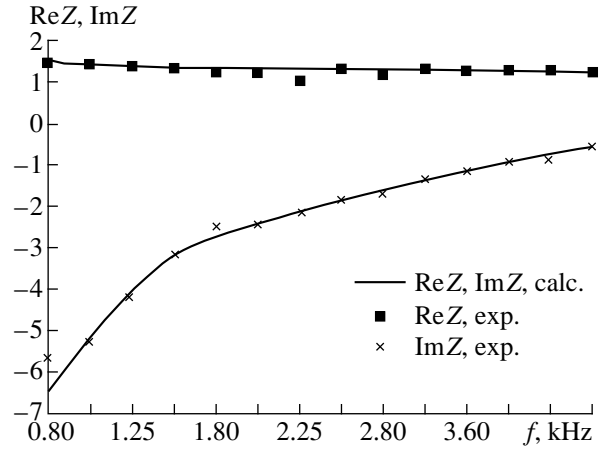


Fig. 3. Frequency dependences of the real and imaginary parts of the impedance of a one-layer net SAS ($h = 10$ mm).

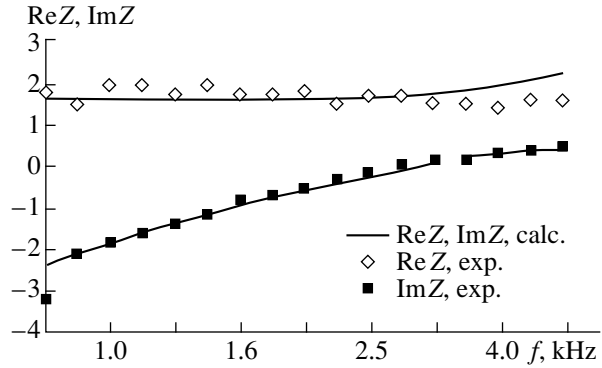


Fig. 4. Frequency dependences of the real and imaginary parts of the impedance of a two-layer net SAS ($h_1 = 10$ mm, $h_2 = 15$ mm).

Figure 3 illustrates the comparison between the calculations and the experiment for the impedance of a one-layer structure with the depth of the air cavity $h = 10$ mm. In the investigated frequency range, the real part of the impedance barely depends on frequency. The inertial parameter M (determined from formula (25) with the eliminated zeroth term, as a quantity multiplied by the wave number) is very small, which corresponds to the gentle slope of the curve $\text{Im}Z$ in this frequency range. For lesser depths of the air cavity, the resistance $\text{Re}Z$ and the inertial parameter increase at low frequencies due to the effect of the back wall. For all investigated one-layer structures, in the resonance region, the real part of the impedance $\text{Re}Z$ is close to the ρc of the air. Away from the resonance to lower frequencies, these relations fail: a slight growth of $\text{Re}Z$ and M is observed. The figure shows a good agreement between the theory and the experiment.

Figure 4 illustrates the comparison of the calculations and the experiment for a two-layer net structure

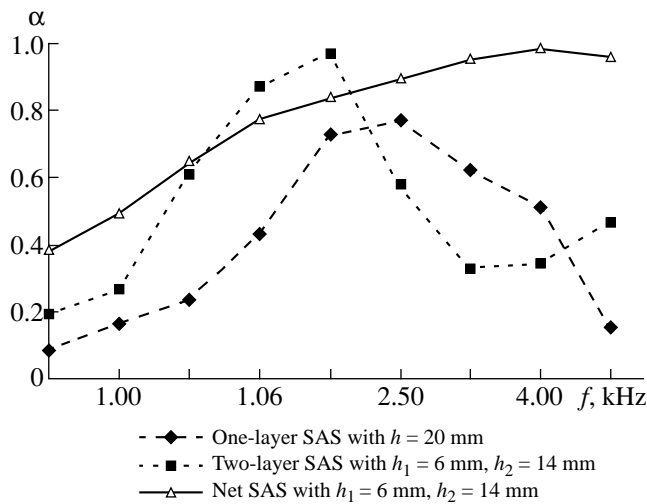


Fig. 5. Comparison of the absorption coefficients of one- and two-layer SAS with perforated panels and two-layer net SAS.

with the depth of the second layer 15 mm and the depth of the first layer 10 mm. The figure demonstrates the agreement between theory and experiment.

The calculations and the experiment show that, with a small depth of the first layer, the two-layer structure behaves like a one-layer structure of the summarized thickness with a higher resistance and a lower resonant frequency. The lower resonant frequency is caused by the greater inertial parameter due to the influence of the second layer. With the increase in the depth of the first layer, the second resonance appears at a higher frequency, and the first resonance shifts to lower frequencies. The operating region of a two-layer structure is a wide frequency range, which includes both resonant frequencies.

Due to the small associated mass, net structures, especially two-layer structures, have a broader frequency band of the absorption coefficient than structures with perforated panels. Figure 5 shows the comparison of the experimentally measured absorption coefficients of one- and two-layer SAS with perforated panels and a two-layer net SAS. The total depth of all structures was 20 mm. The perforation factor of the panels was 10%, the panel thickness 0.8 mm, and the diameter of openings 1.5 mm. As is seen from Fig. 5, the two-layer net structure has a much broader frequency characteristic of α than the two-layer structure with perforated panels.

In some cases, namely, when the face layer of the lining is heavily contaminated, the net structure may lose its absorbing qualities, and it is appropriate to use combined two-layer SAS having a perforated panel as a face layer and a net panel as an inner layer.

Figure 6 displays the comparison of the calculated absorption coefficients for three versions of two-layer structures: with two perforated panels, with the face

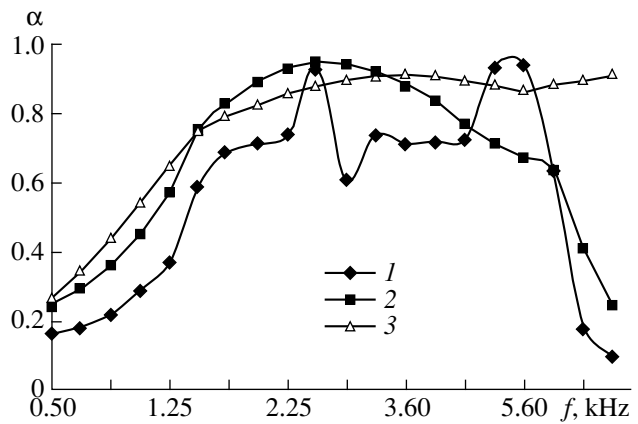


Fig. 6. Frequency dependences of the absorption coefficient of two-layer structures: (1) with perforated panels, (2) with face perforated and inner net panels, and (3) with net panels.

perforated panel and the inner net panel, and with two net panels. In the calculations, we assumed that $h_1 = h_2 = 10$ mm and the parameters of the perforated panels were $F_1 = F_2 = 10\%$ and $d_1 = d_2 = 1.5$ mm. It is seen from Fig. 6 that the SAS with the face perforated panel and the inner net panel is intermediate in terms of the absorption coefficient between the two-layer SAS with perforated panels and nets.

It should be noted that the geometric parameters of SAS were chosen for the calculations on the basis of experimental data for ensuring a high sound absorption in the frequency range of interest. However, these parameters are not optimal from the viewpoint of the earlier paper [19]. By solving the corresponding inverse problem, it is possible to select the geometric parameters in such a way that the absorption coefficient will be unity at two frequencies of the given frequency range. In this case, the advantages of using the nets will be more evident, because the dip in the frequency characteristic of α in the region between the frequencies of tuning will be noticeably less for the net structures.

Thus, the comparison between theory and experiment shows that, for all relations between the depths of the first and second layers, which are of practical interest from the point of view of using them in the ducts of aircraft engines, the calculation of the impedance of a two-layer net structure is in a satisfactory agreement with the experiment. This means that the proposed method of calculating net SAS characteristics can serve as a basis for solving the inverse problem of determining the optimal geometric parameters of net SAS for the ducts of aircraft engines with the aim to provide the maximum sound absorption bandwidth.

ACKNOWLEDGMENTS

I am grateful to R.D. Filippova and N.M. Solov'eva for providing experimental data and helpful discussions.

REFERENCES

1. J. C. Wendoloski, *J. Acoust. Soc. Am.* **104**, 122 (1998).
2. C. Tam and K. Kurbatskiĭ, *AIAA Pap.* **99-1850**, 311 (1999).
3. M. Choudhari, M. Khorrami, and J. Edwards, *AIAA Pap.* **99-1851**, 1 (1999).
4. R. E. Kraft, J. Yu, and H. W. Kwan, *AIAA Pap.* **97-1653**, 557 (1997).
5. S. N. Rzhavkin, *Lectures on the Theory of Sound* (Mosk. Gos. Univ., Moscow, 1960).
6. A. F. Sobolev, N. M. Solov'eva, and R. D. Filippova, *Akust. Zh.* **41**, 146 (1995) [*Acoust. Phys.* **41**, 124 (1995)].
7. C. K. Amedin, Y. Champoux, and A. Berry, *J. Acoust. Soc. Am.* **102**, 1982 (1997).
8. J. Yu, H. W. Kwan, and S. Chiou, *AIAA Pap.* **99-1880**, 547 (1999).
9. K. K. Ahuja and R. J. Gaeta, *AIAA Pap.* **97-1701**, 847 (1997).
10. Y. Nakamura, J. Beck, and T. Oishi, *AIAA Pap.* **97-1702**, 858 (1997).
11. J. Yu, H. W. Kwan, and R. D. Yasukawa, *AIAA Pap.* **97-1705**, 887 (1997).
12. S. N. Rzhavkin and S. T. Terosipyants, *Zh. Tekh. Fiz.* **XI** (1-2), 149 (1941).
13. I. B. Krendall, *Acoustics* (Voennaya Élektrotekh. Akad. RKKA im. Budennogo, Moscow, 1934), pp. 155-162.
14. J. W. Strutt (Lord Rayleigh), *The Theory of Sound* (Macmillan, London, 1896, 2nd ed.; Gostekhizdat, Moscow, 1955), Vol. 2.
15. M. A. Isakovich, *General Acoustics* (Nauka, Moscow, 1973).
16. A. F. Sobolev, *Akust. Zh.* **45**, 404 (1999) [*Acoust. Phys.* **45**, 357 (1999)].
17. L. B. Felsen and N. Marcuvitz, *Radiation and Scattering of Waves* (Prentice-Hall, Englewood Cliffs, 1973; Mir, Moscow, 1978), Vol. 1.
18. U. Ingard, *J. Acoust. Soc. Am.* **25**, 1037 (1953).
19. A. F. Sobolev, in *Proceedings of Third International Congress on Air- and Structure-borne Sound and Vibration, Montreal, Canada, 1994*, pp. 1925-1932.

Translated by A. Svechnikov

Ultrasonic Wave Propagation in a Solid with Frozen-in Magnetization

V. V. Sokolov* and V. V. Tolmachev**

*Moscow State Academy of Instrument Building and Information Science,
ul. Stromynka 20, Moscow, 107846 Russia

**Bauman State Technical University, Vtoraya Baumanskaya ul. 5, Moscow, 107005 Russia
e-mail: postmaster@interd.bmgtn.msk.su

Received March 22, 1999

Abstract—Ultrasonic wave propagation is studied in the framework of the continual model of a nonconducting perfect solid with frozen-in magnetization. The theoretical results are found to agree well with the experimental data. © 2000 MAIK “Nauka/Interperiodica”.

The concept of frozen-in magnetization was used in our previous paper [1] in deducing ferrohydrodynamic equations. The acoustic approximation of these equations allowed us to describe the experimental results on the anisotropy of the ultrasonic velocity in magnetized magnetic fluids [2] and predict a new Alfvén-type hydrodynamic wave [3].

Below, we show that the concept of frozen-in magnetization is also useful for studying solid magnetized media. The proposed theory of elastic wave propagation is based on the model of a perfect solid with a magnetization frozen into it [4]. The limits of applicability of this model are determined by the following conditions: $\omega\tau \gg 1$, where ω is the frequency of the elastic disturbance and τ is the relaxation time of the magnetic field strength relaxing to its thermodynamic-equilibrium value, and $\omega \ll \omega_0$, where ω_0 is the Larmor frequency.

Let us formulate the conditions of the magnetization freezing in the material of a solid. The magnetization of a body can be represented as a result of an infinitesimal displacement of two imaginary “liquids” possessing magnetic charges; these charges completely compensate each other at any point of the medium when the “liquids” are not displaced. A solid with a magnetization \mathbf{M} is magnetically equivalent to such a body with the same magnetization, if the volume density ρ_m and the surface density σ_m of magnetic charges of this body satisfy the conditions

$$\rho_m = -\operatorname{div}\mathbf{M}, \quad \sigma_m = M_n,$$

where M_n is the projection of \mathbf{M} on the outer normal to the body. Then, the condition of the magnetization freezing in the material of the solid at every point of its volume is equivalent to the condition of freezing-in for the magnetic charges and is expressed in the form

$$\rho'_m dV' = \rho_m dV,$$

where the prime indicates the quantities corresponding to the displaced points of the body, the displacement value being characterized by the Lagrange variations $\delta^*\mathbf{q}$. Thus, the magnetic charges of infinitesimal volume elements of the medium remain constant under the variation. Then, we obtain the relation

$$\delta^*\rho_m = -\rho_m \operatorname{div}(\delta^*\mathbf{q}).$$

Now, we consider the displacement vector \mathbf{l} that characterizes the displacement of a particle with a positive charge relative to one with a negative charge. The Lagrange variation of this vector is given by the formula

$$\delta^*\mathbf{l} = \delta^*(\mathbf{r} + \mathbf{l}) - \delta^*(\mathbf{r}) = (\mathbf{l}\nabla)\delta^*\mathbf{q}.$$

Using the two relations obtained above, we derive the expression for the variation of the magnetization $\mathbf{M} = \rho_m \mathbf{l}$:

$$\delta^*\mathbf{M} = (\mathbf{M}\nabla)\delta^*\mathbf{q} - \mathbf{M}(\nabla\delta^*\mathbf{q}).$$

Dividing both members of this equality by an infinitesimal time interval dt , we obtain an equation for the varying magnetization:

$$\frac{d\mathbf{M}}{dt} = (\mathbf{M}\nabla)\mathbf{v} - \mathbf{M}\operatorname{div}\mathbf{v}.$$

It is convenient to introduce the specific magnetization, i.e., the magnetization per unit mass $m = \mathbf{M}/\rho$, where ρ is the density of the solid. With allowance for the continuity equation, we reduce the equation obtained above to the form

$$\frac{dm}{dt} = (\mathbf{m}\nabla)\mathbf{v}. \quad (1)$$

In our previous publication [4], we presented a system of magnetoelastic equations for a nonconducting perfect solid with a magnetization frozen into it:

$$\begin{aligned} \frac{d\rho}{dt} + \rho \frac{\partial}{\partial t} \left(\frac{\partial q_i}{\partial x_i} \right) &= 0; \\ \frac{dm_i}{dt} &= m_k \frac{\partial}{\partial x_k} \left(\frac{\partial q_i}{\partial t} \right); \\ \rho \frac{d^2 q_i}{dt^2} &= \frac{\partial}{\partial x_n} \left(\rho \frac{\partial u}{\partial q_{k,n}} \left(\delta_{ki} - \frac{\partial q_k}{\partial x_i} \right) \right. \\ &\quad \left. + \rho m_n \left(\frac{\partial u}{\partial m_i} \right)_{s,p} \right) - H_i \frac{\partial(\rho m_j)}{\partial x_j}; \\ \nabla^2 \psi &= 4\pi \frac{\partial(\rho m_j)}{\partial x_j}; \quad H_i = -\frac{\partial \psi}{\partial x_i}. \end{aligned} \quad (2)$$

The system of equations is closed by setting a specific form of the internal energy density u , which depends on the invariants of the tensor composed of the spatial derivatives $q_{i,j}$ of the displacement vector q_i for individual points of the solid, on the specific entropy s , and on the components of the specific magnetization vector m_i . The latter two equations of system (2) are the Maxwell magnetostatic equations, where ψ is the scalar potential of the magnetic field.

The derivation of this system of equations is based on the generalized principle of virtual displacements [5] and on the concept of magnetization frozen in the material of the body. It is analogous to the derivation of the ferrohydrodynamic equations with frozen-in magnetization, which is described in detail in our previous publication [1].

The specific feature of system (2) is the equation for the magnetization that expresses (as was shown above) the condition of the magnetization freezing in the material of the solid. The system of magnetoelastic equations (2) makes it possible to study the behavior of solids without restricting oneself to the case of magnetic saturation.

Let us consider the propagation of longitudinal and shear linear waves in an elastically isotropic, nonconducting solid in terms of the system of equations (2). At the first step, we set the form of the functional dependence of the internal energy. We assume that the internal energy density $U = \rho u$ of the solid is an additive function (see [6, 7])

$$\begin{aligned} U &= \frac{\lambda}{2} (\epsilon_{xx} + \epsilon_{yy} + \epsilon_{zz})^2 + \mu (\epsilon_{xx}^2 + \epsilon_{xy}^2 + \epsilon_{xz}^2 + \epsilon_{yy}^2 \\ &\quad + \epsilon_{yz}^2 + \epsilon_{zz}^2) + \beta_1 (m_x^2 \epsilon_{xx} + m_y^2 \epsilon_{yy} + m_z^2 \epsilon_{zz}) \\ &\quad + 2\beta_2 (m_x m_y \epsilon_{xy} + m_y m_z \epsilon_{yz} + m_z m_x \epsilon_{zx}) \\ &\quad + K (m_x^2 m_y^2 + m_y^2 m_z^2 + m_x^2 m_z^2), \end{aligned} \quad (3)$$

where $\epsilon_{ij} = \frac{1}{2} \left(\frac{\partial q_i}{\partial x_j} + \frac{\partial q_j}{\partial x_i} \right) = \frac{1}{2} (q_{i,j} + q_{j,i})$ is the strain tensor, λ and μ are the Lamé coefficients, β_1 and β_2 are the adiabatic constants of magnetoelastic coupling, and K is the anisotropy constant.

We assume that the solid under study is placed in a homogeneous, stationary, constant external magnetic field of strength H , and the z -axis of the Cartesian coordinate system is directed along the magnetic field vector.

Then, in an unperturbed state, the magnetization vector has only one nonzero component $m_z = m_0$. With allowance for the explicit form of the functional dependence of the internal energy (3), equations (2) linearized near the unperturbed state have the form

$$\begin{aligned} \rho_0 \frac{\partial^2 q_x}{\partial t^2} &= (\lambda + 2\mu) \frac{\partial^2 q_x}{\partial x^2} + \mu \frac{\partial^2 q_x}{\partial y^2} + (\mu + m_0^2 \beta_2) \frac{\partial^2 q_x}{\partial z^2} \\ &\quad + (\lambda + \mu) \frac{\partial^2 q_y}{\partial x \partial y} (\lambda + \mu + m_0^2 \beta_2) \frac{\partial^2 q_z}{\partial x \partial z} + m_0^3 K \frac{\partial m_x}{\partial z}; \\ \rho_0 \frac{\partial^2 q_y}{\partial t^2} &= (\lambda + 2\mu) \frac{\partial^2 q_y}{\partial y^2} + \mu \frac{\partial^2 q_y}{\partial x^2} + (\mu + m_0^2 \beta_2) \frac{\partial^2 q_y}{\partial z^2} \\ &\quad + (\lambda + \mu) \frac{\partial^2 q_x}{\partial x \partial y} (\lambda + \mu + m_0^2 \beta_2) \frac{\partial^2 q_z}{\partial y \partial z} + m_0^3 K \frac{\partial m_y}{\partial z}; \\ \rho_0 \frac{\partial^2 q_z}{\partial t^2} &= (\lambda + 2\mu + 2m_0^2 \beta_1) \frac{\partial^2 q_z}{\partial z^2} \\ &\quad + (\lambda + \mu) \left(\frac{\partial^2 q_x}{\partial x \partial z} + \frac{\partial^2 q_y}{\partial y \partial z} \right) + \mu \left(\frac{\partial^2 q_x}{\partial x^2} + \frac{\partial^2 q_y}{\partial y^2} \right); \\ \frac{\partial m_x}{\partial t} &= m_0 \frac{\partial}{\partial z} \left(\frac{\partial q_x}{\partial t} \right); \\ \frac{\partial m_y}{\partial t} &= m_0 \frac{\partial}{\partial z} \left(\frac{\partial q_y}{\partial t} \right); \\ \frac{\partial m_z}{\partial t} &= m_0 \frac{\partial}{\partial z} \left(\frac{\partial q_z}{\partial t} \right). \end{aligned} \quad (4)$$

Without loss of generality, we consider the propagation of plane monochromatic waves with the cyclic frequency ω and the wave vector \mathbf{k} lying in the yz plane. We denote the angle between the wave vector \mathbf{k} and the

z axis by ϑ . As a result, the system of equations (4) takes the form

$$\begin{aligned} &[\omega^2 - k^2(c_{0t}^2 \sin^2 \vartheta + (c_{0t}^2 + \Delta_t) \cos^2 \vartheta)]q_x = 0; \\ &[\omega^2 - k^2(c_{0l}^2 \sin^2 \vartheta + (c_{0l}^2 + \Delta_l) \cos^2 \vartheta)]q_y \\ &\quad - [k^2(c_d^2 + b) \sin 2\vartheta]q_z = 0; \\ &[k^2(c_d^2 + b) \sin 2\vartheta]q_y \\ &\quad - [\omega^2 - k^2(c_{0t}^2 \sin^2 \vartheta + (c_{0t}^2 + \Delta_t) \cos^2 \vartheta)]q_z = 0, \end{aligned} \quad (5)$$

where

$$\begin{aligned} c_{0l}^2 &= \frac{\lambda + 2\mu}{\rho_0}; \quad c_{0t}^2 = \frac{\mu}{\rho_0}; \quad c_s^2 = \frac{c_{0l}^2 + c_{0t}^2}{2}; \\ c_d^2 &= \frac{c_{0l}^2 - c_{0t}^2}{2}; \quad \Delta_l = 4\frac{\beta_1 m_0^2}{\rho_0}; \\ \Delta_t &= \frac{2m_0^2(\beta_2 + m_0^2 K)}{\rho_0}; \quad b = \frac{\beta_2 m_0^2}{2\rho_0}. \end{aligned}$$

From the first equation of this system, it follows that the velocity of the transverse elastic wave is determined by the expression

$$c_t^A = \sqrt{c_{0t}^2 + \Delta_t \cos^2 \vartheta}, \quad (6)$$

because the particle displacements in this wave occur along the x axis ($q_x \neq 0$, $q_y = 0$, $q_z = 0$).

The second and third equations of system (5) yield the dispersion equation

$$\begin{aligned} &\omega^4 - 2\omega^2(c_s^2 + \Delta_s \cos^2 \vartheta) + 2k^4 c_d^2 (\Delta_l \sin^2 \vartheta \\ &\quad + \Delta_t \cos^2 \vartheta + 2B \sin^2 \vartheta) \cos^2 \vartheta + k^4 [(2c_{0t}^2 \Delta_s \\ &\quad + \Delta_l \Delta_t \cos^2 \vartheta + 4b^2 \sin^2 \vartheta) \cos^2 \vartheta + c_{0l}^2 c_{0t}^2] = 0. \end{aligned}$$

The solutions to this equation determine the velocity of the quasi-longitudinal elastic wave ($q_x = 0$, $q_y \neq 0$, $q_z \neq 0$)

$$c_l = \sqrt{c_s^2 + \Delta_s \cos^2 \vartheta + (c_d^2 - \Delta_d \cos^2 \vartheta) \sqrt{1 - A \sin 2\vartheta}} \quad (7)$$

and the velocity of the quasi-transverse elastic wave

$$c_t = \sqrt{c_s^2 + \Delta_s \cos^2 \vartheta - (c_d^2 - \Delta_d \cos^2 \vartheta) \sqrt{1 - A \sin 2\vartheta}}. \quad (8)$$

Here, we use the following notation:

$$\begin{aligned} \Delta_s &= (\Delta_l + \Delta_t)/2; \quad \Delta_d = (\Delta_l - \Delta_t)/2; \\ A &= \frac{c_d^2(\Delta_d + 2b) + b^2}{(c_d^2 + \Delta_d \cos^2 \vartheta)^2}. \end{aligned}$$

In the zero magnetization limit, formulas (6)–(8) yield the well-known results [6]:

$$c_t = c_t^A = c_{0t} = \sqrt{\frac{\mu}{\rho_0}}; \quad c_l = c_{0l} = \sqrt{\frac{\lambda + 2\mu}{\rho_0}}. \quad (9)$$

Relations (9) remain also valid when the magnetic field is orthogonal to the wave vector ($\vartheta = \pi/2$) and the magnetization is arbitrary. At $\vartheta = 0$, the velocities of the transverse and quasi-transverse waves described by relations (6) and (8) coincide.

We note that at $\vartheta = 0$, from the latter two equations of system (5) it follows that the elastic wave whose velocity is determined by formula (7) is a purely longitudinal one, and the elastic wave with the velocity determined by formula (8) is a purely transverse one. The superscript A marking the velocity of the transverse wave in formula (6) means that this wave is an analog of the Alfvén wave in magnetohydrodynamics [8] and ferrohydrodynamics [1–3]. In the limiting case $\mu \rightarrow 0$, which corresponds to a magnetized fluid, expression (6) yields the relation $c_t^A \propto m_0 \cos \vartheta$, which coincides with the expression for the velocity of an Alfvén wave propagating in a magnetic fluid with a frozen magnetization [1–3]. Below, we will call this wave the modified transverse wave.

Experimental studies of the effect of magnetic field on the velocity of ultrasonic wave propagation are usually based on the measurements of the relative variation of the ultrasonic velocity. Therefore, we recast expressions (6)–(8) to the form

$$\begin{aligned} \frac{\Delta c_l}{c_{0l}} &= \frac{c_l - c_{0l}}{c_{0l}} = \frac{1}{2c_{0l}^2} (\Delta_s \cos^2 \vartheta - c_d^2 \\ &\quad + (c_d^2 + \Delta_d \cos^2 \vartheta) \sqrt{1 - A \sin 2\vartheta}); \end{aligned} \quad (10)$$

$$\begin{aligned} \frac{\Delta c_t}{c_{0t}} &= \frac{c_t - c_{0t}}{c_{0t}} = \frac{1}{2c_{0t}^2} (c_d^2 + \Delta_s \cos^2 \vartheta \\ &\quad - (c_d^2 + \Delta_d \cos^2 \vartheta) \sqrt{1 - A \sin 2\vartheta}); \end{aligned} \quad (11)$$

$$\frac{\Delta c_t^A}{c_{0t}} = \frac{c_t^A - c_{0t}}{c_{0t}} = \frac{\Delta_t}{2} \cos^2 \vartheta \quad (12)$$

and consider the behavior of the resulting dependences.

To obtain numerical estimates, we perform the calculations by using the parameters: $\rho_0 = 8.8 \text{ g/cm}^3$, $c_{0l} = 5.5 \times 10^5 \text{ cm/s}$, $c_{0t} = 3 \times 10^5 \text{ cm/s}$, $K = 0$, and $m_s = 55 \text{ Gs}$. These values correspond to nickel [9]. The dependence of the specific magnetization on the external field can be approximated by the simple relation

$$m_0 = m_s \tanh\left(\frac{H}{H_*}\right).$$

The experimental data for nickel are adequately described by this formula at $H_* = 700 \text{ Oe}$.

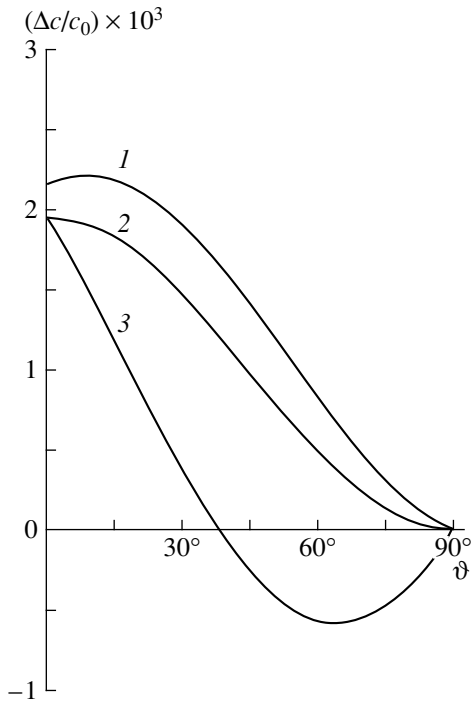


Fig. 1. Dependence of the relative variation of the elastic wave velocity on the propagation direction in the case of magnetic saturation: (1) the quasi-longitudinal wave, (2) the modified transverse wave, and (3) the quasi-transverse wave.

Let the solid be a magnetically isotropic one; then, we set $\beta_1 = 2\beta_2 = 10^6 \text{ g}^2/\text{cm}^6$ and $K = 0$.

Figure 1 shows the angular dependence of the relative variation of the longitudinal wave velocity (curve 1) calculated by formula (10) and similar dependences for the transverse wave velocities (curves 2 and 3) calculated by formulas (12) and (11) (respectively). The dependences presented in Fig. 1 correspond to the case of magnetic saturation ($m_0 = m_s$). We note that the angular dependences of the transverse wave and the modified transverse wave are noticeably different, which can be used in the experimental check of the proposed theory.

The effect of the magnetizing field on the relative variation of the elastic wave velocity is illustrated in Figs. 2 and 3. The curves in Fig. 2 describe the case of the parallel orientation of the wave vectors and the magnetic field vector, i.e., $\vartheta = 0^\circ$; the curves in Fig. 3 correspond to the case $\vartheta = 30^\circ$. In both figures, curves 1 refer to the quasi-longitudinal wave, curves 2 refer to the quasi-transverse wave, and curves 3 refer to the modified transverse wave. We note that, in the case of the parallel orientation of the wave vectors and the magnetic field, the relative variations of the velocities of the transverse and the modified transverse waves are identical, and, therefore, curves 2 and 3 in Fig. 2 coincide.

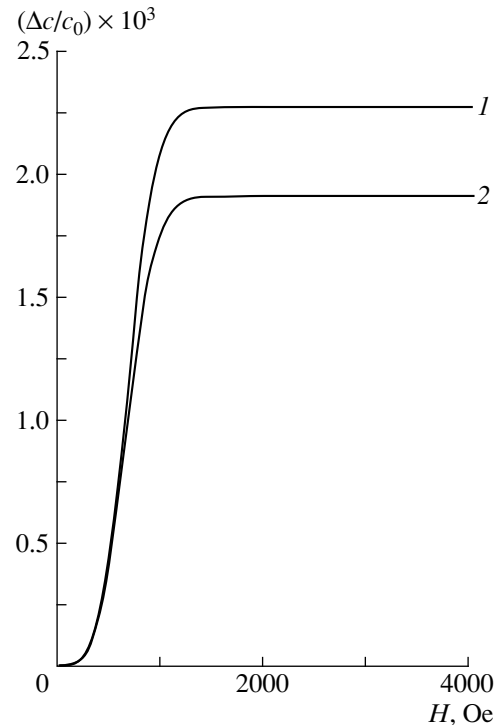


Fig. 2. Dependence of the relative variation of the elastic wave velocity on the magnetic field strength at $\vartheta = 0$: (1) the quasi-longitudinal wave, (2) the quasi-transverse wave, and (3) the modified transverse wave.

The comparison of our results with the known experimental data, which are reviewed in the monographs [9, 10], shows their qualitative agreement. It should be noted that the previous theoretical models provide no adequate explanation for the fact that, in polycrystalline nickel, the relative variation in the transverse wave velocity caused by a magnetic field is two to three times as great as the corresponding variation for the longitudinal waves, while the saturation for shear waves occurs at higher magnetic fields [11].

As one can see from Fig. 4, these results are adequately described by the proposed theory. Curves 1 and 2 are calculated by formulas (11) and (10), respectively. The values of the adiabatic constants were taken to be $\beta_1 = 1.45 \times 10^6 \text{ g}^2/\text{cm}^6$ and $\beta_2 = 1.65 \times 10^6 \text{ g}^2/\text{cm}^6$.

We also point out the qualitative agreement of our theoretical results with the experimental data on the velocity of longitudinal ultrasonic waves in amorphous magnetized ribbons [12]. Unfortunately, an exact numerical comparison with these data is impossible, because the aforementioned publication [12] provides no basic physical parameters of the specimens, such as density, magnetization, and elastic moduli.

The experimental study [13] of elastic waves propagating in magnetite in a wide temperature range showed that, in magnetic field oriented parallel to the wave vector, the velocity of longitudinal waves is

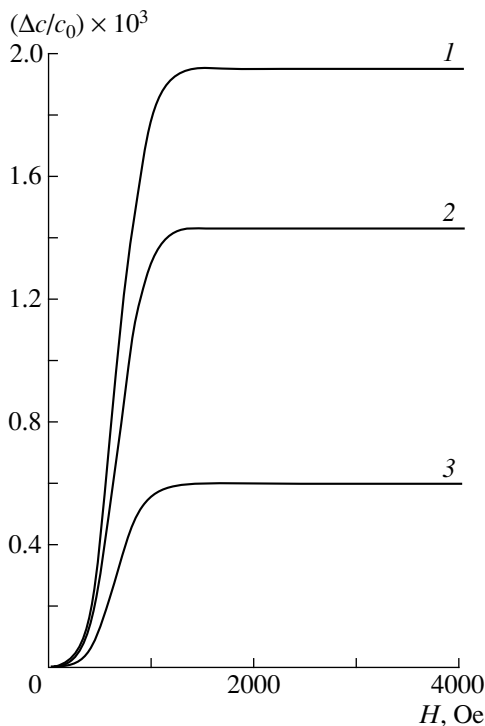


Fig. 3. Dependence of the relative variation of the elastic wave velocity on the magnetic field strength at $\vartheta = 30^\circ$: (1) the quasi-longitudinal wave, (2) the quasi-transverse wave, and (3) the modified transverse wave.

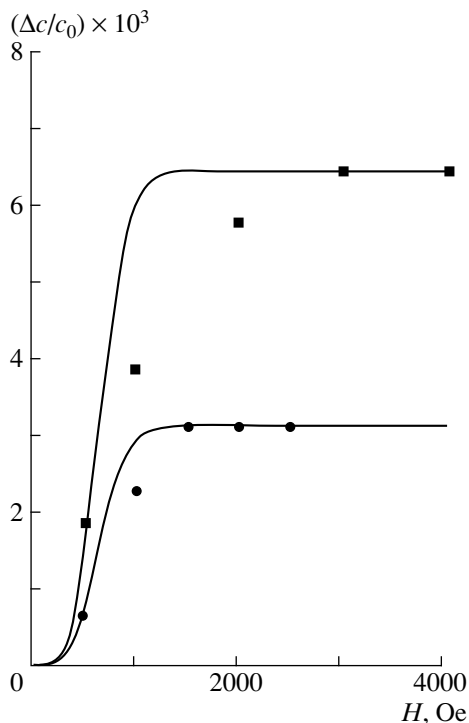


Fig. 4. Comparison of the theoretical results with the experimental data [10]: the relative variation of the propagation velocity for the longitudinal (circles) and transverse (squares) waves.

greater than in the case of the orthogonal orientation of magnetic field, which agrees with our results.

In closing, we formulate the main results of our study.

It is shown that, in a nonconducting solid with a frozen-in magnetization, the propagation of three types of waves is possible: the modified transverse wave, the quasi-transverse wave, and the quasi-longitudinal one.

At $\vartheta = 0$, the quasi-longitudinal wave degenerates into a purely longitudinal one, and the modified transverse wave and the quasi-transverse wave merge into a single purely transverse wave.

The theoretical results are found to agree well with the experimental data on the dependence of the velocity of longitudinal and transverse waves in polycrystalline nickel on the magnetizing field strength.

REFERENCES

1. V. V. Sokolov and V. V. Tolmachev, *Magn. Gidrodin.* **32**, 318 (1996).
2. V. V. Sokolov and V. V. Tolmachev, *Akust. Zh.* **43**, 106 (1997) [*Acoust. Phys.* **43**, 92 (1997)].
3. V. V. Sokolov and V. V. Tolmachev, *Pis'ma Zh. Tekh. Fiz.* **23**, 88 (1997) [*Tech. Phys. Lett.* **23**, 5 (1997)].
4. V. V. Sokolov and V. V. Tolmachev, in *Proceedings of the 11th International Winter Advanced-Study School on Mechanics of Continuous Media* (Institute of Mathematics and Mechanics, Ural Division, Russian Academy of Sciences, Perm, 1997), Vol. 2, p. 266.
5. V. V. Tolmachev, A. M. Golovin, and V. S. Potapov, *Thermodynamics and Electrodynamics of Continuous Media* (Mosk. Gos. Univ., Moscow, 1988).
6. J. W. Tucker and V. W. Rampton, *Microwave Ultrasonics in Solid State Physics* (North Holland, Amsterdam, 1972; Mir, Moscow, 1975).
7. B. A. Goldin, L. N. Kotov, L. K. Zarembo, and S. N. Karpachev, *Spin-Phonon Interactions in Crystals (Ferrites)* (Nauka, Leningrad, 1991).
8. H. Alfven, *Cosmical Electrodynamics* (Clarendon, Oxford, 1950; Inostrannaya Literatura, Moscow, 1952).
9. L. Bergmann, *Der Ultraschall und seine Anwendung in Wissenschaft und Technik* (Hirzel, Zürich, 1954; Inostrannaya Literatura, Moscow, 1957).
10. R. Truell, C. Elbaum, and B. B. Chick, *Ultrasonic Methods in Solid State Physics* (Academic Press, New York, 1969; Mir, Moscow, 1972).
11. S. J. Jonson and T. F. Roges, *J. Appl. Phys.* **23**, 574 (1952).
12. E. Hristoforout, H. Chiriact, M. Neagu, and I. Darie, *J. Phys. D: Appl. Phys.* **27**, 1595 (1994).
13. S. Isida, M. Suzuki, S. Todo, *et al.*, *J. Phys. Soc. Jpn.* **67**, 3125 (1998).

Translated by E. Golyamina

Numerical Modeling of the Reflection Coefficients for the Plane Sound Wave Reflection from a Layered Elastic Bottom

M. S. Fokina and B. N. Fokin

*Institute of Applied Physics, Russian Academy of Sciences,
ul. Ul'yanova 46, Nizhni Novgorod, 603600, Russia
e-mail: fok@hydro.appl.sci-nnov.ru*

Received December 31, 1998

Abstract—The matrix method and its numerical realization are considered in calculating the complex reflection coefficients and refraction indices of plane sound waves for geoacoustic models of the ocean bottom in the form of homogeneous elastic (liquid) absorbing layers overlying an elastic halfspace. In calculating the reflection coefficients at high frequencies or in the presence of a large numbers of sedimentary layers, a passage from the Thomson–Haskell matrix approach to the Dunkin–Thrower computational scheme is performed. The results of test calculations are presented. With the aim of developing resonance methods for the reconstruction of the parameters of layered elastic media, the behavior of the frequency-angular dependences of the reflection coefficient are studied for various geoacoustic bottom models. The structure of the angular and frequency resonances of the reflection coefficients is revealed. The dependence of the structure (the position, width, and amplitude) of two types of resonances on the parameters of the layered bottom is considered. © 2000 MAIK “Nauka/Interperiodica”.

The interest in considering the processes of the reflection and propagation of sound in waveguides with an elastic layered bottom is related to the development of the methods and means for the diagnostics and reconstruction of the bottom characteristics, as well as to the urgency of mineral, oil, and gas prospecting at a sea shelf by acoustic methods. To model the sound interaction with the ocean bottom, the reflection coefficients of plane waves are conventionally used. The mathematical methods of describing plane wave interactions with elastic layered media have been developed in a number of classical works [1–6]. The matrix method of calculating the plane wave reflection coefficients and refraction indices, which was developed by Molotkov [3, 4], was successfully used in our previous paper [7] for interpreting experimental data. The method of tensor impedances allowing the calculation of the reflection coefficients for media with piecewise-constant elastic and inertial parameters is presented by Machevariani *et al.* [5]. In this case, the problem is reduced to a set of Riccati differential equations, which can be solved by the Runge–Kutta method. Prikhod'ko and Tyutekin [6] used the impedance method for numerically calculating the elastic wave characteristics in continuously layered solid media. Many publications [8–11] are devoted to studies of the reflection and propagation of sound in layered elastic media. However, the use of complex bottom models in the modeling of sound reflection and propagation began only in recent years. Our interest is in the study of both the

necessity to take into account the bottom parameter variation with depth [12, 13] and the relation between the sea bottom reflectivity and its acoustic characteristics [14–17].

In this paper, we numerically realized the Thomson–Haskell matrix method [18, 19], which is conventionally used for describing layered elastic media. According to this method, each elastic medium is characterized by a fourth-order matrix, and the whole system is described by a matrix that is obtained by multiplying the characteristic matrices of all media. The elements of this matrix allow one to calculate the interference reflection coefficients and refraction indices, as well as the dispersion characteristics of the interference waves. However, the domain of the validity of the Thomson–Haskell computational scheme turns out to be basically restricted. In this connection, we passed from the fourth-order characteristic matrices to the sixth-order matrices first suggested by Dunkin [20] and Thrower [21]. Theoretically developed by Molotkov [3, 4] and numerically realized in this paper, the Dunkin–Thrower approach allowed one to increase the accuracy of computer calculations of the reflection coefficients of plane waves. A program based on the matrix method was tested, and the test calculations were compared with data on the angular dependences of reflection losses for the reflection from a hypothetical turbidite layers [22]. The numerical calculations were used to illustrate the behavior of the frequency-angular resonances and absorption effects for various

layered elastic/liquid bottom models. Changes in the structure of resonances (their location, width, and amplitude) with the variations in the radiation frequency, grazing angle, and shear elasticity in the layer and the underlying halfspace was considered. These investigations were performed with the aim of developing the resonance methods for the reconstruction of the parameters of a layered elastic bottom.

The physical model of the medium is presented as a set of n plane-parallel elastic layers overlying an elastic halfspace. The z axis is directed upward, along the normal to the horizontally stratified elastic layers $j = 1, 2, \dots, n$, where n is the number of the elastic layers. Within a sedimentary elastic layer, the density ρ_j , the velocities of the longitudinal c_{lj} and transverse c_{tj} waves, and the attenuation coefficients of the longitudinal η_{lj} and transverse η_{tj} waves are deemed to be constant. The water column (0) and the elastic base (∞) are homogeneous halfspaces. In all layers, including the elastic halfspace, the attenuation effects are taken into account by introducing the complex velocities of the longitudinal and transverse waves $c_j = c_{re} + ic_{im}$. In turn, the wave numbers will also be complex quantities.

We consider only vertically polarized waves the SV -type, for which the components of the displacement vector \mathbf{U} are confined in the (x, z) plane and the displacement along the y axis is absent. The displacement vectors can be written in terms of the scalar ϕ and the vector ψ potentials

$$\mathbf{U} = \text{grad}\phi + \text{rot}\psi. \quad (1)$$

For the SV -wave, the potential ψ has a single y -component in an elastic medium and equals zero in water. In the Cartesian coordinates, the displacements in each j th layer are expressed in terms of the potentials ϕ_j and ψ_j :

$$\begin{aligned} U_x &= \partial\phi_j/\partial x - \partial\psi_j/\partial z, \\ U_z &= \partial\phi_j/\partial z + \partial\psi_j/\partial x, \end{aligned} \quad (2)$$

these potentials satisfying the Helmholtz equations

$$\begin{aligned} \Delta\phi_j + \alpha_j^2\phi_j &= 0, \\ \Delta\psi_j + \beta_j^2\psi_j &= 0, \end{aligned} \quad (3)$$

where $\alpha_j^2 = k_{lj}^2 - \xi^2$, $\beta_j^2 = k_{tj}^2 - \xi^2$, and $\xi = (\omega/c_0)\sin\theta_0$. The relation of the normal σ_{zzj} and the tangential σ_{xzj} components of the stress tensor to the potentials ϕ_j and ψ_j has the form

$$\begin{aligned} \sigma_{xzj} &= 2\mu_j(\partial^2\phi_j/\partial x\partial z - \partial^2\psi_j/\partial z^2), \\ \sigma_{zzj} &= -\lambda_j\partial^2\phi_j/\partial x^2 \\ &+ (\lambda_j + 2\mu_j)\partial^2\phi_j/\partial z^2 + \partial^2\psi_j/\partial x\partial z, \end{aligned} \quad (4)$$

where λ_j and μ_j are the Lamé constants; $c_{lj} = \sqrt{(\lambda_j + 2\mu_j)/\rho_j}$ and $c_{tj} = \sqrt{\mu_j/\rho_j}$. The given layered elastic system is excited by a plane wave of the unit amplitude $\phi_0^+ = 1$, which is assumed to arrive from the liquid halfspace. The wave system in the liquid and elastic halfspaces is written as

$$\begin{aligned} \phi_0(z) &= \phi_0^+ \exp(-i\alpha_0 z) + \phi_0^- \exp(i\alpha_0 z), \\ \psi_0(z) &= 0, \\ \phi_\infty(z) &= \phi_\infty^+ \exp(-i\alpha_\infty z), \\ \psi_\infty(z) &= \psi_\infty^+ \exp(-i\beta_\infty z), \end{aligned} \quad (5)$$

where $\phi_0^- = V$ is the reflection coefficient in the liquid halfspace, and $\phi_\infty^+ = W_l$ and $\psi_\infty^+ = W_t$ are the refraction indices of the longitudinal and the transverse waves in the elastic halfspace. At the interface between the liquid and the elastic media, three boundary conditions are set, while, at the boundaries of the elastic media at $z = H_j$, the conditions of the rigid contact are fulfilled, and four boundary conditions can be written [1]. The solutions of equations (3) in the elastic layers j are represented in terms of the potentials ϕ_j and ψ_j describing the longitudinal and the transverse waves

$$\begin{aligned} \phi_j &= \phi_j^+ \exp(i\alpha_j z) + \phi_j^- \exp(-i\alpha_j z), \\ \psi_j &= \psi_j^+ \exp(i\beta_j z) + \psi_j^- \exp(-i\beta_j z), \end{aligned} \quad (6)$$

where ϕ_j^+ , ϕ_j^- , ψ_j^+ , and ψ_j^- are some arbitrary functions that characterize the elastic waves propagating in the positive (with the superscript $-$) and negative (with the superscript $+$) directions of the z -axis. Substituting expressions (6) in the boundary conditions [1] and performing the differentiation at the boundaries, we obtain $4(n+1)$ equations in $4(n+1)$ unknowns. We introduce the column vector $Z_j = (\phi_j^+, \phi_j^-, \psi_j^+, \psi_j^-)^T$, the diagonal matrix $L_j = [\exp(i\alpha_j h_j), \exp(-i\alpha_j h_j), \exp(i\beta_j h_j), \exp(-i\beta_j h_j)]$, and the characteristic matrix of the 4th order A_j for the j th layer, where h_j is the layer thickness [3, 4]. For the system of n elastic layers and the elastic halfspace, the following matrix equation is valid:

$$Z_n = D \times Z_\infty, \quad (7)$$

where $D = A_n^{-1} \times A_{n-1} \times L_{n-1} \times A_{n-1}^{-1} \times \dots \times A_j \times L_j \times A_j^{-1} \times \dots \times A_1 \times L_1 \times A_1^{-1} \times A_\infty$ is the matrix of the 4th order with the elements D_{lm} , where $l, m = 1, 2, 3, 4$, and this matrix characterizes the elastic halfspace. For the combined description of the liquid and layered elastic halfspaces, with allowance for (6), we can write six boundary conditions. In this case, the liquid halfspace is characterized by the matrix of the 2th order Q_{pv} ,

where $p, v = 1, 2$. For solving the system of linear algebraic equations with respect to $\varphi_\infty^+ = W_l, \psi_\infty^+ = W_t$,

$\varphi_0^- = V, U_{x_\infty}, U_{z_\infty}$, and σ_{zz_∞} , we use the principal determinant Δ of the set of equations

$$\Delta = \begin{vmatrix} 0 & (Q_{11}D_{21} + Q_{12}D_{41}) & (Q_{11}D_{23} + Q_{12}D_{43}) & 0 \\ -1 & (Q_{21}D_{21} + Q_{22}D_{41}) & (Q_{21}D_{23} + Q_{22}D_{43}) & 0 \\ 0 & D_{11} & D_{13} & -1 \\ 0 & D_{31} & D_{33} & 0 \end{vmatrix} \begin{vmatrix} 1 \\ 0 \\ 0 \\ 0 \end{vmatrix}. \quad (8)$$

The solutions of the set of equations are found according to Cramer's rule: $\chi_k = \Delta_k/\Delta, k=1, 2, 3$, where χ_k has the meaning of the plane wave reflection coefficient V in the liquid halfspace and the refraction indices of the longitudinal W_l and transverse W_t waves in the elastic halfspace.

In order to write the reflection coefficient and the refraction indices, we introduce the matrix of the 4th order D that characterizes the whole layered elastic medium. However, in the numerical calculation of the matrix D in the domain

$$k_{ij}h_j \operatorname{Re}\alpha_j \gg 1, \operatorname{Re}\alpha_j \gg \operatorname{Re}\beta_j, \quad (9)$$

where $k_{ij} = \omega/c_{ij}, \alpha_j = \sqrt{k_{ij}^2 - \xi^2}$, and $\beta_j = \sqrt{k_{ij}^2 - \xi^2}$, the matrix method using the Thomson–Haskell conventional approach becomes inconvenient because of the error, which is continuously accumulated for high frequencies or for great numbers of layers, as well as in the intervals between the limiting angles relating to the j th layer. In this connection, in writing a program, we used the Dunkin–Thrower [20, 21] matrix formalism, which allows one to extend the domain of validity of the matrix method and to eliminate the basic restrictions of the Thomson–Haskell approach [3, 4]. The direct transition from one approach to the other was realized on the basis of the theorem on the properties of the Gantmakher associate matrices, when the characteristic matrix D of the 4th order is set in correspondence with the matrix \hat{D} of the 6th order, with the elements being second-order minors of the matrix D :

$$D_{lm}^{ip} = \begin{vmatrix} D_{il} & D_{im} \\ D_{pl} & D_{pm} \end{vmatrix}. \quad (10)$$

From the theorem on the properties of Gantmakher associate matrices [23], it follows that the minor matrices $\hat{D}, \hat{A}_j^{-1}, \hat{L}_j$, and \hat{A}_j corresponding to the matrices D, A_j^{-1}, L_j , and A_j satisfy the relationship $\hat{D} = \hat{A}_n^{-1} \times \hat{A}_{n-1}^{-1} \times \hat{L}_{n-1} \times \hat{A}_{n-1} \times \dots \times \hat{A}_j^{-1} \times \hat{L}_j \times \hat{A}_j \times \dots \times \hat{A}_1^{-1} \times L_1 \times A_1 \times A_\infty$ and represent sixth-order matrices. In this case, the determinants of the set of six equations written at the boundaries can be expressed in terms of

the elements of the matrices of the second and sixth orders. Then, the reflection coefficient and the refraction indices of the longitudinal and transverse waves are determined by the following expressions

$$\begin{aligned} \chi_1 &= V = \Delta_1/\Delta = \{Q \times K_{ls} \times \hat{D}\}_{11}/\{Q \times K_{ls} \times \hat{D}\}_{21}, \\ \chi_2 &= W_l = \Delta_2/\Delta = D_{33}/\{Q \times K_{ls} \times \hat{D}\}_{21}, \\ \chi_3 &= W_t = \Delta_3/\Delta = -D_{31}/\{Q \times K_{ls} \times \hat{D}\}_{21}, \end{aligned} \quad (11)$$

where K_{ls} is the transfer matrix between the liquid and layered elastic halfspaces

$$K_{ls} = \begin{vmatrix} 0 & 0 & 0 & -1 & 0 & 0 \\ 0 & 0 & 0 & 0 & 0 & 1 \end{vmatrix}. \quad (12)$$

The use of the sixth-order matrices has some advantages, because the quantities that are very large in domain (9) are canceled in the calculation of the elements of the matrix \hat{D} . This allows one to perform correct calculations, provided that condition (9) is fulfilled.

The Dunkin–Thrower matrix method was realized as a computer program. The results of test calculations are represented as dependences of the bottom reflection losses $RL(\theta)$ or the reflection coefficient $V(\theta)$ on the grazing angle θ : $RL(\theta) = -20 \log(|V(\theta)|)$, where $|V| = \sqrt{\Re(V)^2 + \Im(V)^2}$ is the modulus of the complex reflection coefficient V ; $\Re(V)$ and $\Im(V)$ are the real and imaginary parts of V . For testing the program, we used the computational data for $RL(\theta)$ for a turbidite layer (table), which are presented in the paper by Vidmar and Foreman [22]. The calculations of the reflection losses for all grazing angles were performed with the use of the numerical integration of the Helmholtz equation [22], and the results of these calculations are presented in Fig. 1a. The dependences $RL(\theta)$ obtained in this paper with using the Dunkin–Thrower matrix method are presented in Fig. 1b, where the set of layers with gradients of the longitudinal and transverse velocities of sound, density, and attenuation was approximated by 17 elastic homogeneous layers. The test calculations agree well with the published results. The reflection losses increase between the critical angle $\theta_c = 50^\circ$ for

The physical parameters for the hypothetical turbidite layer [22]

Depth, m	c_l , m/s	η_l , dB/m	c_l , m/s	η_l , dB/m	ρ , g/cm ³
Water	1530	1.03
0	1510	0.0013	116	0.169	1.53
36	1582	0.0020	283	0.112	0.579
120	1674	0.0040	391	0.172	1.689
518	1992	0.0027	621	0.087	2.010
Elastic halfspace	4460	0.00016	2400	0.00079	2.460

transverse waves in the halfspace and the critical angle $\theta_l = 70^\circ$ for longitudinal waves in the same halfspace. The calculations show that the shear elasticity in the sedimentary layers modifies the resonance structure between the critical angles $\theta_l = 50^\circ$ and $\theta_l = 70^\circ$, but its effect is weak outside of this region (Fig. 1). The program for the calculation of the plane wave reflection coefficients and refraction indices for the set of homogeneous elastic layers overlying the elastic halfspace

made it possible to analyze the dependence of the resonance structure on the layered medium parameters both for the previously considered model of a liquid layer overlying a liquid halfspace [24] and for more complicated combinations of liquid and elastic layers.

Consider the effect of the acoustic parameters of the bottom on the resonance structure of the reflection coefficients for various bottom models. Figure 2 exhibits the frequency-angular dependences of the reflec-

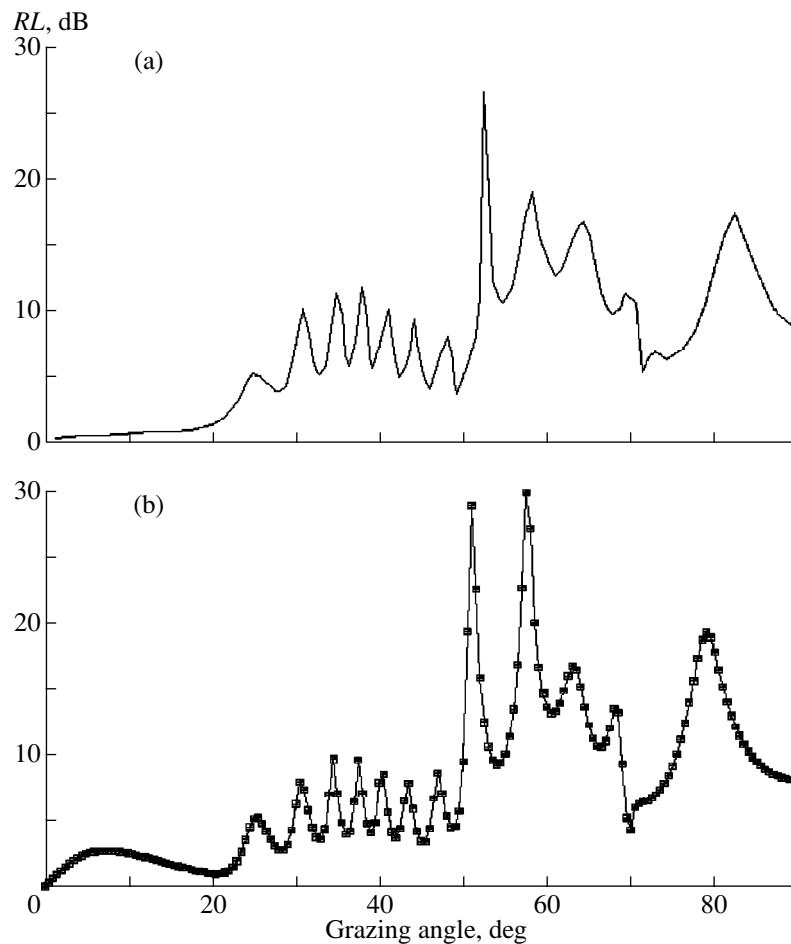


Fig. 1. Reflection loss versus the grazing angle at the frequency $f = 20$ Hz for a hypothetical turbidite layer of thickness 518 m (table): (a) a gradient set of layers (the numerical integration of the Helmholtz equation [22]); (b) an approximation by 17 homogeneous elastic layers (the Dunkin–Thrower matrix method).

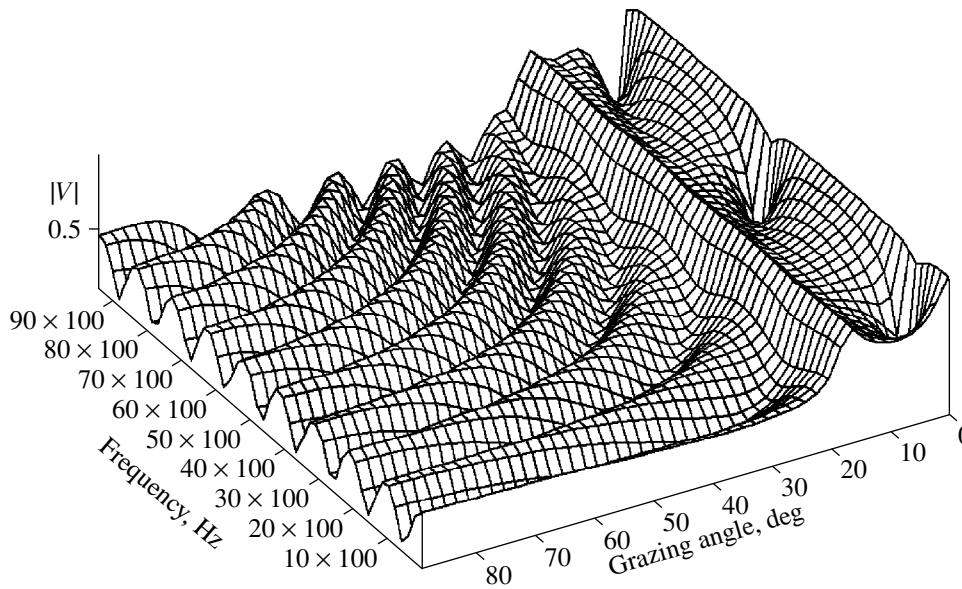


Fig. 2. Absolute value of the reflection coefficient on the frequency–grazing angle plane ($c_0 = 1500$ m/s, $\rho_0 = 1$ g/cm³, $h_1 = 0.7$ m, $c_{l1} = 1455$ m/s, $\eta_{l1} = 0$, $\rho_1 = 1.45$ g/cm³, $c_{l\infty} = 1575$ m/s, $\eta_{l\infty} = 6.35 \times 10^{-4}$, $c_{t\infty} = 1455$ m/s, $\eta_{t\infty} = 6.35 \times 10^{-4}$, and $\rho_\infty = 2.6$ g/cm³).

tion coefficient $V(f, \theta)$ for the simplest bottom model in the form of a liquid layer overlying an elastic halfspace ($c_0 = 1500$ m/s, $\rho_0 = 1$ g/cm³, $h_1 = 0.7$ m, $c_{l1} = 1455$ m/s, $\rho_1 = 1.45$ g/cm³, $c_{l\infty} = 1575$ m/s, $\eta_{l\infty} = 6.35 \times 10^{-4}$, $c_{t\infty} = 1455$ m/s, $\eta_{t\infty} = 6.35 \times 10^{-4}$, and $\rho_\infty = 2.6$ g/cm³). The parameters with indices 0, $j = 1$, and ∞ correspond to the water layer, sedimentary layer, and elastic halfspace, respectively. In the frequency–grazing angle plane, the calculated values of $V(f, \theta)$ form a complicated structure that consists of regular sequences of peaks and dips. The dependences of this kind are ascribed to resonance phenomena, the resonance structure containing all the necessary information on the medium interacting with sound [24]. Usually, the resonances of the reflection coefficients are interpreted as the maximum values of the transmission coefficient. In this case, the reflection coefficients have minimum values. In this paper, the resonances of the reflection coefficient will be interpreted as the behavior of the reflection coefficient near its local minimum.

The characteristic feature of the computational results presented in Fig. 2 is that the frequency resonances are observed even at shallow grazing angles of the order of 1° – 2° , which is associated with the allowance for the velocity of the transverse wave propagation in the halfspace $c_{t\infty}$. The behavior of the reflection coefficients near shallow grazing angles in the case of a liquid halfspace was considered in detail in [24]. The inclusion of the absorption in a liquid sedimentary layer ($\eta_{l1} = 6.35 \times 10^{-4}$) leads mainly to a decrease in the reflection coefficient and the resonance amplitudes with increasing frequency. Note that at grazing angles less than the critical angle, $\theta < \theta_{cr} = 20^\circ$, and at frequencies exceeding 6000 Hz, the resonance peaks are smoothed out and become hardly observable. This is

associated with the fact that a major part of the incident energy is absorbed in the layer at shallow grazing angles. At grazing angles exceeding the critical angle, $\theta > \theta_{cr} = 20^\circ$, this effect is also present, but is much less pronounced.

In realistic bottom models, it is necessary to take into account the intrinsic sediment layering. Therefore, if we add a liquid layer of the same thickness to the model shown in Fig. 2 ($h_1 = h_2 = 0.7$ m, $c_{l2} = 1555$ m/s, $\eta_{l2} = 0$, and $\rho_2 = 1.65$ g/cm³ and the layers are arranged so that their impedance increases with depth), the simple periodicity of resonances in the frequency–grazing angle plane will not be observed. The number of peaks remains the same; however, the resonance structure of the reflection coefficient acquires additional modulation, and the resonance amplitudes change. For layers of different thickness, $h_1 \neq h_2$, the reflection coefficient modulation is even more irregular.

Figure 3 (line 1) exhibits the calculation results for $V(f)$ in the range from 5 to 2100 Hz at a fixed grazing angle of $\theta = 2^\circ$. The bottom model was assumed to be a liquid layer overlying an elastic halfspace. At a frequency of $f_{r1} = 925$ Hz, the first local minimum of the reflection coefficient is observed, i.e., the first frequency resonance. In this case, the structure of resonances is easily distinguished in the representation of the amplitude of the process by the Breit–Wigner resonance curve on the background of a weakly varying base [25]. The width of the frequency resonance Γ is measured near the local minimum of the reflection coefficient when the amplitude of the process reaches half its value $A/2$. We similarly introduce the notions of the position γ and width θ_m of the angular resonances of the reflection coefficient. The structure of the fre-

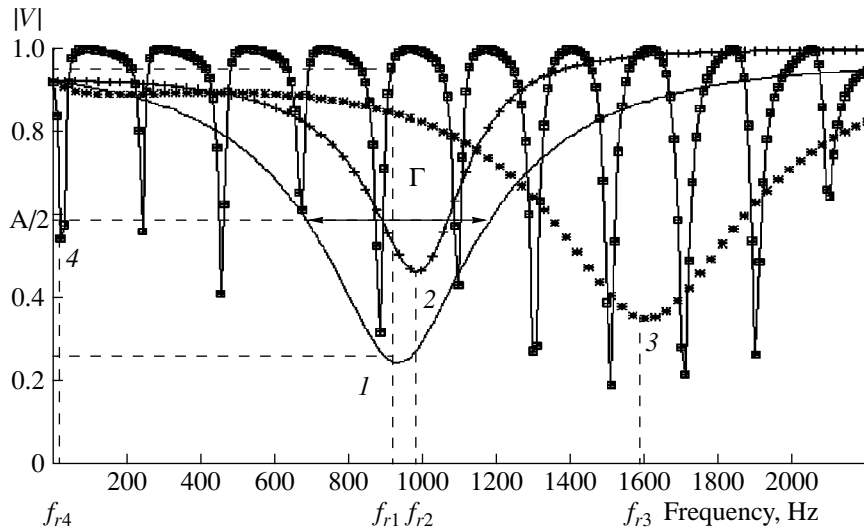


Fig. 3. Frequency dependences of the reflection coefficient $V(f)$ and the resonance structure (f_m is the m th resonance position, Γ is its width, and A is the amplitude) at a fixed grazing angle $\theta = 2^\circ$: (line 1) a liquid layer overlying an elastic halfspace; (line 2) two liquid layers overlying an elastic halfspace; (line 3) a liquid and an elastic layer overlying an elastic halfspace; and (line 4) an elastic layer overlying an elastic halfspace.

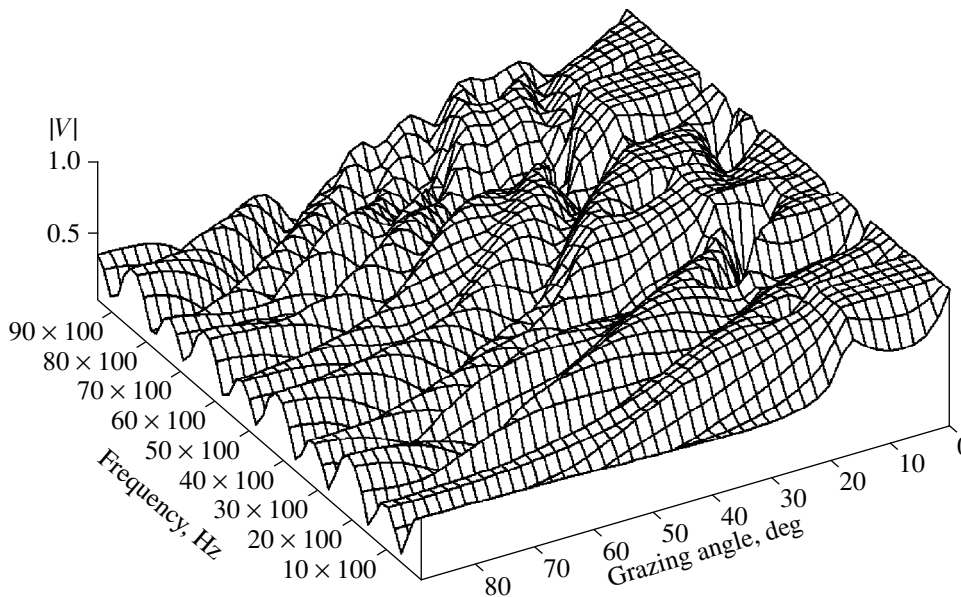


Fig. 4. Absolute value of the reflection coefficient on the frequency–grazing angle plane; the bottom model consists of a liquid and an elastic layer of the same thickness overlying an elastic halfspace ($h_1 = 0.7$ m, $c_{l1} = 1455$ m/s, $\rho_1 = 1.45$ g/cm³, $h_2 = 0.7$ m, $c_{l2} = 1455$ m/s, $c_{l2} = 300$ m/s, $\rho_2 = 1.45$ g/cm³, $c_{l\infty} = 1575$ m/s, $\eta_{l\infty} = 6.35 \times 10^{-4}$, $c_{t\infty} = 1455$ m/s, $\eta_{t\infty} = 6.35 \times 10^{-4}$, and $\rho_\infty = 2.6$ g/cm³).

quency and angular resonances depends on the acoustic properties of the sea bottom and contains all the necessary information on the medium interacting with sound.

The inclusion of additional liquid layers (Fig. 3, line 2) changes the frequency resonance position f_{r2} , decreases the width Γ and the amplitude A of the resonance. The analysis of the resonance structure is complicated because of the considerable increase in the number of the bottom parameters. The inclusion of the

shear elasticity in the second sedimentary layer in the calculation of $V(f)$ (Fig. 3, line 3) leads to further displacement of the first resonance peak f_{r3} and further changes in its width Γ and amplitude A , as compared to the resonance structure measured for more simple models with one liquid layer (Fig. 3, line 1) or two liquid layers (Fig. 3, line 2). If we consider two elastic layers overlying the halfspace ($c_{l1} = 300$ m/s, $c_{l2} = 500$ m/s), then, the frequency dependence of the reflection coefficient at a fixed grazing angle of $\theta = 2^\circ$ (Fig. 3, line 4)

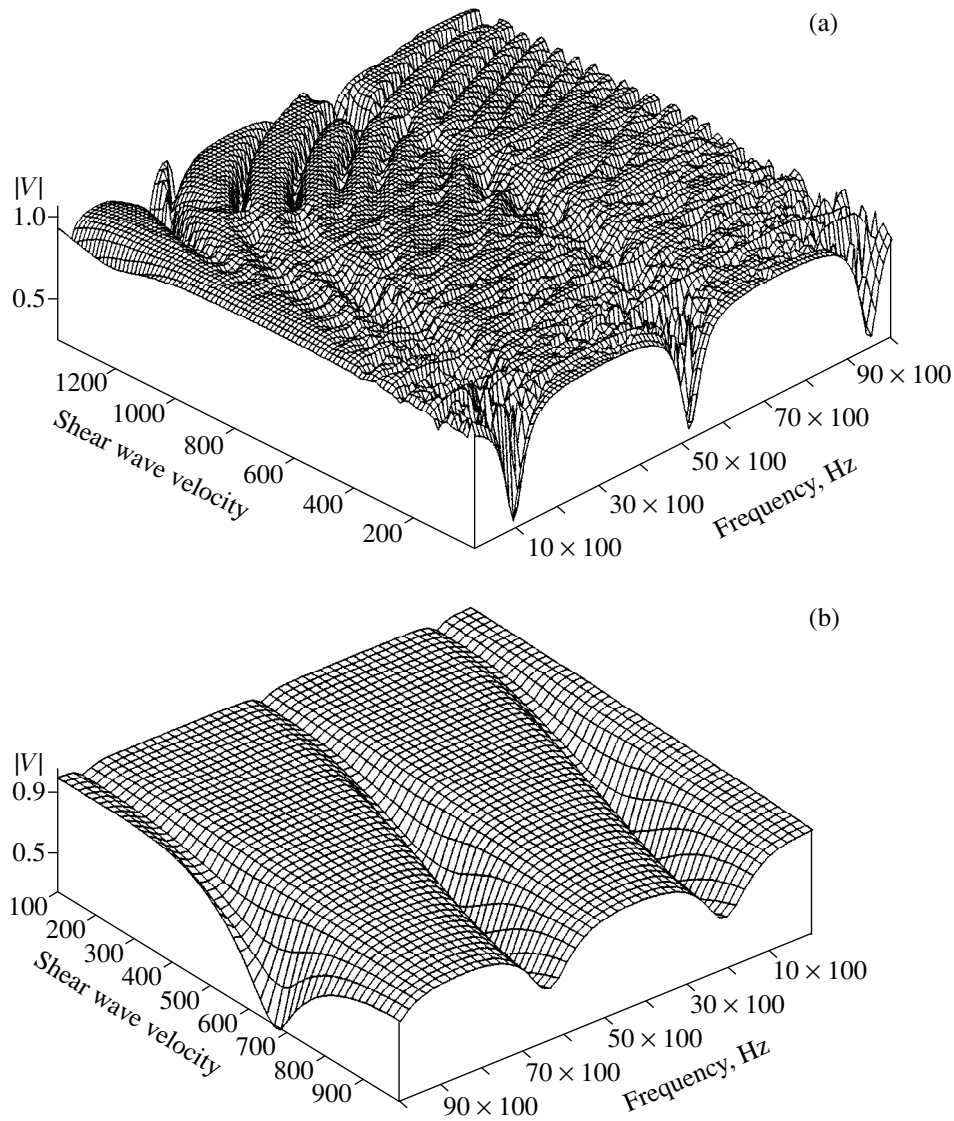


Fig. 5. Reflection coefficient on the frequency–shear wave velocity plane for a fixed grazing angle $\theta = 2^\circ$ and $c_{l\infty} > c_0 > c_{l1}$: (a) in the layer and (b) in the halfspace.

will develop new resonances whose width Γ and amplitude A will differ from those measured for simpler bottom models.

The inclusion of shear elasticity in sedimentary layers is of particular interest in calculating the reflection coefficients. Taking into consideration the transverse waves in the second sedimentary layer ($c_{l2} = 800$ m/s, rest parameters correspond to Fig. 2) significantly changes the frequency-angular dependence of the reflection coefficient (Fig. 4). Now, a simple periodicity in frequency is not observed, and the angular dependence also becomes more complicated. For the grazing angles less than the critical angle $\theta < \theta_{cr} = 20^\circ$, new resonances appear, which contain additional information about the environmental parameters. At the normal incidence of a plane wave on a layered elastic medium

(when the grazing angle is $\theta = 90^\circ$), the shear wave is not excited, because the tangential component of a compression wave is absent at the interface. The strong dependence of the reflection coefficient on many parameters, which occurs in this bottom model, makes it difficult to estimate the effect of shear waves on the sound propagation in a shallow sea. However, in this case the reflection coefficient significantly changes at shallow grazing angles (Fig. 4). Using simpler bottom models at frequencies of several hundreds hertz can lead to errors in the estimates of the sound field intensity. More definite conclusions about the influence of one or another model of the layered elastic bottom on the sound propagation in a shallow sea can be obtained by analyzing the sound reflection coefficients and the angular structure of the acoustic field using specific geophysical data on the bottom structure.

The effect of the transverse waves in the sedimentary layer and the halfspace on the reflection coefficient and the resonance structure can be inferred from the behavior of the reflection coefficients in the frequency–transverse wave velocity plane in the sedimentary layer (f, c_{t1}) and in the halfspace ($f, c_{t\infty}$). We considered a bottom model in the form of an elastic layer overlying an elastic halfspace ($h_1 = 0.7$ m, $c_{t1} = 1455$ m/s, $\eta_{t1} = 0$, $c_{r1} = 5\text{--}1400$ m/s, $\rho_1 = 1.45$ g/cm³, $c_{t\infty} = 1575$ m/s, $\eta_{t\infty} = 6.35 \times 10^{-4}$, $c_{r\infty} = 1455$ m/s, $\eta_{r\infty} = 6.35 \times 10^{-4}$, and $\rho_{\infty} = 2.6$ g/cm³). Figure 5a exhibits the results of the calculations of the reflection coefficient as a function $V(f, c_{t1})$ at a fixed grazing angle $\theta = 2^\circ$ for the frequency and the transverse sound velocity in the sedimentary layer varying within the ranges $f = 1\text{--}10000$ Hz and $c_{t1} = 5\text{--}1400$ m/s, respectively. With allowance for the transverse sound velocity in the layer c_{t1} , an additional modulation of the reflection coefficient appears. As the velocity c_{t1} increases from 50 to 200 m/s, the resonance structure becomes more complex, and with further increase in c_{t1} , additional resonance peaks appear, and the frequency and angular positions of the resonance peaks change. It should be noted that the values of the transverse velocity in solids and in sea sediments cannot be arbitrary. Nevertheless, the use of the wide range of variation for c_{t1} in Fig. 5 seems to be justified for the sake of illustration.

The effect of shear elasticity in the underlying halfspace $c_{t\infty}$ on the resonance behavior is shown in Fig. 5b. The reflection coefficient $V(f, c_{t1})$ is presented at a fixed grazing angle $\theta = 2^\circ$ for the frequency and transverse sound velocity varying in the ranges $f = 1\text{--}10000$ Hz and $c_{t\infty} = 100\text{--}1000$ m/s, respectively. The bottom model in the form of a liquid layer overlying an elastic halfspace (the parameters correspond to Fig. 2) was used. The displacement of the reflection coefficient minima in frequency with increasing $c_{t\infty}$ is evidently related to the change in the phase of signals reflected from the lower boundary of the sedimentary layer. The dependence of the positions of the resonance minima of the reflection coefficient on $c_{t\infty}$ can be used to develop a procedure of determining the shear velocity of sound in the halfspace for known characteristics of the sedimentary layer.

Thus, in this paper, we present the results of calculating the reflection and transmission coefficients for layered elastic media using the matrix method. It is shown that, for increasing the accuracy of these calculations, it is necessary to use matrices of the sixth order. The results of testing the computer program are also presented. The frequency-angular dependences of the reflection coefficient are considered for the bottom models consisting of one and two liquid/elastic sedimentary layers overlying an elastic halfspace. The clearly defined resonance structure revealed for a sim-

ple bottom model is retained as a whole, if we add to it some realistic details such as the layering, attenuation, and shear elasticity. The resonance structure of the reflection coefficients is investigated in order to develop a resonance approach for solving the inverse reflection problem, because the position, width, and amplitude of resonances can easily be measured in experiments. The problem of how to relate such resonances to the acoustic bottom parameters for the cases more complicated than those described in the literature [24–27] is the subject of our current investigations.

ACKNOWLEDGMENTS

This work was supported by the Russian Foundation for Basic Research, project no. 97–05–64712.

REFERENCES

1. L. M. Brekhovskikh and O. A. Godin, *Acoustics of Layered Media* (Nauka, Moscow, 1989; Berlin, Springer, 1990).
2. W. M. Ewing, W. S. Jardetzky, and F. Press, *Elastic Waves in Layered Media* (McGraw-Hill, New York, 1957).
3. L. A. Molotkov, in *Computational Methods in Geophysics* (Radio i Svyaz', Moscow, 1981).
4. L. A. Molotkov, *The Matrix Method in the Theory of Wave Propagation in Elastic and Fluid Layered Media* (Nauka, Leningrad, 1984).
5. M. M. Machevariani, V. V. Tyutekin, and A. P. Shkvarnikov, *Akust. Zh.* **17**, 97 (1971) [*Sov. Phys. Acoust.* **17**, 77 (1971)].
6. V. Yu. Prikhod'ko and V. V. Tyutekin, *Akust. Zh.* **32**, 212 (1986) [*Sov. Phys. Acoust.* **32**, 125 (1986)].
7. V. N. Fokin and M. S. Fokina, *Akust. Zh.* **44**, 676 (1998) [*Acoust. Phys.* **44**, 585 (1998)].
8. N. R. Chapman, M. Musil, and M. J. Wilmut, *Boll. Geofis. Teor. Appl.* **40** (1), 40 (1999).
9. M. Siderius and J. P. Hermand, *J. Acoust. Soc. Am.* **106**, 637 (1999).
10. N. R. Chapman, D. E. Hanny, and K. M. M. Rohr, in *Proceedings of the 3rd European Conference on Underwater Acoustics, 1996*, Vol. 2, p. 613.
11. K. E. Hawker, *J. Acoust. Soc. Am.* **64**, 548 (1978).
12. S. R. Rutherford and K. E. Hawker, *J. Acoust. Soc. Am.* **63**, 750 (1978).
13. H. E. Morris, *J. Acoust. Soc. Am.* **48**, 1198 (1970).
14. T. Akal and R. Stoll, *J. Acoust. Soc. Am.* **100**, 2668 (1996).
15. R. Carbo, *J. Acoust. Soc. Am.* **101**, 227 (1997).
16. R. F. Keltie, *J. Acoust. Soc. Am.* **103**, 1855 (1998).

17. A. I. Lavrentyev and S. I. Rokhlin, *J. Acoust. Soc. Am.* **102**, 3467 (1997).
18. W. T. Thomson, *J. Appl. Phys.* **21**, 89 (1950).
19. N. A. Haskell, *Bull. Seismol. Soc. Am.* **43**, 17 (1953).
20. I. W. Dunkin, *Bull. Seismol. Soc. Am.* **55**, 335 (1965).
21. E. N. Thrower, *J. Sound Vibr.* **2**, 210 (1965).
22. P. J. Vidmar and T. L. Foreman, *J. Acoust. Soc. Am.* **66**, 1830 (1979).
23. F. R. Gantmacher, *The Theory of Matrices* (Fizmatgiz, Moscow, 1966, 3rd ed.; Chelsea, New York, 1959).
24. A. Nagl, H. Überall, and W. R. Hoover, *IEEE Trans. Geosci. Remote Sens.* **GE-20**, 332 (1982).
25. G. Breit and E. P. Wigner, *Phys. Rev.* **49**, 519 (1936).
26. A. Nagl, H. Überall, and Yoo Kwang-Bock, in *Inverse Problems* (Inst. of Physics, Bristol, 1985), Vol. 1, p. 99.
27. R. Fiorito, W. Madigosky, and H. Überall, *J. Acoust. Soc. Am.* **66**, 1857 (1979).

Translated by Yu. Lysanov

SHORT
COMMUNICATIONS

Focusing Ultrasonic Radiators with Electrically Controlled Spatial and Time Structures of the Generated Fields

A. V. Gladilin and A. A. Dogadov

Andreev Acoustics Institute, Russian Academy of Sciences,
ul. Shvernika 4, Moscow, 117036 Russia

e-mail: hfus@mail.ru

Received December 30, 1999

To obtain focused ultrasound in the megahertz frequency range, the usual practice is to employ radiators with the active element in the form of a spherically concave, polarized piezoceramic plate [1–3]. The structure of acoustic fields generated by such radiators is determined by the distribution of the particle velocity over the radiating surface of the piezoelectric plate and by the structural characteristics of the latter. In the cited publications [1–3], the distribution of the particle velocity over the radiating surface of a piezoelectric plate is assumed to be uniform. Ermolov *et al.* [4] showed the possibility of a frequency-modulated excitation of focusing piezoelectric plates of nonuniform thickness. The use of such plates makes it possible not only to extend the frequency range of the generated fields [4], but also to control the distribution of the particle velocity over the radiating surface of the active element. This fact is used as the basis for the development of single-channel focusing ultrasonic radiators with electrically controlled spatial and time structures of the generated fields (EC STS) by means of the frequency modulation of the voltage applied to the focusing piezoelectric plates of varying thickness [5].

In this paper, we present the description of focusing ultrasonic radiators with EC STS, the results obtained by calculating the fields generated by these radiators, and the corresponding experimental estimates. The following ways of controlling the spatial and time structure of the fields are possible: swing of the focal area (in a direction normal to that of the ultrasound propagation), displacement of the focal area (in the direction of the ultrasound propagation), and rotation of the focal area (about the direction of the ultrasound propagation).

The piezoelectric plate of the radiator that excites the swing of the focal area has spherically concave inner and outer surfaces. The centers of the spheres are shifted by the distance Δ in the direction normal to that of the ultrasound propagation. This geometry provides the required distribution of the piezoelectric plate thickness within the radiating surface area. The piezoelectric plate of the radiator that excites the displacement of the focal area has hyperboloid-shaped outer

and inner surfaces with different parameters, which depend on the required range of the focal area displacement.

The acoustic field generated by a radiator with EC STS is calculated by using the Rayleigh integral [3]; the variation of the particle velocity and the acoustic pressure with time is determined by the factor $\exp(-i\omega t)$, where ω is the circular frequency of excitation. The Rayleigh integral has the form

$$p(r) = -i\rho_0 c_0 \frac{k}{2\pi} \int_S \frac{u(\mathbf{r}') e^{-ik|\mathbf{r}-\mathbf{r}'|}}{|\mathbf{r}-\mathbf{r}'|} dS'. \quad (1)$$

Here, the integration is performed over the radiating surface S , $p(\mathbf{r})$ is the acoustic pressure at the point of observation, u is the amplitude of the normal component of the particle velocity of the radiating surface (the normal is directed toward the medium), \mathbf{r} is the radius vector of the observation point, \mathbf{r}' is the radius vector of the surface element dS' , $k = \omega/c_0$ is the wave number, ρ_0 is the density of the medium, and c_0 is the sound velocity in the medium.

Fig. 1a shows the results of calculating the acoustic field (at a level of -3 dB) generated by a piezoelectric plate of typical dimensions (a diameter of 45 mm and a curvature radius of 75 mm) under excitation by a voltage whose frequency discretely varies at a step of 10 kHz in the frequency range from 820 to 940 kHz. The pressure distribution reflects the swing of the focal area about the Z -axis in the XOZ plane. The maximal swing amplitude H_s is about 5 mm, which is confirmed by the experimental results. The effective region of ultrasonic treatment is formed in the swing plane as a result of the spatial averaging of the generated fields; this region differs from the focal area of a radiator with a uniform distribution of the particle velocity by a much greater ratio between its transverse and longitudinal dimensions.

In a piezoelectric plate that provides the displacement of the focal area in the direction of the ultrasound propagation, a sequential excitation of ring-shaped regions with different curvature radii takes place. The inner and outer surfaces of the piezoelectric plate can be approximated by a set of concave, axially symmetric

regions with different curvature radii. This representation simplifies the calculation of the generated field, as well as the manufacture of the radiator prototypes. In this case, the calculation of the generated fields is also performed by formula (1). Figure 1b presents the distribution of the pressure (at a level of -3 dB) generated by the piezoelectric plate with the diameter 78 mm and with the inner surface approximated by a set of three concave, axially symmetric regions with different curvature radii (from 45 to 75 mm). The calculation is performed for the resonance excitation frequencies 820, 880, and 940 kHz.

The results of the calculations and the experimental check show that the centers of the focal areas move along the direction of the ultrasound propagation with the amplitude H_d up to 15–17 mm (for a plate with the aforementioned parameters) at the selected excitation frequencies.

The change in the position of the focal area of a radiator with EC STS is accompanied by a displacement of the point of application of the radiation pressure force. Thus, the focusing ultrasonic radiators with EC STS allow one to excite mechanical vibrations along a given direction deep inside the object under treatment, i.e., in the immediate region of interest. This offers a possibility of using the radiators with EC STS for increasing the resolution of the Doppler ultrasonic diagnostics [6].

Besides, the response of inhomogeneous viscoelastic media to focused ultrasonic fields with EC STS gives rise to an amplitude modulation of the frequency-modulated excitation voltage of the corresponding radiators. The origin of this effect lies in the variation of the acoustic impedance of the object within the focal area displacement, this variation being determined by the structure and state of the object. Thus, the arising amplitude modulation reflects the spatial distribution of the acoustic parameters of the object under treatment. By processing the data on the variation of the modulation depth and its dependence on the modulation frequency, it is possible to estimate the parameters of the object without placing any sensors in the region of interest, i.e., noninvasive measurements are possible.

The noninvasive measurement channel that is formed when a radiator with EC STS is used, can be characterized by the frequency range of the aforementioned modulation and the dynamical range. The modulation frequency range is limited by the mass and elastic properties of the piezoelectric plates. The upper boundary of the modulation frequency range F_{\max} determined from the experiment for the piezoelectric plates with typical parameters reaches 10 kHz.

The dynamical range of the measured values of the modulation depth is determined by the formula

$$D_{AM} = 20 \log \frac{m_{AM}}{m_1 - m_2}, \quad (2)$$

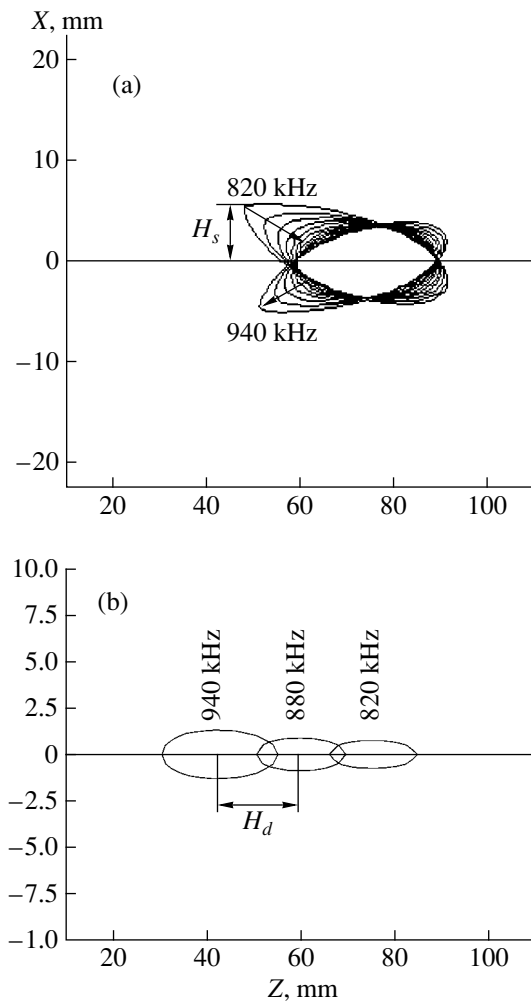


Fig. 1. Distribution of acoustic pressure in the XOZ plane: (a) pressure generated by the piezoelectric plate that excites the swing of the focal area (in the frequency range from 820 to 940 kHz at a step of 10 kHz); (b) pressure generated by the piezoelectric plate that excites the displacement of the focal area (in the frequency range from 820 to 940 kHz at a step of 60 kHz).

where m_{AM} is the maximum possible value of the modulation depth due to the variation in the acoustic resistance of the object under treatment within the displacement of the focal area; m_1 is the extraneous modulation depth, which is determined by replacing the object under treatment by its homogeneous simulator; and m_2 is the deterministic component of the extraneous modulation depth, which is determined mainly by the amplitude-frequency characteristic of the radiator in the excitation frequency range and measured in the course of the channel calibration.

The dynamical range of the modulation depth measured for the object under treatment represented by different simulators of biological tissue reaches 30–40 dB depending on the modulation frequency.

The channel capacity achieved in the noninvasive measurements of the parameters of the object under treatment is determined by the formula

$$V = \Delta F \log_2 \left(1 + \frac{P_S}{P_N} \right), \quad (3)$$

where ΔF is the modulation frequency range ($\Delta F \approx F_{\max}$) and P_S/P_N is the signal-to-noise power ratio corresponding to D_{AM} .

Taking into account the experimental results, i.e., $\Delta F = 10^4$ Hz and the minimal value $D_{AM} = 30$ dB, we obtain that the maximal value of the channel capacity achieved for the noninvasive measurements of the parameters of the object under treatment exceeds 0.1 Mbit/s.

This value provides a high accuracy of the characterization of the object under treatment.

REFERENCES

1. L. D. Rozenberg, in *Physics and Technology of Intense Ultrasound* (Nauka, Moscow, 1967), pp. 149–206.
2. I. A. Vartanyan, L. R. Gavrilov, A. S. Rozenblyum, and E. M. Tsiryul'nikov, in *Sensor Perception* (Nauka, Leningrad, 1985).
3. D. Cathignol and O. A. Sapozhnikov, *Akust. Zh.* **45**, 816 (1999) [*Acoust. Phys.* **45**, 735 (1999)].
4. I. N. Ermolov, *et al.*, in *Ultrasonic Transducers for Non-destructive Testing* (Mashinostroenie, Moscow, 1986).
5. A. A. Dogadov, I. I. Konopatskaya, and A. V. Gladilin, RF Patent No. 2139745 C1.
6. K. J. Parker, S. R. Huang, R. A. Musulin, and R. M. Lerner, *Ultrasound Med. Biol.* **16**, 241 (1990).

Translated by E. Golyamina

SHORT
COMMUNICATIONS

Low-Frequency Sound Field in a Room with a Helmholtz Resonator

A. D. Lapin

Andreev Acoustics Institute, Russian Academy of Sciences, ul. Shvernika 4, Moscow, 117036 Russia

e-mail: bvp@akin.ru

Received June 17, 1999

Abstract—The sound field generated by a point source of volume velocity in a room with a Helmholtz resonator is determined. The shift produced by the resonator in the natural frequencies of the room is calculated.
© 2000 MAIK “Nauka/Interperiodica”.

It is well known that, in the low-frequency range, the natural frequencies of a room are widely separated from each other, and, therefore, the transfer function of such a room is fairly inhomogeneous [1, 2]. To improve the acoustical properties of rooms in the low-frequency range, one can use Helmholtz resonators [3, 4]. Serving as efficient sound absorbers at resonance frequencies, the resonators installed in a room smooth out its transfer function. The problem of the interaction of a resonator with the normal modes of a room is not only of practical, but also of theoretical interest. Due to the strong coupling of oscillations, the resonator may appreciably change the natural frequencies of the room that are close to the natural frequency of the resonator. Below, we determine the sound field of a point source of volume velocity in a room with a Helmholtz resonator and calculate the shift produced by the latter in the natural frequencies of the room.

Let us consider a room of volume V bounded by a rigid surface S . The room is filled with a homogeneous medium of density ρ ; the sound velocity in the medium is c . A harmonic point source with the volume velocity Q_1 is positioned at a point with the radius vector \mathbf{r}_1 . According to [1], the sound pressure $p^{(1)}$ generated in the room by such a source is expressed by the formula

$$p^{(1)}(\mathbf{r}) = i\omega\rho Q_1/V \sum_n \frac{p_n(\mathbf{r}_1)}{(k^2 - k_n^2)} p_n(\mathbf{r}), \quad (1)$$

where $p_n(\mathbf{r})$ are the fundamental functions, ω_n are the natural frequencies, ω is the sound frequency, $k_n = \omega_n/c$, $k = \omega/c$, and the summation is performed over all fundamental functions. The functions $p_n(\mathbf{r})$ satisfy the equation

$$\Delta p_n + k_n^2 p_n = 0,$$

the boundary condition $\frac{\partial p_n}{\partial \mathbf{n}} = 0$ at the surface S , and

the orthogonality and normalization relations

$$\int_V p_n p_m dV = 0 \text{ for } n \neq m, \quad \int_V p_n^2 dV = V.$$

According to formula (1), the sound field formed in the room infinitely grows as the frequency ω approaches one of the natural frequencies of this room. Let us show that the introduction of a resonator into the room changes the natural frequencies of the latter. The resonator provides an efficient sound absorption at resonance frequencies, and the sound field formed in the room with a resonator remains finite at any frequency.

We consider a resonator positioned at a point with the radius vector \mathbf{r}_2 . The resonator being excited by the pressure field $p^{(1)}$ generates the field $p^{(2)}$:

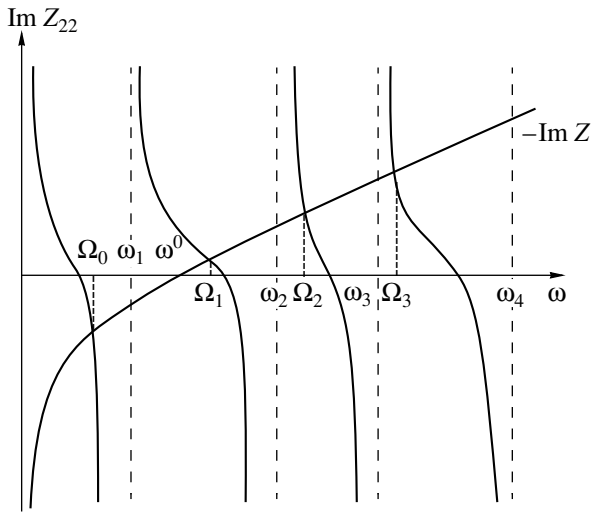
$$p^{(2)}(\mathbf{r}) = i\omega\rho Q_2/V \sum_n \frac{p_n(\mathbf{r}_2)}{(k^2 - k_n^2)} p_n(\mathbf{r}), \quad (2)$$

where Q_2 is the volume velocity of the resonator. The resulting sound field in the room with the resonator is obtained as a sum of the fields $p^{(1)}$ and $p^{(2)}$:

$$p = p^{(1)} + p^{(2)} = i\omega\rho/V \sum_n \frac{1}{(k^2 - k_n^2)} \times \{Q_1 p_n(\mathbf{r}_1) + Q_2 p_n(\mathbf{r}_2)\} p_n(\mathbf{r}). \quad (3)$$

The quantity Q_2 can be obtained from the equation of motion of the resonator under the pressure field $p^{(1)}$. The Helmholtz resonator is an oscillatory system with one degree of freedom, and its dimensions are small relative to the sound wavelength at the resonance frequency. We denote the displacement of the air mass in the resonator gorge by $X(t)$. Then, the equation describing the corresponding forced oscillations can be represented in the form

$$M\ddot{X} + R\dot{X} + \kappa X = -S_0 \{p^{(1)}(\mathbf{r}_2) + p^{(2)}(\mathbf{r}_2)\} \exp(-i\omega t), \quad (4)$$



Determination of the natural frequencies of a room with a resonator.

where M is the air mass in the resonator gorge, R is the friction coefficient, κ is the coefficient of elasticity, and S_0 is the cross-sectional area of the resonator gorge. Equation (4) can be reduced to the form

$$Q_2 Z = -\{Z_{12}Q_1 + Z_{22}Q_2\}, \tag{5}$$

where $Z = 1/S_0^2 \{R + i(\kappa/\omega - \omega M)\}$ is the acoustic impedance of the resonator,

$$Z_{22} = \frac{p^{(2)}(\mathbf{r}_2)}{Q_2} = i\omega\rho/V \sum_m \frac{p_m^2(\mathbf{r}_2)}{(k^2 - k_m^2)}$$

is the added acoustic impedance of the resonator,

$$Z_{12} = \frac{p^{(1)}(\mathbf{r}_2)}{Q_1} = i\omega\rho/V \sum_m \frac{p_m(\mathbf{r}_1)p_m(\mathbf{r}_2)}{(k^2 - k_m^2)}$$

is the mutual acoustic impedance, and $Q_2 = S_0 \dot{X} e^{i\omega t}$.

From equation (4), we obtain the volume velocity of the resonator

$$Q_2 = -Q_1 Z_{12} / (Z + Z_{22}).$$

Substituting Q_2 in formula (3), we obtain the total field in the room with the resonator:

$$p = i\omega\rho Q_1 / V \times \sum_n \left\{ p_n(\mathbf{r}_1) - \frac{Z_{12}}{(Z + Z_{22})} p_n(\mathbf{r}_2) \right\} \frac{p_n(\mathbf{r})}{(k^2 - k_n^2)}. \tag{6}$$

This field can be represented in the form

$$p = i\omega\rho Q_1 / V \sum_n \frac{\left\{ p_n(\mathbf{r}_1) - \frac{Z'_{12}}{(Z + Z'_{22})} p_n(\mathbf{r}_2) \right\}}{\left\{ (k^2 - k_n^2) + \frac{i\omega\rho p_n^2(\mathbf{r}_2)}{V(Z + Z'_{22})} \right\}} p_n(\mathbf{r}), \tag{7}$$

where the prime indicates that the corresponding impedance is calculated by ignoring the term with the number $m = n$. According to formula (7), the field p is finite at $\omega = \omega_n$.

The natural frequencies of the room with the resonator are the roots of the equation

$$\text{Im}[Z(\omega) + Z_{22}(\omega)] = 0. \tag{8}$$

This equation can be represented in the form

$$\omega^2 = \omega_n^2 - \frac{\omega\rho c^2 p_n^2(\mathbf{r}_2)}{\text{Im}[Z(\omega) + Z'_{22}(\omega)]V}. \tag{9}$$

Equation (8) can be solved by the graphical method, by finding the points of intersections of the branches of the curve $\text{Im}Z_{22}(\omega)$ with the curve $-\text{Im}Z(\omega)$. The figure shows the approximate form of these curves. The abscissas of the intersection points yield the sought-for values $\omega = \Omega_n$ of the natural frequencies of the room with the resonator. These frequencies obey the relation

$$\omega_n < \Omega_n < \omega_{n+1}.$$

At high frequencies ($\omega \gg \omega^0$, where ω^0 is the natural frequency of the resonator and $\text{Im}Z(\omega^0) = 0$), the abscissas of the points of intersection are close to the frequencies ω_n and lie to the right of them. For these roots, from equation (9), we obtain the approximate expression

$$\Omega_n^2 = \omega_n^2 - \frac{\omega_n\rho c^2 p_n^2(\mathbf{r}_2)}{\text{Im}[Z(\omega_n) + Z'_{22}(\omega_n)]V},$$

where $\text{Im}[Z(\omega_n) + Z'_{22}(\omega_n)] < 0$.

At low frequencies ($\omega \ll \omega^0$), the abscissas of the points of intersection are also close to the frequencies ω_n , but they lie to the left of them and correspond to the other (preceding) branch of the curve $\text{Im}Z_{22}(\omega)$. According to equation (9), for these roots we obtain the approximate formula

$$\Omega_{n-1}^2 = \omega_n^2 - \frac{\omega_n\rho c^2 p_n^2(\mathbf{r}_2)}{\text{Im}[Z(\omega_n) + Z'_{22}(\omega_n)]V},$$

where $\text{Im}[Z(\omega_n) - Z'_{22}(\omega_n)] > 0$.

At frequencies of the order of ω^0 , the abscissas of the points of intersection of the curves lie well away from the frequencies ω_n , and, therefore, the natural frequencies Ω_n can only be determined by numerical methods. Note that the behavior of the natural frequencies in a room with a resonator is similar to the behavior of the natural frequencies in a narrow tube with impedance plugs [5].

At a frequency ω that is equal to the natural frequency Ω_m , the sound field in the room with a resonator is determined by the formula

$$p(\mathbf{r}) = i\Omega_m \rho Q_1 / V \sum_n \frac{c^2 p_n(\mathbf{r})}{R(\Omega_m^2 - \omega_n^2)} \times [R p_n(\mathbf{r}_1) - S_0^2 Z_{12}(\Omega_m) p_n(\mathbf{r}_2)].$$

This field is infinite at $R = 0$ and finite at any $R \neq 0$. The resonance peaks of the transfer function can be flattened by increasing the friction coefficient of the resonator. It is expedient to place the resonator at one of the antinodes of the normal modes, e.g., at a corner of the room. The resonator can be installed either inside the room or on one of the walls. Resonators of different structures can be used. The dependence of the natural frequency ω^0 of the resonator on its parameters had been studied in a number of publications [6–9].

REFERENCES

1. P. M. Morse, *Vibration and Sound* (McGraw-Hill, New York, 1948; GITTL, Moscow, 1949).
2. W. J. Cavanaugh and J. A. Wilkes, *Architectural Acoustics: Principles and Practice* (Wiley, New York, 1999).
3. E. Skudrzyk, *The Foundations of Acoustics* (Springer, Vienna, 1971; Inostrannaya Literatura, Moscow, 1959), Vol. 2.
4. *Acoustics Handbook*, Ed. by M. J. Crocker (Wiley, New York, 1997).
5. M. A. Isakovich, *General Acoustics* (Nauka, Moscow, 1973).
6. Lord Rayleigh, *The Theory of Sound* (Dover, New York, 1945; GITTL, Moscow, 1955), Vol. 2.
7. R. C. Chanaud, *J. Sound Vibr.* **178**, 337 (1994).
8. N. S. Dickey and A. Selamet, *J. Sound Vibr.* **195**, 512 (1996).
9. A. Selamet, P. M. Radavich, N. S. Dickey, *et al.*, *J. Acoust. Soc. Am.* **101**, 41 (1997).

Translated by E. Golyamina

SHORT
COMMUNICATIONS

Fractal Structure of the Acoustic Signal Excited in a Liquid by an Unstable Laser Radiation

M. L. Lyamshev

General Physics Institute, Russian Academy of Sciences, ul. Vavilova 38, Moscow, 117942 Russia

e-mail: lyamshev@kapella.gpi.ru

Received December 30, 1999

Abstract—Thermo-optical excitation of sound in a liquid by a laser radiation with a harmonically modulated intensity randomly distributed over the beam cross-section is considered. The processes are considered to be statistically homogeneous. It is assumed that the spatial spectrum of the intensity fluctuations in a laser beam is described by a power (fractal) law. It is demonstrated that the acoustic field in a liquid has a fractal structure.
© 2000 MAIK “Nauka/Interperiodica”.

Theoretical treatment of laser-induced sound excitation in condensed media (for example, liquids) is usually conducted under the assumption that the transverse distribution of intensity in a laser beam is quite determinate. It is often assumed that this distribution is axially symmetric and has the Gaussian form [1, 2]. In reality, it is not uncommon that the transverse distribution of intensity in a laser beam fluctuates.

Recently, it has been demonstrated [3] that the mode structure of the radiation of an unstable-cavity laser is fractal. In particular, it has been found that the fractal dimension of the intensity distribution of a laser with the aperture shaped as a narrow slit has the value $D = 1.6$. In the case of a circular aperture, the fractal dimension was found to be $D = 1.3$.

Below, we consider the thermo-optical excitation of sound in a liquid by a laser radiation with a harmonically modulated intensity and a fractal spatial spectrum of the intensity fluctuations. It is necessary to note that the effect of spatial and time fluctuations of the laser radiation intensity on the sound excitation in a liquid was considered earlier by Bunkin [1], but the character of their distribution was not specified.

Let us assume that a laser beam propagating from the upper halfspace (atmosphere) in the positive direction of the z axis of the rectangular coordinate system (x, y, z) is incident upon the free surface of a liquid occupying the lower halfspace $z > 0$. The absorption of the laser radiation in the liquid results in the formation of thermal sources of sound. The equation of the laser thermo-optical generation of sound has the form

$$(\Delta + k^2)p\mu = i\frac{km\omega}{C_p}A\mu I(x, y)\exp(-\mu z). \quad (1)$$

Here, p is the sound pressure; k , C_p , and μ are the coefficient of thermal expansion, the specific heat, and the

absorption coefficient for optical radiation, respectively; A is the coefficient of light transmission through the liquid boundary (from here on, we assume that $A = 1$); m is the modulation index; $I(x, y)$ is the intensity distribution in the laser beam at the liquid surface; $k = \omega/c$; and c is the sound velocity in the liquid. The time factor $\exp(-i\omega t)$ is omitted here and below.

The solution of equation (1) can be written in the form [2]

$$p(r) = i\frac{k\omega m}{C_p}\mu \int_{\Omega} I(x', y') \exp(-\mu z') \times \tilde{p}(x', y', z'/x, y, z) dx' dy' dz', \quad (2)$$

where $\tilde{p}(r'/r)$ is the solution to the boundary problem on the diffraction of the field of a point source positioned at the point r where it is necessary to determine the field $p(r)$. We consider the field $p(r)$ in the Fraunhofer zone. In this case, $\tilde{p}(r'/r)$ can be represented in the form

$$\tilde{p}(r'/r) = \frac{\exp(ikr)}{4\pi r} \{ \exp[-i(\alpha x' + \beta y' - \gamma z')] - \exp[-i(\alpha x' + \beta y' + \gamma z')] \}, \quad (3)$$

where $\alpha^2 + \beta^2 + \gamma^2 = k^2$ and $r = (x^2 + y^2 + z^2)^{1/2}$.

We assume the intensity distribution in the beam to be a random function, so that $I(x, y) = I_0 f(x, y)$, where $\langle f(x, y) \rangle = 0$, and the random processes to be statistically homogeneous.

Taking this into account, substituting expression (3) into expression (2), and integrating with respect to z , we

obtain an expression for the mean-square sound pressure $\langle |p(r)|^2 \rangle$:

$$\langle |p(r)|^2 \rangle = \frac{k^2 \omega^2 m^2}{C_p^2} \frac{1}{4\pi^2 r^2} \frac{\mu^2 \gamma^2}{(\mu^2 + \gamma^2)^2} I_0^2 \sigma \times \iint_{\xi \eta} B(\xi, \eta) \exp[-i(\alpha\xi + \beta\eta)] d\xi d\eta, \quad (4)$$

where $B(\xi, \eta) = \langle f(x', y') f(x'', y'') \rangle$ is the normalized correlation function of the intensity fluctuations of the laser radiation, $\xi = |x' - x''|$, $\eta = |y' - y''|$, and σ is the area of the laser spot at the liquid surface. The integration with respect to ξ and η is extended to the region of the action of laser radiation at the liquid surface. However, if $B(\xi, \eta)$ decreases rapidly within the dimensions of the cross-section of the laser beam and $B(\infty) = 0$, the integration can be extended to the interval from $-\infty$ to $+\infty$.

The properties of statistic fractals are often characterized by structural (correlation) functions and their spectra. Their specific feature is the fact that they are described by power laws. This follows from the property of scaling of the fractal structures [4].

The power spectrum of fluctuations is an important parameter of the statistical fractals in the wave problems. This spectrum has the form

$$G(q) \sim q^{-\delta}, \quad (5)$$

where q is the wave number of spatial fluctuations and the exponent δ for the objects with a fractal surface is determined by the expression

$$\delta = D - 2d, \quad (6)$$

where D is the fractal dimension and d is the space of embedding.

Let us consider the spatial spectrum of the laser radiation when the aperture is shaped as a narrow slit in the x direction. In this case, we can write the expression

$$B(\xi, \eta) = B_1(\xi) B_2(\eta), \quad (7)$$

where $B_2(\eta) \approx 1$, because the distribution of intensity fluctuations of laser radiation in the transverse direction can be considered totally correlated. The normalized correlation function in the longitudinal direction can be represented in the form [5]

$$B(\xi) = \frac{1}{2^{v-1} \Gamma(v)} \left(\frac{\xi}{\xi_0} \right)^v K_v \left(\frac{\xi}{\xi_0} \right), \quad (8)$$

where $\Gamma(v)$ is the gamma-function, $K_v(\xi/\xi_0)$ is the Macdonald function, and ξ_0 is the correlation length of intensity fluctuations of laser radiation in the longitudinal direction. We should note that $B(0) = 1$ and $B(\infty) = 0$, while $B(\xi)_{\xi < \xi_0} \sim (\xi/\xi_0)^v$, i.e., the correlation function has a power-law form, and from this point of view it can be used for describing the fractal structure of the intensity fluctuations of an unstable laser radiation.

Substituting expressions (7) and (8) into expression (4) and performing the integration, we obtain

$$\langle |p(r)|^2 \rangle = \frac{k^2 \omega^2 m^2}{C_p^2} \frac{1}{4\pi^2 r^2} \frac{\mu^2 \gamma^2}{(\mu^2 + \gamma^2)^2} I_0 \sigma \eta_0 G(\alpha), \quad (9)$$

where η_0 is the transverse dimension of the laser spot at the liquid surface and $G(\alpha)$ is the spectral density of intensity fluctuations of laser radiation:

$$G(\alpha) = \frac{\Gamma\left(v + \frac{1}{2}\right)}{\sqrt{\pi} \Gamma(v)} \frac{\xi_0}{(1 + \alpha^2 \xi_0^2)^{v + \frac{1}{2}}}. \quad (10)$$

At $\alpha \xi_0 > 1$, the spectral density $G(\alpha)$ has a power-law (fractal) form

$$G(\alpha)_{\alpha \xi_0 > 1} \sim \alpha^{-(2v+1)}. \quad (11)$$

Now let us consider the case of a circular aperture. The expression for the mean-square fluctuation of sound pressure (4) can be represented in the form

$$\langle |p(r)|^2 \rangle = \frac{k^2 \omega^2 m^2}{C_p^2} \frac{1}{4\pi^2 r^2} \frac{\mu^2 \gamma^2}{(\mu^2 + \gamma^2)^2} I_0 \pi a^2 G(k_{\perp}), \quad (12)$$

where

$$G(k_{\perp}) = \int_{-\infty}^{+\infty} B(\rho) \exp(-ik_{\perp} \rho) d\rho, \quad (13)$$

k_{\perp} is the component of the wave vector k in the horizontal plane, $k_{\perp}^2 = \alpha^2 + \beta^2$, $\bar{\rho} = |\rho' - \rho''|$, and a is the radius of the laser beam at the liquid surface.

We write down the correlation function $B(\rho)$ in the form (8), substituting ρ for ξ and ρ_0 for ξ_0 , where ρ_0 is the correlation length of fluctuations of laser radiation.

We obtain the following expression for spectral density (13):

$$G(k_{\perp}) = \frac{\Gamma(v+1)}{\sqrt{\pi} \Gamma(v)} \frac{\rho_0^2}{(1 + k_{\perp}^2 \rho_0^2)^{v+1}}. \quad (14)$$

At $k_{\perp} \rho_0 > 1$, we have

$$G(k_{\perp}) \sim k_{\perp}^{-2(v+1)}. \quad (15)$$

It is necessary to determine the particular value of the parameter v to calculate the acoustic field in the liquid in each of the considered cases. The value of the dimension of the space of embedding for the conditions of the numerical experiment [5] is equal to $d = 2$. From expressions (5), (6), (11), and (15), we have $v = 0.7$ for a slit aperture and $v = 0.35$ for a circular aperture, if we take the corresponding fractal dimensions $D = 1.6$ and $D = 1.3$ obtained from the numerical experiment [5].

One can see from the analysis of expressions (9)–(11) and (12)–(15) that the acoustic field excited by radia-

tion of an unstable-cavity laser in a liquid has a fractal structure. Indeed, under the conditions $\mu \ll k$, $k\xi_0 \sin\theta > 1$, and $kl \gg 1$, or $k\rho_0 \sin\theta > 1$ and $ka \gg 1$, where l is the length of the slit aperture and a is the radius of the laser spot at the liquid surface, we have the following expression for the mean-square sound pressure at the observation point x_0z :

$$\overline{|p(r)|^2} \sim Cq^\delta \sim k^\delta, \quad (16)$$

where C is a constant determined by the problem parameters.

ACKNOWLEDGMENTS

This work was supported by the Russian Foundation for Basic Research, project no. 99-02-16334.

REFERENCES

1. F. V. Bunkin, *Selected Works* (Nauka, Moscow, 1999).
2. L. M. Lyamshev, *Laser Thermo-optic Excitation of Sound* (Nauka, Moscow, 1989).
3. G. P. Karman and J. P. Woerdman, *Opt. Lett.* **23**, 1909 (1998).
4. M. Schroeder, *Fractals, Chaos, Power Laws* (Freeman, New York, 1990).
5. V. I. Tatarskiĭ, *Theory of Fluctuation Phenomena in the Wave Propagation through a Turbulent Atmosphere* (Akad. Nauk SSSR, Moscow, 1959).

Translated by M. Lyamshev

CHRONICLE

Nikolaĭ Grigor'evich Bibikov (On His 60th Birthday)



February 13, 2000, marked the 60th birthday of the Leading Researcher of the Andreev Acoustics Institute Nikolaĭ Grigor'evich Bibikov, a prominent Russian specialist in biological and physiological acoustics.

Bibikov was born in Moscow in 1940. He was among the first graduates of the Biophysics department of the Faculty of Physics of Moscow State University. This department combined a top-level education in physics with one in modern biology, which was a new subject in Russia at that time.

Upon graduation, Bibikov once and for all selected his area of research: the study of the acoustic signal processing in the animal brain. At the time, this subject attracted the interest of one of the founders of the Acoustics Institute of the Russian Academy of Sciences, Academician N.N. Andreev, who organized a special laboratory for studying this phenomenon. The laboratory was headed by the young graduate of the Moscow Physicotechnical Institute N.A. Dubrovskii—now the director of the Andreev Acoustics Institute.

According to the advice given to Bibikov by Andreev and other researchers (especially G.V. Glekin), the first objects of Bibikov's studies were amphibians, which are characterized by a well-defined set of sounds used for communication and a relatively simple brain. Many basic features of the response of the neural elements of these animals (such as thresholds, spectral and temporal characteristics, and binaural properties) were first described by Bibikov as early as in the 1960s. In these descriptions, he used some physical and mathematical approaches that allowed him to obtain direct numerical estimates of the nerve cell parameters for simulation purposes. These studies were summarized in the candidate dissertation (in physics and mathematics) defended by Bibikov in 1972.

One of the main results obtained by Bibikov contradicted the concepts adopted by his American colleagues and consisted in the fact that the abilities of the amphibian brain are not limited to only classifying the signals of different species, but extend to analyzing in detail the frequency-temporal features of all signals perceived by the auditory periphery. Moreover, the mechanisms of signal processing in the amphibian brain were found to be close to those observed in mammals.

In 1992, Bibikov defended his doctoral dissertation (in biology), and in the following years, he concentrated on studying phenomena first observed by himself: the increase in the differential sensitivity of the auditory system in the process of adaptation, and the role of the internal and external noise in the formation of the huge dynamical range of efficient operation of the auditory system. These studies again revealed the similarity between the main mechanisms of acoustic signal processing in animals and humans. For example, the psychophysical experiments revealed a reduction in the recognition thresholds for the amplitude modulation in the process of adaptation.

Bibikov obtained a number of remarkable results in the course of his objective studies of the auditory system of dolphins (he was the first to use the nontraumatic method of recording the auditory potentials of these animals), as well as in estimating some kinds of biological noise in the ocean.

In parallel with his work at the Andreev Acoustics Institute, Bibikov carried out investigations in cooperation with scientists from Darmstadt Technical University and Konstanz University (Germany), the University of Illinois and the University of Kansas (USA), and

the Beijing Biophysics Institute (China). He is the author of more than 130 publications. His papers have been presented at many international scientific conferences. He has also given lectures at more than 15 universities in Western Europe and the United States.

Being one of the leading Russian specialists in bioacoustics, Bibikov chairs the section of the Russian Acoustical Society; he is a member of the Acoustical Society of America and a member of the International Brain Research Organization. He is also member of

some other Russian and International scientific organizations. In 1998, Bibikov was elected corresponding member of the Russian Academy of Natural Sciences for the Division of Physics.

We wish Nikolaĭ Grigor'evich Bibikov good health and further success in his creative endeavors.

Translated by E. Golyamina

CHRONICLE

Sergeĭ Nikolaevich Gurbatov (On His 50th Birthday)



Sergeĭ Nikolaevich Gurbatov—doctor of physics and mathematics, professor, laureate of the Russian Federation State Award, and chair of the Acoustics department of Lobachevskii State University, Nizhni Novgorod—turned fifty.

Gurbatov was born on February 8, 1950. In 1967, he graduated from high school with a medal and began studying at the Faculty of Radiophysics of Nizhni Novgorod (Gor'ki) State University. Since then, all his activities have been inextricably linked with the Faculty of Radiophysics. In 1977, he completed his post-graduate project and defended his candidate dissertation (under the supervision of Professor A.N. Malakhov). Gurbatov worked as an assistant professor and an associate professor at the department of Statistical Radiophysics. In 1986, he became the chair of the Acoustics department, and since 1994, has been the dean of the Faculty of Radiophysics at Nizhni Novgorod State University. In 1985, he defended his doctoral dissertation (in physics and mathematics), which was entitled

“Nonlinear Interaction and Scattering of Random Waves in Dispersion-Free Media.” In 1988, he received the title of Professor at the Acoustics department.

Gurbatov’s scientific interests are related to the theory of nonlinear random waves and turbulence, waves in randomly inhomogeneous media, nonlinear acoustics, and ocean acoustics.

Gurbatov studied the effect of multiple scattering in plane-layered, randomly inhomogeneous media on the reflection of sound pulses localized in space and time and revealed the universal waveform of the reflected waves. He performed a series of studies related to the problems of remote sensing in the ocean. In connection with the problem of the diagnostics of internal waves in the ocean, he investigated the accuracy of Doppler sensing methods in the presence of sound scattering by discrete inhomogeneities. He also studied the possibility of using parametric acoustic radiators for the remote sensing of the inhomogeneous structure of the ocean.

Gurbatov developed the statistical theory of highly nonlinear random waves and fields of different physical origin, with the only common feature being the absence of dispersion. The latter property leads to an avalanche-type generation of harmonics and to the formation of quasi-ordered structures that determine the dynamics and statistics of random fields. He studied in detail the role of the inertial nonlinearity in the formation of the probabilistic and spectral-correlative properties of fields and waves of different physical origin. In particular, he studied the statistical properties of nonlinear random fields in chaotic particle flows in gases, with allowances for the pressure and the interaction of the diverging waves. He established that, for all these media, the common characteristic feature is the development of a local and statistical self-similarity.

In 1984–1985, Gurbatov, together with his colleagues, proposed the so-called “stick-together” model, which describes the nonlinear stage of the evolution of gas consisting of gravitationally interacting particles (this model received further development in the following publications). The model is based on the three-dimensional Burgers equation and represents a generalization of the known Zel’dovich approximation. It has found application in astrophysics for describing the evolution of the large-scale structure of the Universe.

Gurbatov performed fundamental theoretical studies of nonlinear acoustic noise waves. He proposed the methods of their statistical description that allowed a

detailed analysis of the nonlinear self-action and interaction of waves at all stages before and after the shock formation. He studied the processes of the nonlinear transformation of broadband noise signals and intense acoustic pulses of complex structure. He developed the statistical theory of parametric arrays and performed theoretical and experimental studies of the effect of refraction and waveguide inhomogeneities on the parametric generation of sound. In experiments performed in cooperation with L. Bjørnø (Denmark) on the propagation of intense acoustic noise, the existence of a universal asymptotics of the energy spectrum was confirmed.

Gurbatov is the author of more than 150 scientific papers published in the leading Russian and foreign journals. Together with A.N. Malakhov and A.I. Saichev, he wrote the monograph *Nonlinear Random Waves in Dispersion-Free Media* (Nauka, Moscow, 1990); an extended version of this monograph was published in England in 1991. Gurbatov and Rudenko are the authors of the chapter on statistical nonlinear acoustics in the monograph summarizing the results obtained in nonlinear acoustics within the last twenty years and published under the title *Nonlinear Acoustics* in the United States in 1996 (editors D. Blackstock and M. Hamilton). Gurbatov is a co-author of the textbook *Acoustics in Problems* (edited by S.N. Gurbatov and O.V. Rudenko, Nauka, Moscow, 1998), which was published as a result of the cooperation between researchers from the Acoustics departments of Moscow State University and Nizhni Novgorod State University.

Gurbatov chairs the Council that confers the degrees of doctor of science at the Faculty of Radiophysics of at Nizhni Novgorod State University and the Expert Council on Radio-wave physics of the Competition Center for Fundamental Natural Sciences of the Ministry of Higher Education of the Russian Federation. Gurbatov is the vice president of the Russian Acoustical Society and a member of the American Acoustical Society; he acted as a member of the Program committees of a number of All-Russian and International scientific advanced-study schools; he also chaired the Organizing committee of the International Advanced-Study School on Dynamic and Stochastic Wave Phenomena (Nizhni Novgorod, 1992 and 1994).

In 1997, a team of researchers including Gurbatov received the Russian Federation State Award for the series of works presented under the common title "Dynamics of Intense Noise Waves and Nonlinear Structures in Dispersion-Free Media."

Gurbatov heads (together with Professor Saichev) the leading Russian scientific school in "Physics of Nonlinear and Random Waves in Application to the Problems of Acoustics and Radio-Wave Physics."

Sergeĭ Nikolaevich Gurbatov celebrates his 50th birthday in the prime of his creative life. We wish him further success.

Translated by E. Golyamina

INFORMATION

Papers—Prize Winners from the International Academic Publishing Company “Nauka/Interperiodica” in 1996–2000

In 1995, the International Academic Publishing Company “Nauka/Interperiodica” has founded special prizes to reward the authors of the most remarkable papers that appear in the journals published by this company. The prizes are intended for original scientific works first published in the journals or a series of works mainly published in these journals. The total number of prizes is 55, for more than 90 journals. The prize recipients are selected in yearly competitions.

Five papers from the *Acoustical Physics* were among the prize winners of 1996–2000. These papers are briefly reviewed below.

In 1995, the prize was given to Yu.M. Sukharevskii (from the Andreev Acoustics Institute) for his paper entitled “Statistics of Basic Acoustical Parameters of Deep-Water Oceanic Regions and the Probabilistic Range of Sonar Systems” (*Acoustical Physics*, 1995, vol. 41, no. 5, pp. 749–763).

It is well known that the operating range of a sonar system depends heavily on the hydrophysical conditions in the oceanic medium. Many years of studies in ocean acoustics resulted in the development of algorithms and computer programs, which allow one to estimate the operating range of a sonar system with the given technical parameters in the most severe environmental conditions. The development of hydroacoustic technologies, including their information branch, makes it possible to design sonars with parameters that are optimized to the acoustic conditions of the ocean. New possibilities open up for increasing the operating range and improving the efficiency of the systems. An important but poorly studied aspect of the latter problem is the determination of the sonar probabilistic range that can be realized in actual hydrophysical conditions of the ocean. The paper by Sukharevskii, who is one of the founders of hydroacoustic studies in Russia, is devoted to this topical problem.

For the hydrophysical conditions corresponding to deep-water oceanic regions, Sukharevskii determines the statistics of the basic acoustic parameters of the ocean: the sound propagation anomaly in the oceanic waveguide and the ambient noise level in the ocean; he also studies the statistics of the ratio of these quantities, which determines the signal-to-noise ratio of a sonar and, hence, the sonar operating range. Sukharevskii considers the problem of the determination of the probabilistic range that is realized with a given statistical

probability for a given sonar system in given hydro-physical conditions in the ocean. This problem is solved by using the CRV method (CRV means the logarithmic coefficient of range variation) developed by Sukharevskii on the basis of the theory of optimal frequencies. With this method, it is possible, from the known (i.e., determined from the solution of the echoranging equation) operating range of a sonar system of a given type (passive or active) with arbitrary technical parameters in arbitrary conditions, to directly determine the range of a system of the same type, with other arbitrary parameters in other conditions or a set of conditions (provided that the statistics of the parameters is known). For active sonar systems, Sukharevskii estimates the “reverberation range” in adverse conditions of a shallow sound channel at high wind speeds. This estimate allows for the range decrease in the presence of the reverberation noise, as well as in the case of the suppression of the reverberation noise, by applying a known broadband signal and a coherence processing; i.e., it allows for the range decrease related to the additional attenuation of the coherent part of the signal. The paper by Sukharevskii is a generalization of the results of numerous full-scale and numerical experiments.

Yu.I. Bobrovnikskii and T.M. Tomilina (Blagonravov Institute of Machine Science, Russian Academy of Sciences) received the prize in 1996 for their paper, entitled “General Properties and Fundamental Errors of the Method of Equivalent Sources” (*Acoustical Physics*, 1995, vol. 41, no. 5, pp. 649–660).

Calculating the field of sound radiation or scattering from an elastic body is one of the fundamental problems in acoustics. This problem was formulated more than hundred years ago, and it still attracts the attention of researchers because of the wide area of application of the results and the absence of adequate computational techniques. The problem has no analytical solution for most practically important cases, except those of the bodies of the simplest shapes. The progress in computer technology stimulated the development of numerical methods. Recent years have seen an increasing number of publications in which the problem of sound radiation is solved by the so-called method of equivalent sources. In particular, this method is used as an alternative of the popular boundary-element method. The comparison of these methods showed that the machine time required by the method of equivalent

sources is several times shorter than that required by the other method, provided that the results are obtained with the same accuracy. However, the practical application of the method of equivalent sources is hindered by the absence of justified recommendations for the choice of the algorithms and by the unknown limits of validity of this method.

The purpose of the paper by Bobrovnikskii and Tomilina was to systematically investigate the general properties of the method of equivalent sources in relation to the specific features of the representation of the field produced by a source (scatterer) in the form of equivalent acoustic sources. The authors analyzed the fundamental errors of this method and formulated several problems whose solutions may reveal the possibilities for increasing the accuracy of the method.

Bobrovnikskii and Tomilina studied the method of equivalent sources as it applied to the problem of sound radiation by complex elastic structures. The method consists in replacing a real source by a system of simple internal equivalent sources. It has a number of advantages (high rate and controlled accuracy of computations). However, as was mentioned above, the method is not yet formalized in terms of the algorithms because of the insufficient theoretical basis. Bobrovnikskii and Tomilina considered the problem of the loss of accuracy of the method at the so-called internal resonance frequencies. They showed that, mathematically, this situation means the functional incompleteness of the system of the fields of equivalent sources, and, physically, it can be represented as a "shunting" of the external medium by its inner volume. It was found that a number of general properties of the method (inadequate conditionality, spatial oscillations of sources) are related to the behavioral features of inhomogeneous waves or, in other words, higher spatial harmonics of the field, which are characterized by fast oscillations along some coordinates and fast decay along other coordinates. These spatial harmonics of the field determine the condition of the representability of acoustic fields by equivalent sources. Considerable study was given to the fundamental errors of the method due to the incompleteness of the fields of the internal equivalent sources. The dependence of these errors on the arrangement of sources and on the errors in the input data was discussed. Bobrovnikskii and Tomilina formulated four unsolved theoretical problems related to the choice of the optimal values for the parameters of the algorithm. As an example, they performed an analytical study by using the Neumann radiation problem for a sphere. The validity of the results obtained for the sources of other geometrical shapes and the physical interpretation of the results were discussed in detail.

In 1997, the prize was awarded to V.G. Andreev, V.N. Dmitriev, Yu.A. Pishchal'nikov, O.V. Rudenko, O.A. Sapozhnikov, and A.P. Sarvazyan (Moscow State

University) for the paper entitled "Observation of Shear Waves Excited by Focused Ultrasound in a Rubber-like Medium" (*Acoustical Physics*, 1997, vol. 43, no. 2, pp. 123–128).

Acoustic waves propagating in an absorbing medium transfer their momentum to the medium. In liquids, which do not possess shear elasticity, this effect gives rise to acoustic streaming. In solids, where such hydrodynamic streaming is impossible, elastic stresses occur. As a result, the sound absorption region should become a source of elastic perturbations, specifically, shear waves. It is generally believed that, in the course of longitudinal wave propagation in a homogeneous solid, shear waves can appear only as a result of the longitudinal wave reflection from the boundaries. However, one can expect that even in media with weak sound absorption, the excitation of shear stresses should be noticeable in regions characterized by high intensity gradients of longitudinal waves. The subject of the paper was the experimental study of this effect and its theoretical substantiation.

High intensity gradients of longitudinal waves arise at the "waist" of a focused acoustic beam whose transverse dimensions can be comparable with the longitudinal wavelength. However, even at the focus of a relatively intense and short wave, the arising shear stresses and the corresponding strains may be fairly small, and their measurement may be difficult. To increase the shear strains, the authors used a medium with a small shear modulus that was several orders of magnitude less than the longitudinal elastic modulus. Another important requirement was using a nondestructive method for detecting the effect. For this purpose, the authors chose the optical method.

The paper by Andreev *et al.* presents the results of the experiment in which the shear wave excited owing to the absorption of the longitudinal wave was detected. The authors used a focused beam of longitudinal waves of frequencies 1–2 MHz propagating in a transparent rubber-like medium. The shear waves were detected by a probing light beam. The measured velocity of the sound wave coincided with its theoretical value calculated from the known shear modulus of the medium. A theoretical model of the effect was developed, which made it possible to calculate the characteristics of the generated shear wave as the functions of the parameters of the medium and the initial longitudinal wave. The theory adequately describes the experimental results.

In 1998, the prize winners were Yu.P. Lysanov and L.M. Lyamshev (Andreev Acoustics Institute) for their paper entitled "Sound Scattering by Random Volume Inhomogeneities with a Fractal Spectrum" (*Acoustical Physics*, 1998, vol. 44, no. 4, pp. 434–436).

Numerous experimental data testify that the frequency dependence of the low-frequency sound attenu-

ation in an underwater sound channel in the ocean is described by the so-called “three-halves power law.” This dependence had no explanation. Recently, it has been found that the attenuation and its frequency dependence can be attributed to the sound scattering by volume inhomogeneities, i.e., by fluctuations of the refractive index that occur in the underwater sound channel, if one takes into account the anisotropy of these inhomogeneities and selects an adequate correlation function for their description (Lysanov). However, this model was insufficient for a full understanding of the phenomenon. Lyamshev has put forward the idea that the attenuation may have a fractal origin, because the exponent in the frequency dependence is a fractional number. The study performed in collaboration by the two authors showed that the three-halves power law has a fractal origin, and the volume inhomogeneities in the underwater sound channel have the form of clouds with fractal boundaries, or more precisely, clouds–multifractals.

In their paper, Lysanov and Lyamshev considered the sound scattering by random anisotropic volume inhomogeneities (refraction index fluctuations) in terms of the small perturbation method. The inhomogeneities are assumed to be highly anisotropic, namely, small-scale in depth and large-scale in the horizontal plane. According to the results of multiple experimental studies in the ocean, this type of inhomogeneities is typical of the oceanic medium. The paper reveals the relationship between the observed frequency dependence of the attenuation of low-frequency sound propagating in the underwater sound channel and the fractal properties of highly anisotropic inhomogeneities. Lysanov and Lyamshev were the first to reveal the fractal origin of the low-frequency sound attenuation in the underwater sound channel and to theoretically justify the experimental frequency dependence of attenuation described by the three-halves power law. The attenuation of sound is caused by its scattering from the boundaries of the volume inhomogeneities and the leakage of the scattered waves out of the underwater sound channel. It was found that the fractal dimension of the boundaries of volume inhomogeneities in the ocean virtually coincides with the fractal dimension of the cloud boundaries in atmosphere. Since the atmosphere is a stratified medium, clouds in the atmosphere are generally not self-similar, but self-affine. In this connection, clouds in the atmosphere are considered as multifractals. This is also true for the volume inhomogeneities in a stratified ocean. Hence, one can consider the volume inhomogeneities (refractive index fluctuations) in the ocean as clouds–multifractals with an inherent spectrum of fractal dimensions (spectrum of singularities). The absolute values of the attenuation coefficient, which are calculated for the low-frequency sound propagation in the underwater sound channel in

the ocean on the basis of the proposed theoretical model, agree well with the average values obtained from the full-scale experiments. Thus, one can conclude that not only the frequency dependence of low-frequency sound attenuation has a fractal origin, but also the highly anisotropic volume inhomogeneities in the underwater sound channel represent clouds–multifractals, and in some sense they are similar to clouds in the atmosphere.

The 1999 prize went to A.P. Brysev, F.V. Bunkin, L.M. Krutyanskiĭ, V.L. Preobrazhenskiĭ, A.D. Stakhovskii (General Physics Institute, Russian Academy of Sciences), Yu.V. Pyl’nov (Moscow Institute of Radio Engineering, Electronics, and Automation), M.F. Hamilton, K.B. Cunningham, and S.J. Younghouse (University of Texas at Austin, USA). Their paper was entitled “Nonlinear Propagation of a Quasi-Plane Conjugate Ultrasonic Beam” (*Acoustical Physics*, 1998, vol. 44, no. 6, pp. 738–748).

Phase conjugation is a wave field transformation that results in a reversal of the direction of wave propagation with the initial phase and amplitude distributions being retained. The phenomenon of phase conjugation for ultrasonic waves attracts the attention of researchers because of the specific features of conjugate wavefronts and unique possibilities offered by the phase conjugation technique for physical studies, nondestructive testing, technology, and medicine.

In the last few years, considerable progress has been made in studies of the phase conjugation of ultrasonic beams. This progress is mainly due to the efforts of Russian scientists, namely, the authors of the aforementioned paper. (One of them, Bunkin, pioneered the systematic studies of the physical methods of phase conjugation in acoustics of liquids.) In particular, using the principles of the parametric phase conjugation in magnetostrictive ceramics, they applied a pumping magnetic field and observed the phase conjugation for ultrasound at the frequencies 5–30 MHz with a gigantic (up to 80 dB) amplification relative to the incident wave. These results were published earlier in *Acoustical Physics*.

The propagation of intense conjugate ultrasonic beams is accompanied by nonlinear distortions, which can have an adverse effect on the quality of phase conjugation. This problem is the subject of the paper awarded in 1999.

The paper presents the results of the experimental and theoretical studies of the phase conjugation of ultrasound and the studies of the nonlinear propagation of a quasi-plane conjugate ultrasonic beam in water. A quantitative agreement between the experimental and theoretical results was obtained for the initial intensity of the conjugate beam 2 W/cm^2 in the region before the shock formation. An increase in the waveform distortion was observed with an increasing intensity of the

conjugate beam and with the distance traveled by the beam. By a numerical simulation of the conditions close to the experimental ones, it was demonstrated that, up to the aforementioned intensity of ultrasound, the distortions of the transverse profile of the conjugate beam are mainly caused by the finite size of the conjugator aperture.

The development of highly efficient methods of acoustic phase conjugation opened up a new stage in

the development of both physics and technical applications of conjugate ultrasonic beams. One might expect that, already in the next few years, new ultrasonic phase-conjugation systems will be designed for special applications.

L.M. Lyamshev

Translated by E. Golyamina